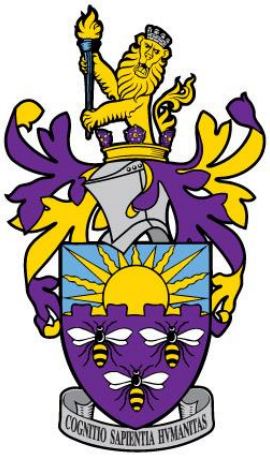

Development of advanced laser processes for multiscale surface modifications of functional electrodes in Liquid Chromatography Mass Spectrometer (LC-MS) instrumentation

A thesis submitted to The University of Manchester for the degree of

Doctor of Philosophy

in the Faculty of Science and Engineering

2023

Anupam Ghosal

School of Engineering

Department of Mechanical, Aerospace and Civil Engineering

The University of Manchester

MANCHESTER 1824
The University of Manchester

UKRI Engineering and Physical Sciences Research Council

Waters
THE SCIENCE OF WHAT'S POSSIBLE.®

[Blank Page]

Table of Contents

List of Abbreviations and Symbols

List of Abbreviations

AFM	Atomic Force Microscopy
EDS/X	Energy Dispersive X-ray Spectroscopy
FAS	Fluoroalkylsilane
HAZ	Heat affected zone
HSFL	High Spatial Frequency LIPSS
LIPSS	Laser Induced Periodic Surface Structures
LSFL	Low Spatial Frequency LIPSS
LC	Liquid Chromatography
LC-MS	Liquid Chromatography – Mass Spectrometry
LST	Laser Surface Texturing
MS	Mass Spectrometry
NOP	Number of pulses in one laser spot
SEM	Scanning Electron Microscope
TEM	Transmission Electromagnetic Mode
ToF-SIMS	Time-of-Flight Secondary Ion Mass Spectrometry
USP	Ultra-short Pulse
UV	Ultra-violet spectrum
XPS	X-ray Photoelectron Spectroscopy

List of Symbols

E_{pulse}	Laser pulse energy (J)
F_p	Peak fluence (J/cm^2)
F_0	Input fluence (J/cm^2)
F_{th}	Ablation Threshold fluence (J/cm^2)
Fa^{max}	Maximum accumulated fluence (J/cm^2)
f_{laser}	Frequency of the pulse laser
fs	Femtosecond (10^{-15} sec)
ns	Nanosecond (10^{-9} sec)
ps	Picosecond (10^{-12} sec)
M^2	Laser beam quality factor
N_{eff}	Number of effective pulses at one spot
Nsc	Number of surface scans
Ra	Average roughness
Sa	Average area roughness
t_{laser}	Pulse duration of the laser
Vsc	Scan velocity
λ	Laser wavelength (nm)
Δx	Pulse-to-pulse distance (μm)
Δy	Hatch distance (μm)
Δz	Gap width between the sample surface and glass cover (μm)
Δ_{LIPSS}	LIPSS periodicity (nm)

Table of Figures

List of Tables

List of Publications

Journals

- Surface engineering with structured femtosecond laser vector fields, *Ghosal, A., Allegre, O., Liu, Z. & Jones, G., Dec 2021, In: Results in Optics. 5, December 2021, 7 p., 100179. DOI: 10.1016/j.rio.2021.100179*

Conferences

- Functional surface modification using tailored ultrashort-pulse laser light for applications in Liquid Chromatography Mass Spectrometry instruments, *Ghosal, A., Allegre, O., Liu, Z. & Jones, G., 6 Sep 2022, 12th CIRP Conference on Photonic Technologies [LANE 2022]. Elsevier BV, Vol. 111. p. 625-628 4 p. (Procedia CIRP).*

- Effect of confined laser plasma plumes on the formation of LIPSS structures on stainless steel 316L, *Ghosal, A., Allegre, O., Liu, Z. & Jones, G., Jun 2021, Lasers in Manufacturing (LiM) 2021. https://wlt.de/lim2021-proceedings/surface-functionalization. 6 p.*

- Structured optical fields for short and ultrashort pulse lasers: principles and example applications, *Ghosal, A., Allegre, O., Liu, Z., Jones, G. & Oh, A., Mar 2023, Industrial Laser Applications Symposium (ILAS) 2023.*

- Development of advanced laser processes for multiscale surface modification of functional electrodes in Liquid Chromatography – Mass Spectrometer instrumentation, *Ghosal, A., Allegre, O., Liu, Z. & Jones, G., Mar 2021, Industrial Laser Applications Symposium (ILAS) 2021.*

Abstract

LC-MS is a critical instrumentation technique for identifying components of mixtures containing both organic and inorganic substances. Because of this, the internal components of the mass spectrometer are susceptible to contamination during instrument operation. Direct contact between the instrument electrodes and the gas-phase ion particles is particularly problematic as it affects the sensitivity of the system. Therefore, there is a need for ion contamination resistant electrode surfaces. Surface modification methods using lasers are widely used for functionalisation applications such as self-cleaning surfaces, antibacterial surfaces, friction reduction and surface enhancement. This research hypothesises that laser surface modification can be controlled and used to create tailored surfaces to reduce surface contamination of critical components during the operation of LC-MS systems. An aperture plate electrode was used to test the hypothesis. As it is used as an ion beam collimator in the mass spectrometer, the aperture plate is susceptible to contamination. The aperture plate electrode is made of stainless steel 316L and has a lapped surface. The bovine insulin protein was used as a surface contaminant in our tests.

Surface texturing on stainless steel 316L surfaces using short and ultrashort pulse lasers was studied to understand the generation of nanoscale surface structures. Selected cases of surface texturing were tested for their impact on the protein contamination behaviour of the aperture plate. A 532 nm nanosecond laser was used to create LIPSS with an extremely low aspect ratio and surfaces with significantly reduced roughness. Both LSFL and HSFL were created using a 355 nm picosecond laser. A novel method for generating HSFL features was identified that uses the laser plasma plume as one of the influencing parameters. The novel method showed finer control in the generation of HSFL features. A 800 nm femtosecond laser was used to experiment with modalities of structured laser vector fields and demonstrated the possibilities of creating complex surfaces with different beam types.

The protein contamination behaviour tests show a reduction in contamination build-up rate on laser-textured aperture plates compared to non-laser-machined aperture plates. In addition, the results demonstrate some level of control over surface topography and surface chemistry. These improvements support our hypothesis that laser processing can be used to mitigate surface contamination. The promising results pave the way for further investigation to control and reduce contamination behaviour. In addition, the results of this study can be applied to other electrodes that are susceptible to surface degradation by analyte ions in the gas phase.

Declaration

No portion of the work referred to in the thesis has been submitted in support of an application for another degree or qualification of this or any other university or other institute of learning.

Anupam Ghosal, March 2023

Copyright Statement

Acknowledgements

I would like to express my deepest gratitude to my supervisor, Dr Olivier Allegre, whose motivation helped me consider this study and for his constant guidance and essential support throughout this journey. I hereby also thank my university's co-supervisor, Dr Zhu Liu, for her guidance and timely suggestions. My sincere thanks go to my industrial supervisor Dr Gordon Jones from Waters Corporation, for his advice and endless optimism and for helping me understand the project from an industrial perspective. Their motivation pushed me to carry on with the project in some of the most challenging times during the COVID-19 pandemic and my visa struggles.

I would like to thank my internal assessment examiner Dr Robert Heinemann, for reviewing my progress reports and for your timely advice. It was a memorable learning experience. My thanks to Dr David Whitehead and Daniel Wilson from the Laser Processing and Research Centre (LPRC) for their help and continuous support.

Thank you to all members and staff of the Electron Microscopy Centre, the Photon Science Institute, the National Graphene Institute and the School of MACE. This work could not have been completed without their facilities and support.

A hearty thank you to the colleagues and staff at the EPSRC CDT on Materials for Demanding Environment for their advice and support over the years. The cohort atmosphere created by the CDT is unprecedented. I wish my fellow students every success. It is a memory worth cherishing.

I am grateful to the UK Engineering and Physical Sciences Research Council (EPSRC) for providing financial support for this research activity within the Materials for Demanding Environment under the University of Manchester's Centre for Doctoral Training [grant EP/L01680X/1]. I am also grateful to the Waters Corporation, Wilmslow, for partnering with this research and providing the necessary support for the work.

I thank my parents, in-laws, brothers and sisters for their unconditional love and support. Special thanks to Amrita, my partner, who has remained a constant inspiration and encouragement throughout this journey. Finally, but more importantly, I am grateful to the Almighty God for this opportunity and the strength to continue.

Dedicated to the Almighty God

for his grace and this opportunity !!!

Chapter 1

Introduction

The chapter introduces the history and the industrial relevance of LC-MS instrumentation. It discusses the industrial problem scenario related to the mass spectrometer and the motivation for the research. The research aims and objectives are defined here, along with the potential challenges of the research. Finally, an outline of the thesis's structure is provided for the reader's reference.

1.1 LC-MS instrumentation: History and industrial importance

Russian botanist Mikhail Semenovich Tsvet devised a method in 1903 to separate plant pigments. He named his technique chromatography, derived from the Greek words for colour (chróma) and writing (graphē). The technique was further developed substantially by the Nobel prize winner chemists Archer John Porter Martin and Richard Laurence Millington Synge during the 1940s and 1950s. Chromatography focuses on separating components of a mixture. Since then, chromatography principles have been applied in different ways, and methods, such as paper chromatography, gas chromatography and high-performance liquid chromatography, have been developed [1]. In liquid chromatography, the mixture (termed the mobile phase) is converted to fluid and

passed over a stationary phase bed. The relative distribution coefficients of the individual fluids in the mobile phase help them get separated [2]. The research in the field of liquid chromatography has led to the development of systems operating at high pressure, such as HPLC (High Performance Liquid Chromatography) around 50-350 bar [3,4] and UPLC (Ultra Performance Liquid Chromatography) operating up to 1030 bar [5].

On the other hand, the mass spectrometry system was first developed by Francis Aston in the early 1920s based on Joseph John Thomson's parabola spectrograph (designed in 1913). His instrument was further modified over the years. It was brought to the masses by several scientists, with Alfred Nier being prominent [6]. The mass spectrometry technique identifies unknown compounds, quantifies known compounds, and explores molecular structures. The substances are analysed using the constituent molecules' mass-to-charge ratio (m/z). It allows both qualitative and quantitative determination.

Victor Tal'roze pioneered the first attempts to couple LC with MS in the late 1960s. They began by directly spraying liquid into the ionisation chamber of a low-pressure electron impact mass spectrometer [7]. The coupling of LC to the MS system is complex as both systems operate in different phases, i.e. liquid and gas. The interfacing problem was solved by introducing ionisation techniques [8]. The advantage of using the LC-MS system is that the separation and the determination of the atomic/molecular masses can be performed simultaneously. It can be used with both organic and inorganic substances. It finds application in forensic science such as doping tests [9], pharmacokinetics [10,11], determination of assay of drugs and intermediates [12–14], agriculture [15], the food industry [16–20], environmental studies [21,22], and in the analysis of volatile explosive residues [23]. Recently, LC-MS was used to search peptide biomarkers for pathogens such as the SARS-CoV-2 virus [24,25].

The LC-MS system is now widely used across the globe. The global LC-MS market was valued at US$ 2.317 billion in 2022 and is forecast to a readjusted size of US$ 3.087 billion by 2028 [26]. The primary players in the LC-MS market are Agilent Technologies Inc, Waters Corporation, Shimadzu Corporation, Thermo Fischer Scientific Inc, Sciex, PerkinElmer Inc, and Bruker Corporation. They are focused on research and development in the healthcare sector. For example, Waters [25,27,28], Thermo Fischer Scientific [29], and Sciex [30] collaborated with universities and research labs to develop the LC-MS instrumentation for the SARS-CoV-2 pathogen (COVID-19 virus).

1.2 Industrial problem scenario and Research focus

The LC-MS system is rigorously used for analysing complex mixtures, both organic (such as blood plasma and saliva)[31] and inorganic [32]. Analysing such mixtures leads to contamination and degradation of the Mass-Spectrometry instrument's electrode surfaces over time. Reducing surface contamination is one of the primary research focus areas [33]. The contamination build-up is often significant with organic molecules such as protein complexes. Also, as the LC-MS market focuses on the healthcare sector, the analysis of organic compounds increases with time, making contamination of the instrumentation surfaces with organic compounds a significant concern.

The mass spectrometer phase in the LC-MS system generates ions from the input mixture through ionisation. The ionised particles with hypothermal energies move along a designated path guided by electrodes and reach the detector for identification. The contamination occurs in the mass spectrometer when these irradiated ions collide with the electrode surfaces. The collision can be due to stray divergent ions or by design. Ideally,

as per the instrument design intent, the ions that collide with the electrode surfaces should get neutralised and fall off by gravity. However, some of the ions continue to stick to the electrode surfaces. The phenomenon by which these irradiated ions stick to the surface can be best associated with the surface adsorption theory. Due to the contamination, the quality of the electrodes decreases with time, affecting the instrument's overall performance. Some contamination-prone electrodes are aperture plates, pusher plates, einzel lens plates, and quadrupole rods. Out of these electrodes, the aperture plate was selected for investigating the contamination behaviour. An organic contaminant (*bovine insulin protein*) was chosen for the study as the industry focus is reducing organic contamination.

The aperture plate is made of stainless steel 316L (SS316L) and is a beam collimator. The plate material SS316L is mainly used for its non-magnetic properties and excellent outgassing property. Figure 1.1 shows the image of the aperture plate the industrial sponsor Waters Corporation provided. The side facing the ion beam has a high surface finish. The potential region where the ions collide with the aperture plate surface is shown in Figure 1.2. The plate blocks the divergent ions and only allows the almost parallel central ions to pass through. The electrode surface is charged opposite to the ions. The blocked ions are supposed to fall off the surface after being neutralised. The contamination build-up happens when the ions remain on the surface and becomes an active zone for retaining the subsequent ions colliding on them. Any charged particle near or on the aperture plate's central opening can induce a slight divergence on ions close to the opening's surface, affecting collimated ions' paths. The affected ions induce errors such as signal loss and the spread of the signal peaks during the detection phase and impact the system's overall sensitivity. Furthermore, the LC-MS system is a high vacuum system and the frequent instrument maintenance downtime due to electrode contamination results in further

degradation. Hence, improving the surface resistance towards protein contamination is vital in improving the overall performance of the mass-spectrometry and the LC-MS system.

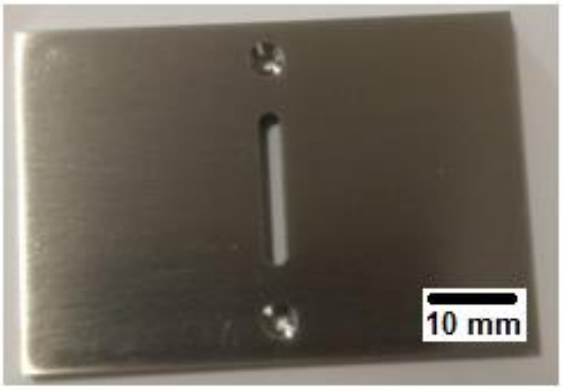

Figure 1.1: Optical image of the aperture plate electrode (design copyright Waters Corporation)

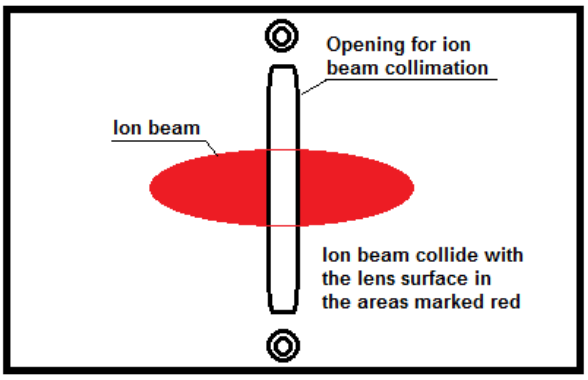

Figure 1.2: Illustration of aperture plate design and ion beam contamination

The industrial partner specifications indicate that the irradiated ions move with soft-landing energy and do not permanently cling to the electrode surface after the collision. They noted it from the fluctuations in the surface potential of the electrodes. Most accumulated contamination in a region falls off the surface after a specific build-up. Hence, it is difficult to identify a consistent location of contamination. However, the pattern of the contamination indicates more of a temporary or unstable connection with the surface and can be associated with the physical adsorption phenomenon. Surface roughness plays a

crucial role in protein physical adsorption as rougher surfaces provide more contact area for the endpoints of the protein ions. The organic contaminants, i.e. proteins ions, are soft gelatinous globules with diameters from 2.4 nm (insulin protein [34]) to 11 nm (rubisco [35]) only. Hence, improving the surface topography should affect the contamination behaviour.

Many surface engineering processes are available to improve the surface characteristics, such as sandblasting, mechanical machining, chemical etching, and the use of laser. Out of these methods, laser surface modification is one of the versatile methods to meet surface requirements for advanced engineering materials [36]. In laser surface modification, the material surface is modified through heating, melting and ablation using the laser as the energy providing medium. It allows for modifying surface topography and surface chemistry by controlling the laser processing parameters to achieve highly functional surfaces. Some laser-based processes that allow both topography and chemistry changes are laser surface texturing, laser surface remelting, and laser shock peening.

Figure 1.3 shows laser modified surfaces containing microstructures in (a) and nanoscale structures in (b). The microstructures in the matrix pattern are on the scale of 30-50 μm. The nanostructures are termed Laser-Induced Periodic Surface Structures (LIPSS), with a periodicity of ~580 nm and a peak-to-valley depth of ~250 nm. Such complex topographies can be produced employing different micro/nano texturing approaches or a combination of them, showing the degree of control over the scale of the structures.

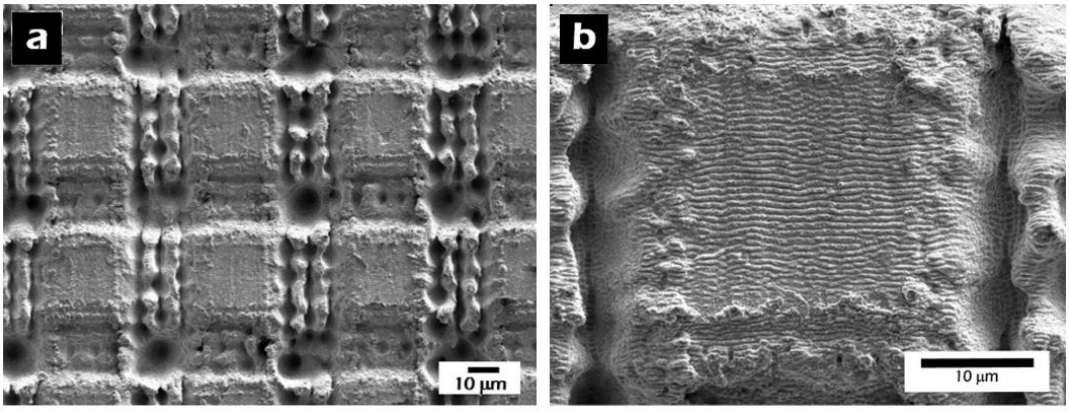

Figure 1.3: Microstructures vs Nanostructures (LIPSS) – SEM micrographs of hierarchical structures fabricated on stainless steel (adapted from [37]**). (a) Microstructures: Matrix micro pattern with a pitch distance of 50 µm and covered by LIPSS on the flat top surface; (b) Nanostructures: LIPSS of periodicity ~580 nm and depth 250 nm.**
Laser source: λ=800 nm, t_{laser}=130 fs, and f_{laser}=1 kHz.

Therefore, laser surface modification was the choice of process for this research, and also it satisfies the engineering research specifications from the industrial partner. Thus, understanding the potential of laser surface modification methods for producing protein contamination resistant surfaces is the primary objective of this research.

1.3 Aims and objectives

The research aims to develop a tailored surface on the 316L stainless steel based aperture plate electrode, using laser surface modification, that is resistant to contamination from irradiation of soft-landed bovine insulin protein ions in vacuum conditions.

The objectives of the research are:-

1. To investigate and understand the effect of laser processing parameters and the laser processing environment on generating surface topographies. And to analyse the generated surface topographies and chemistry.

2. To generate shallow depth low aspect ratio features and almost flat surfaces using nanosecond laser where the surface roughness is of the scale similar to the size of protein ions where the sizes of the ions vary from 2.5 nm to 11 nm in diameter.
3. To produce uniform high spatial frequency LIPSS (HSFL) features using an ultrashort pulse laser for a large working area (around 20x20 mm) using a reliable and straightforward method.
4. To laser process the aperture plate electrode with the selected laser cases and investigate the protein contamination behaviour using a test rig. The test rig simulates the mass-spectrometer operation, and the electrode is irradiated with a controlled beam of protein ions.

1.4 Scientific and technological challenges

The research is driven by the need to address the problems identified in the industry and the solutions that can be developed by laser surface processing. Many scientific questions may be raised during the identification of a potential solution. Different surface topographies can be obtained by controlling the laser processing parameters. So, the first question is: ***For the given material SS316L, what are the laser processing parameters for generating nanoscale surface structures, and what is the scale of those structures?*** This research uses different laser types, i.e. 532 nm wavelength nanosecond laser, 355 nm picosecond laser and 800 nm femtosecond laser, to generate nanoscale surface structures. The laser material interaction changes with the different laser regimes, i.e. from nanosecond to femtosecond, affecting the type of topographies generated on the surface.

Analysing these nanoscale structures provides a deeper understanding and a perspective of the scale and the type of structures.

Protein ions are sticky, gelatinous and very small, especially the protein selected for this research, i.e. bovine insulin (diameter ~2.5 nm). In our case, the proteins land on the electrode surfaces with soft-landing energies while travelling in the mass spectrometer. So, it can be hypothesised that controlling surface roughness is crucial to reducing physical adsorption. Therefore, the second question is: ***Is it possible to create surface topographies similar to the scale of protein ions?*** Three approaches have been experimented with from the mentioned hypothesis. The first approach is to generate small features with low depth, such as high spatial frequency LIPSS (HSFL) structures over the entire surface with the picosecond laser. In this approach, a new novel method to generate uniform HSFL features was developed with the laser plasma plume as one of the impacting parameters. The second approach was to generate shallow features, i.e. with a very low aspect ratio, and the last one was to generate almost flat surfaces where the laser is used to polish the surface, both approaches using the nanosecond laser. These approaches were based on the hypothesis to reduce the nucleation sites of the contamination build-up in the crevices/valleys of the surface structures.

1.5 Thesis outline

This thesis comprises seven chapters, including the introduction (**Chapter 1**).

Chapter 2 reviews the existing literature related to the research and contains two sections. The first section provides an overview of the interaction of the protein with the metal surface. It contains the background related to proteins, ionisation of proteins, and soft

and reactive landing of proteins ions. The section also helps to understand organic particles' contamination of metal surfaces during mass-spectrometry operations. In our case, irradiated protein ions with soft-landing energies moving in a vacuum environment collide and stick to the metal surface. The second section provides an overview of laser fundamentals and laser surface modification techniques where surface topography and chemistry are affected. Past research on lased-induced nanostructures was reviewed to understand the relevance to the current work and identify research gaps.

Chapter 3 briefly describes stainless steel 316L test samples and electrodes used in the experiments, the laser system and the instruments used to characterise the samples. It also details the experimental setup for laser processing the test samples and the aperture plate electrodes. A section on the protein contamination behaviour of a non-laser processed aperture plate, i.e. the reference electrode, is presented. It is for a comparative study with laser processed aperture plates after their protein contamination behaviour.

Chapter 4 presents laser processing results with the ***532 nm nanosecond*** laser. It reports the nanoscale surface textures such as LIPSS, shallow periodic structures and nano-polished type surfaces (Ra ~2.2 nm) produced in the air environment on local test samples. Selected laser processing cases were used to process the aperture plate electrode surfaces for protein contamination behaviour testing. The protein contamination behaviour of the laser processed aperture plates is presented and compared with the reference electrode.

Chapter 5 presents laser processing results with the ***355 nm picosecond*** laser. It presents the laser induced nanostructures, such as LSFL and HSFL, obtained on the surface after laser processing. It also presents a novel method of producing uniform HSFL structures, using the laser plasma plumes as one of the impacting parameters. Selected cases were used for producing laser processed aperture plate electrodes. The protein

contamination behaviour of the laser processed aperture plates is presented and compared with the reference electrode.

Chapter 6 presents laser processing results with the ***800 nm femtosecond*** laser. Nanoscale surface structures were produced for different polarisations such as linear, circular, radial and azimuthal. It also presents the application of the polarisation conditions for real-world case scenarios. Laser processing of the aperture plates was not done for the femtosecond laser.

Chapter 7 summarises the general conclusion of this work, the contribution to knowledge and recommendations for future work.

Chapter 2

Literature review

The chapter reviews the essential knowledge needed for the progress of the work. It is divided into two parts: the first part provides an overview of proteins and their interaction with metal surfaces to understand the background of the research problem. The second part presents an overview of lasers and their application in modifying surface topographies and properties. This part also highlights the laser-material interaction mechanism and the generation of nanoscale surface structures.

2.1 Protein's interaction with the metal surface

Complex organic molecules such as proteins and keratins are primary organic contaminants on the metal surfaces of electrodes and spray orifices during the operation of the mass spectrometers [38]. This section tries to provide an insight into the possible nature of contamination by organic ions during the mass-spectrometry operation.

2.1.1 Proteins

Proteins, derived from the Greek word "*proteios*", meaning "of primary importance", are the essential building blocks of most living cells and play an important role in biological processes. They have different structural and functional properties, such as enzymes, antibodies, and hormones. Other proteins are essential for mechanical support, generation and transmission of nerve impulses, and regulation of gene transportation, among other things [39].

Proteins are large organic molecules containing carbon, oxygen, hydrogen, nitrogen, sulphur and phosphorous. The primary structure of proteins constitutes 20 common types of amino acids along with their derived variations. The general structure of the amino acid (Figure 2.1) consists of a central α-carbon atom to which an amino group, a hydrogen atom, a carboxyl group and a functional side chain (R) are attached. Amino acids can be grouped into nonpolar (hydrophobic), polar, and positively or negatively charged [39,40]. Some amino acids can also react with noble metals, such as *Cysteine* and *Methionine* containing sulphur bonds and actively react with gold [41]. Notably, the peptides consist of 2 to 50 amino acids, whereas molecules with more than 50 amino acids are considered proteins.

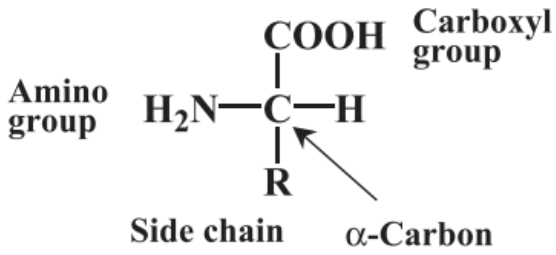

Figure 2.1: General structure of amino acid showing the amino group, a hydrogen atom, a carboxyl group, and a functional side chain (R) attached to the central α-carbon atom.

The interactions between the primary proteins, the carboxyl and amino groups, result in 3-dimensional structures such as α-helices, β-sheets/turns, random coils and disordered structures, also known as the secondary structures. The interactions between the side chains (the secondary structures) result in the tertiary structure of the protein. The spatial arrangement of these structures results in the formation of a quaternary structure, i.e. an overall 3-dimensional structure of the protein, as illustrated in Figure 2.2 [39,40].

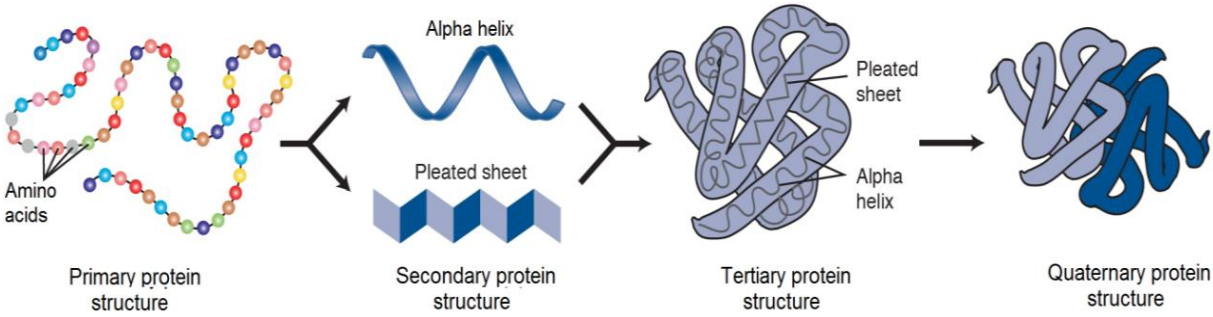

Figure 2.2: Protein's four structural arrangements (adapted from [42]**)**

In an aqueous environment, the protein's non-polar side chains (hydrophobic) tend to embed themselves inside the folded protein, and the polar side chains (hydrophilic) arrange on the surface. These polar/non-polar regions are one of the central protein-surface interaction regions.

2.1.1.1 Bovine Insulin

The bovine insulin ($C_{254}H_{377}N_{65}O_{75}S_6$) is a small protein consisting of 51 amino acids with a mass close to 5740 Da (Dalton) and one of the smallest proteins. It consists of two small α-chains of amino acids connected by two disulphide bridges, as shown in Figure

2.3. It contains the following amino-acid residues[1]: 3 alanines, 1 arginine, 3 asparagines, 6 cysteines, 3 phenylalanines, 4 glycines, 4 glutamic acids, 3 glutamines, 2 histidines, 1 isoleucine, 6 leucines, 1 lysine, 1 proline, 3 serine, 4 tyrosines, 1 threonine, and 5 valines. The protein is globular in shape with a diameter of around 2.5 nm [34,43]. It differs from human insulin by three amino acids.

It is used as a test specimen for performance benchmarking of mass spectrometers and is one of the organic surface contaminants of the electrodes. Generally, this protein was used to treat diabetes but is rapidly replaced with pork insulin and other varieties.

Bovine insulin (cow insulin) is the selected test protein for this research work.

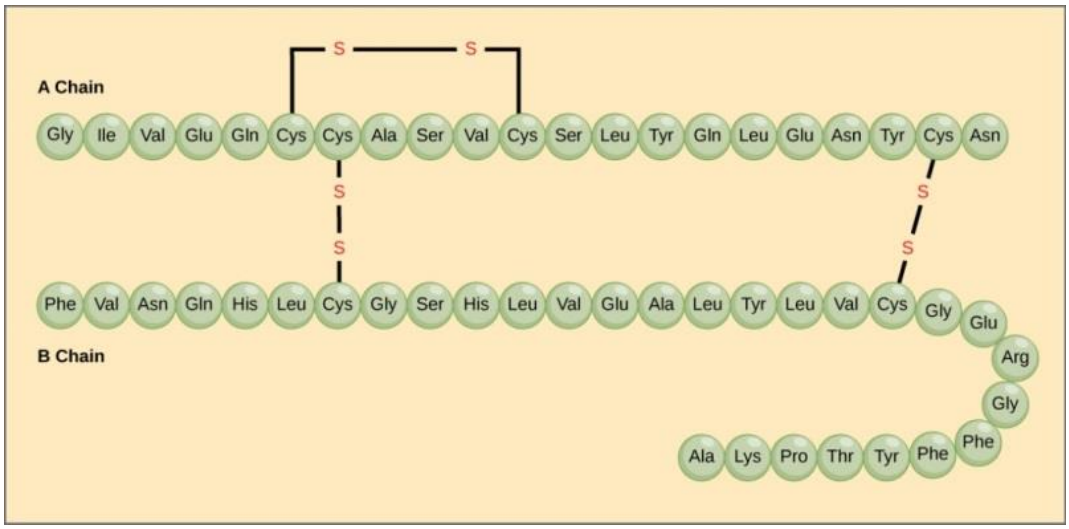

Figure 2.3: The schematic of the bovine insulin protein structure. Two sulphide linkages join the two amino acid chains. A third sulphide link joins two cysteine amino groups in the same chain. [44]

[1] When two or more amino acids combine to form a peptide, the elements of water are removed, and what remains of each amino acid is called an **amino-acid residue**.

2.1.2 Ionisation of proteins

Electrospray Ionisation (ESI) is the most commonly used process to generate gas phase protein ions from liquid mixtures under atmospheric pressure conditions. It is a soft ionisation method and produces ions without the fragmentation of the analyte. Both positive and negative ions can be generated through this process [45,46].

Figure 2.4 shows positive ions generation through ESI and eventually neutralising through reduction. A liquid solution is prepared using the analyte (the protein molecules) and the ion carrier (such as acetic acid). The ion carrier facilitates ionisation by introducing a charge to the liquid. This liquid is dispersed into a fine aerosol. The fine droplets become more and more charged with rapid evaporation and fragment explosively, leaving a stream of charged ions of the analyte molecules. The charged ions can be neutralised with an oppositely charged plate.

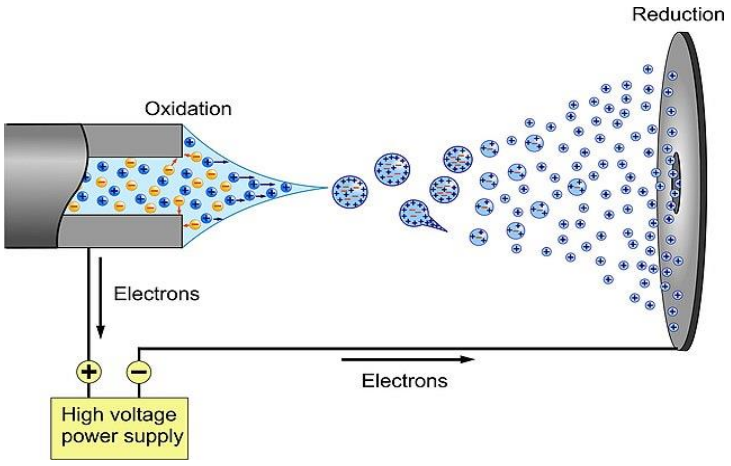

Figure 2.4: Diagram of electrospray ionisation in positive ion mode [47]

It is noticed that the proteins unfold when converted into the gas phase in the vacuum. The secondary structure changes due to the loss of α-helices and, in some places, β-sheets (especially in insulin) [48–50]. It may lead to a slight increase in the size of the protein in

the ion state. Interestingly, the charge state of the proteins in ESI depends on the tertiary state of the protein.

2.1.3 Soft and reactive landing of protein ions on the surface

The biomolecules are very fragile molecules and are handled to have kinetic energies in the soft landing zone to retain the structures in the mass spectrometers [51]. In soft landing, the gas phase ions have kinetic energies in the range of 1-100 eV [52]. Also, the ions that collide with the surface with kinetic energies of around 40-50 eV get stuck to the surface oxide layer through a process known as reactive landing [53]. Additionally, it was observed that soft landing ions are not much affected by the applied potential [54].

Soft landing retains the charge on the biomolecule [55], preventing molecule fragmentation [56] and even biological activity [51]. So, it has been of interest to the research community and is well summarised by Gologan et al. (2005) [57] in their review of the topic. Soft landing helps detect ions in mass spectrometers when they collide with the final detector plate. However, soft-landed ions tend to stick to the electrode surfaces while retaining their charge and interfering with the movement of the ion beam.

2.1.4 Protein adsorption on the metal surfaces

During their travel towards the detector in the high vacuum of the mass spectrometers, the protein ions sometimes collide with the electrodes' surfaces. The collision may be due to the ions being divergent or due to the collimation of the ion beam. The protein ions strike the electrode surfaces with soft-landing energies. The ions are expected to fall due to gravity after the collision. However, some of the ions remain on the surface, and this phenomenon may be similar to surface adsorption. Therefore, this section

tries to understand the phenomenon of surface adsorption and protein adsorption on the metal surface by delving into previous research in this field.

However, it should be kept in mind that, in our case, the protein ions collide with the metal surface while moving with hypothermal energies in a vacuum environment.

2.1.4.1 Overview: Surface Adsorption phenomenon

Adsorption is the process of adhesion of ions, atoms or molecules from the gas phase, liquid phase or dissolved solid phase to the interacting surface through physical forces or chemical bonds. Most solid surfaces have residual surface energy due to unbalanced forces and are the centre points for attracting the substances that collide with these surfaces. The adsorbed material does not diffuse in the bulk of the interacting surface, and this process is usually reversible [58].

Physical adsorption is produced by the intermolecular forces (i.e., van der Waals forces) attraction compared to the formation and destruction of chemical bonds in chemical adsorption (refer to Table 2.1). Physical adsorption is fast but unstable and easily disturbed as the attracting van der Waals forces are weak, and the adsorption energy is negligible. Chemical adsorption is comparatively more stable as it is selective, and the activation energy needed for absorption is high [59].

Table 2.1: Comparison of physical adsorption with chemical adsorption [59]

	Adsorption categories	
	Physical adsorption	**Chemical adsorption**
Adsorption force	Van der Waals force	Chemical bond force
Selectivity	Nonselective adsorption	Selective adsorption
Adsorption layer	Single or multiple layers	Single layer
Adsorption heat	Low	High
Adsorption rate	Fast	Slow
Stability	Unstable	Stable

2.1.4.2 Factors affecting protein adsorption

Protein adsorption is an extensively researched topic, mainly in the liquid-solid interface domain. It is advantageous in many places, such as biosensors, implanting cells on artificial implants, and coating the surface with the desired protein, such as in the case of bovine serum albumin (BSA) coatings on test tubes to avoid bio-analyte loss [60]. On the other hand, this can be a severe industrial problem, such as adsorption on surfaces of mass spectrometers leading to a loss of sensitivity.

Past research has demonstrated that the mechanism of protein adsorption on the surface depends on diverse factors, including the type of protein and the interacting surface. For example, in metal surfaces, it depends on the size of the proteins, reactivity to metal and metal oxides, the surface energy and the surface roughness, among other factors [61]. Moreover, proteins comprise the same 20 common types of amino acids. So, a general understanding of the adsorption behaviour of the proteins with the metal and metal oxides may show a possible trend in protein reactivity.

2.1.4.3 Impact of reactivity of proteins with the metal surface

The reactivity of proteins and other biomolecules with the metal oxide layer heavily affects the food and medical industry. So, protein adsorption in these domains is a commonly researched topic. Protein molecules such as trypsin or bovine serum albumin (BSA) react with the stainless steel surface when exposed to the surface through solution phase or gas phase ion in soft/reactive landed conditions. Studies of soft-landed proteins on stainless steel surfaces show a significant reduction of iron and chromium and increased nitrogen content from the surface compared to the native surface. A proton transfer cascade non-destructively discharges the first layer of the protein ions landing on the surface to the metal oxide layer. These gas phase ions were considered acidic, and the proton transfer can cause a reduction reaction to the Fe_2O_3, where Fe^{3+} reduces to Fe^{2+} [53,62,63].

The research project focuses on protein reactions in the gas phase ions. However, past research on protein reactivity with metals in the solution phase will help us understand the nature of reactions associated with proteins. Atapour et al. (2019) observed that a significant amount of Fe, Cr and Ni was released into the system when whey proteins (milk proteins) interacted with stainless steel milk containers. Iron reduction and chromium enrichment were also observed on the oxide layer of SS316L [64]. Iron was released from almost all grades of stainless steel and chromium-based alloys. A low amount of Nickel and Manganese loss is also noticed in SS304 and SS316L [65–67]. Okazaki et al. (2008) concluded that Ni-Ti alloys showed more resistance to metal release than stainless steel and Co–Cr–Mo–Ni–Fe alloys while researching suitable vascular implants [68].

Even noble metals such as gold dissolve in amino acids, mainly with the ones containing sulphide bonds like cysteine [69]. Welinder et al. (2010) analysed the self-organisation and binding of insulin on the single-crystalline gold surfaces in the solution

phase. The disulphide bonds unfold and adsorb on the gold layer [70] due to the high affinity of gold for sulphur and form Au-S bonds [71]. Figure 2.5 shows the identified mechanism of protein adsorption on gold.

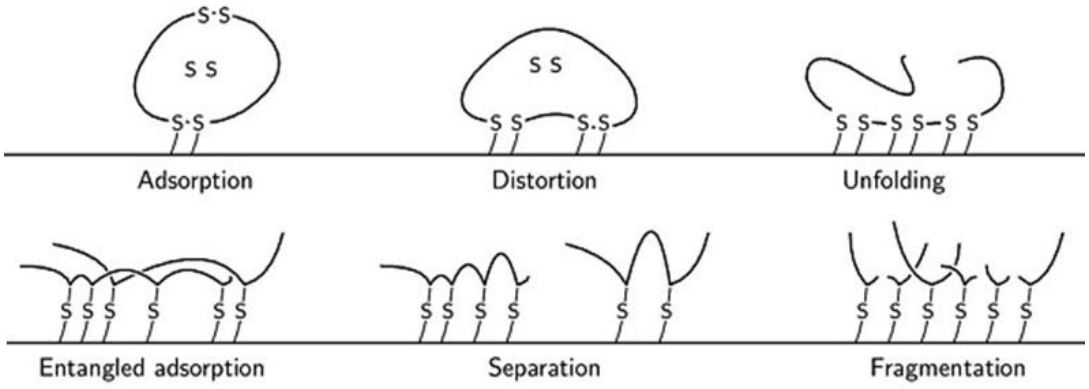

Figure 2.5: Schematic view of the events during insulin adsorption on the gold surface [70]**. The sulphide bond chemically reacts with gold on the surface to form Au-S bonds. It illustrates the chemical adsorption on the surface.**

Silva-Bermudez and Rodil (2013) study summarised the reactivity of various metals and their combinations, such as Ta, Ti, Nb, Al, Zr, Cr, Ni and Cu, on their reactivity with proteins (mainly albumin and fibrinogen) in the solution phase. It was seen that aluminium oxide (Al_2O_3) was the most resistant to adsorption than the other metal oxides [61].

2.1.4.4 Impact of other factors on protein adsorption

The factors that protein adsorption in the solution phase, such as pH, ionic strength and buffer composition, will not be available for proteins ions in the gas phase striking the surface with soft landing energies in vacuum conditions such as mass-spectrometers. In the case of soft-landed protein ions, the kinetic energy of the ion beam will impact the protein ion collision with the surface. Hence the protein size and the interacting surface's roughness will likely impact the adsorption of protein.

The protein size affects the number of endpoints available for connecting with the surface. It is evident in Figure 2.6 that the larger protein has more connecting endpoints with the surface for surface adsorption. For example, the diameter of the insulin protein is only 2.4 nm [34] compared to larger proteins such as rubisco, having an 11 nm diameter [35].

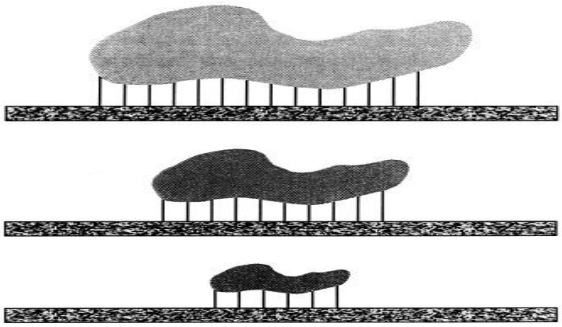

Figure 2.6: Effect of protein size on interaction with the surface. The bigger the protein size, the more potential endpoints for connecting with the surface.

Surface roughness also plays a crucial role in the adsorption of proteins. The bulk of the research on the adsorption of soft-landed proteins on the metal surface can be broadly categorised into two categories, i.e. adsorption on metal surfaces containing a self-assembled monolayers (SAM) layer [55,56,72] and on metal surfaces without the SAM layer [73,74]. The review focuses on cases of surfaces without the SAM layer to align with the primary aim of the research problem. A mention of plasma treatment of the native metal surfaces was observed in some of the research, but the surface topography details are not clear in the literature [53,73–75]. However, during the plasma treatment, the surface is exposed to reactive partially ionised gases, which changes surface morphology and chemistry. Reduction of the surface roughness is observed as the topographical change [76–78]. The chemical change, such as an oxide and nitride composition, depends on the plasma composition.

Figure 2.7 shows the topographical impact of plasma treatment on stainless steel X12CrNi 18 8 (1.4300) as an example.

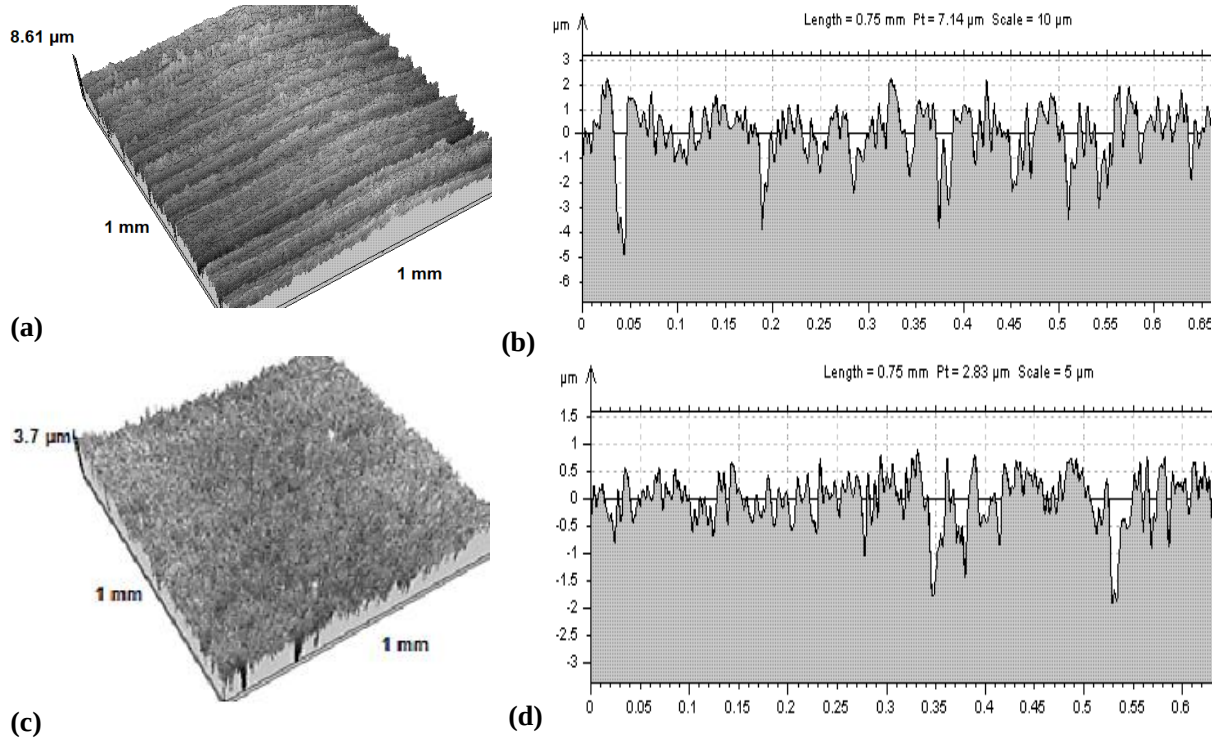

Figure 2.7: Plasma treatment on a stainless steel sample (adapted from [76]**)**
(a) 3D surface topography of the non-treated surface. (b) Roughness profile, Ra=0.799 µm
(c) 3D surface topography of the plasma-nitrided surface (d) Roughness profile, Ra=0.358 µm

Further, considering the small sizes of the proteins, i.e. insulin (2.4 nm diameter) or BSA (3 nm diameter) [79], the surface roughness needs to be on a nano-scale to impact protein adhesion. The proteins have a definite shape and behave like a nanoparticle. Figure 2.8 provides a perspective on the effect of surface roughness. Several investigations on the impact of surface roughness exist related to the solution phase [80–84], but there isn't any information related to the soft-landed protein on surfaces. Even though the solution phase is unsuitable for this project, it still provides information on protein interaction.

Figure 2.8: Adsorption of protein on a rough surface.

The effect of nano-topographies on protein adhesion was researched in the liquid phase for different shapes of proteins. Such as Galli et al. (2001 and 2002) [80,81] analysed the impact of nano-grooves, in the order of the size of proteins, on protein adhesion of filament and globular proteins. The nano-grooves were etched on the surface by modifying the oxide layer using the Local Anodic Oxidation (LAO) method and dimensions 40 nm width and 3-4 nm & 1-2 nm high. The proteins used in the experiments were actin with filament shaped with a width of 6.5-8.2 nm and a globular protein with a diameter of 3 nm. The filament protein only demonstrated some preferential alignment with the 3-4 nm high grooves. They concluded that the proteins have a sense towards nano-topography. It can be deduced that the solution phase allows the alignment of the proteins on the surface.

Mathematical modelling to analyse the impact of nano-topography on protein adsorption is also employed. Webster et al. (2013) [84] analysed protein (serum albumin) adsorption on nano-topographies (bead-like structures, as shown in Figure 2.9) with varying surface roughness. It was also identified experimentally that the surfaces of roughness more than the protein size show a more significant increase in protein adsorption. Rechendorf et al. (2006) [83] also observed similar results on surface roughness. They also identified that after the initial adsorption of BSA, the protein relaxes on the surfaces, reducing the surface for adsorption.

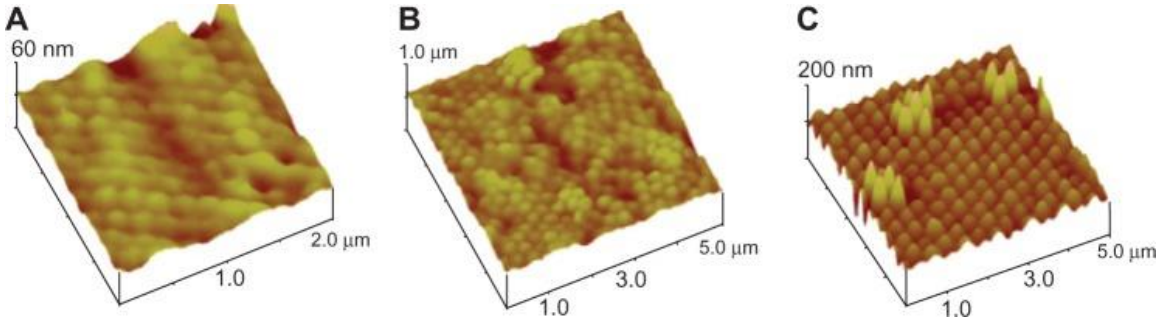

Figure 2.9: AFM images of surfaces synthesised for protein adsorption analysis [84]**.**
Surface generated with RMS_{eff}: (A) 2.7±0.1 nm, (B) 28.0±1.0 nm, (C) 13.3±1.1 nm.
The dimensions of the polystyrene nano-beads were: (A) 190 nm, (B) 300 nm, and (C) 400 nm.
The final polylactic-co-glycolic acid (PLGA) surface film was created through a mold of the nano-beads on a flat surface, and the film was derived from it.

From the investigated research on the impact of surface roughness, although in the solution phase, it can be stated that surface roughness near the protein size adversely affects protein adsorption. The dimension of the protein selected for the research project, i.e. bovine insulin with a diameter between 2.2-2.5 nm, provides a perspective on the scale of the surface roughness. However, due to the lack of information, the impact of gas phase protein ions and their associated kinetic energies on protein adsorption could not be established.

2.2 Laser surface texturing

Laser surface texturing is a technique of surface engineering used to modify the material's surface properties through micro/nano structures created using laser technology. It provides a versatile method to generate surfaces to reduce tool wear by improving tool chip contact area and improving lubricant availability at the contact point [85]. It can

generate functional surfaces for application needs, such as super-hydrophobic surfaces [86] or control surfaces for anti-fouling behaviour [87,88].

2.2.1 Principle of Laser technology

LASER stands for Light Amplification by Stimulated Emission of Radiation, an acronym coined by Gould in 1959 [89]. The laser sources use the principle of stimulated radiation discovered by Albert Einstein in 1917 [90]. The first working laser was built by Theodore Maiman in 1960 based on the principle of photon amplification by stimulated emission in a ruby crystal, producing a beam with a wavelength of 694.3 nm [91].

Figure 2.10 shows a basic laser system consisting of a lasing material/medium between two mirrors (with one of them partially transparent). A flashlight or another diode-based laser excites the lasing medium in this example. The excited electrons in the lasing medium decay when a photon with energy equivalent to the energy gap is present, producing extra photons of the same properties in the process, also known as stimulated emission. This effect is repeated numerous times within the lasing cavity (between the two mirrors) until the photon amplification is high enough for transmission through one of the mirrors (partially reflective one). This process eventually results in a light beam that is monochromatic and coherent [92]. Many types of sources have been demonstrated since 1960, all using this same fundamental principle. Laser sources can be classified based on the type of lasing medium, of which there are three types: gas (CO_2, excimer), solid-state crystals(semiconductor lasers, Nd:YAG lasers) and liquids (dye lasers)). Also, they can be classified as continuous wave (CW) and pulsed beam based on the emission type, as illustrated in Figure 2.11. The pulsed lasers typically have low average power but high peak

power. The pulse lasers' pulses are categorised as short (nanosecond) and ultrashort (picosecond or femtosecond).

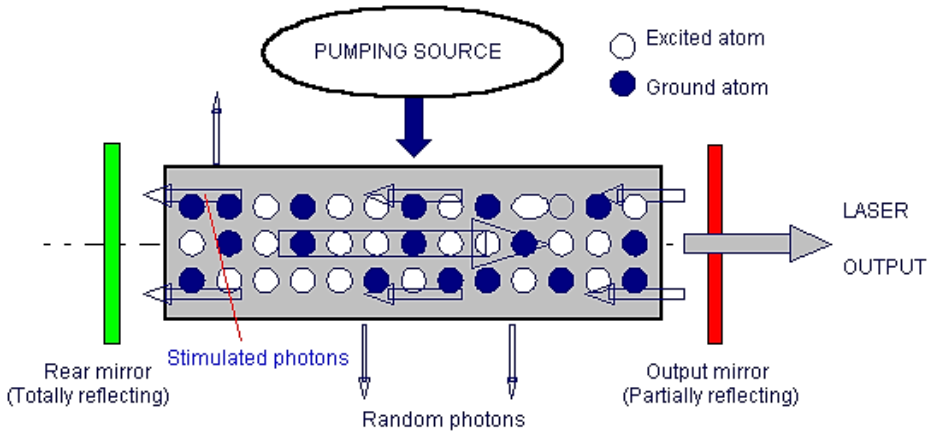

Figure 2.10: Schematic of a basic Laser system [93]**. The lasing medium is between the two mirrors, and stimulated photons to move within this lasing medium until it is transmitted through the partially reflecting mirror.**

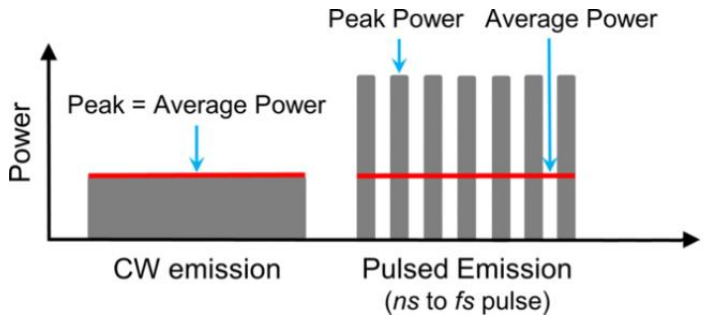

Figure 2.11: Laser based on emission type: continuous wave (CW) or pulsed emission

2.2.2 Laser interaction with the material surface

A large portion of the beam energy is lost during laser material processing due to the surface's reflectivity. In contrast, the remaining energy is absorbed and converted to heat through electronic excitation and relaxation within a brief period of time. The absorbed energy affects only the ultra-thin layer of the material, and extreme heating and cooling rates are achieved. Other parameters that affect laser processing are laser energy absorption

mechanism (thermal or photochemical), material response to laser fluence, ablation threshold and the processing atmosphere. Laser processing allows modification of the surface topography, chemistry and crystal structure [94].

The absorption mechanism depends on the pulse duration. Such as, in the short pulse regime (nanosecond), the ablation process is thermal, and the Beer-Lambart law governs the laser absorption. However, at the ultrashort pulse regime (femtosecond), the short pulse duration and high peak intensity transforms the ablation from thermal to photoionisation due to a strong electric field ionisation. The absorption mechanism typically for metals is shown in Figure 2.12. Photoionisation is the dominant process at very high intensities (above 10^{13} W/cm2) for femtosecond scales. It may lead to multi-photon ionisation, depending on the electric field strength [95–97].

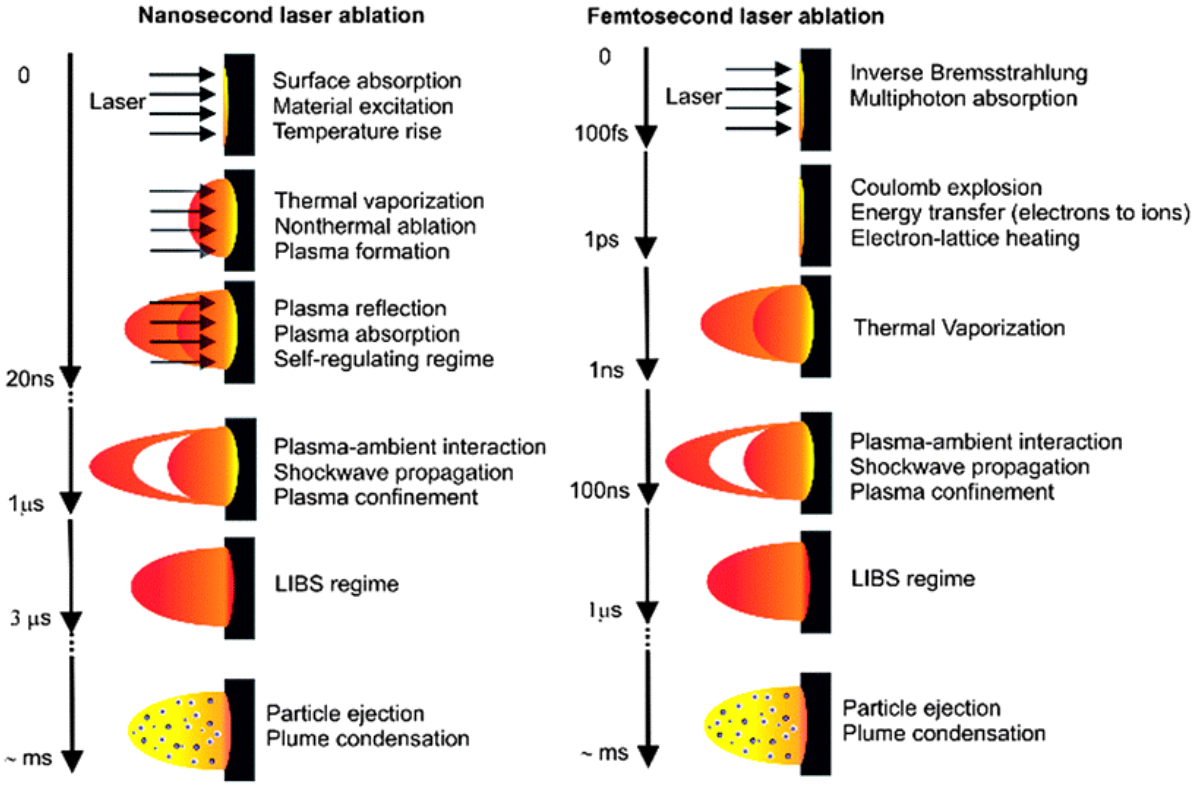

Figure 2.12: Approximate timescale of ns-pulse and fs-pulse laser ablation [98]

The ablation threshold is the critical laser fluence, at which the bonding energy of an irradiated solid is overcome by input radiant energy, and the solid decomposes by ablation[99]. It is a valuable tool for identifying the minimal energy needed to remove material by laser treatment. The ablation threshold depends on the material [100], the applied laser, i.e. the laser wavelength [101] & the pulse duration [102], and the number of pulses applied on the irradiated spot, i.e. the overall fluence [103,104]. Güdde et al. (1998) and Wellershoff et al. (1999) observed that the threshold fluence is affected if the thickness of the material is less than the hot electron diffusion length (L_c). The L_c value for Au is ~800 nm, and for Ni is 50 nm, so it can be stated that L_c affects mostly thin-film laser processing [105,106].

Further, it was observed that the temperature of the material also affects the threshold fluence for some metals. For example, Yahng et al. (2009) [107] found that the threshold value decreased in Si on increasing the temperature from 300K to 900K. On the other hand, SS304 did not change, but its ablation efficiency increased.

Furthermore, the processing medium, such as air, liquid (water, ethanol) or vacuum, also impacts the threshold fluence. Zhu et al. (2001) [108] detected a reduction of the threshold fluence in the water while studying the ablation behaviour in air and water medium for Si substrate. Figure 2.13 shows the observed effect of the atmosphere on laser ablation with more ablation underwater. This behaviour can be attributed to the obstruction in the free expansion of the laser plasma plume during ablation. The plasma plume escaped in air processing mode but was confined in the water, increasing the plasma pressure on the material. The enhanced pressure on the material increases the substrate temperature and decreases the ablation threshold. Gamaly et al. (2005) [109] observed that for certain metals

(Al, Cu, Fe and Pb), the threshold fluence was double in the air as compared to vacuum when processing with a picosecond laser (pulse duration 12 ps).

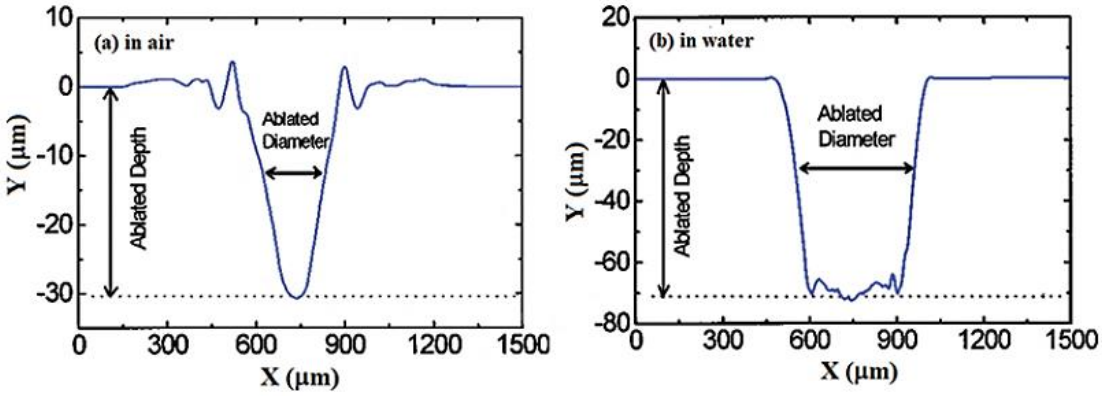

Figure 2.13: Laser-ablated region profile of a Silicon target after 1000-pulse irradiation in air and water medium. [108]

2.2.3 Types of laser surface texturing

The surface texturing can be classified into two broad types, i.e. laser induced structures and laser inscribed structures, as shown in Figure 2.14. The laser induced structures can be further divided based on size, i.e. microstructures or nanostructures. The nanostructures can be nano-bumps, nano-holes, nano-ridges, and nano-protrusions. The generation of these structures mainly depends on laser fluence, scanning speed, number of pulses, and the processing environment. The nanostructures generally form at fluences near the ablation threshold. They eventually convert into microstructures with increased laser fluence [110].

Figure 2.15 shows a femtosecond laser surface texturing case containing microstructures and nanostructures. The features were fabricated in a hierarchical structure on stainless steel. The figure provides a perspective on the difference in the size of the features. It can be observed that the nanostructures are periodic in nature, smaller than the

wavelength of the employed laser (λ = 800 nm), and have a depth of only 250 nm. These nanostructures are laser induced periodic surface structures or LIPSS structures.

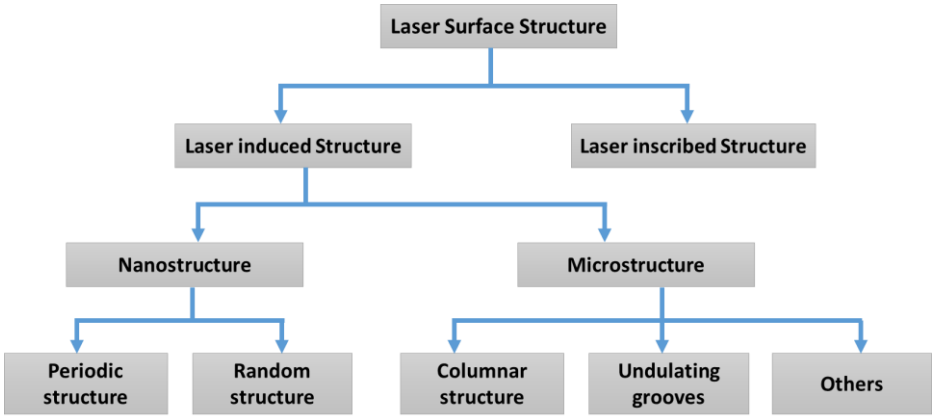

Figure 2.14: Classification of surface structures (adapted from [110] **)**

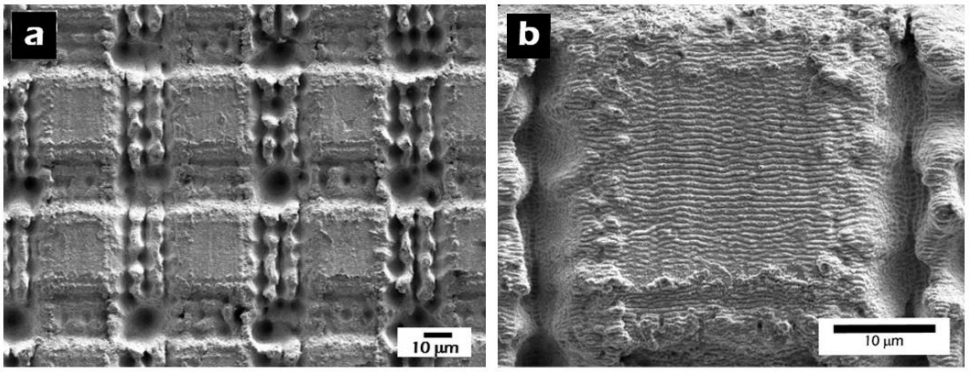

Figure 2.15: Microstructures vs Nanostructures (LIPSS) – SEM micrographs of hierarchical structures fabricated on stainless steel (adapted from [37]**)**
(a) Microstructures: Matrix micro pattern of pitch distance 50 µm and covered by LIPSS;
(b) Nanostructures: LIPSS of periodicity ~580 nm and depth 250 nm
Laser source: λ=800 nm, t_{laser}=130 fs, and f_{laser}=1 kHz.

2.2.4 Laser Induced Periodic Surface Structures (LIPSS)

Laser Induced Periodic Surface Structures (LIPSS) are observed as ripples on the surface irradiated with a laser near the melting threshold of the material. They can be

formed in many materials under short and ultrashort pulse durations [111,112]. Birnbaum first observed these periodic features in 1965 during the ablation of a germanium sample by a ruby laser [113]. The LIPSS structures can be classified into two broad types, i.e. Low spatial frequency LIPSS (LSFL) and High spatial frequency LIPSS (HSFL). Figure 2.16 provides a categorisation of the LIPSS structures based on the periodicity (Λ) and their direction with respect to the laser beam wavelength (λ) and polarisation direction, respectively [114]. An example of a titanium alloy sample with type-I LSFL and type-II HSFL features is shown in Figure 2.17, along with their peak fluence (F_p) [115].

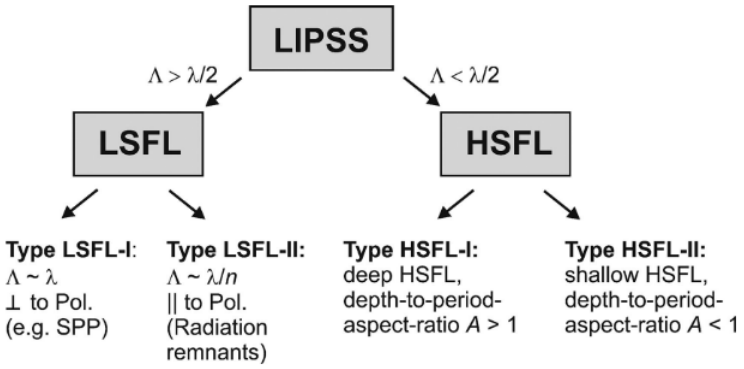

Figure 2.16 Classification scheme of fs-laser LIPSS showing LSFL and HSFL categories [114]

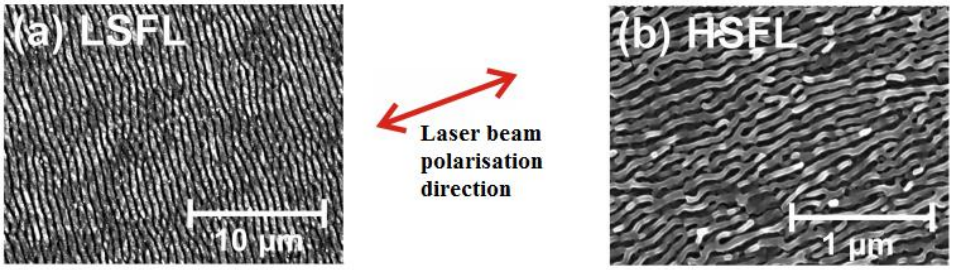

Figure 2.17 SEM image of 2 types of LIPSS formed on Ti6Al4V surface with fs-laser [115] **[30 fs, 800 nm, 1 kHz]. (a) LSFL-I [φ_0 = 0.11 J/cm^2]; (b) HSFL-II [φ_0 = 0.08 J/cm^2].**

2.2.4.1 Low spatial frequency LIPSS (LFSL)

These are classical near the laser wavelength (λ_{laser}) sized LIPSS where the periodicity, $\Lambda_{LIPSS} > \lambda_{laser}/2$. The ripples are perpendicular to the laser beam polarisation

direction for strong absorbing materials such as metals and semiconductors. On the other hand, ripples parallel to the polarisation direction are observed on some large band gap materials, such as fused silica [114,116]. Figure 2.16 illustrates the sub-categorisation of LSFL based on the direction of LIPSS compared to the polarisation direction.

According to the most accepted theory, LSFL features are formed due to the interference of the incident laser beam with the light scattered from the surface. Figure 2.18 shows the scheme of the electromagnetic formation mechanism for the LSFL features. According to this theory, the laser beam may lead to the generation of Surface Plasmon Polaritons (SPP)[2] after it impinges the substrate from the top, as shown in Figure 2.18 (b). The initial roughness of the material is crucial for forming an initial scattering (see Figure 2.18 (a)). The generated SPP interferes with the incident light, leading to an interference pattern on the fluence. Finally, this modulated fluence imprint is absorbed in the material and selectively ablates the material to create parallel periodic structures, as shown in Figure 2.18 (c) [117–119].

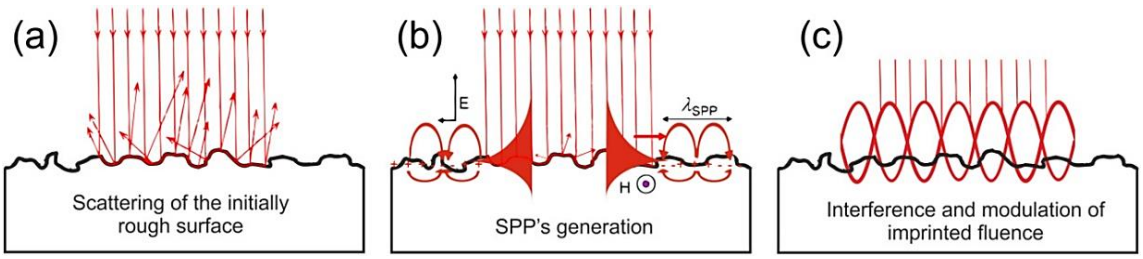

Figure 2.18: Scheme of electromagnetic formation mechanism for the LSFL structures [119]

[2] **Surface Plasmon Polaritons (SPP)** are electromagnetic waves that travel along a metal–dielectric or metal–air interface, practically in the infrared or visible-frequency.

2.2.4.2 High spatial frequency LIPSS (HFSL)

These are the non-classical type of LIPSS with periods ($\Lambda_{LIPSS} < \lambda_{laser}/2$) significantly smaller than the laser beam wavelength (also known as *nanoripples*). They are parallel to the laser beam polarisation direction, as shown in Figure 2.17 (b). They are mainly observed for ultrashort pulse laser durations and at fluences similar to the damage threshold of the material. The type HSFL-I (see Figure 2.16) is observed primarily on dielectrics and semiconductors, and the type HSFL-II is on most metal surfaces [114].

2.2.5 Nano-sale surface texturing

The formation of nano-scale periodic surface structures has been researched extensively since its first observation in 1965 [113]. In general, it is observed that the periodic ripples are dependent on laser wavelength λ, the angle of incidence of the radiation θ and the index of refraction of the processing atmosphere over the material n. The relationship of these parameters is described by the relation $\Lambda = \lambda/(n - \sin\theta)$, where Λ is the periodicity.

LIPSS start to appear mostly at near ablation threshold fluence with a higher number of pulses, and for higher laser fluence, the LIPSS is seen at a lower number of pulses [120]. A high pulse frequency would increase the number of pulses and start affecting the first periodic ripple formed on the surface as the ablation continues. Groenendijk and Meijer (2006) studied the formation of LIPSS structures using a femtosecond laser on a stainless steel surface. They noticed that the laser fluence and the number of pulses transform the ripple morphology from periodic to rough and chaotic as the laser parameter values increase. High pulse frequency would increase the number of pulses and start affecting the

first periodic ripple formed on the surface as the ablation continues. [121]. Similarly, Zhao et al. (2007) noticed that periodicity depends on fluence, the number of pulses, and the incident beam angle, as shown in Figure 2.19. The periodicity decreases on constant fluence and increasing pulses but increases on constant pulses and increasing fluence. Also, the periodicity decreases with an increase in the laser beam's incident angle [122].

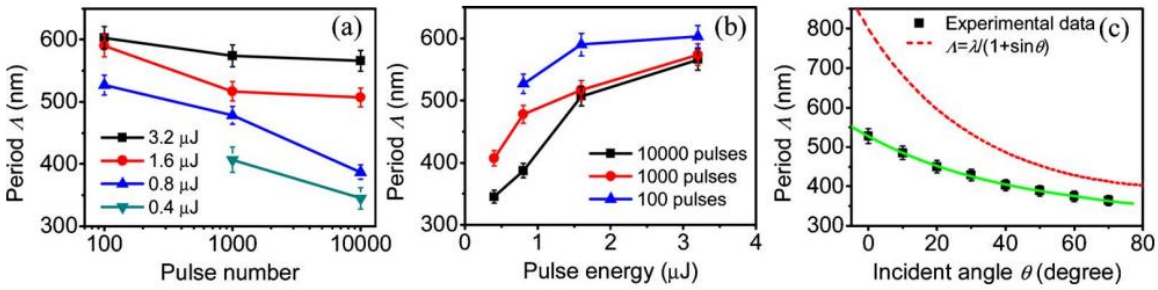

Figure 2.19: Plots showing the dependence of periodicity on (a) the number of pulses, (b) the pulse energy, and (c) the incident angle of the laser beam. The dotted line is the theoretical curve [122]**.**

Short pulses in the nanosecond regime ablate material through thermal mechanisms [123]. The problem of HAZ can be seen while texturing using ns-laser pulses. Heat affected zones (HAZ) were observed by Fiorucci et al. (2015), as shown in Figure 2.20 while texturing Titanium alloy Ti6Al4V using 25 ns and 355 nm laser for biomedical application. Oxides of Aluminium and Titanium were also observed in the HAZ through XPS analysis, confirming surface oxidation during laser texturing [124].

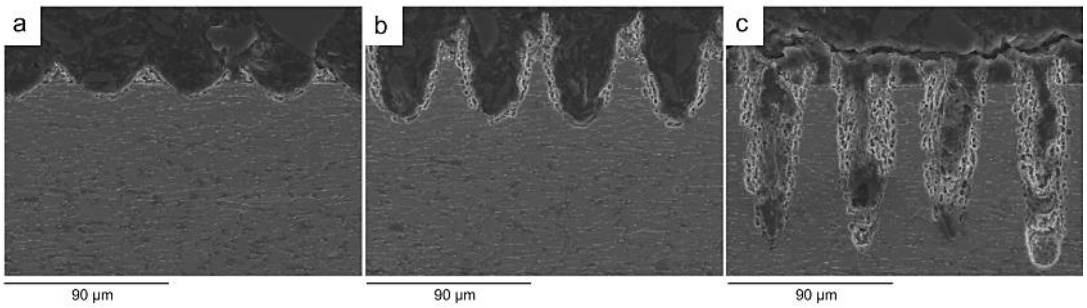

Figure 2.20: SEM images of HAZ in grooves of Ti-alloys due to scan speed variation [124] **Scanning velocities are (a) 25 mm/sec; (b) 10 mm/sec; (b) 5 mm/sec**

Despite the problem of HAZ in nanosecond processing, LIPSS structures have been generated over the years [125–127]. Sanz et al. (2012) [126] generated LIPSS structures using 266 nm wavelength (UV laser) and 6 ns laser on polymer films coated with gold for Raman spectroscopy analysis. The periodicity obtained was 250 nm with a 45 nm height and roughness (Ra) value of 20 nm. Another experiment by Sanz et al. (2013) [127] experimented using the same laser on different semiconductor materials and observed LIPSS patterns on the surface. The periodicity of LIPSS was around the laser wavelength, but shallow ripples of amplitude 5 nm and 9 nm were observed, as shown in Figure 2.21. Due to the smaller wavelength in the UV region, the absorptivity of the material for the laser wavelength was high. Also, the ablation process involved photochemical ablation along with thermal, leading to very low HAZ.

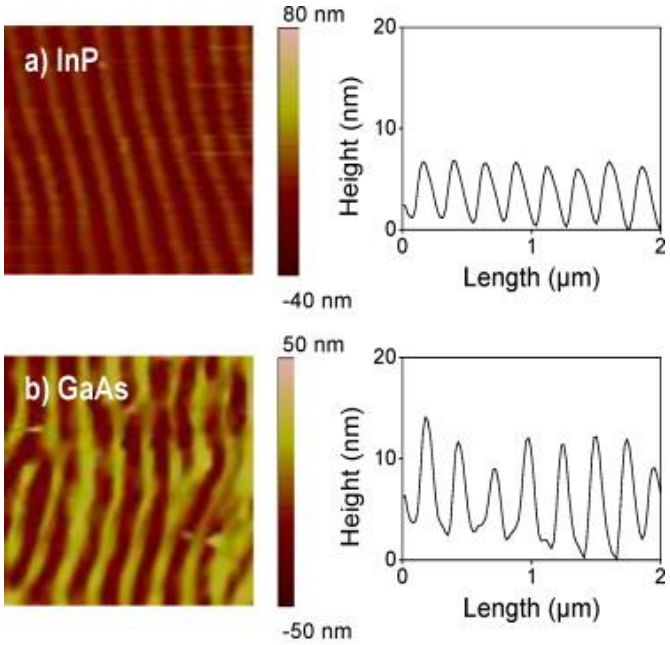

Figure 2.21: AFM images (2×2 μm^2 sizes) with corresponding cross-sections [127]**. Fluence for 200 pulses in (a) InP at 125 mJ/cm^2 (b) GaAs at 150 mJ/cm^2**

Simões et al. (2018) [125] produced high-quality LIPSS on AISI 304 stainless steel surfaces using a 532 nm, 100 ns and 5 kHz laser system with a Gaussian profile beam of

diameter 300 μm (Figure 2.22). They found that the LIPSS homogeneity varied with initial surface roughness and the number of accumulated pulses per spot. Good quality LIPPS could be found with final roughness of 28-35 nm and periodicity of ~530 nm for initial surface roughness of 5 nm.

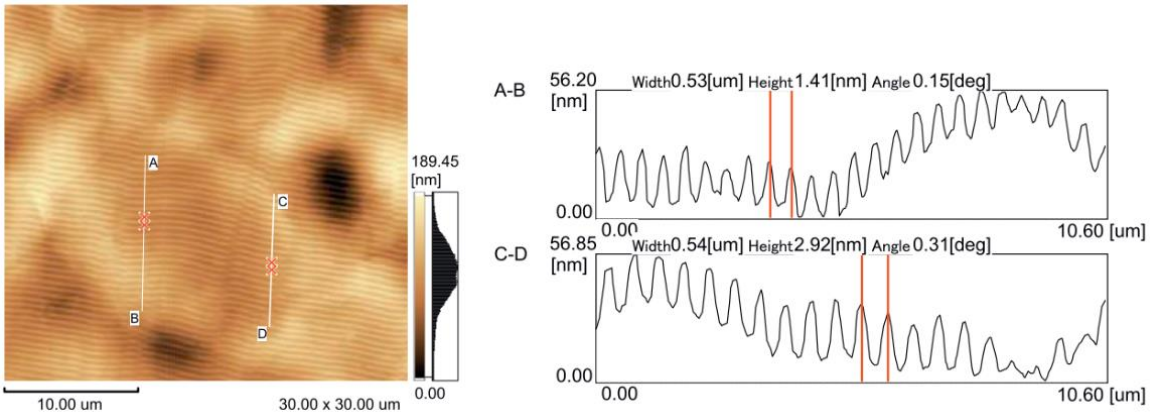

Figure 2.22: AFM image of LIPSS on SS304 and profile of two lines arbitrarily drawn [125]

With the advances in the ultra-short pulse laser (picosecond and femtosecond) range, the complexities in surface texturing identified in short pulses can be handled in this regime, paving the way for more complex surface textures. The ultra-short pulse laser ablation combines thermal and photo-ionisation with minimal heat diffusion. The complexity in the ablation mechanism behaviour can be understood using the phonon relaxation (t_{pr}) as a comparison parameter during the laser processing period. After the initial excitation of electrons by absorption of photons (laser energy), a quasi-equilibrium situation is established by electron cooling (in around 10^{-13} secs) followed by diffusion in the lattice, i.e. phonon relaxation (in around 10^{-12} secs). The rough timescales of this laser-solid interaction can be visualised in Figure 2.23. The time needed for laser heating depends on the laser pulse duration (t_{pulse}). So, using that, the thermal ($t_{pulse} > t_{pr}$) and the non-thermal ($t_{pulse} < t_{pr}$) regime can be identified. The picosecond ablation experiences thermal

diffusion and vaporisation of the molten layer. On the other hand, a direct solid-vapour transition is observed in a femtosecond. However, the ablation behaviour tends to be more photo-ionisation for picosecond lasers with a UV wavelength range due to the high energy of the photons at the UV wavelength [128].

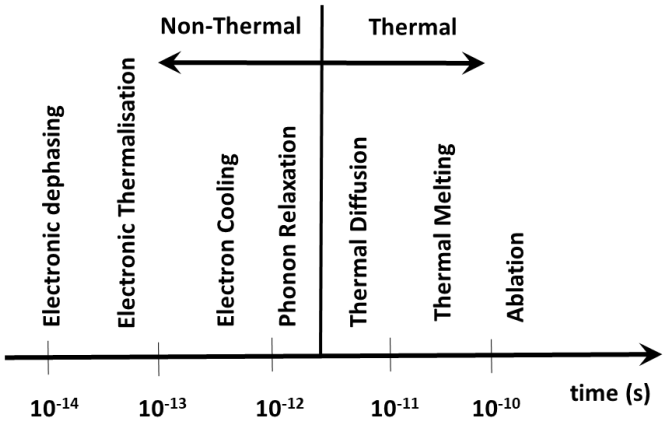

Figure 2.23: Timescales of the various processes in laser-solid interaction [128]

A lot of the research with ultra-short pulse lasers is in the area of wettability and hydrophobicity, leading to real-world applications such as cell adhesion [129,130], anti-fouling [87] and tribological application [131]. The nano-scale structures generated range from the direct rippled surface to multi-scale complex structures. Rajab et al. (2017) [87] analysed the impact of the nanostructured surface on anti-fouling behaviour for titanium surfaces using an IR-picosecond laser in the air. Different types of nanostructured surfaces were developed, as shown in Figure 2.24, containing rippled and non-rippled surfaces. It was noticed that even though the peak-to-valley roughness of surface Ti2 was significantly higher than the other surfaces, it showcased the most hydrophobic nature and anti-fouling behaviour. A macro dimpled surface containing nano-structures on top was seen in Ti2, instead of periodic features like Ti1 and Ti3. A low processing speed of only 1 mm/sec

was used for Ti2, which explains the highest oxygen content of the surface, mostly due to high surface oxidation.

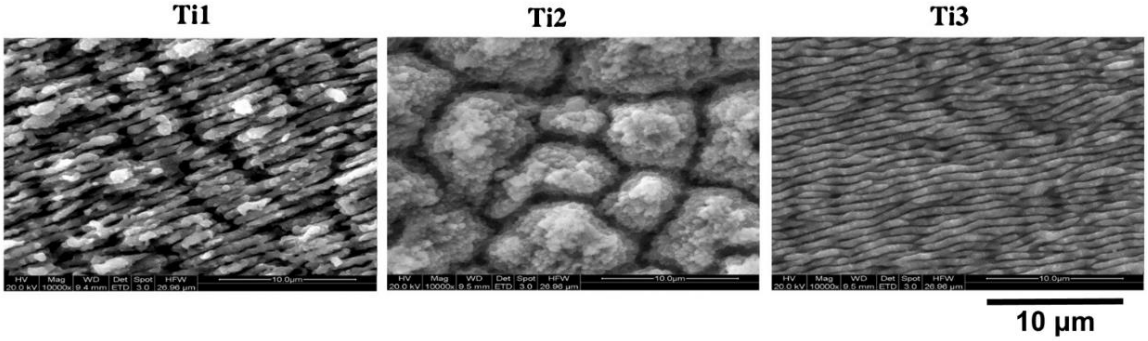

Figure 2.24: SEM images of nanostructured surfaces created on Ti alloy (ref from [87]**)**
(λ_{laser}:1064 nm, f_{laser}: 103 kKz, $Pulse_{laser}$: 10 ps, Spot dia: 125 µm)
Maximum (peaks width/height, valleys width/height): Ti1 (1.4µm/0.8µm, 1.1µm/0.3µm), Ti2 (2.5µm/0.9µm, 3.3µm/0.8µm) and Ti3 (1.0µm/0.3µm, 0.9µm/0.2µm)

Similar research was conducted by Rajab et al. (2018) [132] again using 316L stainless steel surfaces ($S_a = 20.0 \pm 0.1$ nm finish) and created multi-scale structures similar to the previous research, as shown in Figure 2.25. The SS4 and SS5 show complex features with hair like features and round shapes containing hair-like features, respectively. SS5 has the highest oxygen and the least iron content on the surfaces and shows the highest anti-fouling behaviour. These complex topographies present an interesting case for the possibility of generating protein resistant surfaces. However, the lack of information about the surface topographies in this regard makes it challenging to predict the nature of physical adsorption on these surfaces.

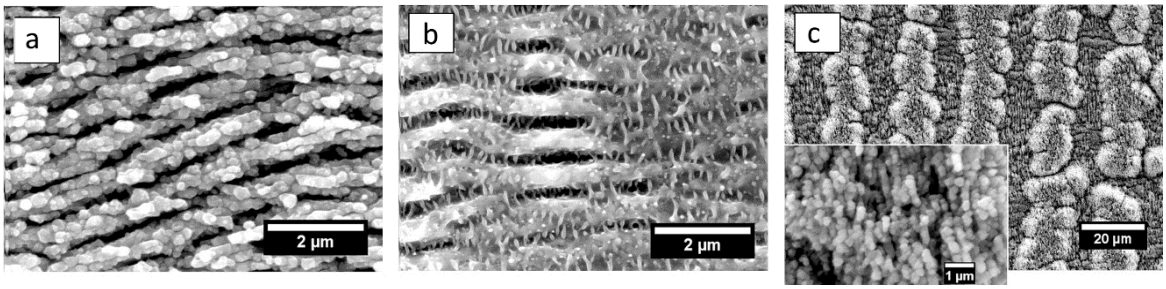

Figure 2.25: SEM images of the topography of the different multi-scale surface features (a) SS3, (b) SS4, and (c) SS5. A magnified image of the surface is shown in the insert (ref from [132]**)**

However, the complex multi-level structures observed in picosecond processing can also be generated with the femtosecond laser with almost zero HAZ. Moradi et al. (2013) [133] experimented with the femtosecond laser and 316L stainless steel to analyse the impact of laser parameters on hydrophobicity. Nano rippled structures were obtained with 400-500 nm periodicity, i.e. nearly half the laser wavelength at a '<u>gentle ablation</u>[3]' regime with no visible signs of HAZ. Similarly, Ardron et al. (2014) [134] generated LIPSS structures on stainless steel with an 800 nm femtosecond laser of periodicity around 650 nm. Complex multi-scale surface geometries were observed on the samples on the rippled surface in both cases. Ardron also identified that if the ablation is below the ablation threshold, the number of pulses increases to obtain similar results compared to the case of gentle ablation. The depth of the ripples was not mentioned in either of them, as the research focused on higher complexity surface structures.

The nano-rippled surfaces generated in the femtosecond laser show a higher aspect ratio in the structures than nanosecond laser of wavelengths in the visible or UV domain. Martínez-Calderon et al. (2016) [37] created combined micro (controlled) and

[3] **Gentle ablation:** The ablation that is just above the ablation threshold and ablates material at skin depth.

nanostructures on 304 stainless steel surfaces using a femtosecond laser, as shown in Figure 2.15. It was observed that the nano-rippled structures have a periodicity of 580 nm and a depth of ~250 nm, as shown in Figure 2.26. Additionally, the ripple surface contained nano-bubbles around the edges. The nano-bubbles structures could be potentially helpful to obstruct smaller particles like protein penetrating deep in the ripple valley.

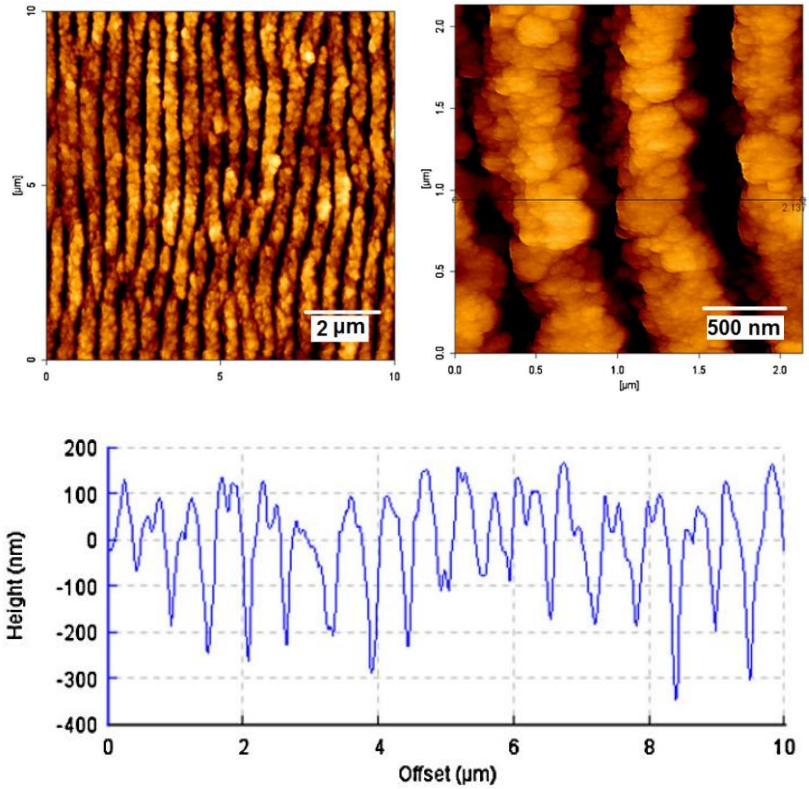

Figure 2.26: AFM micrographs and cross-sectional profiles of samples irradiated with an accumulated fluence per spot of 40 J/cm^2 [37]

Wang et al. (2018) [135] also generated LIPSS structures with a femtosecond laser for the reduction of friction wear on stainless steel 304L but also applied a conformal coating of TiO2 using atomic layer deposition (ALD) without changing the surface morphology and topography of the LIPSS. The LIPSS structures were regular ripples with nano-scale structures similar to Martínez-Calderon et al. (2016), as shown in Figure 2.26. The periodicity of the LIPSS was around 576 nm, but the amplitude decreased from 210

nm to 176 nm for the coated one, along with a slight decrease in surface roughness. It was also observed that the valley between the ripple edges became narrow after the application of a coating, as shown in Figure 2.27. The reduction of the width of the valley between the ripple edges is a use case to prevent protein particles from entering the valley and remaining stuck inside.

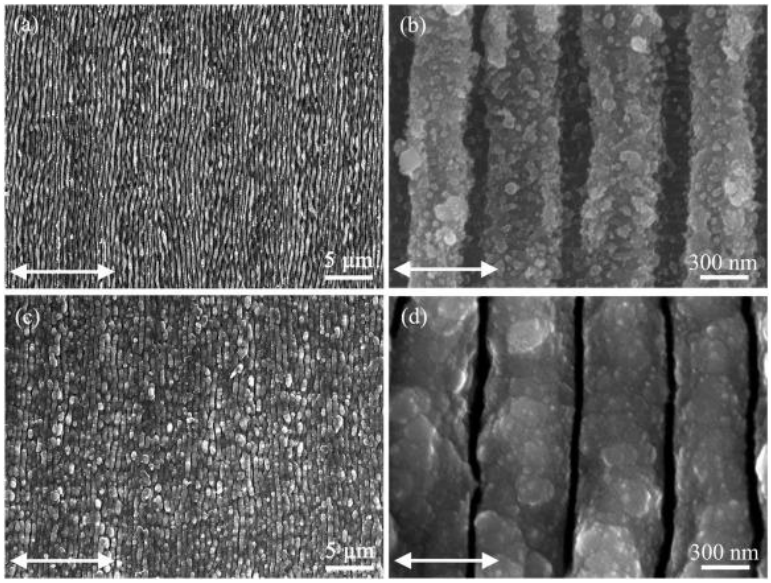

Figure 2.27: SEM micrographs of the LIPSS and LIPSS-ALD
White arrow: laser polarisation. (a) and (b) LIPSS, (c) and (d) LIPSS-ALD. [135]

Vorobyev and Guo (2008) [136] conducted a study on the dependence of LIPSS periodicity on the wavelength of a femtosecond laser. They noticed that the periodicity to wavelength ratio ($\Lambda_{LIPSS}/ \lambda_{laser}$) was similar for various wavelengths. The behaviour was tested for the laser wavelength of 800 nm and its second harmonic generation (SHG) wavelength of 400 nm. They concluded that the periodicity of LIPSS has a linear dependence on the wavelength. In contrast, Maragkaki et al. (2017) [137] conducted a similar analysis with a picosecond laser. They found that only the tendency of dependence of periodicity on wavelength can be explained using the SPP or the Sipe model. However, the LIPSS periodicity to wavelength ratio is similar only when calculated using the model

and does not conform to the experimental data, as shown in Figure 2.28. Gedvilas et al. (2015) [138], during their work on generating LIPSS features on stainless steel 304 with a picosecond laser, observed behaviour similar to Maragkaki. The differences in the observed may be attributed to the subtle differences in the ablation mechanism of picosecond and femtosecond.

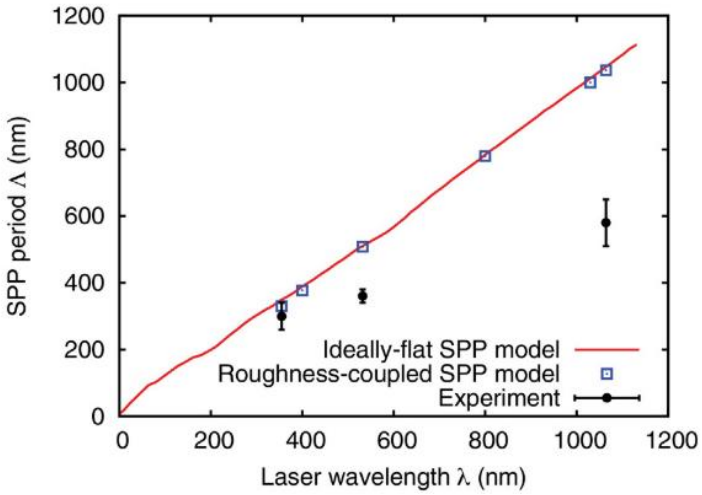

Figure 2.28: Plot of LIPSS period for copper as a function of laser wavelength using the SPP model, along with periodicities obtained with experimental data [137]

The LIPSS structures generated using the laser generally use a linearly polarised beam and produce long or short ripples oriented orthogonal to the electric field. In the case of the high spatial frequency LIPSS (HSFL), the ripples are aligned with the electric field vector. Qi et al. (2009) [139] generated HSFL features on the stainless steel 304 with a femtosecond laser. But, they could not identify the formation mechanism. Still, this is an interesting case since the current research is related to the SS316L variety. However, Nathala et al. (2015) [140] identified the parameters influencing HSFL formation, i.e. laser fluence, pulse duration and the number of pulses per spot, and does not depend on the surface structure and the wavelength. Further, the dependence on surface roughness was

noticed. High polished surface (titanium) helped generate uniformly distributed HSFL compared to an unpolished surface where both LSFL and HSFL features formed [140,141].

Pan et al. (2017) [142] put forward the investigation on the formation of HSFL features on Titanium using a picosecond laser on the peaks and valleys of the LSFL. Pan and co-workers explained that the formation of HSFLs along the surface texture occurs because the absorbed laser energy density is along with the surface texture. It leads to the formation of two types of HSFL features on LSFL features. First, in the concave part of the LSFL due to cavitation instability as interlinking bridges between adjacent LSFL peaks. And the second one is the oxidised nanodots on the convex part of the LSFL as the fluence increases.

Li et al. (2014) [143] presented a novel method to generate HSFL features on the oxide layer of Titanium. The oxide layer was formed on the surface before using a femtosecond laser to texture the surface to generate HSFL. The HSFL features on the surface were at nanoscales with a peak-to-valley depth of ~10 nm, as shown in Figure 2.29. The peak-to-valley depth of ~10 nm shows that the potential of HSFL towards generating surface features is comparable to the scale of the protein molecules.

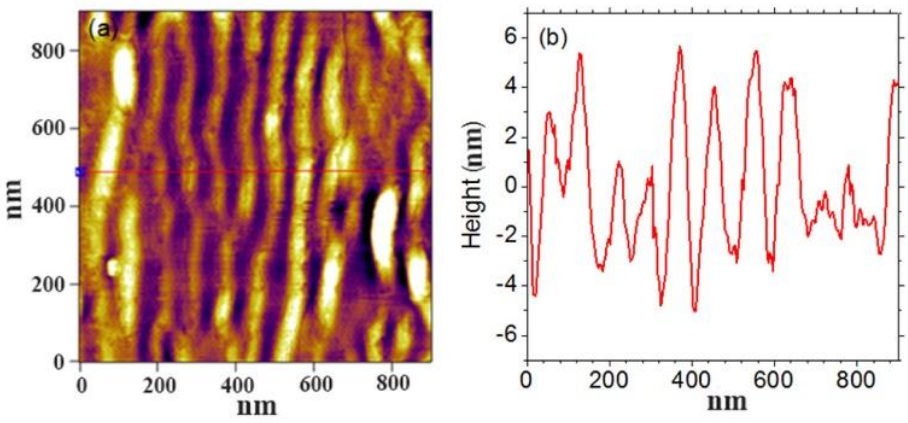

Figure 2.29: AFM image of a typical HSFL in titanium and the section graph [143]**.**

Bonse and Gräf (2021) presented their opinion on HSFL that for ultrashort pulse durations, the initial spatial modulations in the absorbed energy profile can get removed during electron-phonon relaxation time if they are smaller than a critical threshold value. The suggested behaviour is shown in Figure 2.30, where HSFL is removed during the energy transfer from the optically excited electronic system to the lattice of the solid. They concluded that there is a knowledge gap in this area. Future studies with a two-temperature model (TTM) can clarify the impact of phonon-relaxation time on the minimal period limit of HSFL features. This study has already been done to understand the LSFL features [144]. From the suggested behaviour, it can be hypothesised that it is likely to present an opportunity to create nano-polished surfaces with a nanosecond laser. The hypothesis is based on the fact that the thermal diffusion effect is most prominent for nanosecond pulse duration as compared to the ultrashort pulse duration.

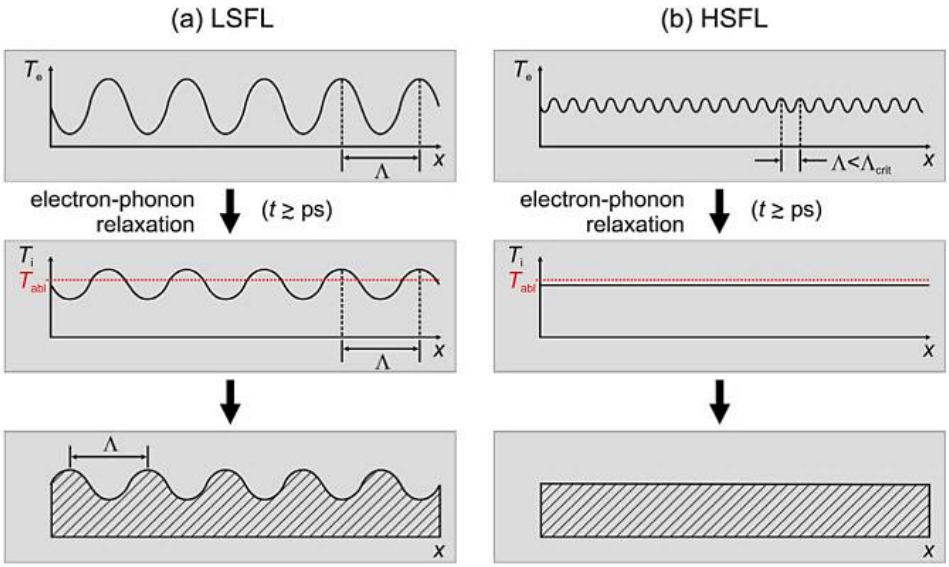

Figure 2.30: Effect of thermal diffusion of the incident laser deposited energy on laser induced features: (a) LSFL-sized spatial modulation (period Λ; imprinted by optical effects) in the electron temperature field (Te, top) are large enough to be imprinted on the surface as reliefs via spatially modulated ablation (bottom). (b) Small-scale HSFL-sized spatial modulations of the electron temperature are washed out during electron–phonon relaxation if the spatial period is below a critical threshold value Λ_{crit}. [144]

Furthermore, a complex pattern of surface structures has been developed by controlling the electric field vector [145–148]. One such example was demonstrated by Ouyang et al. (2015) through the precise tailoring of the optical vector field to create radial, azimuthal and other complex patterns [145]. Similarly, Skoulas et al. (2017) [147] presented the laser machining pattern with linear, radial and azimuthal beams to produce complex surface patterns, as shown in Figure 2.31.

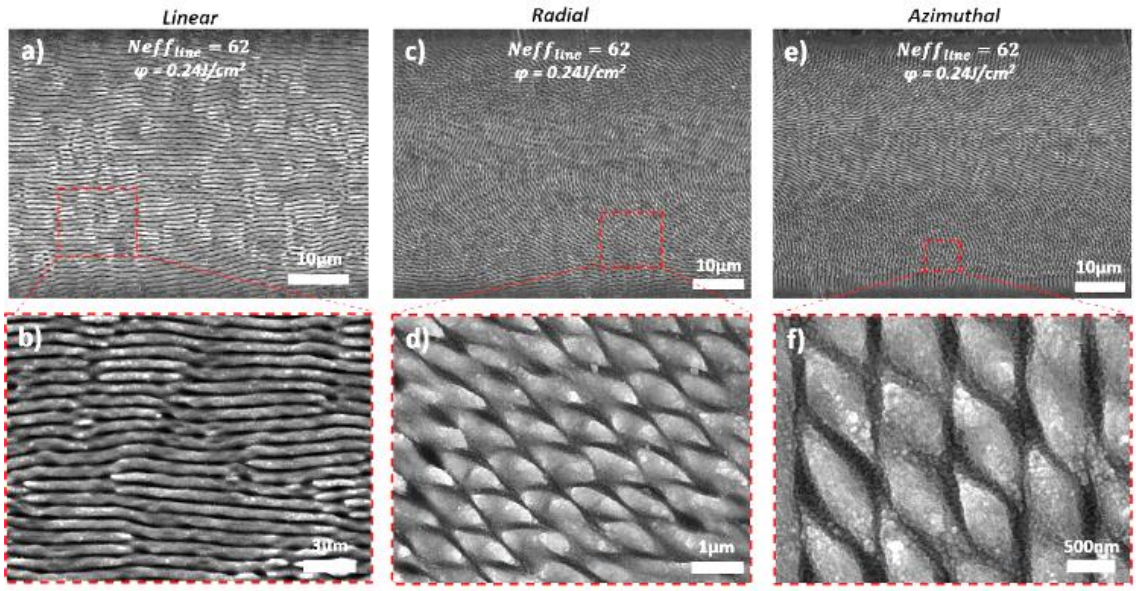

Figure 2.31: SEM micrographs of line scans of linear, radial and azimuthal beams [147]

2.3 Conclusion

The mechanism of protein adsorption and the factors responsible for the adsorption behaviour are highlighted in this chapter's first half. This section on protein also includes a brief introduction to the necessary background information. The protein adsorption section forms a basis for understanding the current research work.

The second section of this chapter discusses the laser-material interaction mechanism and the laser surface texturing techniques while highlighting the effect of processing parameters on the processing method. The state-of-the-art laser surface texturing was a review with emphasis on the nanoscale surface structures. It demonstrated the degree of control in generating nanostructured surfaces and the versatility of laser surface texturing as a surface engineering technique for creating tailored surfaces.

Some of the observations from this chapter are as follows:-

1. The protein used in the research is bovine insulin. It has a diameter of around 2.4 nm. The sulphide bonds in the proteins are active sites for chemical adsorption. Soft landing energies are used to drive the protein ions in the mass spectrometer to prevent fragmentation and retain the biological property.

2. A lack of research was identified for protein interaction with the metal surface in a vacuum environment. Still, most of the understanding of protein adsorption was developed through the literature on protein adsorption in the liquid phase, such as in the case of chemical adsorption. The protein ions with soft landing energies collide with the surface of the electrodes. Based on the gelatinous structure of the protein, surface topography plays an essential role in physical adsorption.

3. The literature search on the interaction of the workpiece and the laser parameters identified that the various parameters are essential for the ablation process, especially regarding the generation of laser induced nanostructures. The electron-phonon relaxation time and the thermal diffusion stage during

laser processing were identified as critical to the ablation mechanism process for the various laser pulse duration regimes.

4. The femtosecond regime has been extensively used for generating nanostructures to take advantage of its high intensity and non-thermal regime. However, the UV-picosecond has been used only in a limited way.

5. HSFL features are small and shallow features in metals compared to LSFL features and present a good opportunity for generating highly polished surfaces. Yet, limited information is available for uniform HSFL features on generation on a relatively big area (400 mm^2). Also, a research gap was identified for shallow surface features with a feature depth of less than 10 nm.

6. There is a lack of research on surface texturing for applications related to vacuum, such as metal surfaces used in characterisation instruments like the mass spectrometer.

Chapter 3

Material and Experimental Methodology

This chapter introduces the material (AISI Stainless steel 316L), the laser systems, the experimental test rig to analyse the protein contamination behaviour, the analytical equipment and the experimental methodology used in the research. Laser processing experimentation was conducted on three laser systems, i.e. nanosecond laser, picosecond laser and femtosecond laser. The analytical equipment for analysing the surface topography and chemistry is mentioned in brief. The last section of the chapter explains the experimental methodology used for laser processing and testing the protein contamination behaviour of the aperture plate electrodes.

3.1 Materials

AISI Stainless steel 316L is the material selected for this research since the aperture plate electrodes supplied by Waters Corporation are manufactured with the same material. The aperture plate electrode is one of the optics used in the mass spectrometer. It will be used to understand protein contamination behaviour.

3.1.1 Overview: AISI Stainless steel 316L

Stainless steels are ferrous alloys with a minimum of 10.5% chromium by weight and other elements. It shows high corrosion resistance due to the formation of a passive oxide layer on the surface. There are several families of stainless steel: Austenitic, Martensitic, Ferritic, and Duplex (combined austenitic-ferritic) [149,150].

3.1.1.1 Material properties

The stainless steel grade 316L is a low carbon content (indicated by L) austenitic stainless steel of series 300. This series has at least 7% Ni content to stabilise FCC γ-phase (austenite) and is also non-magnetic. The presence of molybdenum provides resistance to pitting and crevice corrosion. The low carbon content reduces the susceptibility to sensitisation, i.e. lowers the precipitation of carbides at grain boundaries [151,152].

Table 3.1 shows the composition of SS 316L in terms of its alloying elements, and the remainder of the material is iron.

Table 3.1: Chemical composition of SS 316L (mass%) [153]

	C %	**Si %**	**Mn %**	**P %**	**S %**	**Cr %**	**Ni %**	**Mo %**	**N %**
Min	-	**-**	**-**	**-**	**-**	16.0	10.0	2.0	**-**
Max	0.03	1.00	2.00	0.045	0.03	18.0	14.0	3.0	1.0

SS 316L forms a passivating surface oxide layer comprising chromium (oxide and hydroxide) followed by nickel, iron and molybdenum oxides, as shown in Figure 3.1. It forms on the stainless steel surface upon its contact with air. A high Nickel enriched layer

is seen just below the surface oxide layer [152,154,155]. The oxide layer thickness varies from 1-3 nm [156] and forms in air and water conditions. The oxide layer thickness is usually more in the air than underwater, with fewer concentrations of chromium hydroxide. Tardio et al. (2015) observed a preferential dissolution of the Fe_2O_3 in the oxide layer formed underwater [151].

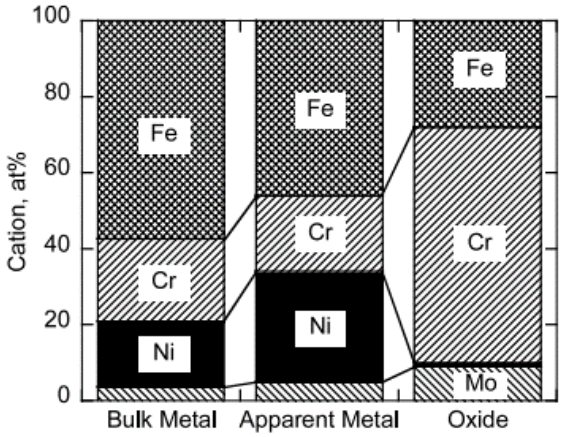

Figure 3.1: Schematic of the composition in the surface oxide layer and below layers in stainless steel [155]**.**

3.1.1.2 SS316L Useful for vacuum operations – Excellent outgassing property

Outgassing is one of the sources of gases in the vacuum system. Outgassing refers to the spontaneous liberation of gases from the materials in the vacuum system, such as the vacuum chamber's walls. The entrapment of gases occurs as diffusion from the surfaces to the material's interior. These gases are released during vacuum operations.

Stainless steel exhibits excellent outgassing properties as the outgassing rate of austenitic steel is very low compared to mild steel. It eliminates the need to coat the inner walls with protective coatings and is suitable for high vacuum operations [157]. The outgassing property can be improved by vacuum remelting or prebaking at 150º C for 14

hrs [158]. The outgassing property of SS316L is crucial since the mass spectrometer is a high vacuum device, and it is quite sensitive to variations in pressure conditions.

3.1.2 SS316L Aperture plates electrodes (supplier: Waters Corporation)

The aperture plate electrodes supplied by Waters Corporation are manufactured in AISI 316L stainless steel. The plate surface facing the ion beam is processed with lapping operation. The processed surface is smooth and reflective with an average area roughness Sa < 20 nm. The aperture plate has a central slot and a beam collimator. The region around the central slot is prone to contamination due to ion beam collision. The surface around the central opening of the plate marked by the red rectangle, as shown in Figure 3.2, is the region of interest and potential area for ion beam collision. Laser processing will be done in the marked region. The laser processing is scheduled in the university's laser processing facility.

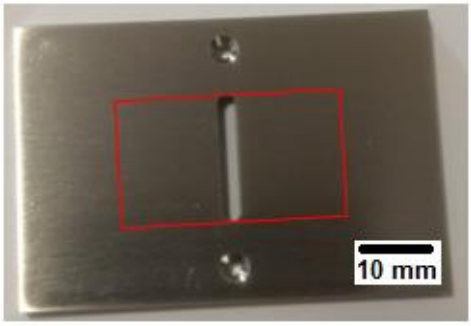

Figure 3.2: Optical image of an aperture plate as supplied by Waters Corporation

AFM analysis shown in Figure 3.4 revealed initial surface roughness Ra=10.5±2.1 nm for the as-received aperture plates, and the area roughness is estimated to be Sa=11.6±1.1 nm. SEM surface scan of the surface, shown in Figure 3.3, is similar to the 3D image in the AFM scan (Figure 3.5). The scratches in the images reflect results seen in

mechanically polished surfaces. The SEM scan was conducted with the Ultra-55 SEM. AFM scan was performed using the JPK Nanowizard AFM, and the data analysis was done using the Gwyddion software.

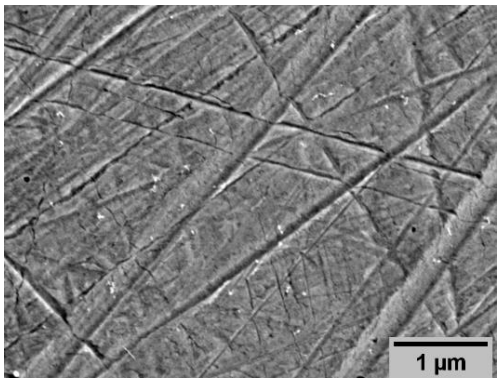

Figure 3.3: SEM micrograph of the aperture plate surface. Scratches on the surface reflective of mechanical surface polishing are seen in the image.

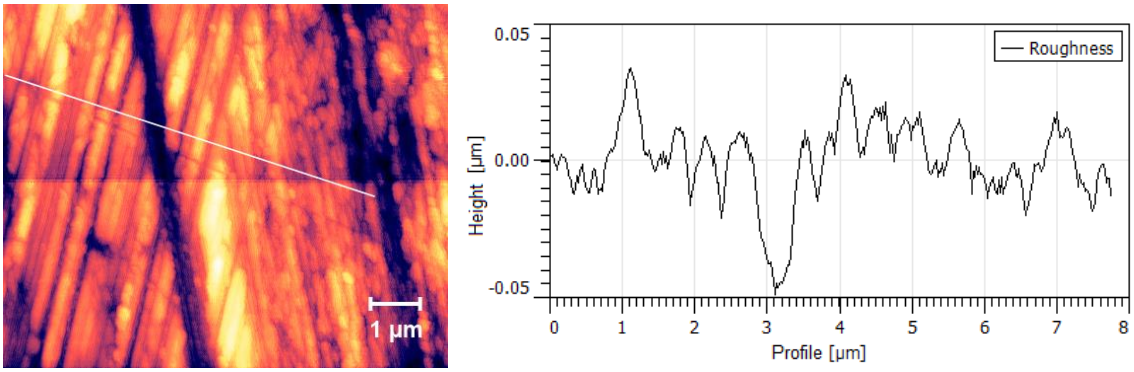

Figure 3.4: AFM scan of the aperture plate surface from with the marked region shown in Figure 3.2. The scratch marks seen in the image are reflective of mechanical polishing; (left) AFM scan with profile line in white; (right) the plot of the profile line

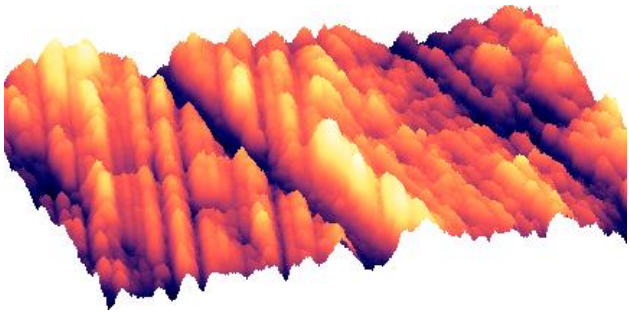

Figure 3.5: 3D representation of the AFM scan. The scratch marks from mechanical polishing can be seen clearly in the 3D image.

3.1.3 Mirror finish SS316L test samples (supplier: Goodfellow)

The precision machined aperture plate electrodes from Waters Corporation were available in limited numbers and thus cannot be used for investigating the surface textures produced by the laser systems. Hence, stainless steel SS316L samples from Goodfellow Ltd. were used for the investigation stage. These samples were of thickness 1.2 mm, annealed and polished with roughness Ra of 11.8±2 nm. The samples were available as 100 mm x100 mm. These samples were cut into 15x20 mm strips and cleaned with ethanol before experimentation.

After the initial investigation of laser surface texturing capabilities on the Goodfellow sample surfaces, the selected results were repeated on the aperture plate electrodes for further experimentation.

3.2 Laser Systems

The laser surface texturing experiments for the first stage were conducted on the short pulse (nanosecond) and the ultrashort pulse (picosecond and femtosecond) laser systems. The section introduces the laser systems with their respective setups.

3.2.1 Nanosecond laser: Violino Green marker 532 nm

The nanosecond laser-based experiments were conducted using the Violino Green marker laser designed to generate pulses of 7 ns for wavelength 532 nm (green, visible). The 532nm wavelength is generated using a diode pumped Nd:YAG laser source producing laser at wavelength 1064nm coupled with a frequency doubling module. It is a Class 4 laser manufactured by Laservall [159]. The pulse frequency of the laser is between 20 kHz

to 100 kHz, and TEM00 $M^2 < 1.2$. The laser was delivered through a 3-axis galvanometer. The standard focal spot size is 55 μm at a focal distance of 199.5 mm. The pulse frequency of **30 kHz** was selected for the experiments.

3.2.1.1 Laser Power Calibration

A Gentec-EO power meter was used to measure the average laser power of the laser system at a pulse frequency of 30 kHz. The power meter was rated with a power sensitivity of 0.65 mV/W, repeatability ±0.5%, a maximum energy density of 1 J/cm², and convection cooled. The average power values are shown in Table 3.2.

Table 3.2: Average laser power of nanosecond laser

Power %	Average Power (W)	Power %	Average Power (W)
100	2.80 – 3.10	75	0.93 – 1.02
95	2.50 – 2.80	70	0.70 – 0.80
90	2.07 – 2.25	65	0.42 – 0.50
85	1.56 – 1.72	60	0.18 – 0.20
80	1.25 – 1.40	55	0.08 – 0.12

3.2.2 Picosecond laser: EdgeWave 400W (Nd:YVO_4)

The ultra-short pulse picosecond laser used in this research is the EdgeWave PX400-3-GH (EdgeWave GmbH Innovative Laser Solutions, Germany), designed to generate pulses of 10 ps [160]. It is a high-power Class 4 laser of max 400W average power and can produce three different wavelength modes, i.e. 1064 nm (IR), 532 nm (green, visible) and 355 nm (UV). The laser operates at a high pulse frequency between 400 kHz and 20 MHz. The beam has a quality factor M^2 of 2.1 and is linearly polarised.

A beamline of **355 nm (UV)** with a pulse frequency of 404.7 kHz was selected for the experiments for the research. The schematic of the beamline is shown in Figure 3.6. The beam is focussed through an F-Theta lens of an effective focal length of 214.852 mm [161] attached to the Digi-Cube Galvo head [162]. The Galvo head is attached to the Aerotech linear stage and can move in the Z direction to focus the laser beam on the workpiece. The movement of the Galvo head mirrors is controlled using the third-party control software, DigiStruct® [163].

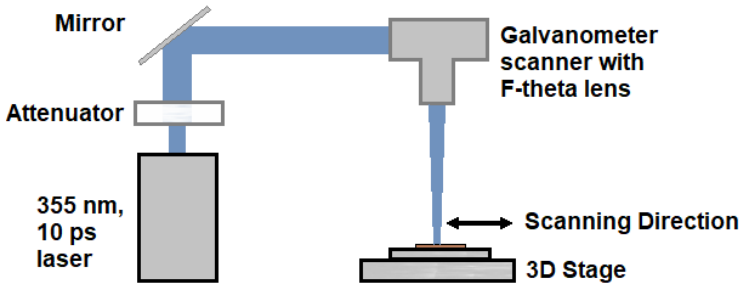

Figure 3.6: Schematic of the EdgeWave Picosecond laser (λ=355 nm, p=10 ps, f=404.7 kHz)

3.2.2.1 Laser Power Calibration of UV Picosecond beamline

The average laser power was measured with a Gentec-EO power meter at a pulse frequency of 404.7 kHz is shown in Table 3.3. The power meter was rated as power sensitivity of 0.23 mV/W, repeatability ±0.5%, maximum energy density of 1 J/cm², and fan cooled.

Table 3.3: Average laser power of UV Picosecond laser

Power %	Average Power (W)	Power %	Average Power (W)
100	23.9	55	8.5
90	23.0	50	6.3
80	20.9	45	4.7
70	17.0	40	3.1
65	13.8	35	2.0
60	10.8	30	1.8

3.2.2.2 Verification of the galvo head response to control software

High scan speeds, more than 5000 mm/sec, were used to control the pulse overlap of this high pulse frequency laser. The galvo is controlled using the DigiStruct® software. The time for 250 scans of 30mm x 30 mm square was recorded through the software, and the speed of the galvo was calculated. Figure 3.7 shows the galvo response to the input speed. A non-linear lag was noticed at higher speeds. It is possibly the lag in the motors of the mirrors of the Galvo head and deceleration at sharp corners. The table of recorded times is available in Appendix A.1.

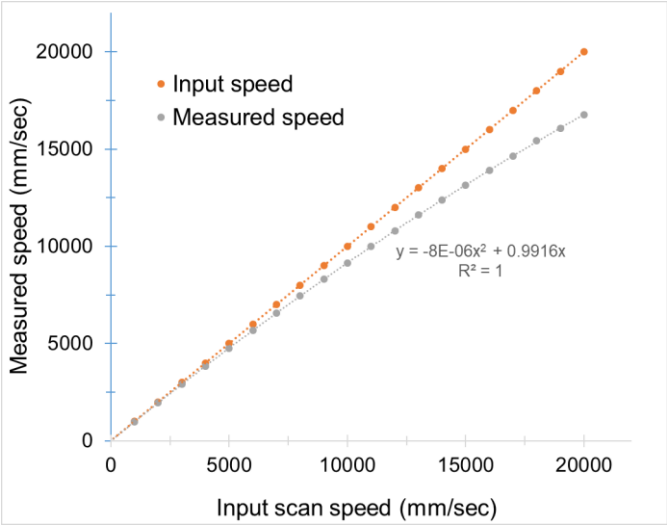

Figure 3.7: Galvo response to control software based on laser movement over a square shape

A second-level verification was done on the galvo response by measuring the laser ablation spot gaps to compute the actual speed. The single-pulse ablation laser spot was drawn out on the stainless steel sample at 23500 mm/sec to maintain a pulse-to-pulse gap of 58-59 µm. The scan drew lines 100-120 mm long, with a sample width of 10 mm set in the middle, as shown in Figure 3.8. This strategy ensured a stable laser power scan over the sample, verified through a power meter.

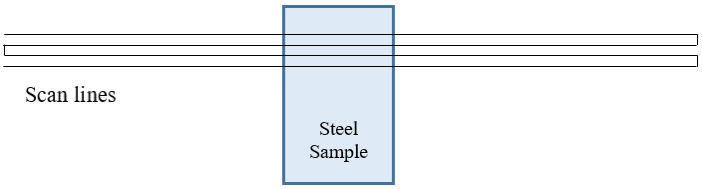

Figure 3.8: Scan procedure for galvo verification

Figure 3.9 shows the SEM micrograph of laser spots made using the power of 7W and a frequency of 404.7 kHz. The distance of the spots from the image and the profile plot can be measured as 58±1 µm. It was concluded that scans with longer linear lengths helped maintain galvo response accuracy and reduce lag.

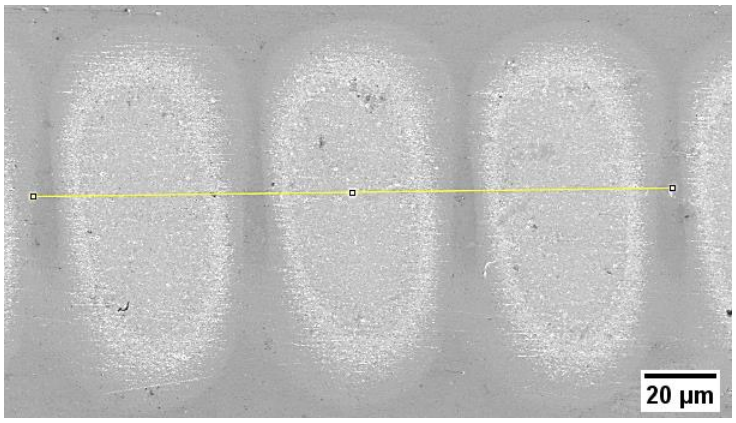

Figure 3.9: SEM image of single pulse laser spots with the profile

(a) Image of single pulse laser ablation spots using galvo at a speed of 23500 mm/sec

(b) Profile of the laser spots on the SEM image using ImageJ.

3.2.3 Femtosecond laser: Libra Ti-sapphire 800 nm 1W

The Coherent Libra laser used in the experiments uses the principle of chirped pulse amplification in a Ti-sapphire crystal to deliver femtosecond laser pulses (λ=800nm, t_{laser}=100fs, f_{laser}=1000Hz, linear polarisation and maximum pulse energy Ep=1mJ) was used for the femtosecond experiments. The pulse energy is attenuated using a set of OD filters, together with an attenuator consisting of a ½ waveplate and a Glan laser polariser (WP1 and Polarizer in Figure 3.10). The state of polarisation is then converted using either a ¼ waveplate (Newport) or an S-waveplate (Altechna), referred to as WP2 in Figure 3.10, to produce circular, radial or azimuthal, or remains linear if no waveplate is used. M1 to M3 are dielectric-coated low-dispersion mirrors (Thorlabs). A scanning galvanometer (Scanlab) with dielectric coated mirrors and a 100mm focal length f-theta lens (Thorlabs) focus the beam on the surface of the workpiece, which is accurately located in the focal region thanks to a 3-axis nano-precision positioning stage (ANT95 with Npaq, from Aerotech).

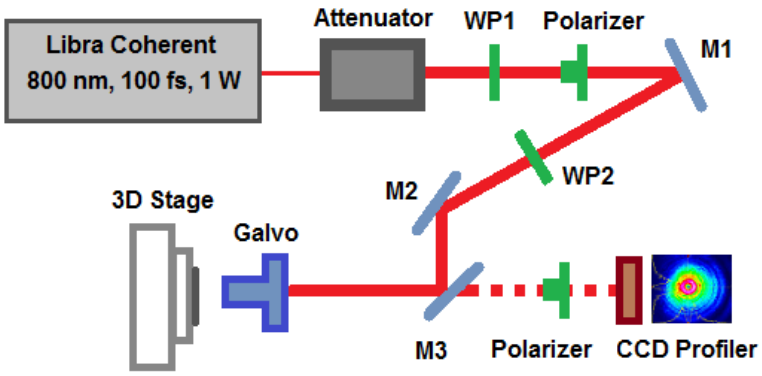

Figure 3.10: Schematic representation of the femtosecond experimental setup.
The beam attenuator consists of OD filters and uses a Glan laser polariser & waveplate to control the incident pulse energy. The waveplates (WP1 and WP2) convert its polarisation. The laser motion is controlled through a scanning galvanometer before it textures the workpiece. Beam intensity profiles can be analysed by a CCD profiler by flipping mirror M3 (azimuthal polarised beam is shown here).

3.3 Experimental test-rig to analyse protein contamination behaviour

The test rig is the experimental adaption of the mass spectrometer phase of the Liquid Chromatography Mass Spectrometer (LC-MS) system. This section provides a brief background on the LC-MS systems and introduces the experimental test rig.

3.3.1 Overview: Mass spectrometry (MS)

Mass spectrometry (MS) is a powerful analytical method to identify and analyse compounds in their quantification and composition. In the mass spectrometer, gas phase ions of the analyte are generated through ionisation by an ionisation source and separated based on their mass-to-charge (m/z) ratio. These ions pass through various electrodes and are collected in the detector for analysis. The result is a spectrum showing the abundance of the ions showing the composition of the analyte [164,165]. The mass analysers (m/z) are of different types, such as magnetic sector, quadrupole, time-of-flight, and trapped ion [32,166,167]. It has a wide variety of applications, especially in medical research [13,14,168], the food industry [19,20] and environmental research [21,22].

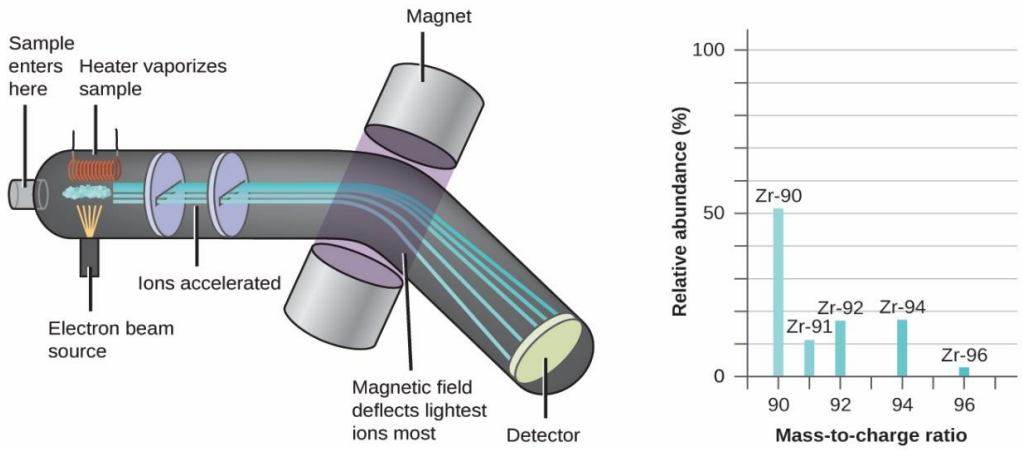

Figure 3.11: Diagram of a Mass Spectrometer (MS) (left); Analysis of zirconium in an MS system produces a mass spectrum with peaks showing its different isotopes (right) [169]

3.3.2 Overview: The LC-MS system

In liquid chromatography, the mixture (termed the mobile phase) is converted to fluid in the LC system and passed over a stationary phase bed. The relative distribution coefficients of the individual fluids in the mobile phase help them get separated.

Both liquid chromatography and mass spectrometry techniques have been combined as LC-MS systems to analyse components of mixtures. Figure 3.12 shows a general schematic of the LC-MS system. The LC phase separates the mixtures, and the mixture's components are passed as analytes to the MS phase. The analytes are ionised at the LC-MS interface for analysis in the MS phase. The most commonly used techniques for producing ions under atmospheric pressure conditions are Electrospray ionisation (ESI) (see section 2.1.2). The LC phase can be HPLC or UPLC system. The MS phase is generally a complex hybrid system of different mass analysers for improved performance [32].

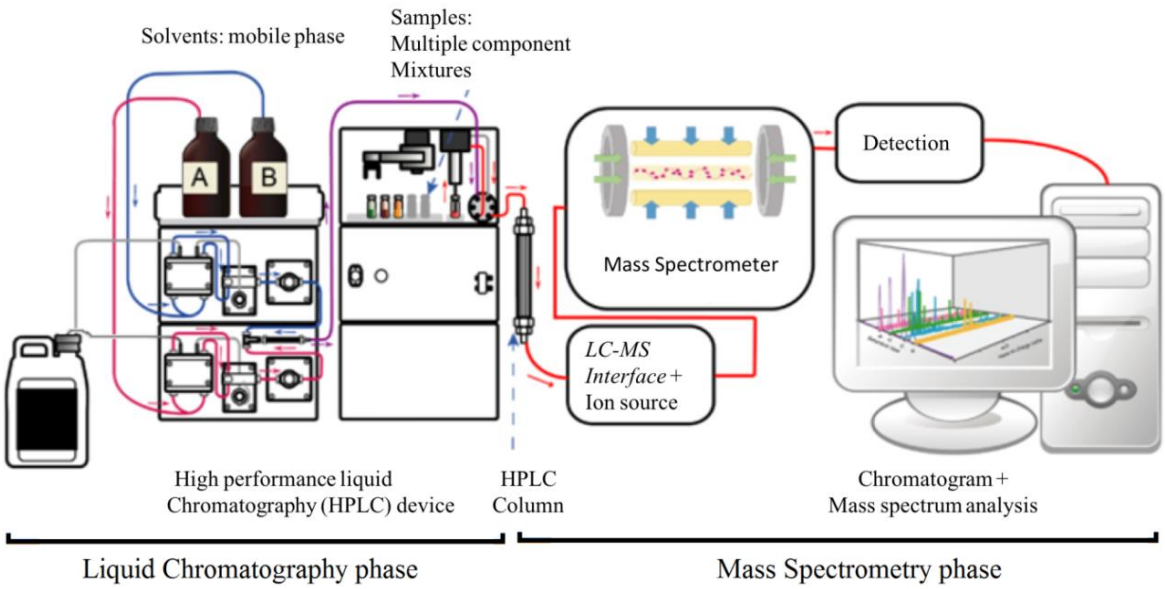

Figure 3.12: Diagram of the LC-MS system (Adapted from [170]**)**

3.3.3 Experimental test-rig based on Waters mass spectrometer

The experimental test rig to conduct the protein contamination behaviour testing was built by Waters at their facility in Wilmslow, Cheshire. It has a simplified input system instead of the liquid chromatography phase, focusing mainly on the mass spectrometer phase. The test rig is based on the Waters orthogonal acceleration time-of-flight platform model XEVO G2-XS. It is designed to reproduce and analyse the actual scenario of the MS instrumentation electrodes. The test rig facilitates for comfortable replacement of the electrodes as needed for analysis. In our research, we used the aperture plate electrode to understand the protein contamination behaviour of its surface exposed to ion beam contamination.

3.4 Surface Characterisation Equipment

The laser textured surfaces were ultrasonically cleaned with an ethanol bath to remove ablation debris. The surfaces were then characterised topographically with the optical microscope, SEM and AFM. Additionally, after protein contamination behaviour tests, the laser processed aperture plate surfaces were characterised for surface chemistry using XPS and ToF-SIMS.

3.4.1 Optical and Confocal Microscope

The topography of the samples was initially analysed optically using the optical microscope (Keyence VHX-5000 digital microscope [171]) and the confocal microscope

(Keyence VK X-200 series [172]). These microscopes were primarily used to measure the single laser spot crater dimensions, which is helpful in ablation threshold measurements.

The optical microscope, Keyence VHX-5000, shown in Figure 3.13, has a magnification between 100-1000x and is equipped with a 1/1.8-inch CMOS image sensor with virtual pixels: 1600 (H) x 1200 (V). It displays a 16-bit resolution through RGB data from each pixel. The microscope produced quality micrographs of the single ablation spots, which is helpful in ablation threshold measurements. However, an in-depth analysis of the surface structures could not be carried out due to the high reflectance of the surfaces.

Figure 3.13: Image of the Keyence VHX-5000 setup. (left) microscope; (right) visualisation monitor along with control panel.

The laser processed surfaces were also analysed using the confocal microscope from the Keyence VK X-200 series, shown in Figure 3.14(left) [172]. The microscope has a magnification range between 200x to 24000x (cumulative magnification of the objective lens 10x-150x, magnification in the display monitor 200x-3000x, and optical zoom 1x-8x), and a 1/3-inch CCD image sensor. It uses the laser beam of wavelength 408 nm with a diameter of 0.4 μm as the illumination source instead of white light, as shown in Figure 3.14(right). As mentioned in the catalogue, the instrument's resolution is 0.5 nm for width

and 1 nm for height. It is an excellent system for creating 3D images by reconstructing multiple 2D images at various depths at the same location. Hence, it was further used as a quick tool for coarse analysis to determine the presence of periodic laser surface structures.

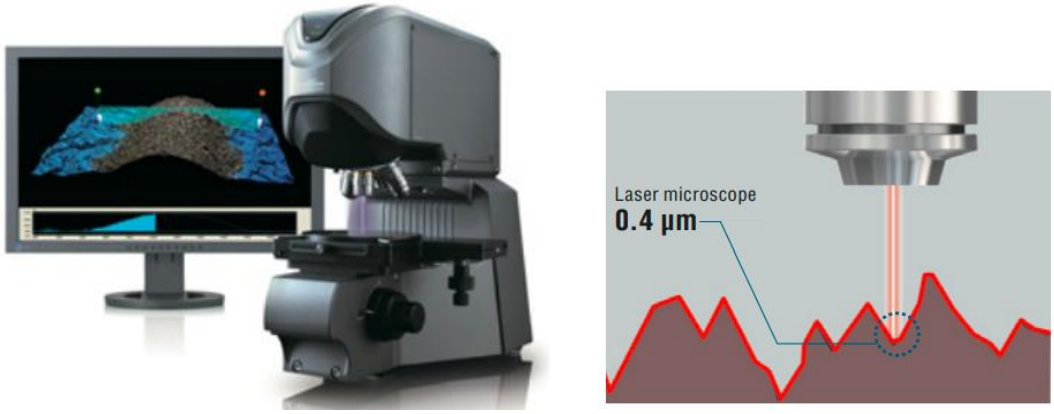

Figure 3.14: (left) Image of the VH X-200 confocal microscope set up showing the microscope and the display monitor; (right) The microscope uses a laser pointer for scanning instead of taking images. 3D reconstruction is directly available after the scanning. The laser pointer diamter is 0.4 µm.

3.4.2 Scanning Electron Microscope (SEM)

A Field Emission Scanning Electron Microscope (SEM) from Zeiss model Ultra 55 was used to analyse the morphology of the laser-induced microstructures and the quality of the micro-machined surfaces. The system is shown in Figure 3.15. This microscope allows magnification factors up to 500000X, with a resolution of 1 nm at a beam accelerating voltage of 15 kV. The InLens (for surface imaging) and Secondary Electron detector (SE2) were used during the research.

The samples were cleaned with high pressure nitrogen gas to remove dust particles. They were then placed in the chamber of the SEM and locked securely. The Ultra-55 provides a platform to fit samples up to 50 mm x 50 mm. The precaution was taken during

focussing and scanning to prevent the samples from colliding with the detectors. The aperture plate from Waters was comfortably set up on the scanning table.

The SEM was useful in imaging the nano-scale periodic structures compared to the optical microscopes. These systems use electrons instead of photons to interact with the material and measure the beam interaction. The shorter wavelength of the electrons compared to the white light (in optical microscopes) have a lower diffraction limit and provide better resolution.

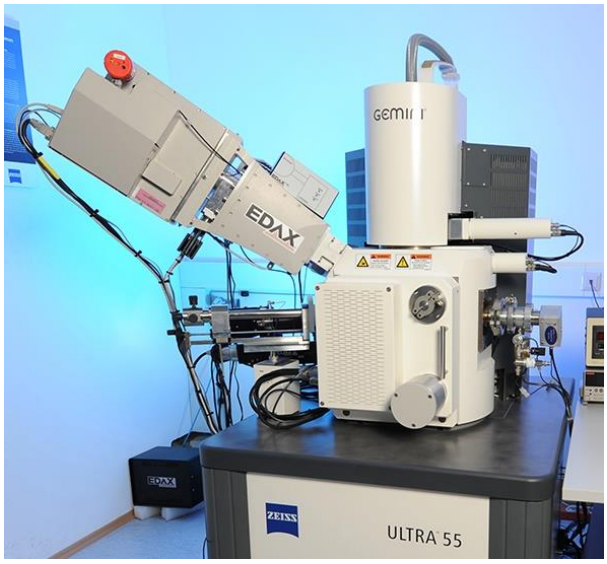

Figure 3.15: Image of the Zeiss Ultra 55 FEG-SEM [173]

3.4.3 Atomic Force Microscopy (AFM)

The atomic force microscope (Bruker JPK Nanowizard Series 6.0 AFM [174]) was used to evaluate the surface topography, especially the depth profile (Δz). It has a scan area coverage of 100x100 μm and a depth range of 15 μm. The semi-contact mode (tapping mode), with a tip apex size of 10 nm, was used to acquire the AFM images, as it overcomes the issues of friction or/and adhesion occurring in contact mode and that of low resolution in non-contact mode. AFM tips Tap300Al-G from BudgetSensors [175] and high aspect

ratio HAR1-200A-10 from Bruker [176] were used in tapping mode during image scan. The employed optical head allows viewing of the tip-sample positioning during the scan and achieves a high resolution. The AFM's resolution is subjective and depends on the scanning parameters.

The sample cleaning may be required depending on situations. In our case, the sample surface was cleaned with dry nitrogen to get rid of dust particles. The AFM measurements were carried out in dry air, i.e. under normal conditions. Precautions were taken to avoid the AFM tip colliding with the surface while setting up the instrument. The instrument provides a platform to fit samples up to 50 mm x 50 mm x 3 mm. The aperture plate from Waters was comfortably set up on the scanning table.

Figure 3.16: Optical image of the JPK Nanowizard AFM (left); Sample holder XY stage that fits samples up to 50 mm x 50 mm x 3 mm [174] **(right).**

3.4.4 X-ray Photoelectron Spectroscopy (XPS)

X-ray photoelectron spectroscopy (XPS) is a quantitative technique for measuring the elemental composition of the surface of a material, and it also determines the binding states of the elements. In XPS, the sample is irradiated with an X-ray source, and core electrons are emitted from the sample following the adsorption of the incident photons. Only electrons close to the surface escape without an energy loss. A schematic diagram of the XPS system is shown in Figure 3.17. The resulting XPS spectrum is a plot of the number of photoelectrons emitted vs the binding energy derived from the measured kinetic energy of the ejected photoelectrons [177,178]. A sample of the XPS spectra of the C 1s is shown in Figure 3.18.

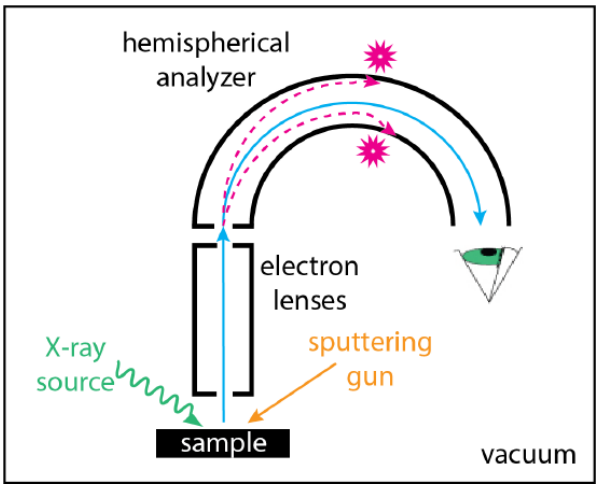

Figure 3.17: Schematic diagram of the basic instrumentation for X-ray photoelectron spectroscopy: an X-ray source for generating photoelectrons; a sputtering gun for removing layers of the sample; a set of electron lenses for collecting and focusing the photoelectrons; a hemispherical analyser for isolating electrons by their kinetic energies; and a transducer to count electrons. The entire instrument is held under a vacuum [179]**.**

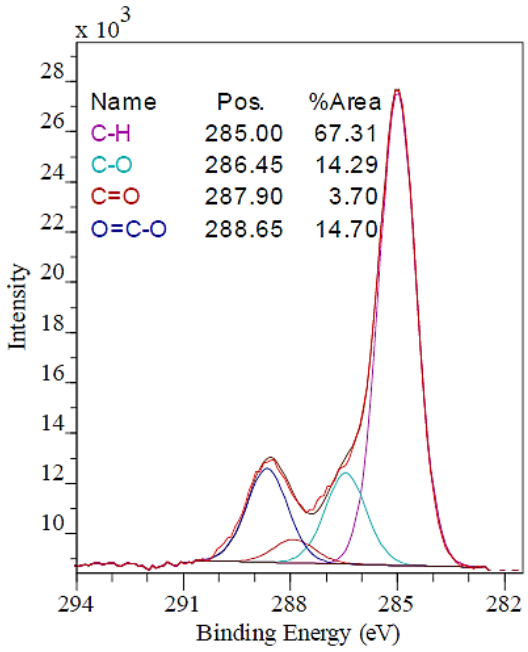

Figure 3.18: XPS core spectra of C 1s highlighting identified elements' peak binding energy positions. The intensity is the number of photoelectrons emitted.

XPS measurements were performed by Lucideon Ltd (Staffordshire, UK) with a Kratos Axis Ultra DLD spectrometer using monochromatic Al Kα X-rays (1486.6 eV). Survey spectra were acquired from sample areas measuring around 2 mm x 0.8 mm with a pass energy of 160 eV, and the surface elemental compositions were determined. Selected high resolution spectra were recorded with pass energies of 20 eV. Elements and chemical states present on the surface of SS 316L were determined by looking for peaks such as C 1s, O 1s, and N 1s. Charge compensation was achieved using a beam of magnetically focussed electrons as a flood current. The standard photoelectron take-off angle used for analysis is 90° giving a maximum analysis depth in the range of 5-8 nm.

CASA XPS software is used to process the data, and the surface elemental and chemical state compositions are tabulated. The assumption that the sample volume probed is homogeneous is considered during data processing. The error values (σ) are calculated from the statistical noise on the data and represent one standard deviation confidence limit;

i.e. there is a 68% probability that the actual composition lies between the calculated compositions given in the results table $\boldsymbol{c \pm \sigma}$. There is a 95% probability that the actual composition lies between $\boldsymbol{c \pm 2\sigma}$. If the $\boldsymbol{\sigma}$ value is comparable to $\boldsymbol{c}$, the element is at or very close to its detection limit for the analysis conditions. The absolute accuracy of the composition results depends upon several factors, but the error values enable the significance of compositional differences between physically similar samples to be assessed.

The oxygen 1s peak has been curve-resolved, but there are many oxygen atom environments, making precise assignment of the component peaks difficult. As a guide, three typical components are used (a) an inorganic oxide, (b) hydroxide or carbonyl type (O=C) groups and (c) organic contamination O-C groups.

3.4.5 Time-of-Flight Secondary Ion Mass Spectrometry (ToF-SIMS)

Time-of-Flight Secondary Ion Mass Spectrometry (ToF-SIMS) is a surface sensitive analysis technique in which an ion beam (primary ions such as Cs^+, Au^+, Au_3^+, Bi^+, Bi_3^+, Bi_3^{++} [180]) is irradiated on a solid sample to remove molecules from the outermost surface. The primary ion energy is transferred to target atoms via atomic collisions, and a so-called collision cascade is generated. Part of the energy is transported back to the surface, allowing surface atoms and molecular compounds to overcome the surface binding energy. The removed particles/ions emitted from the surface (secondary ions) are then accelerated through a flight path to hit a detector. Their mass is determined using the difference in time-of-flight. A schematic diagram of the ToF-SIMS is shown in Figure 3.19. The instrument can obtain information regarding elements or molecular species within 1 nm of the sample surface at a very high detection sensitivity.

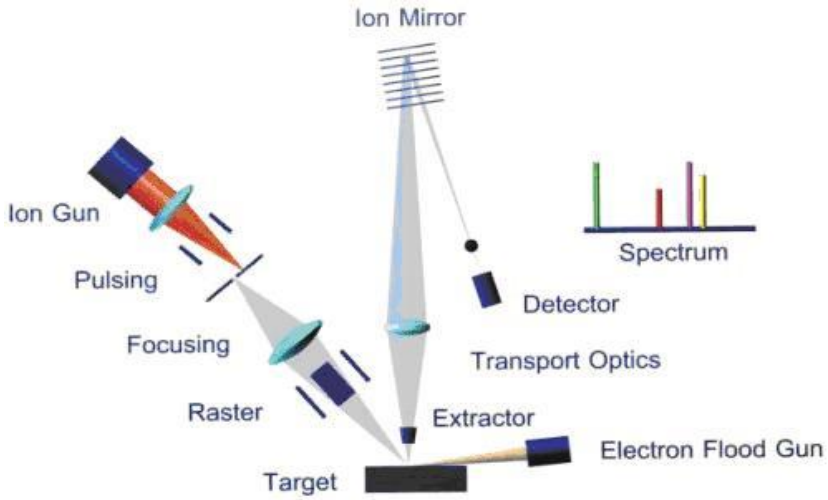

Figure 3.19: Schematic diagram of IONTOF ToF-SIMS instrument [181]

ToF-SIMS measurements were done by Lucideon Ltd (Staffordshire, UK) using an ION-TOF TOF.SIMS 5 instrument equipped with a bismuth primary ion source (Bi^{3+}). The images were acquired under static conditions from sample areas measuring 20 mm x 20 mm using the positive-ion macro-raster mode with a patch size of 400 μm x 400 μm, 15 frames/patch and a total pixel density of 50 px/mm. In this mode, a full spectrum is acquired at each pixel and saved as raw data, thus allowing retrospective image and spectral reconstructions. The spectra are a plot of signal intensity or ion counts on the Y-axis versus m/z on the X-axis. The height of a signal is representative of the ion count present in the spectrum, and the m/z value is its mass–to–charge ratio.

ToF-SIMS analysis was done on the aperture plates to identify the protein contamination on the surface of a non-laser processed reference aperture plate electrode (section 3.6.2.3), nanosecond laser processed aperture plates (section 4.4.3) and picosecond laser processed aperture plates (section 5.4.3). The protein used in the research for protein contamination study is bovine insulin. Its presence is identified by observing the signals of

its amino acids. Some of the amino acid signal identifiers used for detecting bovine insulin in ToF-SIMS spectra (positive ion polarity) [182–184] are listed in Table 3.4.

Table 3.4: Amino acid residue signal identifier for bovine insulin in ToF-SIMS [182–184]

Amino acid residue	Chemical representation	m/z ratio
Glycine	CH_4N^+	30
Alanine	$C_2H_6N^+$	44
Serine	$C_2H_6NO^+$	60
Proline	$C_4H_8N^+$	70
Valine	$C_4H_{10}N^+$	72
Threonine	$C_3H_8NO^+$	74

Amino acid residue	Chemical representation	m/z ratio
Lysine	$C_5H_{10}N^+$	84
Glutamic acids	$C_4H_6NO^+$	84
Isoleucine/Leucine	$C_5H_{12}N^+$	86
Histidine	$C_5H_8N_3^+$	110
Phenylalanine	$C_8H_{10}N^+$	120
Tyrosine	$C_8H_{10}NO^+$	136

3.5 Experimental Procedure: Laser surface texturing of test samples and aperture plate electrodes

3.5.1 Laser processing on SS 316L test samples from Goodfellow

Nano-scale surface structures can be generated from both short (nanosecond) and ultra-short (picosecond and femtosecond) pulse regimes. The structures are affected by the laser processing parameters such as wavelength, pulse duration, and overall laser fluence at one spot. The formation of these structures is a complex phenomenon. The experimentation with both short and ultrashort pulses is to develop an understanding of the generation of nano-scale structures and select potential cases of surface texturing that can be used for laser processing of the aperture plate electrodes.

3.5.1.1 Optical characterisation of the laser beam

The laser beam shape is critical in determining the laser scanning strategy. Hence, the beam profile was investigated before the surface texturing experiments were carried out. Depending on the laser system facilities, the laser beam profile and the polarisation purity was analysed using an optical/SEM image or a CCD profiler.

3.5.1.2 Ablation threshold fluence for single spot single laser pulse

The laser ablation threshold fluence (F_{th}) was estimated using the method proposed by Liu [185] based on the experimental measurement of the size of ablation craters obtained at different laser fluences. The craters were produced by focusing the laser beam on the sample surface.

The ablation threshold fluence (F_{th}) depends on several experimental parameters, including the material, laser Gaussian beam radius (ω_0) and the peak fluence (F_0). It can be estimated using Liu's model [185], based on the experimental measurement of the size of ablation craters obtained at different laser fluences. Single laser ablation spots are considered for determining the threshold fluence.

The spatial fluence profile F(r) of a Gaussian beam is given by

$$F(r) = F_0 e^{\frac{-2r^2}{\omega_0^2}} \quad \text{..... (Eq 3.1)}$$

where r is the distance from the beam centre. The peak fluence and pulse energy are directly related by

$$F_0 = \frac{2E_p}{\pi\omega_0^2} \quad \text{..... (Eq 3.2)}$$

And the ablated crater diameter D for the threshold fluence (F_{th}) can be related to both peak fluence through the equation

$$D^2 = 2\omega_0^2 \ln\left(\frac{F_0}{F_{th}}\right) \quad \text{..... (Eq 3.3)}$$

The linear dependence of the peak laser fluence on the pulse energy makes it possible to determine the beam radius (ω_0) from the plot of crater diameter squared (D^2) to pulse energy (E_p). And the plot of crater diameter squared (D^2) to fluence can provide the threshold fluence. Extrapolating the linear fit function to zero gives the fluence for zero D^2 value.

The relationship between pulse energy, beam radius, and crater diameter squared (D^2) can be established by substituting equation 3.2 in equation 3.3. The new relationship is given as

$$D^2 = 2\omega_0^2 \, ln\left(\frac{E_p}{E_{th}}\right) \quad \text{..... (Eq 3.4)}$$

3.5.1.3 Ablation threshold fluence for single spot multiple laser pulses

With increasing pulses at one spot, the threshold fluence changes, hinting at an accumulative phenomenon. Several approaches have been cited to account for the phenomenon [103,186,187], with the first model being proposed by Jee et al. (1988) [187]. The damage behaviour was attributed to the change in absorbance due to increased roughness and the change in the thermal stress-strain energy storage cycle with increased pulses at the spot. And so, the ablation fluence reduced with each consecutive pulse.

The equation for the threshold fluence with multiple pulses (N) is given as:-

$$F_{th}(N) = F_{th}(1).N^{S-1} \quad \text{..... (Eq 3.5)}$$

where N = Number of pulses, $F_{th}(N)$ = threshold fluence for N pulses, $F_{th}(1)$ = threshold fluence for 1 pulse, S = coefficient to characterise the nature of incubation within the material, whereas $S = 0$ (complete incubation), $S = 1$ (absence of incubation), $0 < S < 1$ (material softening) and $S > 1$ (material hardening).

Since the laser scan was done as a line scan, equation 3.5 can also be written in the form of pulse overlap (OL%), where the overlap $OL\% < 1$

Pulse overlap percentage, $OL\% = 1 - (1 / N)$ ……. **(Eq 3.6)**

Appropriately, the equation for the threshold fluence for N pulses can be rearranged to use the overlap percentage for estimation.

$$F_{th,OL}(N) = F_{th}(1).\left(\frac{1}{1-OL}\right)^{S-1} \quad \text{……. (Eq 3.7)}$$

The equation does not cover large pulse numbers (N_∞) but works satisfactorily for a shorter number of pulses ($N < 100$ kHz) [186]. The incubation coefficient for AISI 316L stainless steel is between 0.8 and 0.9 [104,188,189], and the value selected for the experiments is 0.86 [104].

3.5.1.4 Surface texturing experiments

Laser texturing was performed with bi-directional hatch lines at different laser parameters. Square with sizes around 2.5 mm was textured for nanosecond and femtosecond lasers. In the case of the UV-picosecond laser, long linear scans, as shown in Figure 3.8, were done to control pulse overlap and avoid galvo response lag during high-speed movement. The scan speed (Vsc) and hatch distance (Δy) were calculated based on

the pulse overlap percentage. Scan lines were drawn in the X direction, and the hatch offset was provided in the Y direction for all the surface textures, as shown in Figure 3.20.

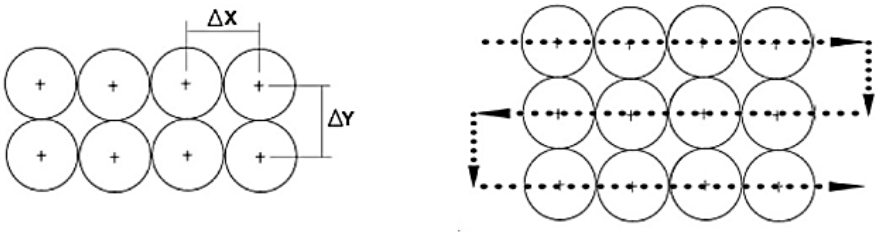

Figure 3.20: Scanning procedure for laser. Δx is spot offset distance, and Δy is hatch distance (left); Scan movement is shown in a dotted line (right)

The spot displacement in the X direction, **Δx = Vsc / f** ……. **(Eq 3.8)**

Where **Vsc** is scan speed (mm/sec), and ***f*** is the pulse repetition rate

Pulse overlap percentage, **OL = 1 – Δx / 2ω₀** ……. **(Eq 3.9)**

Based on equations 3.8 and 3.9, we can determine the scan speed (***Vsc***) and hatch distance (**Δy**) based on pulse overlap percentage.

Vsc = 2ω₀ .*f*. (1 – OL) ……. **(Eq 3.10)**

Hatch distance, **Δy = 2ω₀. (1 – OL)** ……. **(Eq 3.11)**

The effective number of pulses at a spot (N_{eff}) and the maximum accumulated fluence (F_a^{max}) can be calculated based on the equations by Mezera & Römer (2019) [190]. Both the cases when Δx = Δy, and Δx ≠ Δy is presented below.

$$N_{eff} = \left(\frac{\pi}{8}\right).\left(\frac{\mathrm{d}}{\Delta \mathrm{x}}\right).\left(\frac{d}{\Delta \mathrm{y}}\right) = \frac{\pi}{8(OL-1)^2} \quad \text{…… (Eq 3.12)}$$

$$F_a^{max} = N_{sc}.F_0.\frac{\pi}{8(OL\ -1)^2}\left[1 + 2.exp\left(\frac{-\pi^2}{8(OL\ -1)^2}\right)\right]^2 \quad \text{…… (Eq 3.13)}$$

$$F_a^{max} = N_{sc}.F_0.\frac{\pi.d^2}{8(\Delta x)(\Delta y)}\left[1 + 2.exp\left(\frac{-\pi^2.d^2}{8(\Delta x)(\Delta y)}\right)\right]^2 \quad \text{..... (Eq 3.14)}$$

Where ***d*** is beam diameter, i.e. $\mathbf{2\omega_0}$ (μm), ***OL*** is the pulse overlap percentage, Δx is pulse-to-pulse distance, Δy is hatch distance, $\boldsymbol{F_0}$ is the applied fluence (J/cm^2), and $\boldsymbol{N_{sc}}$ is the number of scans on the surface.

The beam profiles/polarisations that were tested for the various laser systems are:-

1) Nanosecond: Linear polarisation
2) Picosecond: Linear polarisation
3) Femtosecond: Linear, Circular, Radial and Azimuthal polarisations

The morphology of the scan regions was analysed using the optical microscope, SEM and AFM.

3.5.2 Laser processing of aperture plate electrodes from Waters

The aperture plates provided by Waters Corporation were laser processed and analysed for protein contamination behaviour. The bovine insulin contaminant particles to be used as the protein contaminant for testing are very small (~2.5 nm in diameter). In this regard, laser surface texturing with low surface roughness will be tested to understand the contamination behaviour. Due to the limited quantity of aperture plates and time available for testing, only selected cases from the initial surface texturing experimentation were used for laser processing the plates. The plates were topographically analysed using SEM and AFM before and after laser processing.

3.6 Experimental Procedure: Protein contamination behaviour analysis of aperture plate electrode

The aperture plate is one of the ion optics needed for controlling the ion beam and producing an optimised parallel beam that enters the time-of-flight mass analyser in a time-of-flight mass spectrometer. The effectiveness of the ion optics determines the successful functioning of the instrument. Some optics, such as the aperture plate, are subjected to continuous irradiation and contamination build-up (organic and inorganic). When considering organic contamination, the protein adsorption behaviour analysis is essential in determining the optics' robustness, and studying these contaminations is one of the motivations in this thesis.

3.6.1 Experimental methodology

The aperture plate electrode is positioned as the exit element and does the final collimation of the ions to generate an optimised parallel beam. The ion beam is elliptical as it reaches the aperture plate, so it continuously irradiates the aperture plate on the beam facing side. The ions irradiating the surface of the aperture plate typically have hyperthermal energies of around 5 to 50eV. The ion energy value indicates that the ion-surface interaction is likely to be either a soft, dissociative, or reactive landing. Under soft landing conditions, ions with energies 5-20 eV are deposited onto the aperture plate surface intact with or without retention of their ionic charge. Figure 3.21 shows the schematic of the ion optics and the aperture plate. The face marked B in Figure 3.21(a) faces the ion beam continuously during operation and is prone to contamination. An approximation of

the ion beam shape and its collision area on the aperture plate surface is shown in Figure 3.21(b) with the blue elliptical region.

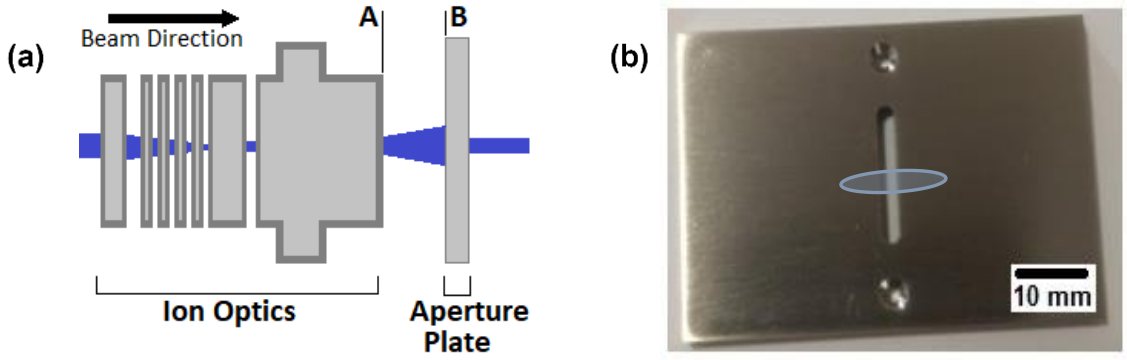

Figure 3.21: (a) Schematic of the ion optics, the aperture plate, and the ion beam (highlighted in blue). The aperture plate collimates the divergent ion beam; (b) Image of a sample aperture plate. The face shown in the image faces an incoming ion beam collision. The blue outline is the approximation of the ion beam striking the surface of the plate.

The experiments were conducted on a test-rig built by Waters® at their facility in Wilmslow, Cheshire. The test-rig is based on the Waters orthogonal acceleration time-of-flight platform model XEVO G2-XS. It is designed to reproduce and analyse the actual scenario of the MS instrumentation electrodes. The experiments used the bovine insulin m/z 956, [M+6H+] ion as the incident ion. The experimental method analyses the active area of the aperture plate and allows us to understand the broad interaction between the ion beam and the aperture plate electrode. It uses the Waters owned pre-set calibration procedure for the aperture plate called ‘sweep’. The ‘*sweep*’ process deduces the end voltage by calibrating the aperture plate voltage from 16V to 21V in steps of 0.1V to

identify the voltage at which the maximum resolution[4] is obtained. It is to be noted that the aperture plate in the test-rig is designed to tune at 17V, i.e. achieve the maximum resolution at this voltage, and a deviation up to +0.5V is considered a suitable operating voltage. If the identified voltage exceeds 17V, the aperture plate surface is considered to have a surface charge[5] build-up. The main potential reason for an increase in surface charge is the reduction in the surface's conductivity due to the build-up of an insulating layer of protein ion contamination over the plate surface. Hence, the surface charge is a helpful indicator for analysing the protein contamination behaviour on the surface of the aperture plate electrode.

For our experimentation, 120 sweeps were done as a single calibration test cycle. The optimum (maximum) resolution and surface charge results were used to qualitatively compare and demonstrate the protein contamination behaviour of the aperture plate electrode. Tests were conducted on laser processed aperture plates and one non-laser processed aperture plate. The non-laser processed aperture plate acts as the reference electrode to be used as baseline results for the comparison.

[4] **Resolution:** It is regarded as the ability of the mass spectrometer instrument to separate ion beams that differ in m/z ratio in the mass spectrum. It is calculated as $m/\Delta m$, where m is the nominal mass (actually m/z) for a particular peak in the mass spectrum, and Δm is peak width at 10 or 50% of the peak height. It is dimensionless [233,234].

[5] **Surface charge of aperture plate:** It is the offset of the identified end voltage from the design-expected voltage (i.e. 17V). If the voltage is more than 17V, the surface is considered to be charged.

3.6.2 Protein contamination behaviour baseline: Test results of a non-laser processed aperture plate (or the reference electrode)

A non-laser laser processed aperture plate was used to identify the protein contamination behaviour on standard plates and act as the baseline result for comparative analysis with laser processed aperture plates. This non-laser laser processed aperture plate is known as this report's '*reference aperture plate electrode*' or simply '*reference electrode*'.

Before protein tests, the reference electrode was topographically characterised with SEM and AFM. The native surface show profile roughness Ra=10.5±2 nm, shown in Figure 3.5, and the area roughness is estimated to be Sa=11.6±1.1 nm (refer to section 3.1.2). Surface chemistry analysis using XPS and ToF-SIMS was done after the protein behaviour tests to identify the chemical composition of the surface.

3.6.2.1 Results of protein contamination behaviour tests at Waters® test rig

The protein contamination behaviour of the reference electrode was analysed through the surface charge and the optimum resolution for each sweep, as explained in the experimental methodology in section 3.6.1 above. The profiles for surface charge (Figure 3.22) and the optimum resolution (Figure 3.23) were drawn with the data measured for 120 sweeps. The instrument measures the resolution. It should be noted that there was a rest period between the test cycle 'Ref_1' and 'Ref_2', but the instrument was not vent during this period.

The ***surface charge profile*** (Figure 3.22) is plotted with a moving average of 5. Hence, it is presented from sweeps 5-120. It shows an increasing surface charge trend, indicating a potential insulating layer build-up on the surface during the test cycle run time.

It is known that proteins are electrically semiconductors [191], so a potential build-up of protein layers increases the surface charge over time. The surface charging rate (mV/sweep), i.e. the profile's slope, can be used as a quantifiable indicator for the surface contamination build-up over one test cycle. The surface charging rate was calculated using the data from sweep indices 21 to 120 only. The initial 20 sweeps are considered the settling-in period and thus skipped from the slope calculations. Table 3.5 lists the surface charging rate and the maximum offset voltage for one cycle. The charging rates in the table show a considerably large difference between the two cycles, indicating the inconsistency in the surface charging behaviour. The inconsistency adds a degree of unpredictability to the results of the surface contamination behaviour and highlights the difficulty in using a quantitative trend to explain the results.

The surface charge profile graph also indicates the possibility that the contamination build-up is not continuous, and the contamination layer peels off the aperture plate surface after certain intervals. The protein ion beam colliding with the aperture plate surface has either soft or reactive landing energies and stays on the surface. The layer peels off over time because physical adsorption uses weak Van der Waal forces to hold the soft-landed protein layer. Only the reactive landed protein ions stay on the surface due to being strongly bonded to active sites on the surface through covalent bonds. It is likely possible to have a few monolayers of reactive-landed protein ions and soft-landed ones on top of that. When the soft-landed layer peels off, a momentary reduction in the surface charge is observed as the region becomes conductive. It is one of the reasons that the surface charge does not continuously increase with each sweep.

Further, it can be observed from Figure 3.22 that a test cycle starts at a lower end voltage as compared to the previous cycle’s endpoint. It shows the likely possibility of

removal of the soft landed protein ion layer during the instrument rest period after a test cycle. However, we don't know the percentage of soft-landed protein ions contributing to charge development and how much it has fallen away.

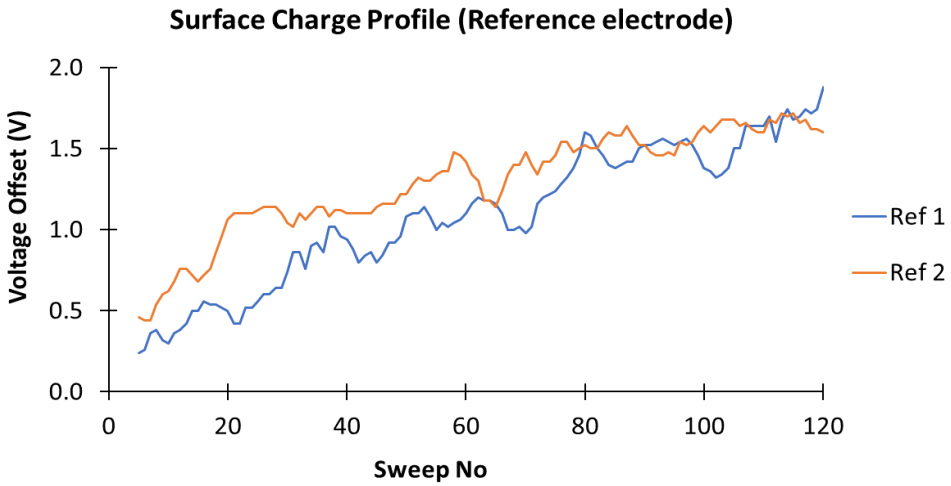

Figure 3.22: Plot of the Surface charge profile of reference electrode. The voltage offset is the difference in the end voltage of each sweep from 17V.

Table 3.5: Surface charging of the reference electrode

Description	Experiment No	Max Offset Charge (V)	Charging Rate (Slope) (mV/Sweep)	Average charging rate (mV/Sweep)	Std. Deviation (σ) (mV/sweep)
Reference electrode	Ref 1 Ref 2	1.72 1.88	6.94 11.48	9.21	3.20

The ***measured optimum (maximum) resolution*** for each sweep, as shown in Figure 3.23, can also be used to quantify the surface's contamination build-up and analyse the test cycle's overall stability. The instrument's resolution data is directly obtained, and the profile is presented from sweeps 1-120. It is to be kept in mind that, unlike the surface charge information, the resolution data is obtained after the ions reach the detector. Hence, the resolution is affected by the cumulative effect of all the ion optics' performance.

Therefore, the resolution information is more helpful in understanding the generic stability of the instrument during its operation time.

The optimum resolution falls quickly during the first 20 sweeps and stabilises over the remaining test runtime. Hence, the first 20 sweeps are considered the instrument's settling-in period. Table 3.6 lists the measured slopes of the optimum resolution profile. The slope of the profile from sweep indices from 21-120, shown in Table 3.6, is low, showing generic instrument stability during the experiment. Also, the negative slope is implied for a fall in resolution and increasing contamination. It can be seen from the table that the slope of the cycles shows unpredictability. Furthermore, there is an 8.55% drop in the average resolution between the cycles 'Ref_1' and 'Ref_2'. The drop in resolution over cycles and an average negative slope demonstrate the potential contamination build-up on the ion optics and the aperture plate during the cycle test run.

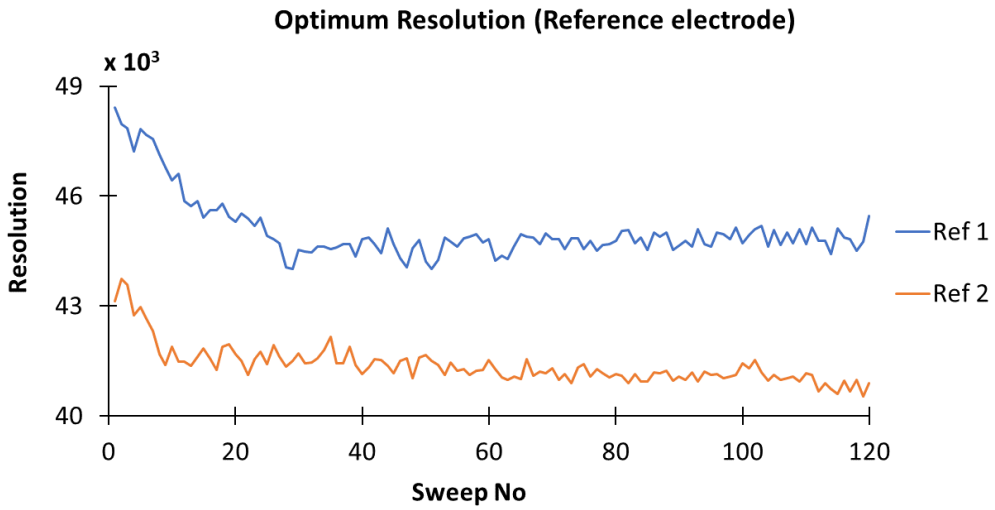

Figure 3.23: Plot of the measured optimum resolution for the reference electrode

Table 3.6: Trend for the optimum resolution of the reference electrode

Description	Experiment No	Average resolution in each cycle	Resolution drift rate (slope) (resolution/sweep)	Avg. resolution drift rate (resolution/sweep)	Std. Deviation (σ) (resolution/sweep)
Reference electrode	Ref 1 Ref 2	44753.86 41230.64	2.41 -7.21	-2.40	6.80

It can be observed that, between the two indicators, the surface charge profile is a more accurate representation of the contamination build-up on the aperture plate surface since the measurement of the end voltage for each sweep is recorded at the aperture plate. In contrast, the performance of the other ion optics can also affect the resolution.

3.6.2.2 Surface chemistry analysis post protein tests: *XPS results*

Lucideon Ltd conducted the XPS analysis. The analysis was done away from the slot to understand the surface composition of the polished surface of the reference electrode. Also, the XPS results from the reference electrode become a basis for understanding the effect of laser surface modification on the laser processed aperture plates later.

The XPS survey spectrum of the reference aperture plate electrode, shown in Figure 3.24, was recorded with a pass energy of 160 eV at a step size of 1 eV. It highlights the identified primary peaks of the elements along with carbon and oxygen. The major components of stainless steel on the surface are iron (10.89%), chromium (3.31%), nickel (0.80%), molybdenum (0.18%), manganese (0.04%) and phosphorous (0.71%). There is also carbon (21.85%), oxygen (60.45%), nitrogen (0.80%) and trace impurities. The values are presented in atomic weight percentages. The carbon layer present on the surface is formed due to the adsorption of air-borne carbonaceous material when the surface is

exposed to the atmosphere [192]. The oxygen layer is from the thin passivating oxide layer on the surface [151,193].

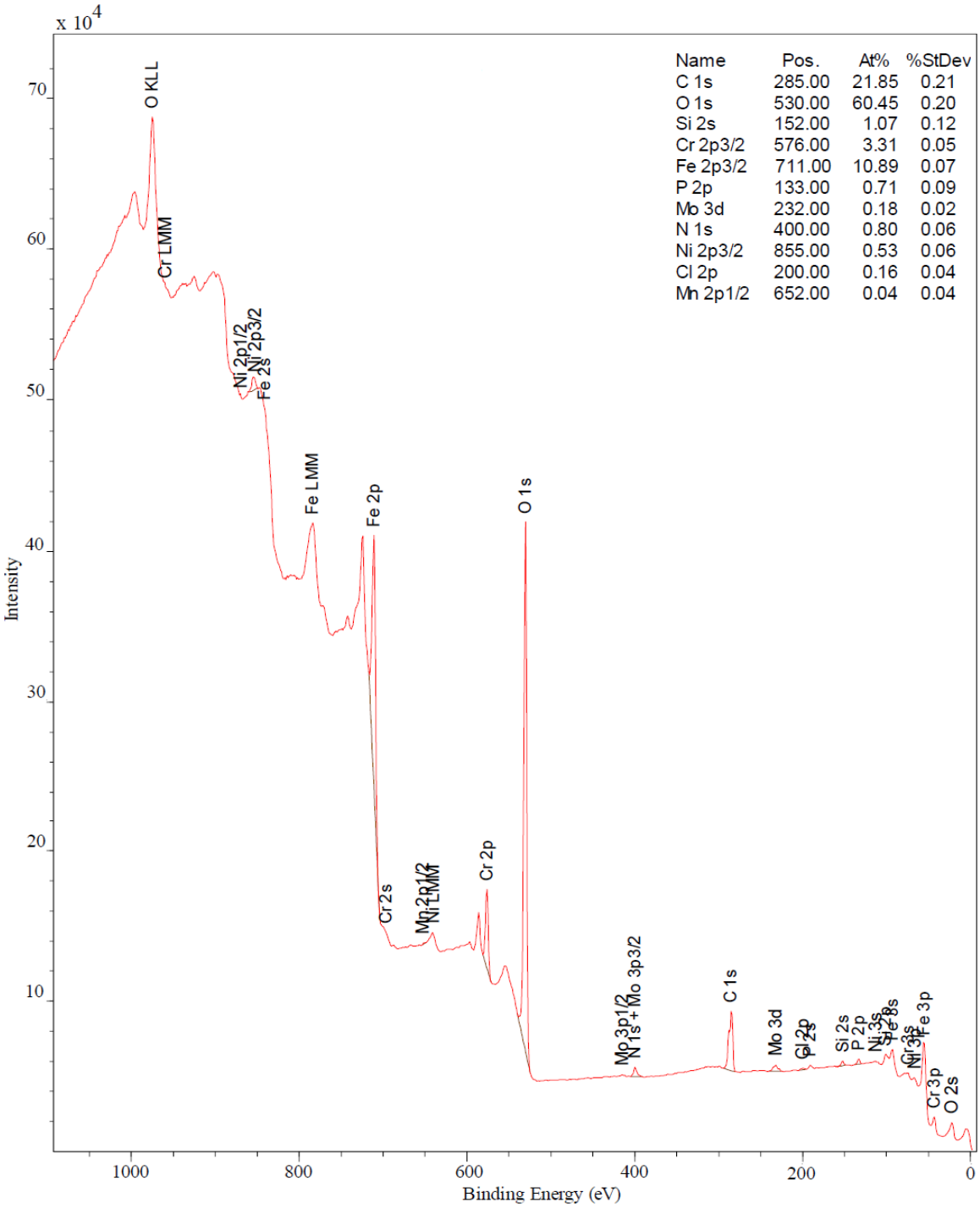

Figure 3.24: XPS survey spectra of the reference electrode. The summary in the top-right corner lists the atomic percent (At %) of the identified elements.

The core level spectra of O 1s, C 1s, Fe 2p, Cr 2p, Ni 2p and Mo 3d, as shown in Figure 3.25, were recorded with the pass energy of 20 eV at a step size of 0.1 eV. The take-off angle of the analysed photoelectrons was 90°. The binding energies were calibrated by setting the C 1s signal corresponding to C–C and C–H at 285.0 eV. The peaks of the C 1s spectra are mostly signals for organic/polymeric compounds such as C–C & C–H (285.0 eV), single bonds C–N & C–O (286.60 eV), and O=C–O & O=C–N peptide bonds (288.85 eV) [194–196]. The O 1s core level spectra show that the surface has metal oxides (530.15 eV), metal hydroxides (531.68 eV), and contamination of the type O-C group (533.28 eV). The organic contamination, i.e. O-C group is in the form of hydroxyl groups bonded to aromatics [196,197]. Iron is mainly oxidised, possibly a mixture of Fe (II) & Fe (III), and has a single peak at 710.88 eV. Identifying iron's oxidation states is not possible due to the complex nature of the iron 2p peak envelope. Chromium is mainly in the Cr (III) oxidation state (576.86 eV) and a small percentage of Cr (II) oxide (575.86 eV). Nickel is mainly in the oxidation state (855.72 eV) along with a substantial presence of metallic form (852.89 eV). The core level spectra of Mo 3d are complex as it contains doublet peaks due to low spin-orbit splitting between Mo $3d_{3/2}$ and Mo $3d_{5/2}$ with an energy gap of ~3.13 eV [198]. Hence, four sets of doublets peaks were identified for the metallic form Mo (0) and oxide forms of Mo (II), Mo (IV) and Mo (VI), as shown in the core level spectra of Mo 3d in Figure 3.25, listed in Table 3.7 [199,200]. The Mo 3d spectra show that all four forms have an almost similar presence on the surface.

Table 3.7: Doublet peaks in core level spectra of Mo 3d (reference electrode)

State	Form	Mo $3d_{5/2}$ (BE in eV)	Mo $3d_{3/2}$ (BE in eV)
Mo(0)	Metallic Mo^{0}	227.74	230.89
Mo(II)	Oxide Mo^{2+}	230.06	233.26
Mo(IV)	Oxide Mo^{4+}	231.71	234.91
Mo(VI)	Oxide Mo^{6+}	232.56	235.76

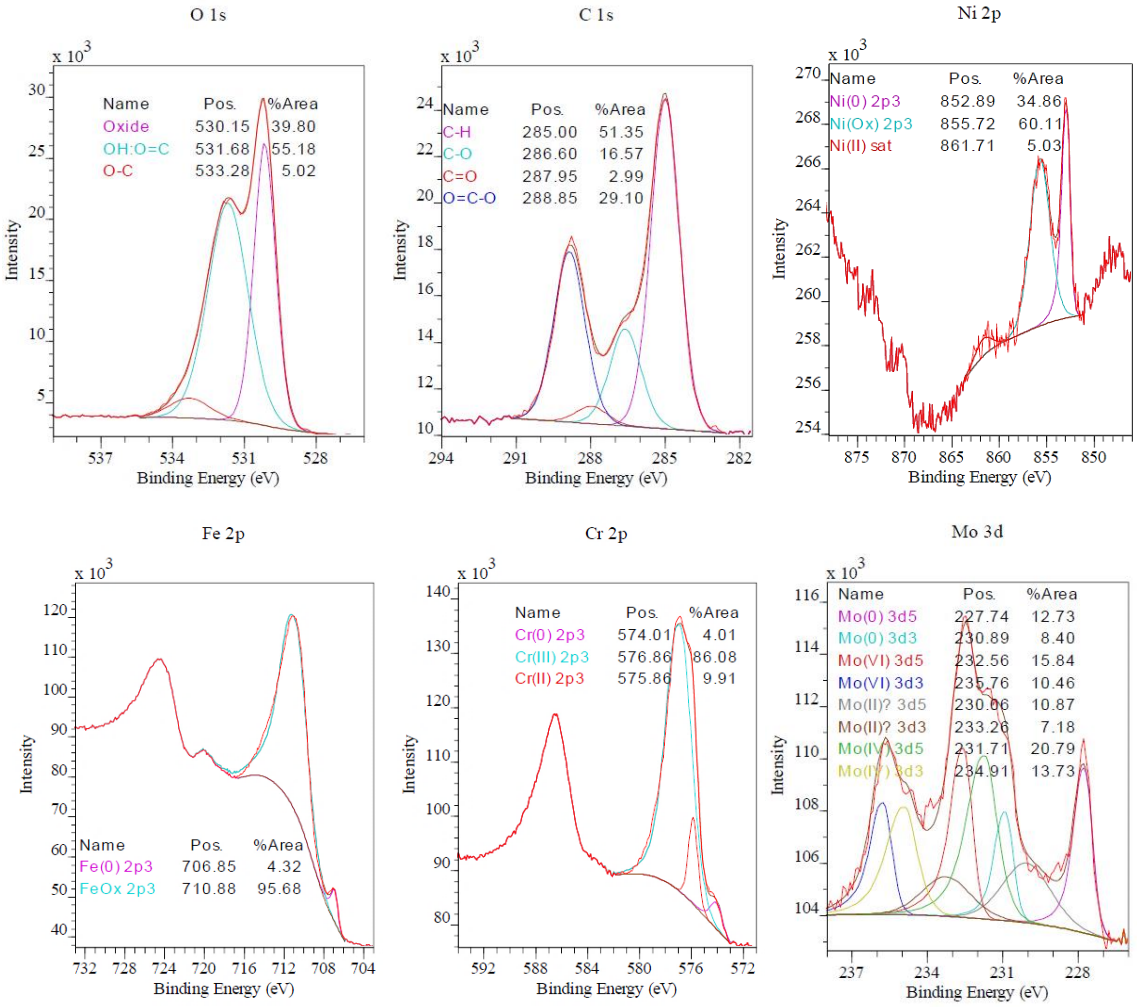

Figure 3.25: Core level spectra of O 1s, C 1s, Fe 2p, Cr 2p, Ni 2p and Mo 3d of the reference electrode (pass energy of 20 eV and step size 0.1 eV)

A summary of the surface composition is listed in Table 3.9. The error values (σ) are calculated from the statistical noise on the data and represent one standard deviation confidence limit; i.e. there is a 68% probability that the true composition lies between the calculated compositions given in the surface composition table $c \pm \sigma$. There is a 95% probability that the true composition lies between $c \pm 2\sigma$. The ratio of elemental composition compared to their oxides and iron is mentioned in Table 3.8. The surface mainly comprises iron and chromium oxides, as expected in the passivated surface condition of stainless steel 316L.

Table 3.8: Oxide:Metal & Elemental Ratios by XPS of the reference electrode

Comparison	Ratio value
Fe(Ox):Fe(0)	22
Cr(Ox):Cr(0)	24
SS(Ox):SS(0)*	17
Cr:Fe	0.30
Mn:Fe	0.004
Ni:Fe	0.05
Mo:Fe	0.02

***SS(Ox) = sum of the principal SS 316 elements (Fe, Cr, Ni, Mo, Mn) in their oxidised states.**
SS(0) = sum of the principal SS 316 elements (Fe, Cr, Ni, Mo, Mn) in their metallic state.

Table 3.9: XPS Surface Composition Table (At %): Reference Aperture Plate Electrode

Elements	Composition (At %)
Carbon	***21.9***
σ	*0.2*
C-C:C-H	11.2
C-O:C-N	3.62
C=O:N-C=O	0.65
O=C-O	6.36
Oxygen	***60.53***
σ	*0.2*
Oxide	24.1
OH:O=C	33.4
O-C	3.03
Iron	***10.9***
σ	*0.1*
Fe(0)	0.47
FeOx	10.4
Nickel	***0.53***
σ	*0.06*
Ni(0)	0.18
Ni(Ox)	0.35
Nitrogen	***0.8***
σ	*0.06*
Amine:Amide	0.8

Elements	Composition (At %)
Molybdenum	***0.18***
σ	*0.02*
Mo(0)	0.04
Mo(II)	0.03
Mo(IV)	0.06
Mo(VI)	0.05
Chromium	***3.31***
σ	*0.05*
Cr(0)	0.13
Cr(II)	0.33
Cr(III)	2.85
Manganese	***0.04***
σ	*0.04*
Mn(II)	NA
Mn(III)	NA
Silicon	***1.07***
σ	*0.12*
Si(0)	0.35
Si-C	0.72
Phosphorus	***0.71***
σ	*0.09*
Phosphate (PO_4)	0.71

3.6.2.3 Surface chemistry analysis post protein tests: *ToF-SIMS results*

ToF-SIMS surface imaging measurements were done using an ION-TOF instrument by Lucideon Ltd., and Bismuth (Bi^{3+}) was the primary ion source with an ion energy of 30 keV. The analysis current was 0.2 pA, and the analysis was conducted on an area of 15x15 mm^2. The surface imaging scan identified different surface constituents similar to XPS but over an area of 15x15 mm^2. The wide area scan provides an overview of the central slot in the aperture plate, the ion beam shape, and its collision location. Figure 3.26 shows the surface scan (15x15 mm^2) using RGB overlays of different constituents. Here, the protein residue is the summation of the different amides and peptides residues. The protein residue is almost contained within a narrow band near the centre of the slot and is present above and below the slot. The spread of the protein residues and aromatic hydrocarbons indicates that the organic contamination is mainly in the ion beam collision region as it forms a shape representative of the ion beam.

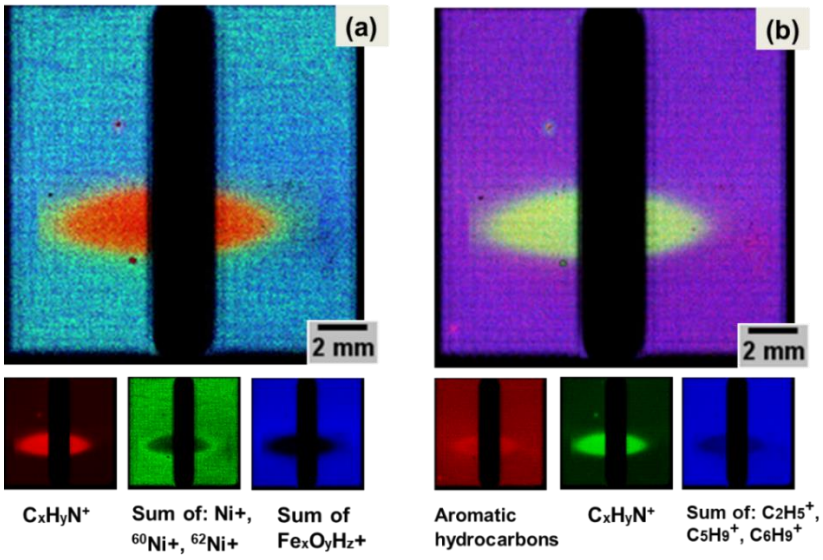

Figure 3.26: RGB overlay of ToF-SIMS scan of 15x15 mm^2 of the reference electrode
(a) Summation of metal oxides/hydroxides (iron & nickel) and amines ($C_xH_yN^+$)
(b) Summation of organic residues: hydrocarbons and amines ($C_xH_yN^+$)

The ToF-SIMS spectra was generated for a scan area of 500x500 μm^2. Figure 3.27 shows the positive ion polarity spectra generated from a location within the ion-beam collision region. Amino acid signal identifiers for bovine insulin (refer to Table 3.4) can be seen from the peaks in the spectra such as CH_2N^+ (m/z: 28), CH_4N^+ (m/z: 30) [*Glycine*], $C_4H_8N^+$ (m/z: 70) [*Proline*], $C_5H_{10}N^+$ (m/z: 84) [*Lysine*], $C_5H_{12}N^+$ (m/z: 86) [*Isoleucine/Leucine*], $C_8H_{10}N^+$ (m/z: 120) [*Phenylalanine*], and $C_8H_{10}NO^+$ (m/z: 136) [*Tyrosine*]. Higher order amines and hydrocarbon peaks were identified for m/z values from 300 – 650. The spectra clearly indicate protein/organic residues on the surface.

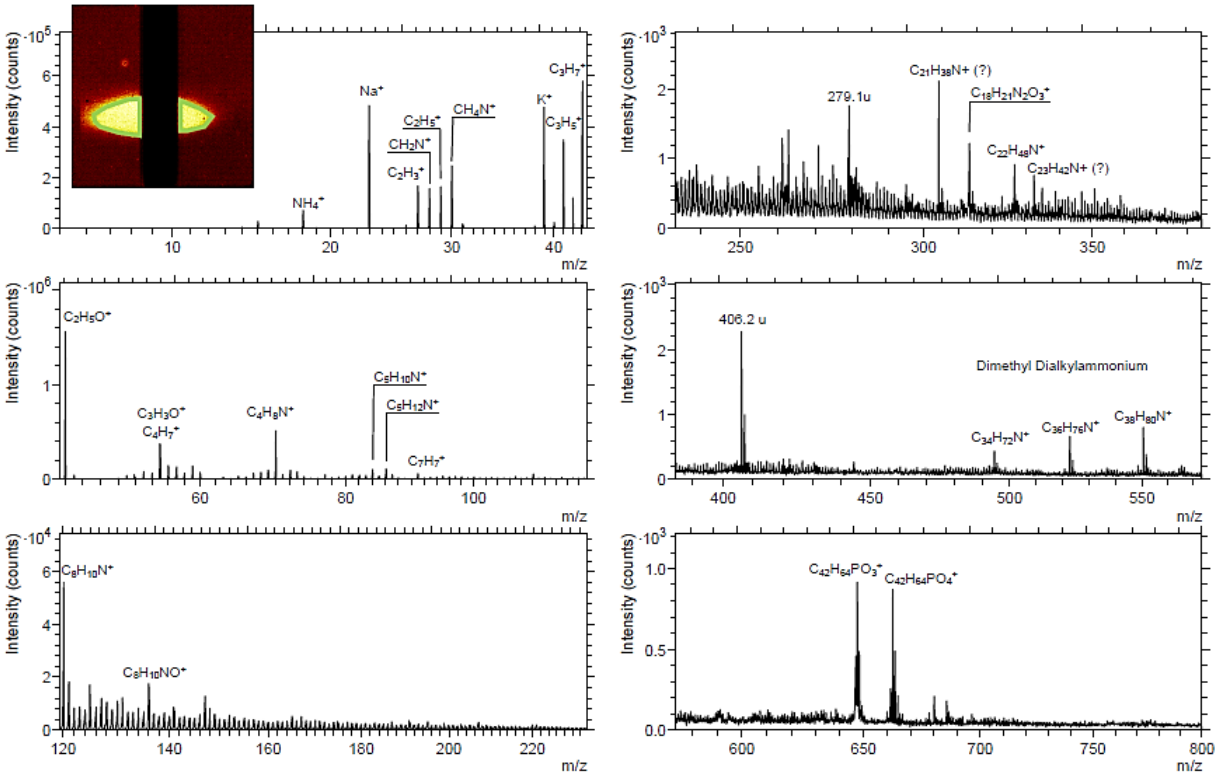

Figure 3.27: ToF-SIMS spectra of an area within the reference electrode's ion beam collision region (in yellow). The picture on the top left is a stage scan for $C_xH_yN^+$ within the green region. Spectrum parameter: Ion ($Bi3^+$), Scan area (500x500 μm^2), Polarity positive

However, the positive ion polarity spectra of the region outside the ion-beam collision area (Figure 3.28) show more metal oxides/hydroxides peaks than amines/hydrocarbon peaks. Metallic iron (Fe^+) and in the form of iron oxides/hydroxides, i.e. FeO^+, $FeOH^+$, Fe_2O^+, $Fe_2O_2H^+$, $Fe_3O_2^+$, $Fe_3O_3H^+$, $Fe_4O_3^+$ and $Fe_4O_4H^+$, is present in the spectra. Also, metallic chromium (Cr^+) and hydroxide ($CrOH^+$) peaks are seen in the spectra. The presence of iron and chromium oxides/hydroxides indicates passivated oxide layer surface, as expected in stainless steel 316L. Other metal oxide signals were also detected between m/z 410 and 440. Organic residue signals of the amino acid residue of bovine insulin or aromatic hydrocarbons were not detected in the area away from the ion beam collision region.

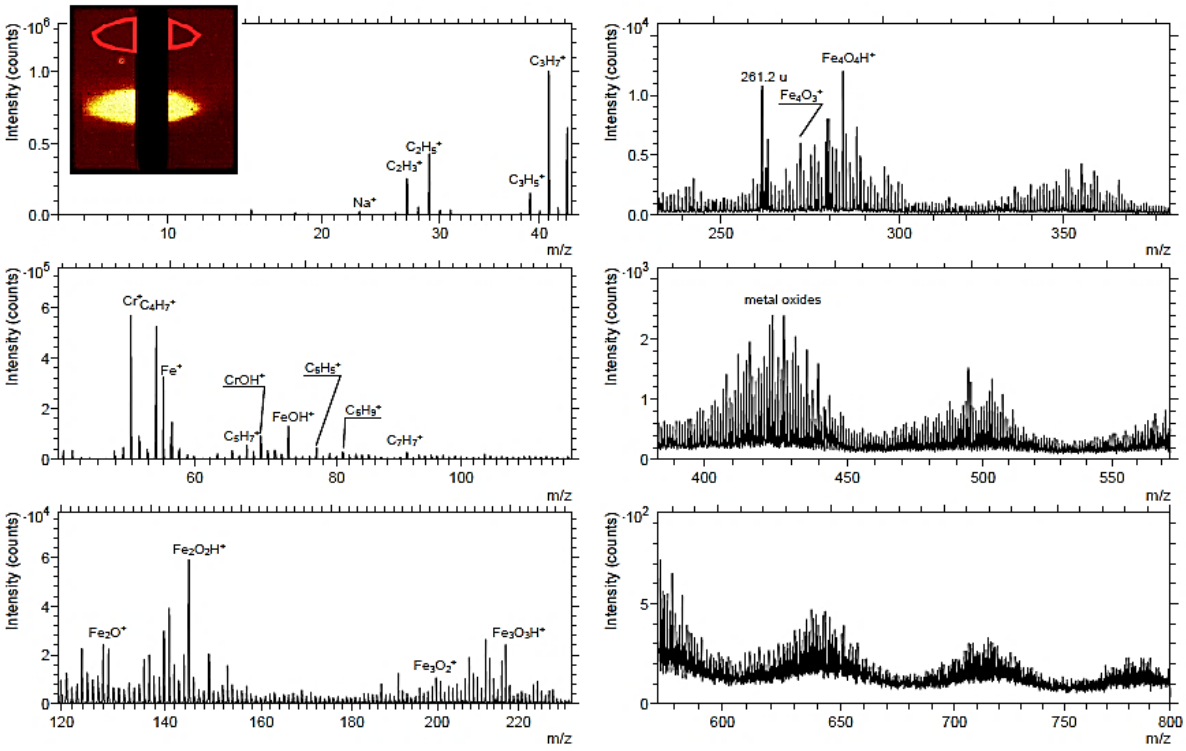

Figure 3.28: ToF-SIMS spectra of area away from the reference electrode's ion beam collision region (in yellow). The picture on the top left is a stage scan for $C_xH_yN^+$ within the red region. Spectrum parameter: Ion ($Bi3^+$), Scan area (500x500 µm^2), Polarity positive

Furthermore, some tentative signal identifiers of aerosol particles in the form of inorganic ions such as Na+ (m/z: 23), aliphatic hydrocarbon ions such as $C_3H_5^+$, $C_3H_7^+$, and $C_4H_7^+$ (m/z: 55), and unsaturated/aromatic ions such as $C_7H_7^+$ (m/z: 91) [201–204], were detected in both the spectra, i.e. region within the ion beam (Figure 3.27) and away from the ion beam (Figure 3.28). The signal strength of dust particles may vary within the aperture plate, but these do not account for any characteristic contamination issue discussed in this research.

3.6.2.4 Protein contamination behaviour of reference electrode: *Conclusion*

A non-laser processed aperture plate electrode, also termed the reference aperture plate electrode, was investigated for protein contamination behaviour using bovine insulin at the Waters® facility. Through an internally developed algorithm at the facility, the charge on the aperture plate surface and the optimum resolution of the instrument was monitored and recorded. The end voltage offset profile showed an increasing slope for multiple cycle runs of the instrument, demonstrating a potential build-up of an insulating layer on the surface. ToF-SIMS analysis of the surface displayed ion beam residue (amides and aromatic hydrocarbons), confirming protein contamination on the surface. Peaks of amino acid signal identifiers for bovine insulin were identified mainly at the region of the ion beam residue. The surface composition was also recorded using an XPS analysis. The protein contamination behaviour on the reference aperture plate electrode will be used as the baseline results for comparison with laser processed aperture plate electrodes.

3.7 Summary

The chapter introduced the material for the research (AISI stainless steel 316L) and the samples to be used for experimentation, the laser systems and the characterisation instruments. The research is categorised into two stages. The first stage is about developing and understanding the research relevant laser processing capabilities of SS316L. A brief overview of the experimental methodology for laser processing was provided. The second stage focuses on understanding the effect of laser processing on the contamination behaviour of the aperture plate electrode. The experimental methodology for testing the contamination behaviour was introduced. The results of studying the contamination behaviour of a non-laser processed aperture plate (referred to in this work as reference aperture plate electrode) have been presented in detail. The results of the reference electrode become the basis for comparing and understanding the contamination behaviour of the laser-textured aperture plates.

Chapter 4

Nanosecond Laser Processing Results

This chapter reports the results of the experimental investigation of the surface structures obtained on the stainless steel sample targets with the short pulse (nanosecond) laser system. The nanosecond laser with a wavelength of 532 nm falls under the thermal dominated laser ablation regime. The effect of fluence, pulse overlap and number of scans on the surface structure are discussed. Aperture plate electrodes were developed using selected cases of laser processing and investigated for protein contamination behaviour.

4.1 Optical characterisation

A laser system (λ=532 nm, t_{laser}=7 ns and f_{laser}=30 kHz) having a gaussian beam with linear polarisation, as described in section 3.2.1, was used for the experimentation. The laser beam profile was slightly elliptical at the highest power level (2.95 W) and progressively became circular with a reduction in laser power, as observed under an optical microscope. The ellipticity induced in the beam is due to the slight astigmatism of the beam and is consistent with those expected of a Gaussian beam. Hence, the profile can be

considered circular for lower laser power. Figure 4.1 shows the behaviour of a single pulse laser ablation spot for the applied laser power.

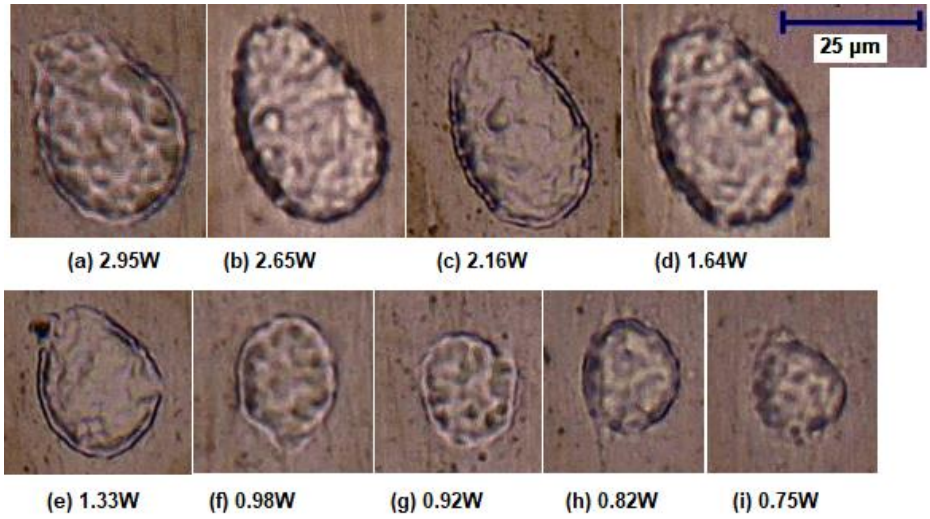

Figure 4.1: Optical images of laser ablation spots at different power levels

4.2 Surface Texturing Results

Surface texturing experiments were done on SS316L samples from Goodfellow due to the limited availability of aperture plate electrodes for experimentation use. The samples are annealed and have a surface roughness similar to the aperture plate electrodes from Waters®. The ablation threshold of SS316L samples from Goodfellow was deduced for laser processing in the air. Experiments were conducted for laser processing with high fluence and fluences around the threshold fluence.

4.2.1 Ablation threshold fluence

The laser ablation threshold fluence (F_{th}) estimation is based on Liu's model, as discussed in section 3.5.1.2. The pulse energy threshold (E_{th}) of 18.13 µJ was obtained from the graph-based method, shown in Figure 4.2 (left), by solving the fitting curve

equation with crater diameter $y \rightarrow 0$. Using the value of pulse energy threshold (E_{th}), the beam radius (ω_0) was calculated as 25.63 µm (or 51.26 µm in diameter). The threshold fluence (F_{th}) was estimated to be **1.71 J/cm^2** using the logarithmic curve fit in the plot of the fluence vs the crater diameter squared, as shown in Figure 4.2 (right). The threshold fluence is in agreement with the literature [125]. The reflectivity of stainless steel of around 64% was not accounted for during the calculation of the threshold fluence. Further, the threshold fluence for pulse overlap can be estimated based on section 3.5.1.3 using equation 3.7. The plot for the fluence vs pulse overlap is shown in Figure 4.3.

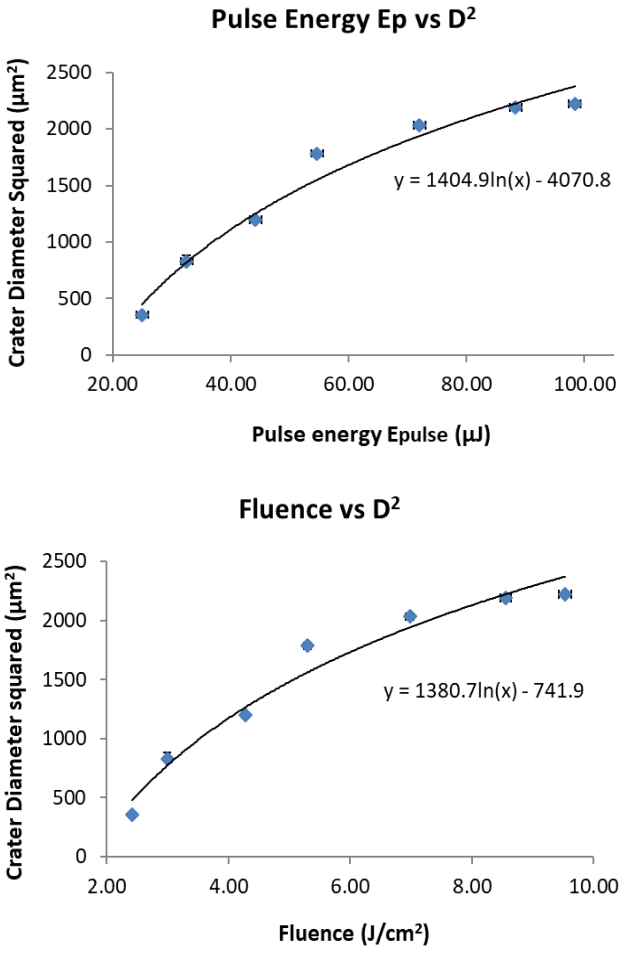

Figure 4.2: Plots to deduce the ablation threshold through crater diameter method using SS316L samples from Goodfellow (laser: λ=532 nm, t_{pulse}=7 ns, f_{laser}=30 kHz)
(top) to find threshold pulse energy; (bottom) to compute ablation threshold fluence

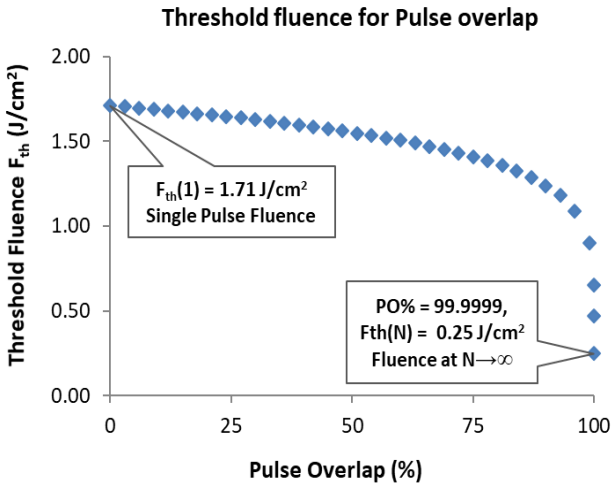

Figure 4.3: Threshold fluence for pulse overlap based on single pulse threshold value.

4.2.2 Experimental parameters

Surface textures were generated with bidirectional hatch lines, as discussed in section 3.5.1.4. A spot size of **52 µm**, identified during ablation threshold fluence computation, was used to define the laser scan parameters for experiments. The overlap percentages were selected randomly to have a spread on the pulse overlap from minimum to maximum overlap.

Table 4.1: Nanosecond laser processing parameters considering spot size of 52 µm

Hatch Distance Δy (µm)	Pulse-to-pulse distance Δx (µm)	Scan speed (mm/sec)
45	45	1350
42	42	1260
35	35	1050
25	25	750
20	20	600
10	10	300
5	5	150
5	5	150
2	2	60

4.2.3 Ablation and oxidation in nanosecond laser processed surfaces

Higher accumulated fluence over a spot above the ablation threshold resulted in material ablation and surface oxidation with the nanosecond laser in stainless steel samples. High surface oxidation and vaporisation levels were observed in experiments with high fluences between 6.3-13.6 J/cm^2 (ablation threshold is 1.71 J/cm^2). Figure 4.4 shows the effect of high fluence and pulse overlap on the surface (laser parameters: F_0=13.6 J/cm^2, Δx=2 µm, Δy=80 µm). Due to high pulse overlap on the surface (Δx=2 µm) and high fluence, the accumulated fluence increases and causes ablation. This effect is visible due to the high hatch distance, as the deep trenches in the surface profile (peak-to-valley depth of 3.2±0.1 µm). Further, surface oxidation results from surface heating due to high accumulated fluence, creating a more conducive environment for surface oxidation [205].

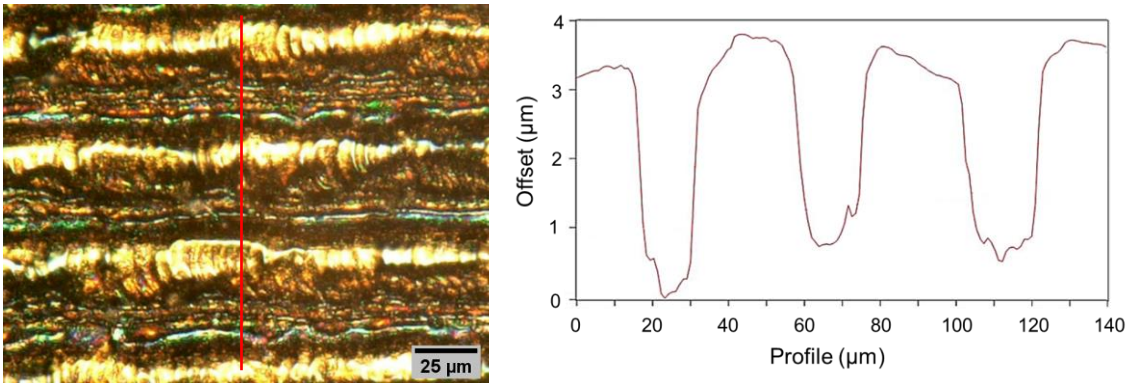

Figure 4.4: Optical image of a surface produced at F_0=13.6 J/cm^2, Δx=2 µm, Δy=80 µm, Nsc= 1, and Fa^{max}=90.26 J/cm^2. High surface oxidation and ablation are observed. (right) Profile of the red line in the left image. The deep trenches are the ablated regions.

The ablation reduces as the pulse-to-pulse distance increases, as shown in Figure 4.5, but the surface oxidation remains due to high input fluence. The effect of oxidation can be further observed with a comparatively lower fluence of 9.7 J/cm^2, as shown in Figure 4.6. The oxidation behaviour was noticed to change with the number of scans. It can be due to the variation in the oxides formed on the surface. A higher number of scans will change

the surface texture at the micro-level and induce the dispersion of alloying elements on the surface. Different composition of the oxides results in different colour [205]. It clearly shows that the laser parameters of pulse-to-distance (Δx), hatch distance (Δy), and the max accumulated fluence (Fa^{max}) minutely affects the ablation behaviour and the oxidation of the surface in the case of stainless steel 316L. Through controlled laser parameters, desired surface oxidation can be achieved in stainless steel. However, in the case of the current research, the resultant surface structures produced with high fluences are relatively huge compared to the protein contaminant, so these surfaces will not likely be effective in reducing surface contamination. Hence, further studies with high fluence with not be considered for the research.

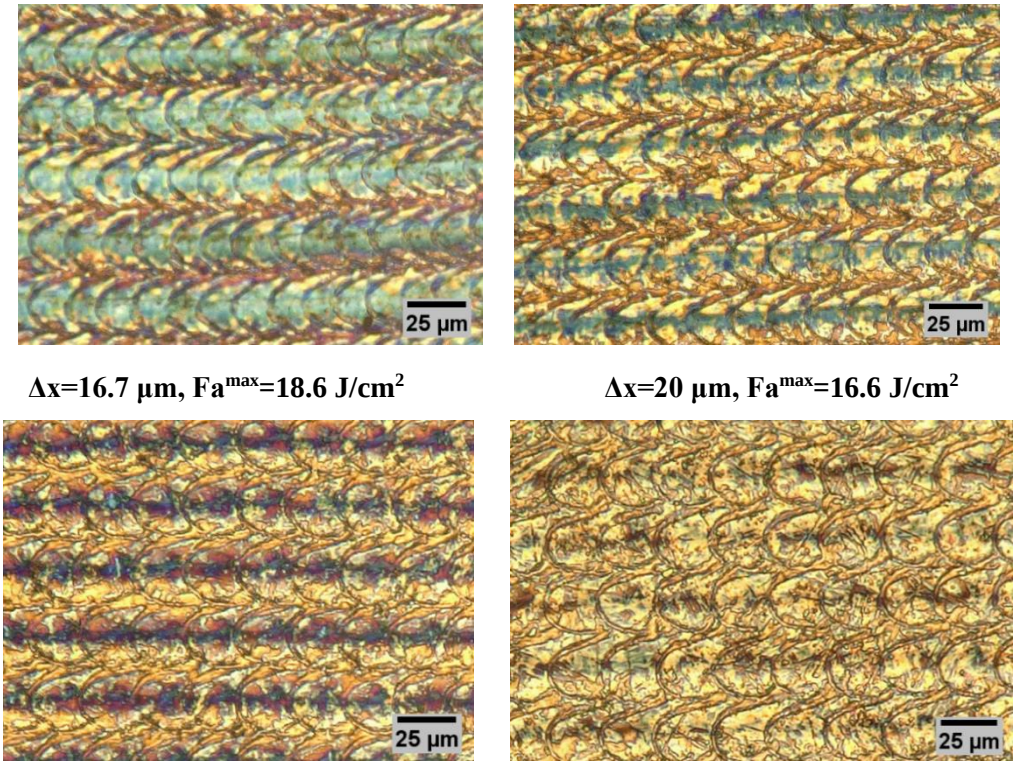

Δx=16.7 µm, Fa^{max}=18.6 J/cm² **Δx=20 µm, Fa^{max}=16.6 J/cm²**

Δx=23.3 µm, Fa^{max}=15.4 J/cm² **Δx=26.7 µm, Fa^{max}=14.7 J/cm²**

Figure 4.5: Optical images of laser processed surfaces with high input fluence (F_0=13.6 J/cm²), Δy=50 µm, and Nsc=1. The pulse-to-pulse distance (Δx) and the max accumulated fluence is mentioned for each surface. The increasing pulse-to-pulse distance (Δx) reduces the accumulated fluence Fa^{max}, thus affecting surface ablation and oxidation.

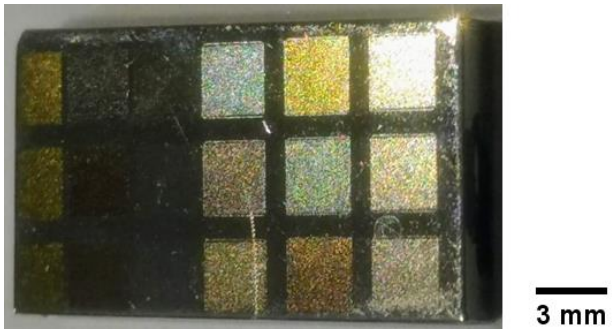

Figure 4.6: Optical image of a sample surface showing surface oxidation with different colours. Laser parameters: F_0=9.7 J/cm^2, Δx=4.5-18.0 µm, Δy=4.5-18.0 µm, Nsc=4-14.

4.2.4 Laser Induced Surface Structures

Laser processing around the ablation threshold of 316L stainless steel produced laser induced surface structures such as the periodic structures (LIPSS). However, as the 532nm nanosecond laser absorption is more thermal than photochemical, only low spatial frequency LIPSS (LSFL) features are produced. According to the classical LIPSS model [118], these LIPSS structures are produced by surface melting and re-solidification. The LIPSS model also mentions that periodicity depends on the wavelength of the laser (λ) and the angle of incidence measured from the normal to the surface (θ). The equation to calculate periodicity is:-

$$\text{Periodicity, } \Delta_{\text{LIPSS}} = \lambda/(1 \pm \sin\theta) \quad \text{..... (Eq 4.1)}$$

Also, any incident light at an angle (θ_{inc}) will be diffracted based on the equation:

$$\Delta_{\text{LIPSS}}.\sin\theta_{inc} = \lambda_{inc} \quad \text{..... (Eq 4.2)}$$

where λ_{inc} is the final wavelength of the diffracted light.

4.2.4.1 Input fluence higher than the ablation threshold

LIPSS structures are generated just above the ablation threshold of the material [206]. Laser processing of the Goodfellow stainless steel 316L samples (roughness Ra=10±2 nm) was done at low input fluence F_0 = 2.3±0.3 J/cm^2 and spot diameter 52 μm to generate laser induced structures. The pulse-to-pulse distance (Δx) was varied between 2-20 μm, and mostly hatch distance (Δy) was kept consistent with the pulse-to-pulse distance. The laser processing was conducted at incident angles between 0° and 3°. The laser induced features are expected to be low spatial frequency LIPSS features. According to the classical LIPSS model and based on equation 4.1, the expected periodicity is between 460-532 nm. Due to the wavelength in the visible spectrum, these features should diffract light between the violet and the blue region, with green seen at extreme angles, considering equation 4.2.

Figure 4.7 shows an example of the LIPSS surface generated on the stainless steel surface for F_0=2.13 J/cm^2, Δx=9.33 μm, Δy=10 μm, and the number of over scans Nsc = 6. The optical scan of the surface show periodic surface structures in line with the LIPSS structures and is confirmed with the SEM micrograph. The structures have a periodicity of Δ_{LIPSS}=425±20 nm, i.e. near the laser wavelength and are an expected value for LIPSS generated with a 532 nm nanosecond laser. The observed periodicity is in line with the mathematical model in the literature and can be confirmed as the low spatial frequency LIPSS features. Also, based on the information provided by Mezera & Römer (2019) [190], the equations for the max accumulated fluence (Fa^{max}) can be stated as shown in equations 3.13 and 3.14. The max accumulated fluence Fa^{max} was calculated to be 145.5 J/cm^2. The AFM analysis in Figure 4.8 revealed the peak-valley depth to be 16.3±2.2 nm. The roughness on the surface ripples and valleys was around Ra=1.22±0.2 nm. The measured

area roughness is Sa=4.20±0.12 nm, and the profile roughness is Ra=3.98±0.44 nm. The surface roughness was measured using the Gwyddion software.

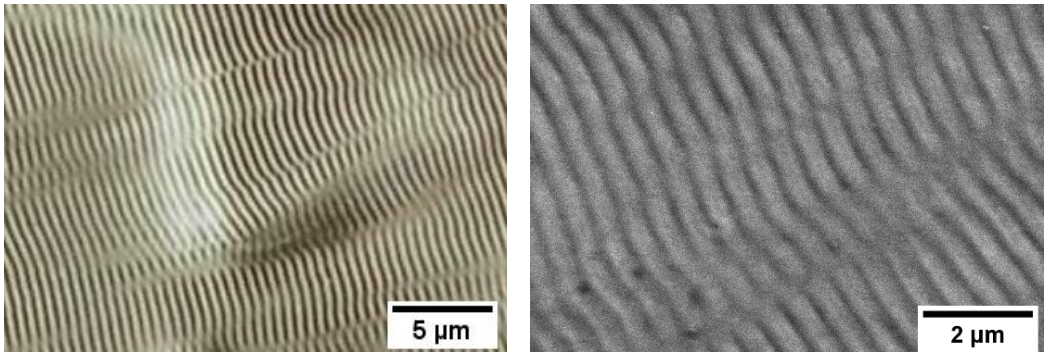

Figure 4.7: Images of LIPSS on SS316L surface formed with parameters F_0=2.13 J/cm^2, Δx=9.33 µm, Δy=10 µm, Nsc=6, Fa^{max}=145.5 J/cm^2, and having periodicity 425±20 nm. (left) Optical image of LIPSS region; (right) SEM micrograph of LIPSS region

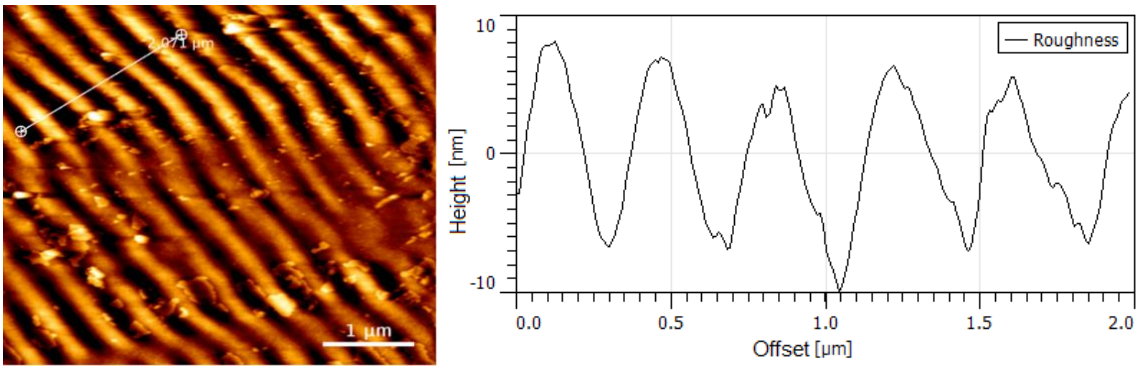

Figure 4.8: AFM scan of 5x5µm region (left); Profile of line across LIPSS surface (right)

LIPSS features affect the light reflected from the surface. The reflected light wavelength depends on the periodicity and the incident angle and is governed by equation 4.2. Diffraction of the white light was observed in the generated LIPPS. Figure 4.9 shows the optical image of the LIPSS region when viewed from the top and at an angle. In Figure 4.9 (left), the darkened areas on the sample surface corresponding to LIPSS regions when viewed from the top. When the sample surface was viewed from an angle, the LIPSS regions were visible in the shades of the blue spectrum, as seen in Figure 4.9 (right).

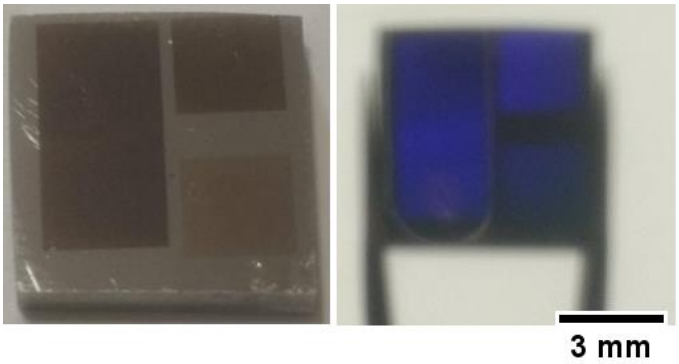

Figure 4.9: Optical image of SS316L sample with LIPSS structures. LIPSS is seen as darkened regions when viewed from the top (left); Diffraction of light is seen when the surface is viewed at an angle (right).

Further, it was observed that the growth of the LIPSS structures depended on the increasing overall fluence on the surface. The overall fluence can be increased by increasing the number of over scans on the surface. The effect of the number of over-scans (Nsc) on the surface for the input fluence F_0=2.13 J/cm^2 is shown in Table 4.2. The LIPSS structures start appearing on the surface at Nsc=4 and reach a high density by Nsc=10. It can be stated that with each successive scan, an adequate layer of the material on the surface is melted and recast, changing the surface roughness. The onset of LIPSS happens when the surface roughness is adequate for surface scattered waves to interfere with the incident laser beam creating an interference pattern of inadequate melting of the surface to produce the surface ripples [207].

The onset of surface oxidation was seen with the increased number of scans. The blue regions in Figure 4.10 result from surface oxidation along with LIPSS structures spread out between the oxidised regions. LIPSS features have been engulfed due to the build-up of oxides at most places. The blue colour of the oxide layer can be a spinel oxide of Iron and Chromium [205].

Table 4.2: Laser parameters for LIPSS formation (Spot diameter 52 µm)

Input Fluence F_0 (J/cm^2)	Hatch Distance Δy (µm)	Pulse-to-pulse distance Δx (µm)	No. of scans (Nsc)	Max. accumulated fluence Fa^{max} (J/cm^2)	Comment
2.13	10	9.33	4	97.0	Sparse onset of LIPSS
2.13	10	9.33	6	145.5	
2.13	10	9.33	8	193.90	
2.13	10	9.33	10	242.40	High density LIPSS
2.13	10	9.33	12	290.90	LIPSS with surface oxidation.

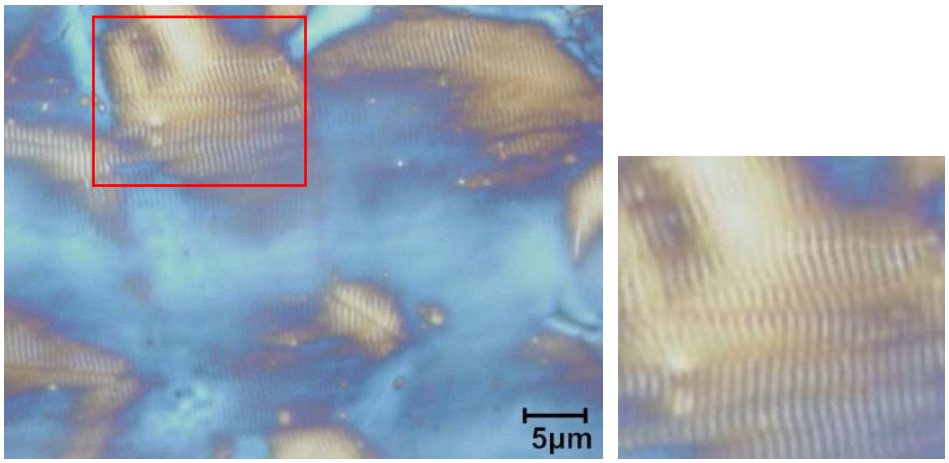

Figure 4.10: Optical image of the surface containing LIPSS along with oxidation for F_0=2.13 J/cm^2, Δx=9.33 µm, Δy=10 µm, and Nsc=12 (Fa^{max}=290.9 J/cm^2). Oxidation is the blue coloured region, and LIPSS not visible in these areas (left); the LIPSS region is highlighted (right)

4.2.4.2 Input fluence lower than the ablation threshold

The ablation threshold plays an essential role in the ablation mechanism. The ablation of the material happens when the fluence crosses the ablation threshold. Also, the ablation mechanism is affected due to the laser employed for processing. The laser used in this study (λ=532 nm, pulse=7ns) is more inclined towards the thermal regime of the ablation mechanism. Thus, the laser-material interaction will cause heating of the material and, in

turn, can affect the ablation threshold [208]. Our study identified the ablation threshold for the Goodfellow stainless steel SS316L samples (surface roughness Ra=10±1 nm) as 1.71 J/cm^2. Experiments were designed to study the effect of laser processing with fluences lower than the ablation threshold. Further, considering the protein contaminant to be analysed in this research (bovine insulin) has a diameter of ~2.5 nm, the targeted surface structures will be in the nano-scale.

The input fluence used in this study is F_0 = 0.29±0.02 J/cm^{2,} considering the spot diameter to be 52 μm. As the laser fluence is relatively low compared to the ablation threshold, the effective number of pulses at one spot needs to be high for the effective transformation of the surface topography. The laser parameters for processing are pulse-to-pulse distance Δx=5-15 μm, hatch distance Δy=5-10 μm, and the number of over scans Nsc=1-8. The changes in the surface topography were analysed for the increase in the number of over scans.

Figure 4.11 show the stage when the surface is scanned twice (Nsc-=2) with laser parameters of pulse-to-pulse distance Δx=8.85 μm, hatch distance Δy=5.5 μm, and max accumulated fluence Fa^{max}=12.7 J/cm^2 (input fluence F_0=0.29 J/cm^2). The high pulse overlap resulted in the reduction of the original surface roughness. The decrease in surface roughness can be the melting of a thin surface layer, especially the original peaks in the surface before laser processing. The accumulation of heat on the sharp peaks in the surface will cause it to melt and thus reducing the overall surface roughness. These surfaces were generated at low over scan count and did not show identifiable laser induced features, as shown in Figure 4.11. The AFM scan (refer to Figure 4.12), estimates the roughness Ra=2.68±0.08 nm (without considering embedded particles) and area roughness Sa=9.4±0.1 nm. These surfaces were termed ‘nano-polished’ surfaces.

With the increase in the number of over scans, the onset of laser induced structures can be seen to occur on the surface. Figure 4.13 shows the SEM scan of the earlier discussed surface with the number of over scans Nsc=3. Faint periodic structures can be seen in the SEM micrograph. Further accumulation of fluence by increasing the number of over scans Nsc=5 (Fa^{max}=31.7 J/cm^2), shallow LIPSS like structures can be seen in the SEM micrograph in Figure 4.14. The AFM scan of the same surface, as shown in Figure 4.15, reveals a periodic surface with a periodicity of Δ_{LIPSS}=505±17 nm, peak-to-valley depth of 12.8±3.3 nm, and area roughness Sa=6.9±0.5 nm. The roughness profile over the periodic feature reveals a roughness of Ra=7.1±0.3 nm, and on the peak of the periodic features, Ra=2.0±0.2 nm. The AFM scan further indicates that the surface contains periodic features, but the overall surface has a very low roughness similar to the earlier discussed nano-polished surface. The AFM data analysis was done with the Gwyddion software.

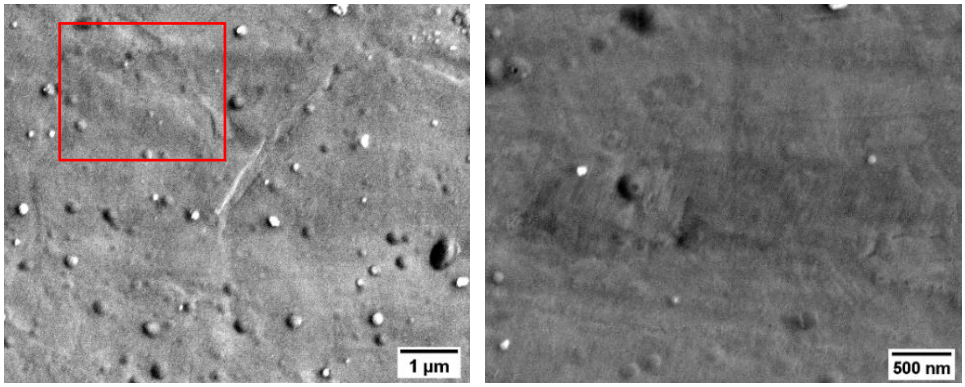

Figure 4.11: SEM micrograph of the nano-polish surface laser processed in the air with F_0=0.29 J/cm^2, Δx=8.85 µm, Δy=5.5 µm, and Nsc=2 (max accumulated fluence Fa^{max}=12.7 J/cm^2). (left) Embedded particulates have sizes of a few nanometers; (right) magnified images of flat area.

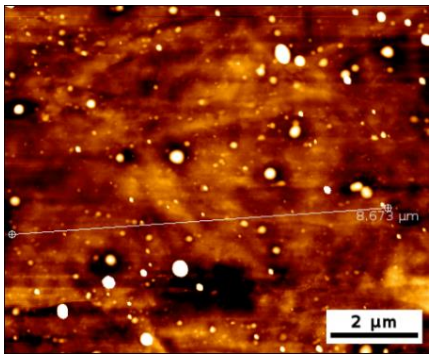

AFM Scan image

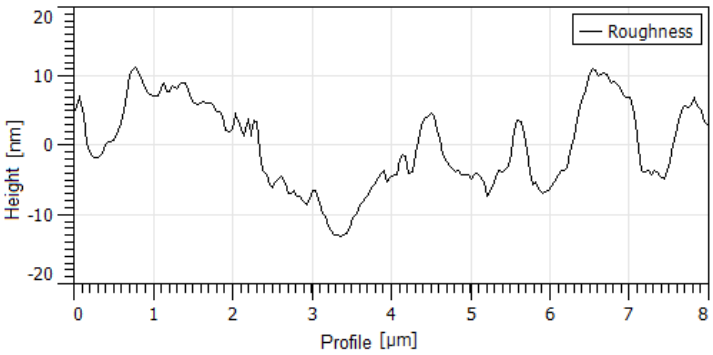

Roughness profile over the LIPSS features

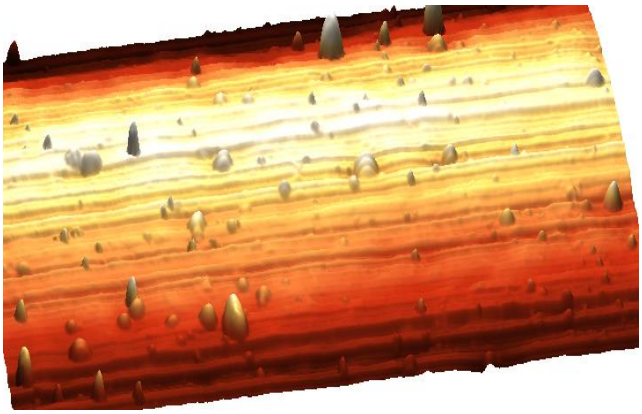

3D representation of the AFM scan.

Figure 4.12: AFM scan of the nano-polish surface for F_0=0.29 J/cm^2, Δx=8.85 µm, Δy=5.5 µm, and Nsc=1. Embedded particulates can be noticed in the AFM scan and its 3D representation.

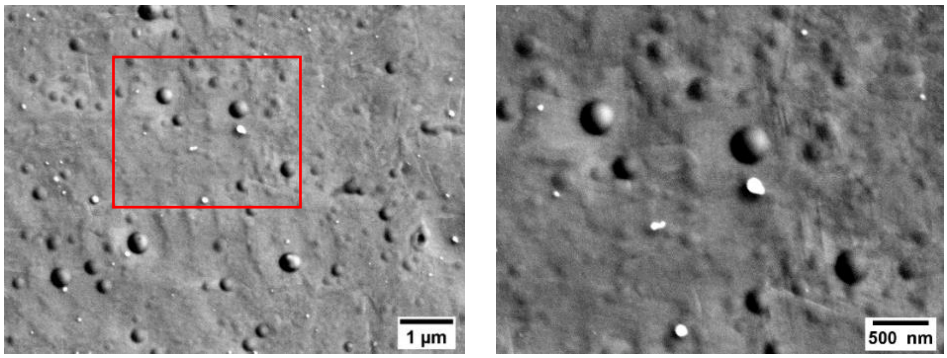

Figure 4.13: SEM micrograph of the laser processed surface with F_0=0.29 J/cm^2, Δx=8.85 µm, Δy=5.5 µm, and Nsc=3 (Fa^{max}=31.6 J/cm^2). The faint onset of laser induced structures can be observed in the SEM scan; (right) Magnification of the region marked with the red line.

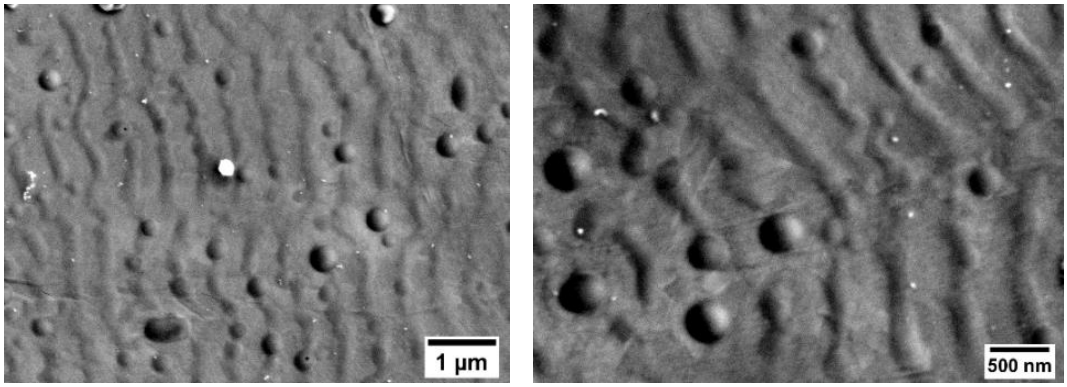

Figure 4.14: SEM micrograph of the shallow LIPSS surface laser processed with F_0=0.29 J/cm^2, Δx=8.85 µm, Δy=5.5 µm, and Nsc=5 (Fa^{max}=31.7 J/cm^2). Periodic feature with Δ_{LIPSS}=505±17 nm is noticed on the surface.

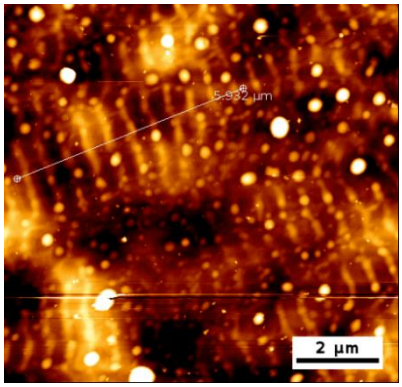

AFM Scan image

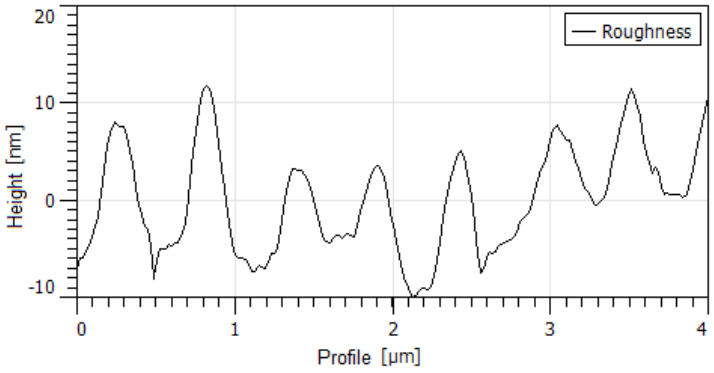

Roughness profile over the LIPSS features

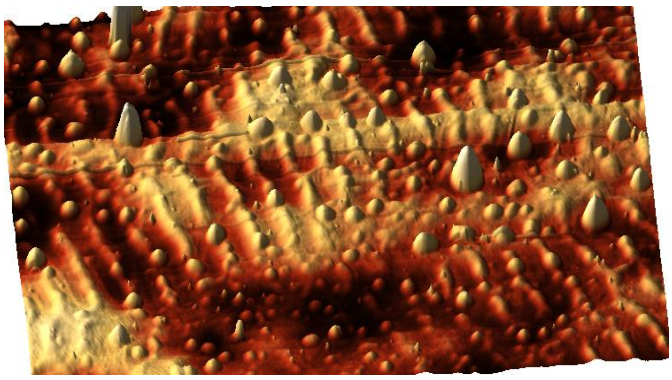

3D representation of the AFM scan.

Figure 4.15: AFM scan of shallow LIPSS features. Laser parameters F_0=0.29 J/cm^2, Δx=8.85 µm, Δy=5.5 µm, and Nsc=5 (Fa^{max}=31.7 J/cm^2). The embedded particles in the AFM scan can be seen as small mounds on the surface in the 3D representation.

4.2.5 Discussion on surface texturing results

The effect of laser processing with the 532nm nanosecond laser was studied for stainless steel 316L. The ablation mechanism of this laser is mainly thermal due to the longer wavelength and the short pulse length (nanosecond). Laser ablation behaviour at high and low fluence was observed. The ablation threshold of the material was estimated to be 1.71 J/cm^2. High ablation and surface oxidation was observed when input fluence was much higher than the ablation threshold. The surface roughness of those features was found to be in microns and hence was not investigated further, as our focus is on developing nano-scale features. LIPSS features were generated for input fluences around the ablation threshold. The nanosecond laser does not produce high spatial frequency LIPSS (HSFL) features [144]. LIPSS with input fluence near the ablation threshold required a max accumulated fluence Fa^{max}=145.5 J/cm^2 and resulted in periodicities 425±20 nm with peak-to-valley height 16.3±0.3 nm.

On the other hand, low input fluence features were obtained with Fa^{max}=31.7 J/cm^2 having periodicities 505±17 nm and peak-to-valley distance 12.8±0.3 nm. The latter type was named ‘shallow LIPSS’. The surface conditions precursor to shallow LIPSS were called ‘nanopolish’ surfaces. The average roughness of the nanopolish surface is Ra=2.68±0.08 nm. The shallow LIPSS can find applications requiring very low aspect ratio feature-based surfaces. The nanopolish surface is similar to the surface finish operation to reduce surface roughness. Further study on the nanopolish surface can show the effectiveness of laser surface modification in the area of surface roughness reduction.

4.3 Laser processing of aperture plate electrodes

The next experimentation phase was to laser process the aperture plates and analyse their protein contamination behaviour. The bovine insulin contaminant particles are nano-scale sized (~2.5 nm in diameter), so laser surface processing cases resulting in low surface roughness were selected for modifying the aperture plate's surface. Also, the quantity of the aperture plates was limited, so the further motivation to use selected cases only. The laser processing was performed at an input fluence F_0=0.32±0.02 J/cm^2 considering the laser spot diameter as 52 μm.

Nano-polished surface and the shallow LIPSS case were selected for the aperture plates. Minor adjustments were needed on the laser processing parameters used for Goodfellow samples to recreate the features on the features on aperture plate surfaces. An optical image of an aperture plate after laser processing is shown in Figure 4.18 as a reference to visualise the laser processed region. The darkened rectangle surrounding the central slot is the laser processed region.

4.3.1 Aperture plate with shallow LIPSS features

The LIPSS features generated with the input fluence much lower than the threshold fluence had a shallow peak-to-valley depth, a very low aspect ratio, and a low roughness value (Figure 4.14). It shows potential in reducing the entrapment of protein ions by removing the possible locations of protein endpoints physically adsorbed to the surface. Hence, this case was explored as the selected case for laser processing on the aperture plat surface.

On the aperture plate surface, shallow LIPSS features were obtained at pulse-to-pulse distance Δx=4.4 µm, hatch distance Δy=5.5 µm, and a number of over scans Nsc=6 for the given input fluence of F_0=0.33 J/cm^2. The max accumulated fluence on the surface was estimated to be Fa^{max}=86.9 J/cm^2. Figure 4.16 shows the SEM micrograph of the laser processed surface showcasing the LIPSS features on the surface with a periodicity of Δ_{LIPSS}=500±10 nm. The AFM scan of the surface, as shown in Figure 4.17, confirms the periodic structures with a peak-to-valley height of 17.9±1.1 nm. The roughness across the features was Ra=5.41±0.48 nm, and over the peaks of LIPSS was Ra=1.53±0.12 nm. The area roughness was estimated as Sa=4.78±0.12 nm. Additionally, an optical image of the actual aperture plate with the shallow LIPSS surface is shown in Figure 4.18 as a reference for ease of understanding. The darkened region around the central slot is the laser processed region.

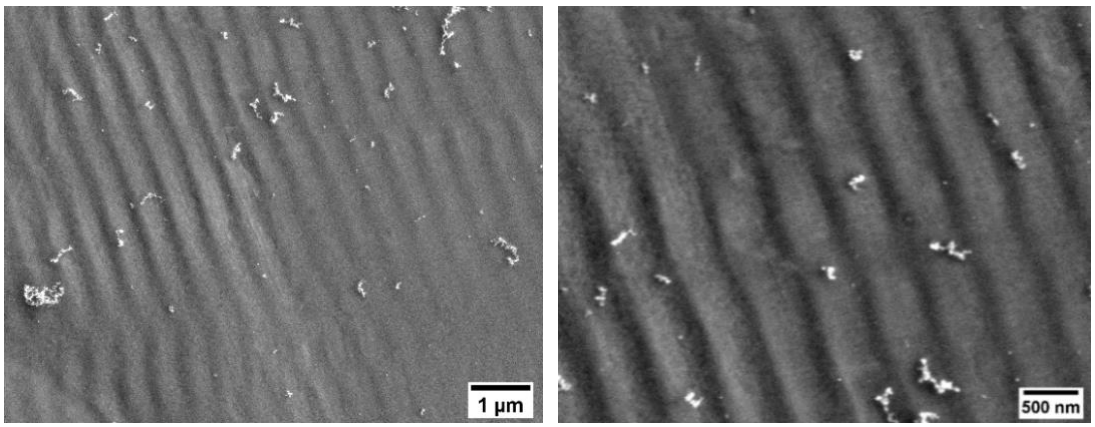

Figure 4.16: SEM micrograph of the shallow LIPSS generated on the aperture plate surface with F_0=0.33 J/cm^2, Δx=4.4 µm, Δy=5.5 µm, and Nsc=6 (Fa^{max}=86.9 J/cm^2); Magnified view of the LIPSS features is shown in the right image.

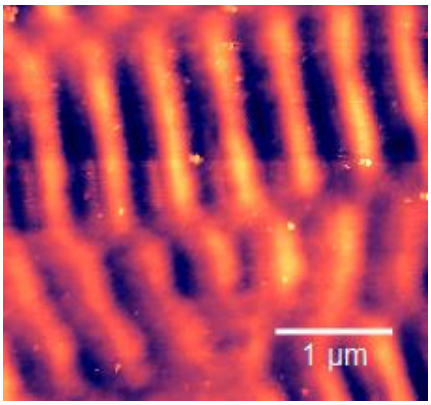

AFM scan of 4x4 µm

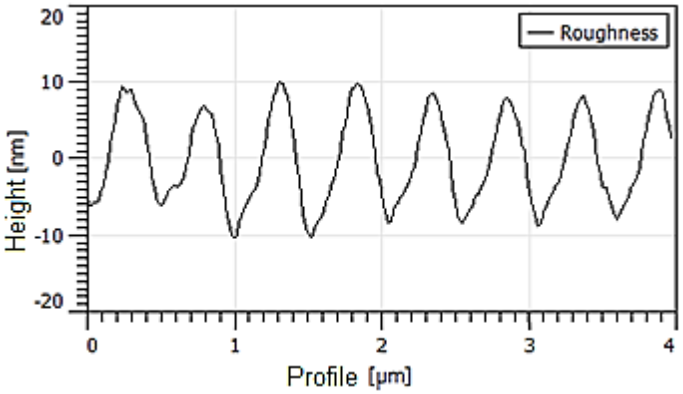

Roughness profile of line drawn on the AFM scan

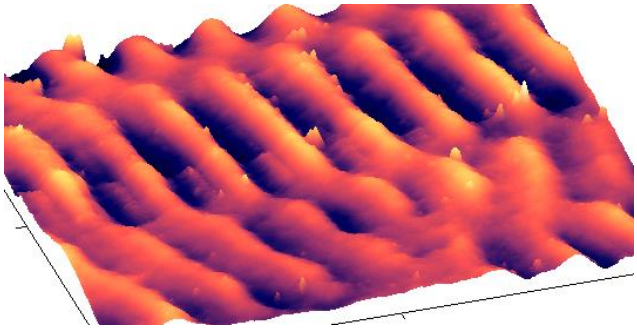

3D representation of the surface. The representation is similar to the SEM micrograph.

Figure 4.17: AFM scan of shallow LIPSS surface on the aperture plate (F_0=0.33 J/cm^2, Δx=4.4 µm, Δy=5.5 µm, and Nsc=6). Profile roughness average Ra=5.41±0.48 nm.

Figure 4.18: Optical image of an aperture plate after laser processing. The central darkened region above and below the central slot is a laser processed region with LIPPS features.

4.3.2 Aperture plate with nanopolish surface (processed in the air)

The nano-polish surfaces were generated at low input fluence, high pulse overlap and low over scan count, similar to the nanopolish surface produced on the Goodfellow sample (refer to Figure 4.11). These surfaces did not show identifiable laser induced features, mostly resulting in the reduction of original surface roughness.

The nano-polish surface was generated on the aperture plate surface using the laser parameters of pulse-to-pulse distance Δx=4.4 μm, hatch distance Δy=5.5 μm, and a number of over scans Nsc=4, for the given input fluence of F_0=0.32 J/cm^2. The max accumulated fluence on the surface was estimated to be Fa^{max}=56.1 J/cm^2. The SEM micrograph from different locations on the aperture plate shows that the surface is without any discernible features, as seen in Figure 4.19. The AFM scan (Figure 4.20) and the generated 3D surface representation (Figure 4.21) confirm that the surface topography is as observed in the SEM micrographs. The area roughness (Sa=2.95±0.92 nm) and the roughness profile average (Ra=2.79±0.74 nm) on the developed surface have a low roughness value.

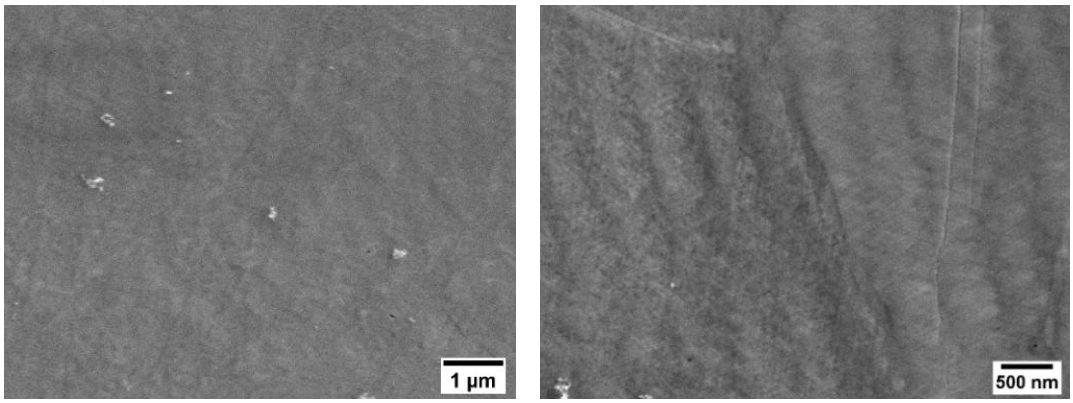

Figure 4.19: SEM micrographs showing different locations of nanopolish aperture plate surface processed in air. Laser parameters are F_0=0.32 J/cm^2, Δx=4.4 μm, Δy=5.5 μm, and Nsc=4 (Fa^{max}=56.1 J/cm^2). The surface is rather smooth and without any discernible features.

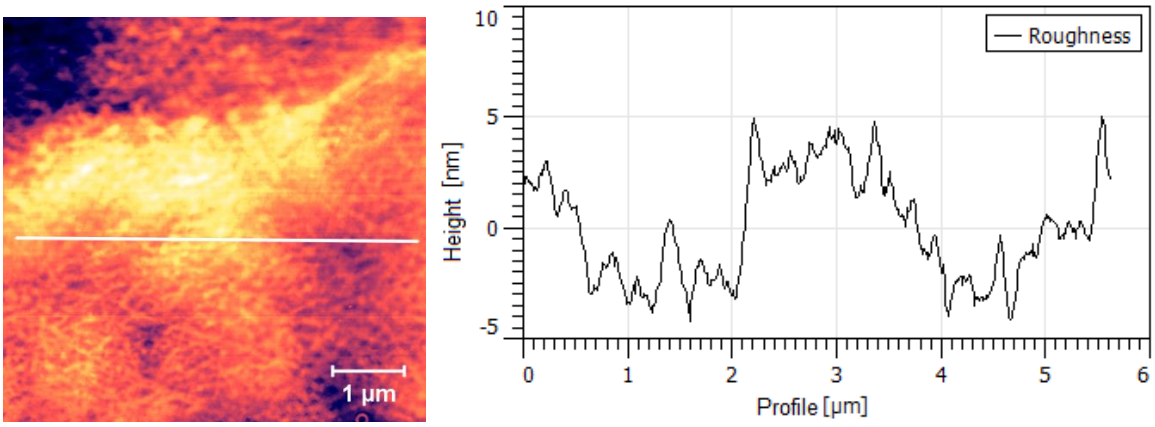

Figure 4.20: AFM scan image of nano-polish processed in the air. A profile line in white is drawn on the image (left); the profile plot shows a roughness average Ra=2.115 nm (right).

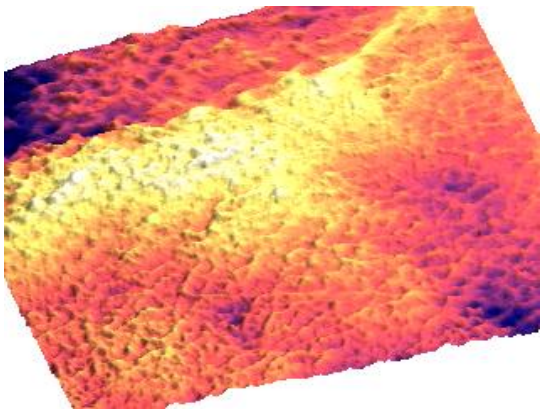

Figure 4.21: 3D representation of the AFM scan (refer to Figure 4.20) of the nano-polished aperture plate surface.

4.3.3 Aperture plate with nanopolish surface (processed in argon environment)

An aperture plate was processed with the laser parameters of the nano-polish surface used in section 4.3.2 in an argon environment, this time to observe the effect of process gas. The laser parameters used in processing are pulse-to-pulse distance Δx=4.4 µm, hatch distance Δy=5.5 µm, and a number of over scans Nsc=4, for the given input fluence of F_0=0.32 J/cm^2. The max accumulated fluence on the surface was estimated to be Fa^{max}=56.1 J/cm^2. The laser processing in an argon environment should affect the surface chemistry, i.e. oxide formation after the surface is processed. In order to improve the

effectiveness of the argon environment, the gas flow was operational from 2 mins before laser processing and remained active for another 2 mins post laser processing.

The developed surface, as shown in Figure 4.22, is similar to the one achieved earlier in the nano-polish surface processed in the air. There are no discernible laser induced surface features, which is confirmed with the AFM scan (refer to Figure 4.24). The AFM scan shows a reduction of surface roughness, wherein the profile roughness average is Ra=5.55±2.19 nm, and the area roughness is Sa=6.28±0.82 nm.

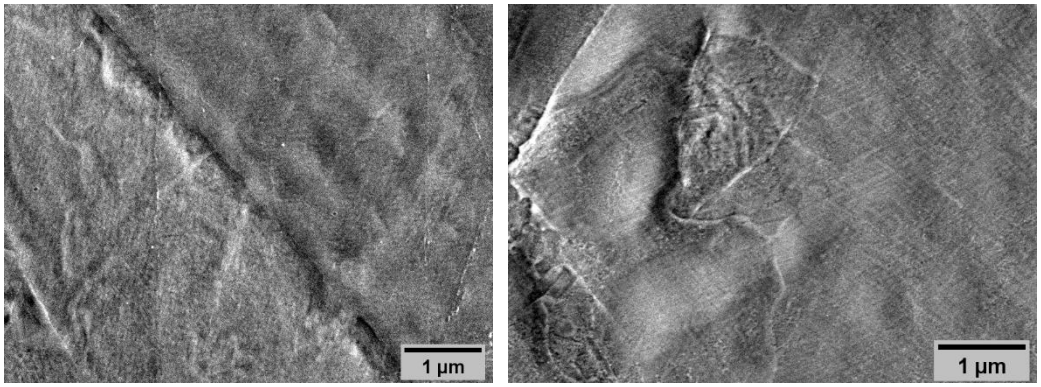

Figure 4.22: SEM micrographs showing different locations from nanopolish aperture plate surface processed in an argon atmosphere. Laser parameters are F_0=0.32 J/cm^2, Δx=4.4 µm, Δy=5.5 µm, and Nsc=4 (Fa^{max}=56.1 J/cm^2)

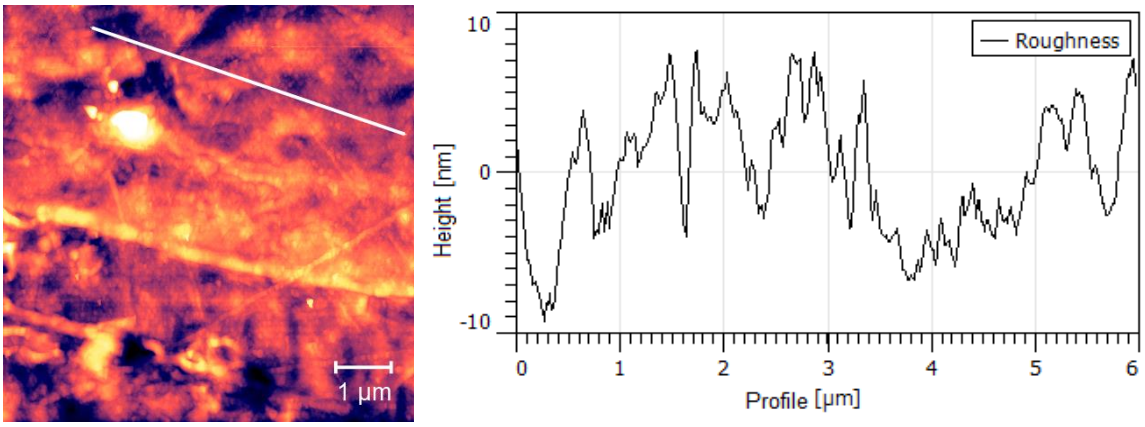

Figure 4.23: AFM scan of nanopolish surface processed in an argon environment. Profile line in white drawn on the scanned image (left); Plot of the profile line on the AFM scan showing roughness average Ra=3.36 nm (right).

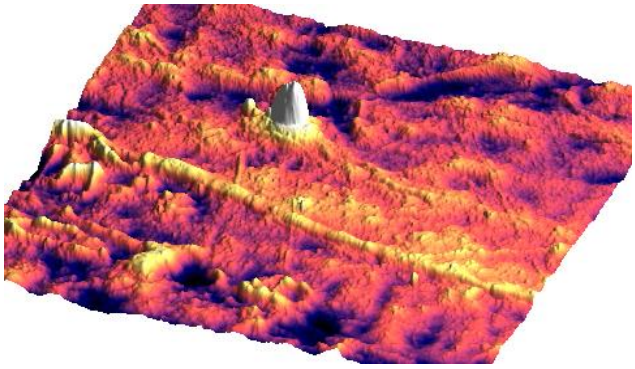

Figure 4.24: 3D representation of the AFM scan (refer to Figure 4.23) of the nanopolish surface processed under an argon environment. The white mound near the image centre is most probably a dust particle.

4.4 Protein contamination behaviour of laser processed aperture plates

The laser processed aperture plates were experimented with for protein contamination behaviour in the test-rig at the Waters facility. The experimental process parameters and the methodology, as explained in section 3.6.1 above, were consistent for all the aperture plates. The data set for resolution and surface charging obtained from the test rig were analysed to understand the behaviour of the plates towards protein adsorption. After protein testing, the surface composition was analysed using XPS. The presence of protein contamination on the surface was done using ToF-SIMS on the aperture plates' ion beam facing side. After laser processing, the XPS analysis was conducted away from the slot to understand the surface composition. But, the ToF-SIMS was done in the region where the ion beam collides with the surface to verify the surface contaminants, i.e. bovine insulin protein residue.

4.4.1 Results of protein contamination behaviour tests

The experimentation consisted of running cycles of 120 sweeps of the instrument. Here, the 'sweep' is the custom term for a pre-set calibration test used by Waters (refer to section 3.6.1). The optimum (maximum) resolution and surface charge were recorded to qualitatively compare and demonstrate the protein contamination behaviour of the aperture plate electrode.

4.4.1.1 Surface charging of the aperture plates

The **surface charge profile** is plotted for the case of the shallow LIPSS based surface laser processed in the air (Figure 4.27), the nanopolish based surface laser processed in the air (Figure 4.25), and the nanopolish based surface with laser processing done in an Argon environment (Figure 4.26). All the plots are done with a moving average of 5; hence, it is presented from sweeps 5-120. The test cycles shown in the surface charge profile plots were done consecutively on the aperture plate. For example, in the nanopolish based surface (Figure 4.25), the test cycle follows the order 'NP1', 'NP2', and 'NP3'. A short break was given before starting a new test cycle, but the instrument was not vented. The surface charge builds up with each test cycle, and all the profiles follow a gradual increase of surface charge trend. It indicates a potential insulating layer build-up on the surface during the test cycle run time. The profile plots also show that each cycle starts at a lower voltage offset than the previous cycle's end voltage offset, thus demonstrating that the insulating layer falls off from the surface in the gap between the two cycles. Also, it can be noticed that the voltage offset drops off and increases within the cycle, hinting at the possibility of contamination chunks being removed from the surface within the cycles. Additionally, it was found that there are some sweeps with an unexpected spike in the end

voltage, such as in the case of shallow LIPSS (refer to Figure 4.27) – test cycle 'SL1' (sweep 109, end voltage 20.9) and 'SL2' (sweep 49 and 84, end voltage 20.9 and 20.8 respectively). It is difficult to explain these spike cases as they were rarely observed during the testing.

The surface charge trend can be quantified using the slopes of the profile and is presented in Table 4.3. The slope here is the charging rate of the aperture plate, measured in mV/sweep. They were calculated using the sweep data from 21-120 only. The initial 20 sweeps are considered the settling-in period and thus skipped. The table also contains the information on the reference electrode, i.e. a non-laser processed aperture plate, for comparison.

The surface charging behaviour of nanosecond cases, i.e. gradual build-up of charge and the potential of insulating later keep rebuilding, looks similar to the reference electrode (refer to Figure 3.22 and section 3.6.2.1). However, compared to the reference electrode, there is a definite improvement in the charging rates in nanosecond cases, especially shallow LIPSS and nanopolish surface laser processed in the air. The trend of increasing surface charge seems slower for the laser textured electrode surfaces than for the reference electrode. The average charging rates for the laser textured electrodes are 6.08 mV/sweep (shallow LIPSS surface) and 7.73 mV/sweep (nanopolish surface processed in the air), and it is lower than the reference electrode (9.21 mV/sweep). The nanopolish case in an argon environment shows a charging rate of 10.6 mV/sweep comparable to the reference electrode.

Moreover, laser textured case, such as the shallow LIPSS surface, has a standard deviation of only 1.16 mV/sweep showing more stability and predictability in the surface charging behaviour compared to the reference electrode (std. deviation of 3.21 mV/sweep).

Further, the nanopolish surface processed in the air shows promising results even though the standard deviation is 3.43 mV/sweep. Thus, based on the current results, it may be stated that laser processed plates in the air show an improvement in surface charging, especially in the case of shallow LIPSS. More tests can help understand the long-term trend of the contamination behaviour.

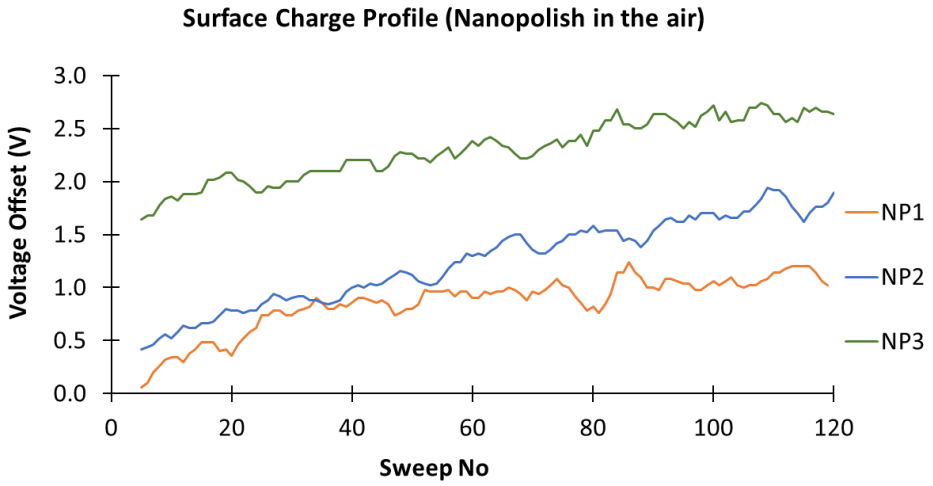

Figure 4.25: Plot of the surface charge profile of the aperture plate surface with nanopolish condition (laser processed in the air). The voltage offset is the difference in the end voltage at the electrode surface from 17V.

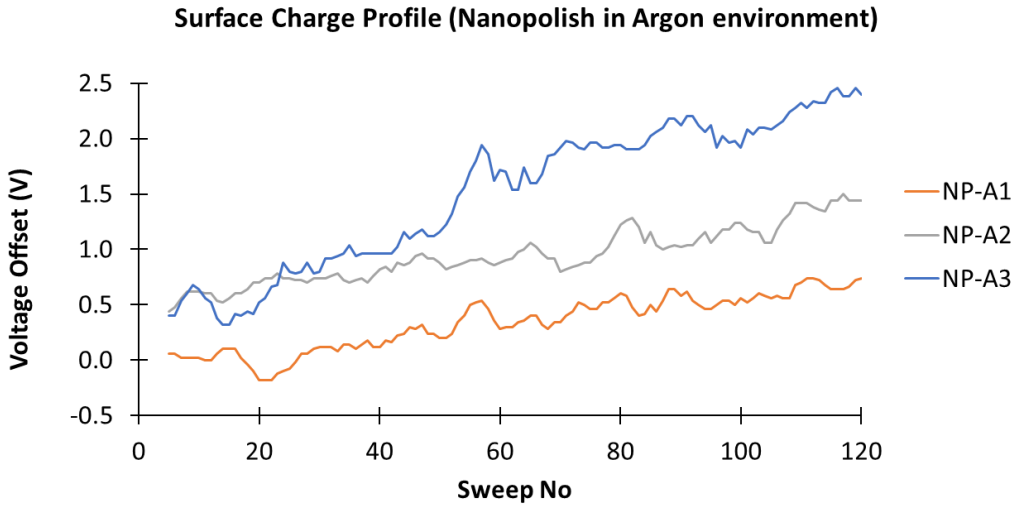

Figure 4.26: Surface charge profile of the aperture plate surface nanopolish condition (laser processed in Argon environment). The voltage offset is the difference in the end voltage at the electrode surface from 17V.

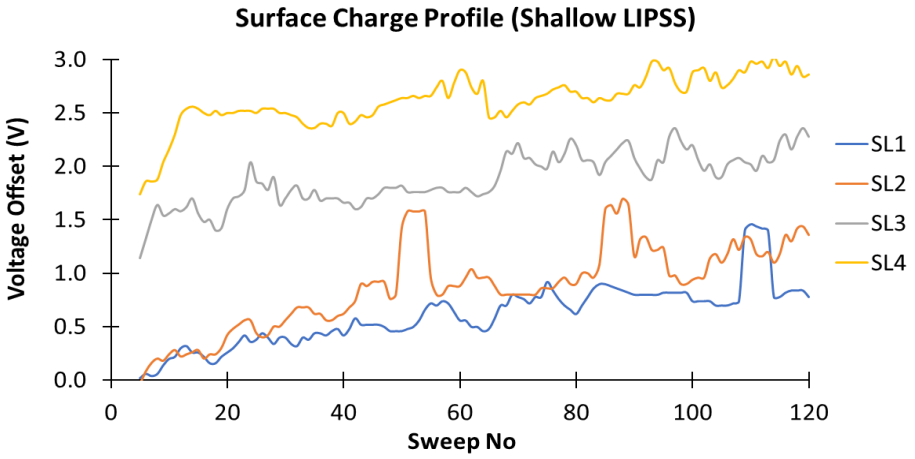

Figure 4.27: Plot of the surface charge profile of the aperture plate surface with shallow LIPSS features. The voltage offset is the difference in the end voltage at the electrode surface from 17V.

Table 4.3: Surface charge development in nanosecond laser processed aperture plates

Description	Experiment No	Max Offset Charge (V)	Charging Rate (Slope) (mV/Sweep)	Average charging rate (mV/Sweep)	Std. Deviation (σ) (mV/Sweep)
Reference electrode*	Ref 1 Ref 2	1.72 1.88	6.94 11.48	9.21	3.20
Laser - Shallow LIPSS case	SL1 SL2 SL3 SL4	1.46 (0.92) 1.70 (1.44) 2.36 3.02	6.63 (5.27) 7.44 (7.67) 5.29 4.97	6.08 (5.80)**	1.16 (1.26)
Laser - Nanopolish case	NP1 NP2 NP3	1.24 1.94 2.74	4.29 11.14 7.76	7.73	3.43
Laser - Nanopolish case (done in Argon environment)	NP-A1 NP-A2 NP-A3	0.74 1.50 2.46	7.17 6.95 17.68	10.60	6.13

* Please refer to Table 3.5 and section 3.6.2 for details on the reference electrode.

** Results without the outliers are in brackets

4.4.1.2 Effect on the resolution of the instrument

The **optimum (maximum) resolution** is the second indicator obtained during the protein contamination behaviour testing. It allows us to understand the instrument's stability during one test run cycle of 120 sweeps. The resolution information is obtained from the instrument directly, and the profile is plotted using the sweep data from 1 to 120. The resolution data profile of the test cycles for shallow LIPSS (Figure 4.30), nanopolish surface laser processed in the air (Figure 4.28) and nanopolish surface laser processed in an argon environment (Figure 4.29) is shown below. It is noticeable from the profile plots that the optimum/maximum resolution mainly decreases during the test cycle run. However, it does not follow a distinct trend, as seen in the surface charge profile plots.

The resolution drops faster for the first 20 to 25 sweeps and stabilises during the rest of the cycle run. Hence, the first 20 sweeps are taken as the test cycle run's settling-in period and skipped from the resolution drift rate calculation. The resolution drift rate is the resolution profile's slope, measured as ‘res/sweep’ and is dimensionless. Table 4.4 lists the average resolution and the resolution drift rates for the nanosecond laser processed aperture plates and the reference electrode. Nanosecond laser processed cases show improved resolution in the consecutive test run cycles. For example, both nanopolish cases show an improvement in the average resolution for each test cycle. The average resolution drops for shallow LIPSS initially, and improvement is seen in the later consecutive cycles. Further, the resolution drifts for shallow LIPSS show two cycles, ‘SL2’ and ‘SL3’, having positive drift values, i.e. 3.42 re/sweep and 10.27 res/sweep, which is a sign of improvement in the resolution. But, it still does not provide a conclusive trend on the resolution as even the reference electrode has a test cycle ‘Ref_2’ with positive resolution drift (2.41 res/sweep). Further, as noticed in Table 4.4, the resolution drift is mostly negative, hinting towards the

loss of resolution of the instrument during the test run cycle. The negative resolution drift rate clearly indicates contamination of the instrument during the operation phase. So, we can use the optimum resolution information to qualitatively ascertain the presence and gradual build-up of the contamination during the instrument's operation time.

Moreover, the resolution is affected by the performance of the overall ion optics. Hence, it is difficult to segregate the contribution of a particular ion optics, such as the aperture plate, towards the resolution drift. Therefore, based on the results set, we can conclude that the shallow LIPSS case is the most stable during the operation phase and can be considered a promising prospect for further investigation.

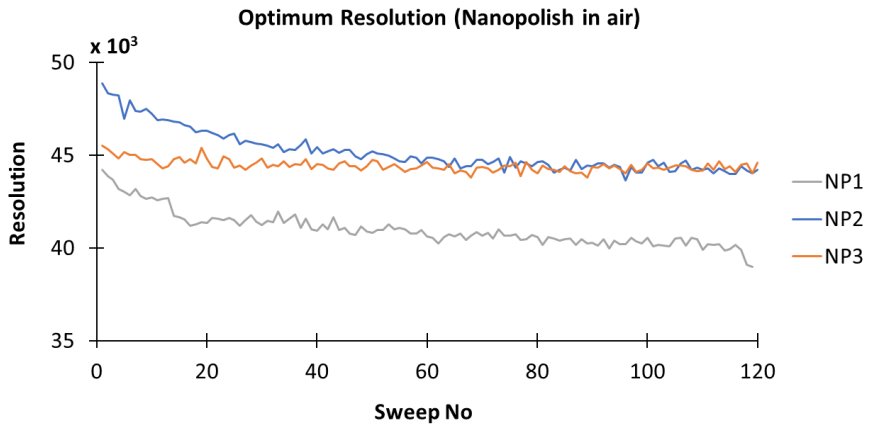

Figure 4.28: Plot of optimum resolution profile of nanopolish surface (processed in the air) based aperture plate.

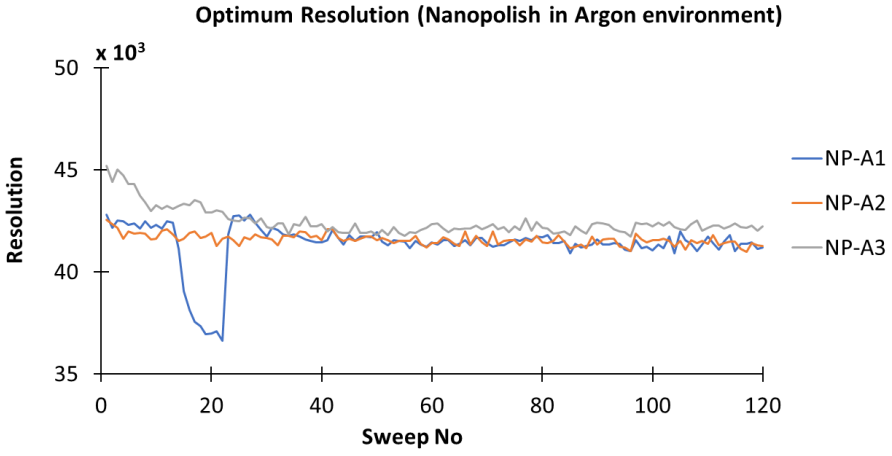

Figure 4.29: Plot of optimum resolution profile of nanopolish surface (processed in argon) based aperture plate.

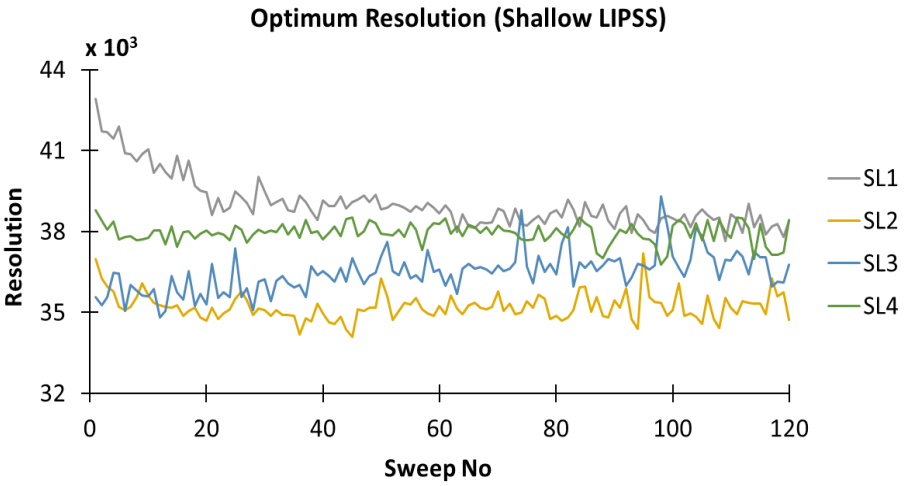

Figure 4.30: Plot of optimum resolution profile of aperture plate with shallow LIPSS features.

Table 4.4: Trend of the optimum resolution for nanosecond laser processed aperture plates

Description	Experiment No	Average resolution in each cycle	Resolution drift rate (Slope) (res/sweep)	Avg. resolution drift rate (res/sweep)	Std. Deviation (σ) (res/sweep)
Reference electrode*	Ref 1	44753.86	-7.21	-2.4	6.8
	Ref 2	41230.64	2.41		
Laser - Shallow LIPSS case (No venting in between)	SL1	38682.72	-9.37	0.44	8.38
	SL2	35162.69	3.42		
	SL3	36629.79	10.27		
	SL4	37946.49	-2.55		
Laser - Nanopolish case	NP1	40294.22	-17.26	-12.22	8.64
	NP2	44769.15	-17.16		
	NP3	44351.64	-2.24		
Laser - Nanopolish case (done in Argon environment)	NP-A1	41450.44	-1.87 (-7.84)	-2.25 (-4.24)**	0.91 (3.23)
	NP-A2	41528.94	-3.28		
	NP-A3	42199.67	-1.59		

* Please refer to Table 3.6 and section 3.6.2 for details on the reference electrode.

** Results without the outliers are in brackets

4.4.1.3 Protein contamination behaviour: Conclusion

The surface charge and resolution results show the trend of the contamination build-up on the aperture plate and the overall instrument stability during the instrument's operation time. The nanosecond laser processed aperture plate affects the protein contamination behaviour as the results vary from the non-laser processed reference electrode. Out of the three case types tested, the shallow LIPSS show the most improved behaviour towards resistance to protein contamination. However, since the result set is small, it requires further experimentation to verify the repeatability of the observed behaviour.

4.4.2 XPS results: Surface chemistry analysis after protein testing

The surface chemistry analysis XPS was conducted through Lucideon Ltd. on the nanopolish case (processed in an argon environment) and the shallow LIPSS (processed in the air). The XPS analysis was conducted away from the slot to understand the surface composition after laser processing.

The XPS results contain the wide area survey spectrum and the core level spectra of the various elements. It also presents a surface composition table and compares the results with the reference aperture plate electrode. The survey spectrum highlights the identified primary peaks of the elements along with carbon and oxygen. The components of stainless steel 316L are identified in the survey spectra, along with trace elemental impurities. The survey spectrum was recorded with a pass energy of 160 eV at a step size of 1 eV. The carbon layer is formed due to the adsorption of air-borne carbonaceous material when the surface is exposed to the atmosphere [192]. The oxygen layer is from the thin passivating oxide layer on the surface [151,193]. Figure 4.31 shows the survey

spectrum of the nanopolish surface processed in an argon environment, and Figure 4.33 shows the case of shallow LIPSS. The core level spectra of O 1s, C 1s, Fe 2p, Cr 2p, Ni 2p and Mo 3d were recorded with the pass energy of 20 eV at a step size of 0.1 eV. The take-off angle of the analysed photoelectrons was 90°. The binding energies were calibrated by setting the C 1s signal corresponding to C–C and C–H at 285 eV [194,195]. The core level spectra for the nanopolish surface (processed in argon) and the shallow LIPSS are shown in Figure 4.32 and Figure 4.34, respectively.

4.4.2.1 Nanopolish surface (laser processed in Argon environment)

The survey spectrum for the nanopolish surface is shown in Figure 4.31. The major components of stainless steel on the surface are iron (4%), chromium (16 %), nickel (0.15%), molybdenum (0.11%), manganese (1.85%) and phosphorous (0.9%). The values are presented in atomic weight percentages. Apart from that, there is a carbon (20.73%), oxygen (53.96%) and nitrogen (0.73%). A significant change is seen in the percentage of iron and chromium for the nanopolish surface compared to the reference electrode surface (iron: 10.89%, and chromium 3.31%), hinting towards changes in the passivated oxide layer of the nanopolish surface.

The core level spectra of O 1s, C 1s, Fe 2p, Cr 2p, Ni 2p and Mo 3d are shown in Figure 4.32. The binding energies were calibrated similarly to the reference electrode, i.e. by setting the C 1s signal corresponding to C–C and C–H at 285.0 eV. The significant peaks in the C 1s spectrum, i.e. C–N & C–O single bonds (286.45 eV) and O=C–O & O=C–N peptide bonds (288.80 eV), are organic/polymeric materials, as noticed for the reference electrode also. The core O 1s spectra show the presence of metal oxides (530.86 eV), metal hydroxides (532.16 eV) and hydroxyl groups from aromatic compounds (533.76 eV). An

increase in oxide and reduction in the metal hydroxide is observed for the nanopolish compared to the reference electrode's surface. Iron is mainly in the oxide form (709.89 eV), as seen in the Fe 2p spectra, along with iron precipitate in the metallic form (706.82 eV) in a ratio of 5.2:1. Similarly, chromium is present mainly in the oxide form with an oxide:metal ratio of 266:1. The primary oxide is in the form Cr (III) (577.10 eV) with a small amount in the form of Cr (II) oxide (576.1 eV). The oxide:metal ratio is listed in the Table 4.6. Nickel is present as a precipitate in the metallic form only (852.83 eV). The core level spectra of Mo 3d shows double peaks for the metallic form Mo (0) and its oxide forms of Mo (II), Mo (IV) and Mo (VI), but the significant contribution is from the metallic Mo (0) and the oxide Mo (IV).

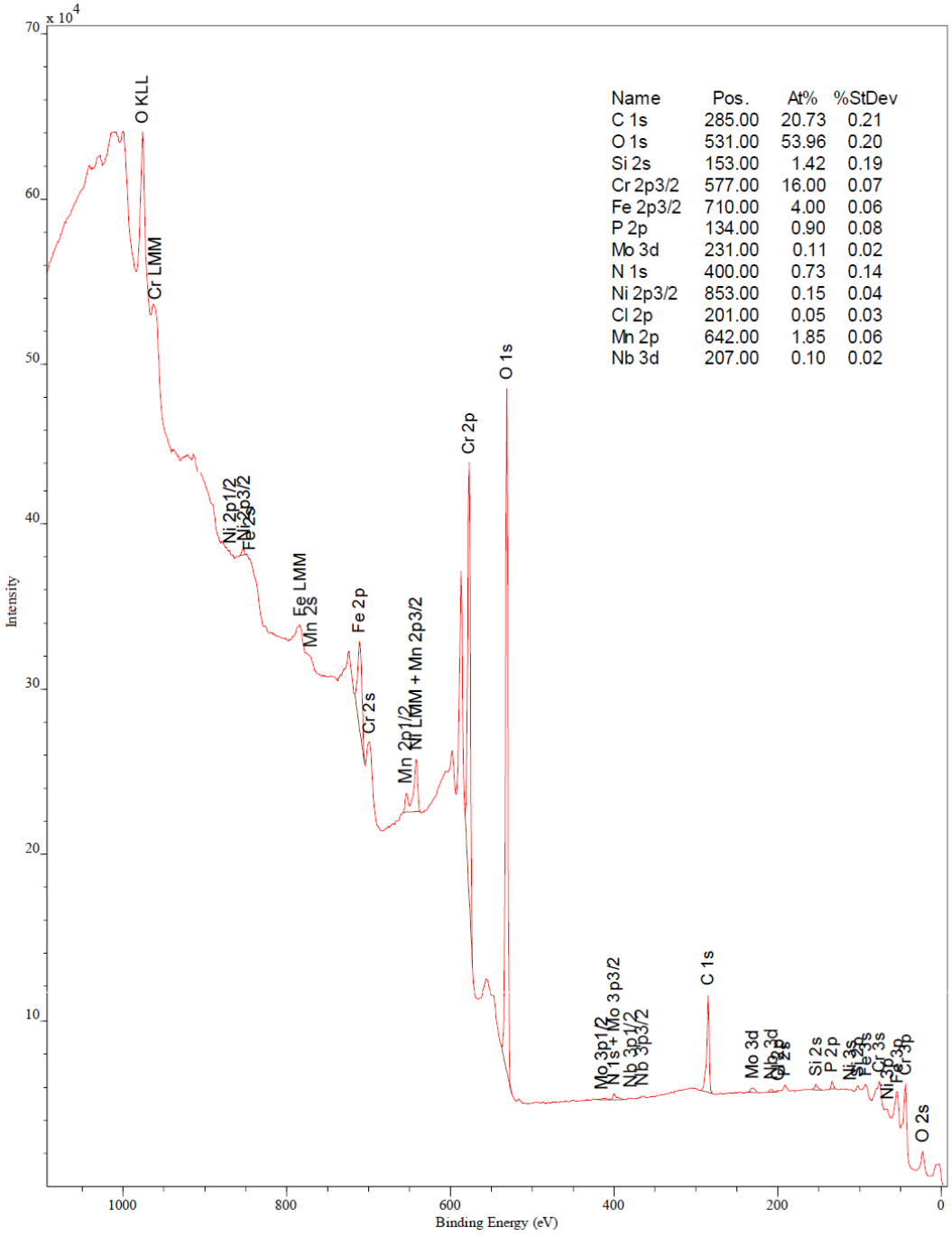

Figure 4.31: XPS survey spectra of the nanopolish surface based electrode (processed in an Argon environment). The summary in the top-right corner lists the atomic percent (At %) of the identified elements.

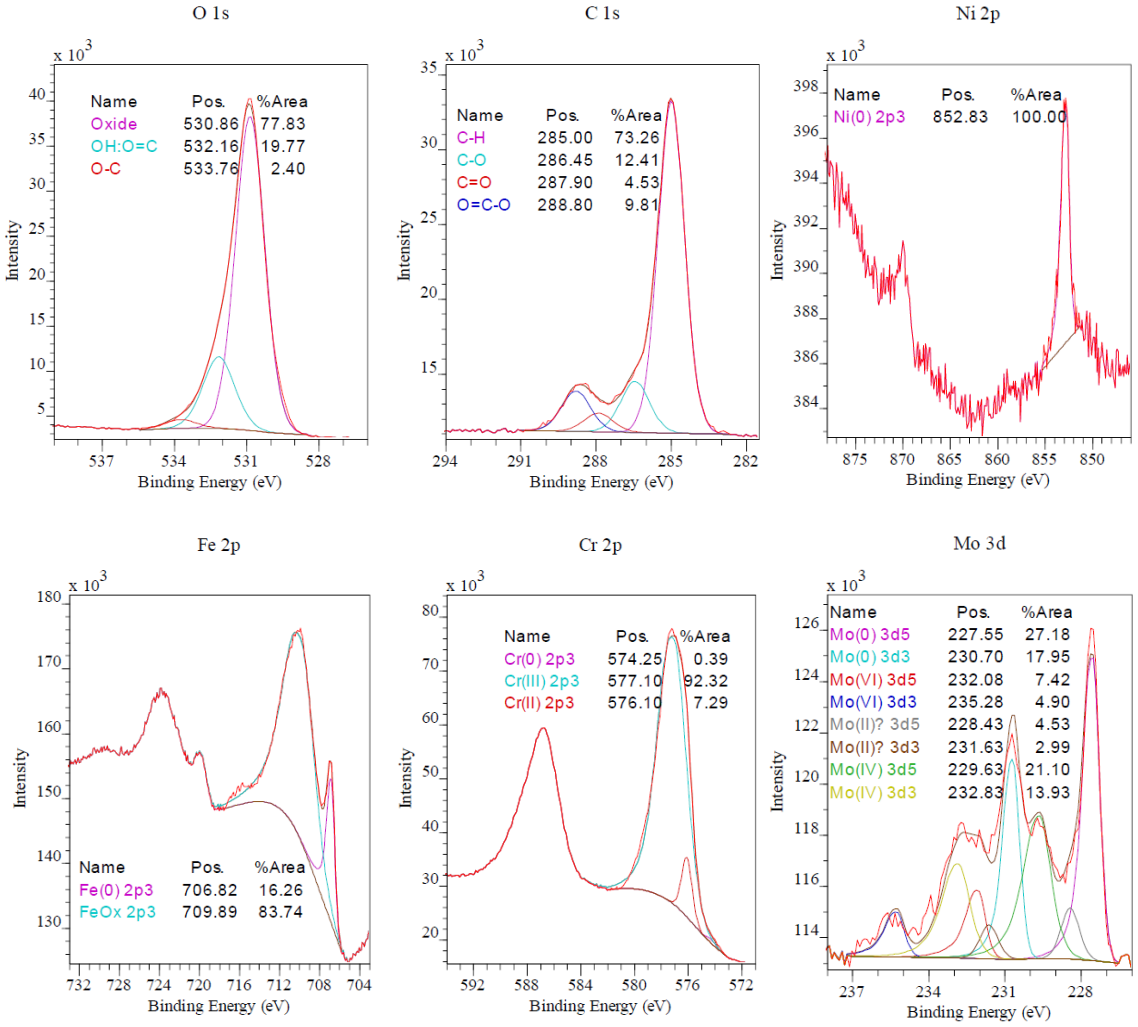

Figure 4.32: Core level spectra of O 1s, C 1s, Fe 2p, Cr 2p, Ni 2p and Mo 3d of the nanopolish surface (processed in Argon) based aperture plate (pass energy of 20 eV and step size 0.1 eV).

4.4.2.2 Shallow LIPSS surface (processed in the air)

The survey spectrum for the shallow LIPSS surface is shown in Figure 4.33. The major components of stainless steel on the surface are iron (3.61%), chromium (14.06%), nickel (0.30%), molybdenum (0.04%), manganese (3.83%) and phosphorous (0.08%). The values are presented in atomic weight percentages. Apart from that, there is carbon (18.87%), oxygen (54.88%) and nitrogen (0.43%). The shallow LIPSS surface shows a significant change in the percentage of iron and chromium compared to the reference electrode's surface (iron: 10.89%, and chromium 3.31%), hinting towards changes in the

passivated oxide layer on the surface. The behaviour is similar to the nanopolish surface (laser processed in argon atmosphere).

The core level spectra of O 1s, C 1s, Fe 2p, Cr 2p, Ni 2p and Mo 3d are shown in Figure 4.34. The binding energies were calibrated similarly to the reference electrode, i.e. by setting the C 1s signal corresponding to C–C and C–H at 285.0 eV. The significant peaks in the C 1s spectrum, i.e. C–N & C–O single bonds (286.45 eV) and O=C–O & O=C–N peptide bonds (288.65 eV), are organic/polymeric materials, as noticed for the reference electrode also. The core O 1s spectra show an almost equal amount of the metal oxides (530.90 eV) and the metal hydroxides (531.59 eV). Iron is present mainly as oxides (709.89 eV), with iron precipitate in the metallic form (706.72 eV) in a 3.1:1 ratio. Similarly, chromium is present as Cr (III) oxide (576.97 eV) with some negligible amount of Cr (II) oxide form (576.1 eV) and metallic Cr (0) (574.12). Nickel is present as a precipitate in the metallic form only (852.70 eV), similar to the nanopolish surface. The core level spectra of Mo 3d show double peaks for the metallic form Mo (0) and its oxide forms of Mo (II), Mo (IV) and Mo (VI), but around 70% is in the form of metallic Mo (0). Further, a comprehensive table of the surface composition is shown in Table 4.5 for reference. And a summary of the oxide:metal and metal:iron is listed in Table 4.6.

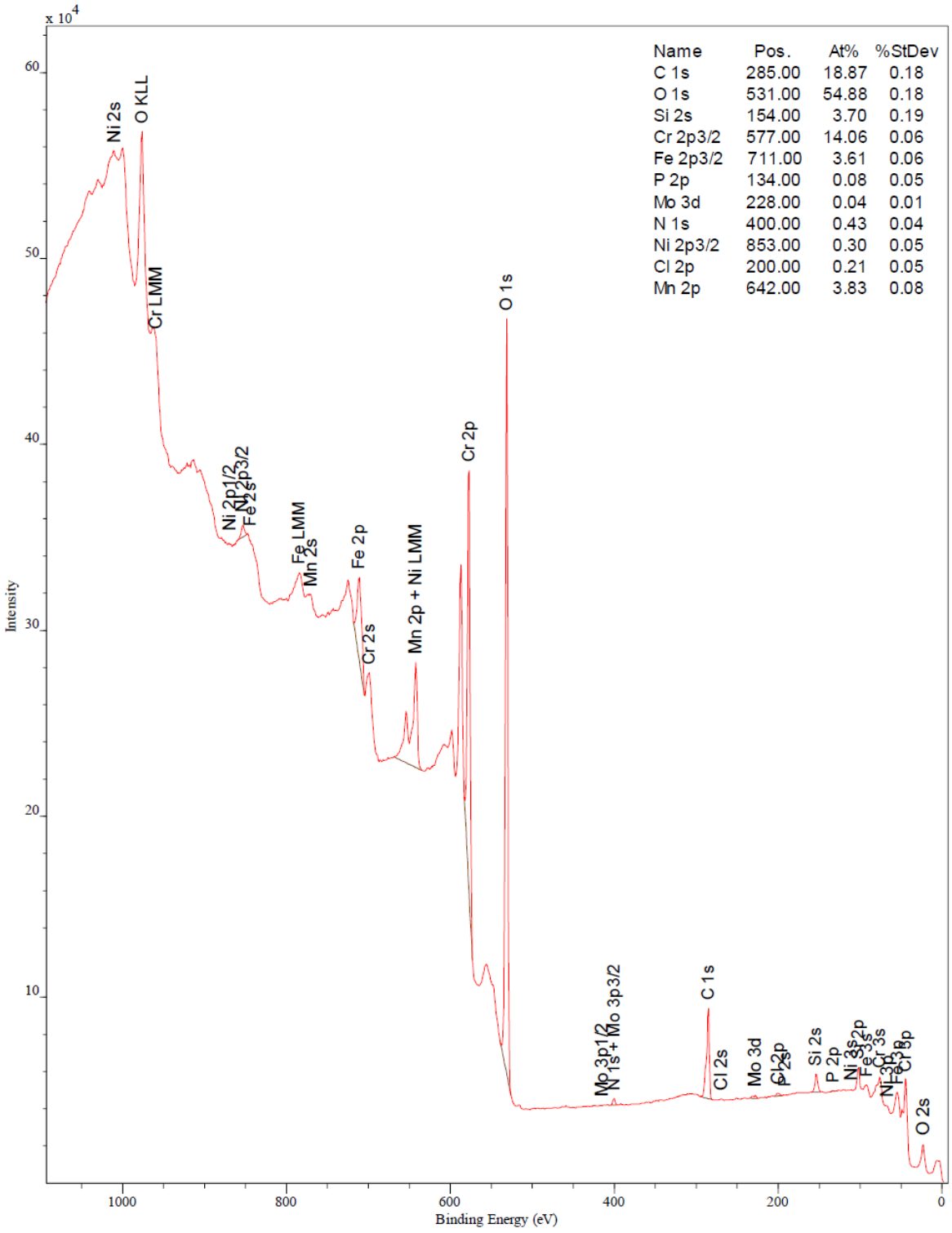

Figure 4.33: XPS survey spectra of the shallow LIPSS surface based electrode. The summary on the top- right corner lists the atomic percent (At %) of the identified elements.

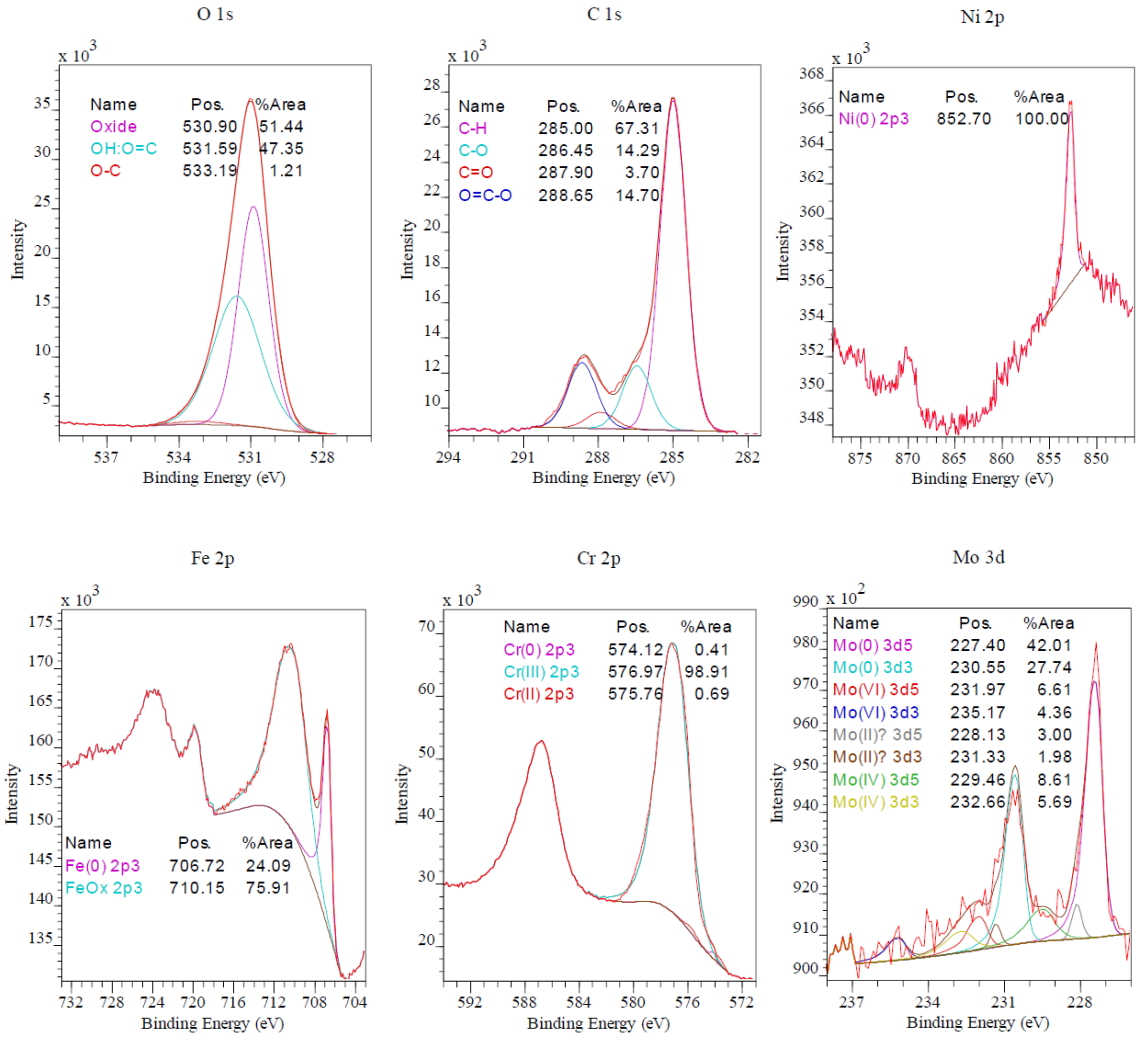

Figure 4.34: Core level spectra of C 1s, O 1s, Fe 2p, Cr 2p, Ni 2p and Mo 3d of the shallow LIPSS surface based aperture plate (pass energy of 20 eV and step size 0.1 eV)

4.4.2.3 XPS results in comparison with reference electrode

XPS analysis of the nanopolish surface (processed in an argon environment) and shallow LIPSS surface (processed in the air) indicated their surface composition. A summary of the surface composition in atomic weight percentage is shown in Table 4.5. Additionally, a summary of oxide:metal and metal:iron ratio of other constituents of SS316L is listed in Table 4.6. Both the laser processed surfaces show a similar trend in the surface composition compared to the mechanically polished reference aperture plate

electrode. Such as, the laser processed surfaces had declined levels of iron, nickel and molybdenum. In the case of iron, the iron oxide decreased by 67.78% for nanopolish in the argon case and 73.65% in the shallow LIPSS case, but there is a slight increase in metallic iron. No nickel oxide was seen in the XPS analysis of the laser processed plates. Only nickel precipitate was identified in the core spectra of laser processed electrodes, and the shallow LIPSS had double the amount of nanopolish in the argon case. However, the laser processed plate's overall nickel content is lower than the reference electrode's. Changes in the overall composition of molybdenum are seen in both laser cases, but a trend cannot be established from the cases alone. Both the laser processed plates have increased percentages of chromium and manganese in the surface composition. Oxide of manganese is detected for laser processed plates only with shallow LIPSS showing double amount than nanopolish. The percentage of chromium increased significantly, mainly in the form of Cr(III) oxide for the laser processed plate, such as a 419.3% increase in nanopolish in argon and a 387.72% increase in shallow LIPSS case. The iron reduction and the significant increase in chromium indicate the passivation of the surface and regeneration of the oxide layer for both the laser processed electrodes.

However, comparing the laser processed electrodes only, the effect of the argon environment on the nanopolish surface can be observed from the surface composition. Low oxygen content in the argon atmosphere affects the oxide layer composition, with precedence to chromium and molybdenum in oxide formation [209].

It should be noted that the XPS analysis was conducted in a region away from the slot and the ion beam collision region. Hence, the XPS analysis was more utilised to identify the changes in surface composition due to laser processing. The significant changes

in the composition of iron, chromium, nickel and manganese highlight the change in surface chemistry and the capability of laser processing to affect the surface chemistry.

Table 4.5: XPS Surface Composition Table (At%): Nanosecond laser processed plates

Elements	Reference Electrode**	Nanopolish in Argon	Shallow LIPSS	Elements	Reference Electrode**	Nanopolish in Argon	Shallow LIPSS
Carbon	***21.9***	***20.7***	***18.9***	***Molybdenum***	***0.18***	***0.11***	***0.04***
σ	*0.2*	*0.2*	*0.2*	***σ***	*0.02*	*0.02*	*0.01*
C-C:C-H	11.2	15.2	12.7	Mo(0)	0.04	0.05	0.03
C-O:C-N	3.62	2.57	2.7	Mo(II)	0.03	0.01	<0.01
C=O:N-C=O	0.65	0.94	0.7	Mo(IV)	0.06	0.04	~0.01
O=C-O	6.36	2.03	2.77	Mo(VI)	0.05	0.01	<0.01
Oxygen	***60.53***	***54***	***54.86***	***Chromium***	***3.31***	***16***	***14.1***
σ	*0.2*	*0.2*	*0.2*	***σ***	*0.05*	*0.1*	*0.1*
Oxide	24.1	42	28.2	Cr(0)	0.13	0.06	0.06
OH:O=C	33.4	10.7	26	Cr(II)	0.33	1.17	0.1
O-C	3.03	1.3	0.66	Cr(III)	2.85	14.8	13.9
Iron	***10.9***	***4***	***3.61***	***Manganese***	***0.04***	***1.85***	***3.83***
σ	*0.1*	*0.06*	*0.06*	***σ***	*0.04*	*0.06*	*0.08*
Fe(0)	0.47	0.65	0.87	Mn(II)	NA	0.92	2.28
FeOx	10.4	3.35	2.74	Mn(III)	NA	0.93	1.55
Nickel	***0.53***	***0.15***	***0.3***	***Silicon***	***1.07***	***1.42***	***3.7***
σ	*0.06*	*0.04*	*0.05*	***σ***	*0.12*	*0.19*	*0.19*
Ni(0)	0.18	0.15	0.3	Si(0)	0.35	0.2	0.12
Ni(Ox)	0.35	NA	NA	Si-C	0.72	1.22	3.58
Nitrogen	***0.8***	***0.73***	***0.43***	***Phosphorus (PO_4)***	***0.71***	***0.9***	***0.08***
σ	*0.06*	*0.14*	*0.04*	***σ***	*0.09*	*0.08*	*0.05*
Amine:Amide	0.8	0.64	0.43				

**** Reference electrode data added for comparison (refer to Table 3.9 in section 3.6.2.2)**

Table 4.6: Oxide:Metal & Elemental Ratios by XPS of laser processed aperture plates

Comparison	Reference electrode**	Nanopolish in Argon	Shallow LIPSS
Fe(Ox):Fe(0)	22	5.2	3.1
Cr(Ox):Cr(0)	24	266	234
SS(Ox):SS(0)*	17	23	16
Cr:Fe	0.30	4.0	3.9
Mn:Fe	0.004	0.46	1.06
Ni:Fe	0.05	0.04	0.08
Mo:Fe	0.02	0.03	0.01

**** Reference electrode data added for comparison (refer to Table 3.8 in section 3.6.2.2)**

***SS(Ox) = sum of the principal SS 316 elements (Fe, Cr, Ni, Mo, Mn) in their oxidised states.**

SS(0) = sum of the principal SS 316 elements (Fe, Cr, Ni, Mo, Mn) in their metallic state.

4.4.3 ToF-SIMS Results: Protein contamination analysis

ToF-SIMS surface imaging measurements were primarily done to identify bovine insulin residue on the surface. The analysis was conducted by Lucideon Ltd. using an ION-TOF instrument. The primary ion source was bismuth (Bi^{3+}) with an ion energy of 30 keV. The analysis current was 0.2 pA, and the analysis was conducted on an area of 20x20 mm^2. The wide area scan provides an overview of the central slot in the aperture plate, the ion beam shape, and its collision location.

The image overlay of the aperture plates with nanopolish surface processed under argon and shallow LIPSS based surface is shown in Figure 4.35 and Figure 4.36, respectively. The image overlays present the summation of bovine insulin and stainless steel constituents on the surface of the plates. It also provides an overview of the central slot in the aperture plate and the residue of the ion beam at its collision location. In both

cases, the bovine insulin residue is present as a narrow band near the centre of the slot, and the residue is present above and below the slot. The protein residue behaviour is similar to that observed for the reference electrode (Figure 3.26). The continued presence of the organic residue hints at contamination by adsorption after the reactive landing of the protein ions on the surface. However, the thickness of the organic residue layer could not be determined due to the unavailability of the depth profile information.

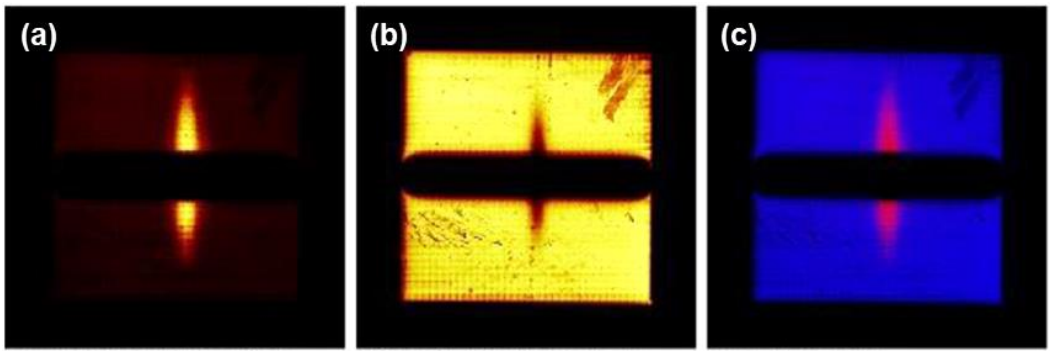

Figure 4.35: Image overlay of ToF-SIMS scan of 20x20 mm^2 of the aperture plate with nanopolish surface (processed in argon); (a) Bovine Insulin (summed image), (b) Stainless steel (summed image), (c) Bovine Insulin (red) & stainless steel (blue)
Spectrum parameter: Species Bi^{3+}, Area 20x20 mm^2, Polarity positive

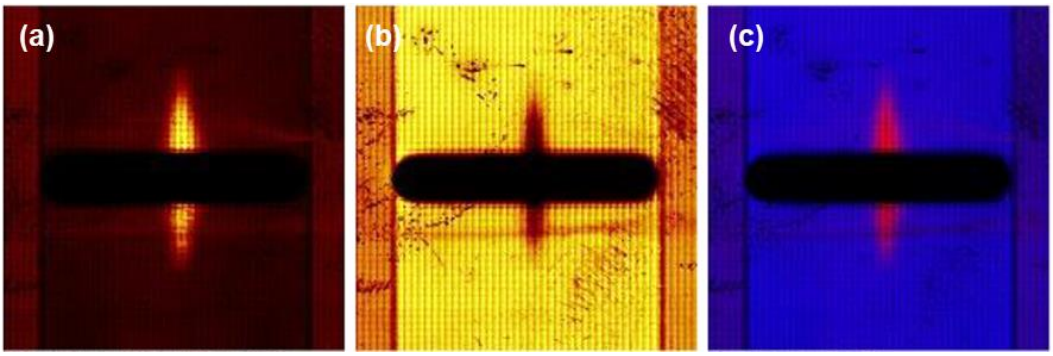

Figure 4.36: Image overlay of ToF-SIMS scan of 20x20 mm^2 of the aperture plate with shallow LIPSS features on the surface. (a) Bovine Insulin (summed image), (b) Stainless steel (summed image), (c) Bovine Insulin (red) & stainless steel (blue)
Spectrum parameter: Species Bi^{3+}, Area 20x20 mm^2, Polarity positive

The ToF-SIMS spectra for both nanopolish surfaces processed under argon and shallow LIPSS based surface were generated from a location within the area marked as the summed bovine insulin region in their image overlays shown in Figure 4.35 and Figure 4.36, respectively. This location was selected for further analysis as the protein residue is more concentrated in this area than the rest of the surface. The scan size was 400x400 μm^2. Figure 4.37 and Figure 4.38 show the positive ion polarity spectra generated for nanopolish and shallow LIPSS surfaces, respectively. Amino acid signal identifiers for bovine insulin (refer to Table 3.4) can be seen from the peaks in the spectra. The signal identifiers used for summation of bovine insulin are listed for both cases: CH_2N^+ (m/z: 28), CH_4N^+ (m/z: 30) [*Glycine*], $C_2H_6N^+$ (m/z: 44), $C_2H_6NO^+$ (m/z: 60) [*Serine*], $C_4H_8N^+$ (m/z: 70) [*Proline*], $C_4H_{10}N^+$ (m/z: 72) [*Valine*], $C_5H_{10}N^+$ (m/z: 84) [*Lysine*], $C_5H_{12}N^+$ (m/z: 86) [*Isoleucine/Leucine*], $C_5H_8N_3^+$ (m/z: 110) [*Histidine*], $C_8H_{10}N^+$ (m/z: 120) [*Phenylalanine*], and $C_8H_{10}NO^+$ (m/z: 136) [*Tyrosine*]. Carbonaceous contamination on each plate surface overlaps with the amino acid signals from the bovine insulin. The carbonaceous contamination was also noticed in the XPS results for these cases in the form of organic/polymeric materials in the core level spectra of C 1s. Thus the presence of protein/organic residue on the surface is confirmed using the ToF-SIMS results.

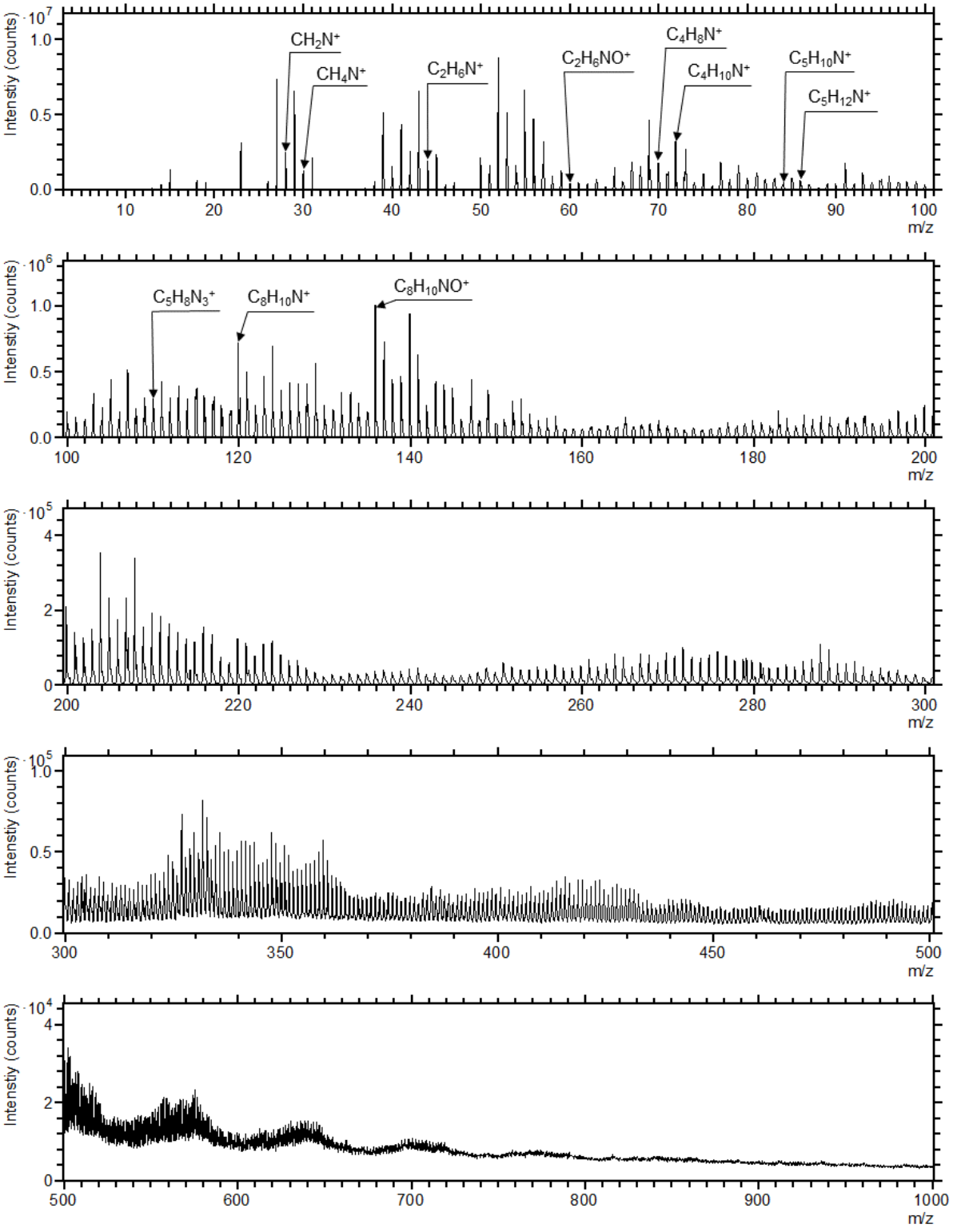

Figure 4.37: ToF-SIMS spectrum of nanopolish surface on aperture plate (processed under argon environment) highlighting the bovine insulin signal identifiers. The data was collected from a location within the ion beam collision region shown in the summed image of bovine insulin. Spectrum parameter: Species Bi^{3+}, Area 400x400 μm^2, Polarity positive

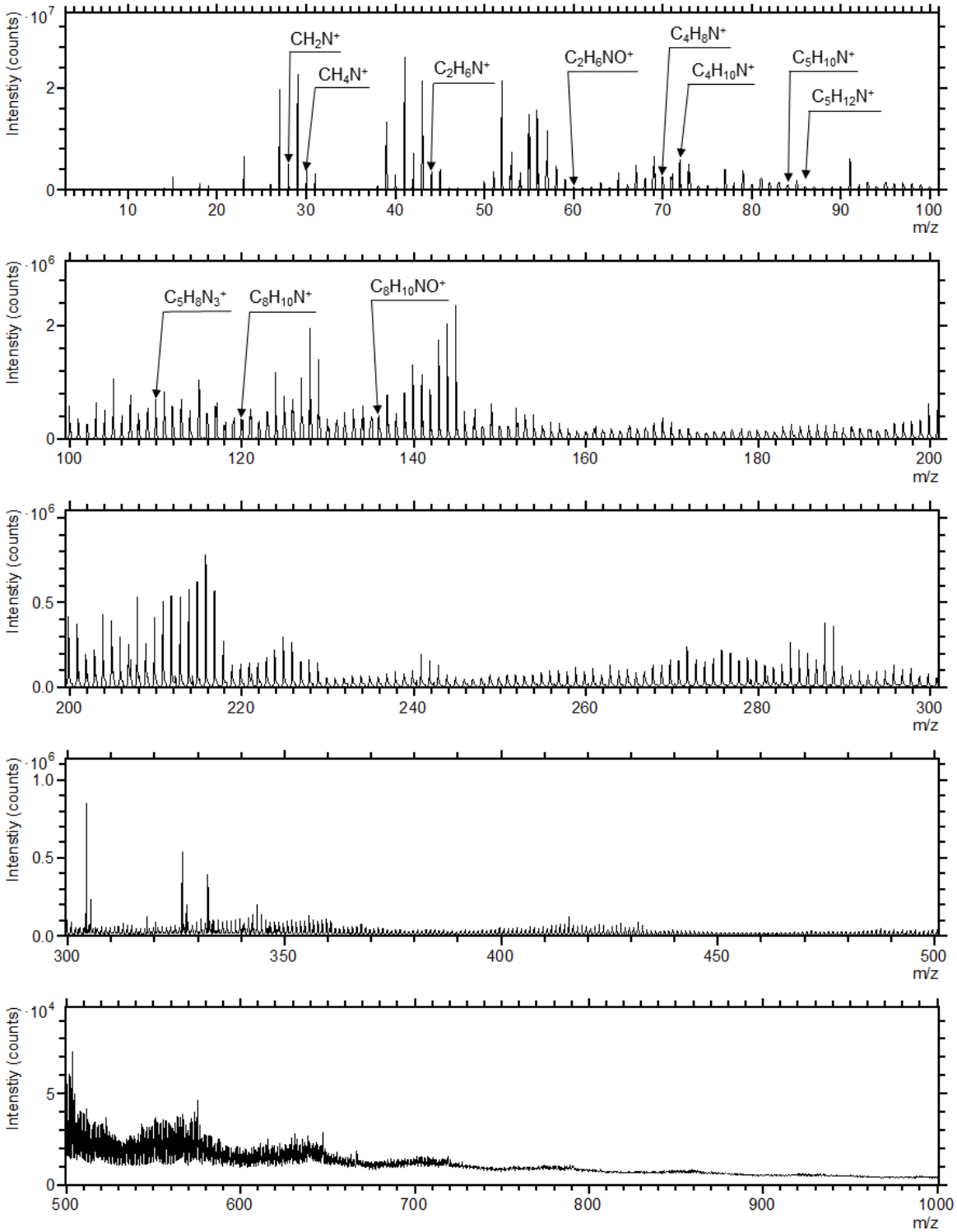

Figure 4.38: ToF-SIMS spectrum of shallow LIPSS surface on aperture plate highlighting the bovine insulin signal identifiers. The data was collected from a location within the ion beam collision region shown in the summed image of bovine insulin.

Spectrum parameter: Species Bi^{3+}, Area 400x400 μm^2, Polarity positive

4.5 Conclusion

The ablation mechanism of a 532nm nanosecond laser is mainly thermal due to the longer wavelength and the short pulse length (nanosecond). Both high fluence and low fluence laser processing were investigated to understand the features produced. The current research focus is on nano-scale features. Hence emphasis was given to laser induced features. LIPSS features were generated on the stainless steel 316L surfaces when the input fluences were maintained near or lower than the ablation threshold (1.71 J/cm^2). Control on the laser processing was demonstrated through nano-polished surfaces and shallow LIPSS surfaces generated at low fluences. The resultant surface roughness (Ra=2.8 nm for nanopolish and Ra=5.4 nm for shallow LIPSS) was lower than the native sample surface (Ra=10.5 nm). Also, the shallow LIPSS showed a lower aspect ratio (0.025) than the LIPSS generated with input fluence near the ablation threshold (0.038).

Nanopolish surfaces (processed in air and argon) and shallow LIPSS surface cases were reproduced on aperture plate surfaces. The protein contamination behaviour was tested on the laser processed aperture plates using the test rig at Waters Corporation. Shallow LIPSS and nanopolish surface (processed in the air) showed promising results in terms of surface charging compared to the reference electrode. Therefore, it can resist surface contamination better than the reference electrode. The other indicator of surface contamination, i.e. the resolution, however, showed mixed results. Both positive and negative resolution drift was observed during the analysis. Still, the present findings highlight that shallow LIPSS fared better than the other cases regarding resolution behaviour. But, due to the small result set, any conclusive trend cannot be established. Despite the limitations, these results demonstrate that laser processing affects the protein

contamination behaviour and can be considered for investigation in the future, especially the shallow LIPSS feature based surface.

Chapter 5

Picosecond Laser Processing Results

This chapter reports the results of the experimental investigation of the surface structures obtained on the stainless steel sample targets with the ultrashort pulse picosecond laser system. With a wavelength of 355 nm and 10 ps pulse length, this laser falls in the UV spectrum of light and shows primarily photochemical dominated laser ablation in the case of polymers while demonstrating precision ablation on metals. The effect of fluence, pulse overlap and the number of scans on the surface structure are discussed. Aperture plate electrodes were developed using selected cases of laser processing and investigated for protein contamination behaviour.

5.1 Optical characterisation

The laser system has a wavelength of 355 nm, a pulse length of 10 ps and a pulse frequency of 404.7 kHz, as described in section 3.2.2. The laser beam was linearly polarised, and the profile was analysed using the SEM micrographs of the laser ablation spots. The profile is elliptical with a low aspect ratio in shape. Figure 5.1 shows the

progression of the beam profile from high to low power. The minor axis width was used as the beam diameter to measure the ablation threshold and scan speed. The profile's major axis was used to determine the hatch distance during surface scans.

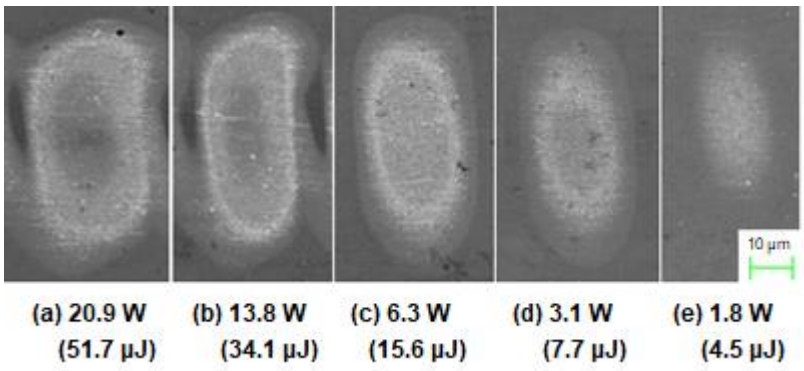

Figure 5.1: SEM micrograph of the laser spot on SS316L surface showing the effect of average power; Pulse energy mentioned in brackets; Laser: λ=355 nm, t_{laser}=10 ps, f_{laser}= 404.7kHz.

5.2 Surface texturing results

The aperture plate of Waters® is made from Stainless steel 316L, annealed and polished to surface roughness Ra = 7±2 nm. Due to the limited availability of an aperture plate, annealed and polished (Ra = 9±2 nm) SS316L samples from Goodfellow were used for the surface texture experimentation. The ablation threshold calculation was done on Goodfellow samples. Selected laser texturing cases were reproduced on the aperture plates and tested for protein contamination behaviour.

5.2.1 Ablation threshold fluence

Single-pulse laser ablation measurements were conducted to estimate the threshold fluence. Figure 5.2(left) shows the plot of the pulse energy vs crater diameter squared (D^2). The logarithmic-based curve fitting estimates the pulse energy threshold and the beam

radius (ω_0) to be 0.69 µJ and 11.85 µm, respectively. The threshold fluence (F_{th}) was estimated to be **0.32 J/cm^2** using the logarithmic curve fit in the plot of the fluence vs the crater diameter, as shown in Figure 5.2(right). The threshold fluence is in agreement with the literature [210]. Further, the threshold fluence for pulse overlap can be estimated based on section 3.5.1.3, and the plot is shown in Figure 5.3.

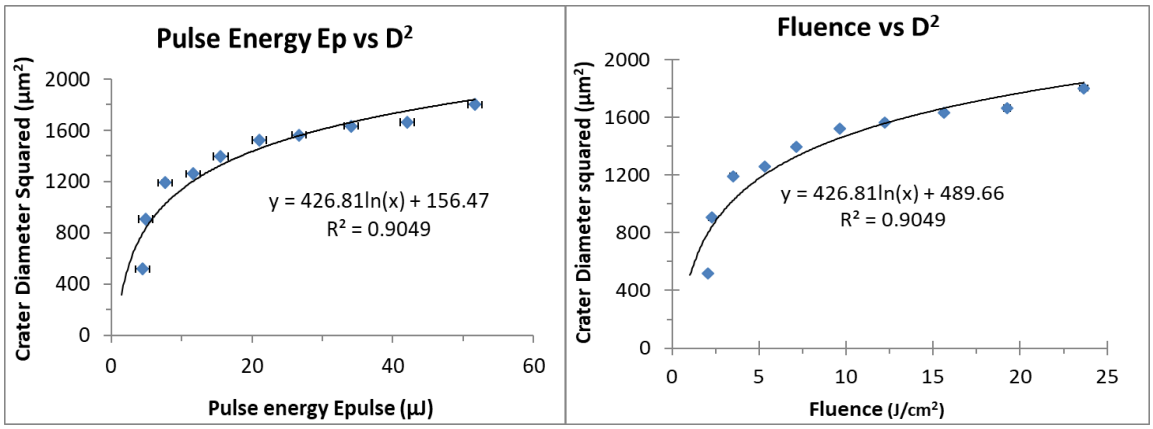

Figure 5.2: Plot showing deduction of ablation threshold through crater diameter method using SS316L samples from Goodfellow (laser: λ=355 nm, t_{pulse}=10 ps, f_{laser}=404.7 kHz) (left) to find threshold pulse energy; (right) to compute ablation threshold fluence

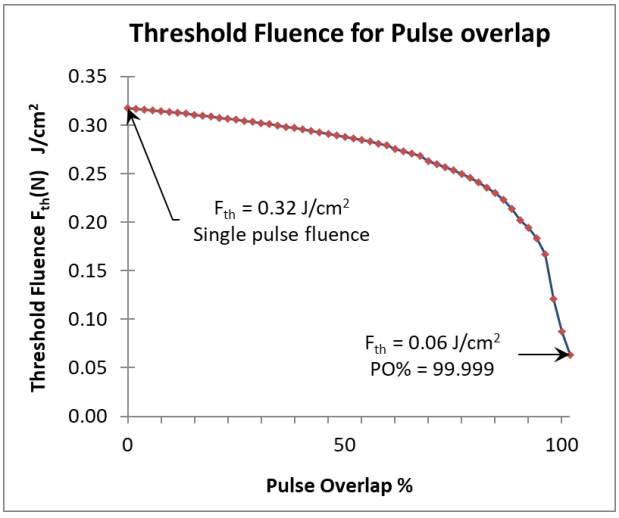

Figure 5.3: Plot of multiple pulse ablation threshold fluence (F_{th} = 0.32 J/cm^2)

5.2.2 Surface texturing in air

Laser processing was done in an air environment without any processing gas. The input fluence was maintained at 1.98±0.2 J/cm^2 (average power, P=1.8W), considering the beam diameter as 24±0.2 μm. The laser beam is elliptical with dimensions 24 μm (X-dir) and 52 μm (Y-dir), as shown in Figure 5.1(e). The experiments were designed considering this beam shape. The laser scan direction is X-dir, and hatch distance was considered in the Y-dir, as shown in Figure 3.20. Also, since the input fluence is higher than the threshold fluence (0.32 J/cm^2), the laser processing would induce gentle ablation of the material, and the ablation increases with higher pulse overlap. So, to reduce the material removed from the surface, the surface scans were done with a low pulse overlap percentage. Table 5.1 lists the selected scan speeds based on pulse overlap. The number of scans per area (***Nsc***) was kept between 1 and 18. The focus of the experiments was developing laser induced structures on the surface.

Table 5.1: Scan parameters for UV picosecond surface texture tests

Pulse Overlap %	Pulse-to-pulse distance Δx (μm)	Scan speed V_{SC} (mm/sec)	Hatch Distance Δy (μm)
5	22.8	9230	20
10	21.6	8740	20
30	16.8	6800	20

Laser-induced structures, notably LIPSS, developed for all the listed overlap percentages from Table 5.1. The confocal microscope scan of the surface textured region shows LIPSS over the surface (Figure 5.4), for Δx=16.8 μm, Nsc = 15, and at max accumulated fluence Fa^{max}=30.8 J/cm^2. The SEM micrograph of the same confirmed the presence of LIPSS having a periodicity of Δ_{LIPSS}=250±30 nm and valley width of 105±15

nm. The surface scan was further characterised using AFM to verify the aspect ratio of the scan. As shown in Figure 5.5, the AFM profile estimates the LIPSS features have a periodicity of Δ_{LIPSS}=250±30 nm, high peak-valley depth of 90±15 nm, and area roughness Sa=43.80 nm. The periodic structures were not correctly identifiable in the AFM scan image. HSFL features as interlinking bridges can be seen in the concave part of the LSFL features. The formation of the HSFL features with the concave regions of LSFL is due to the cavitation instability mechanism [142].

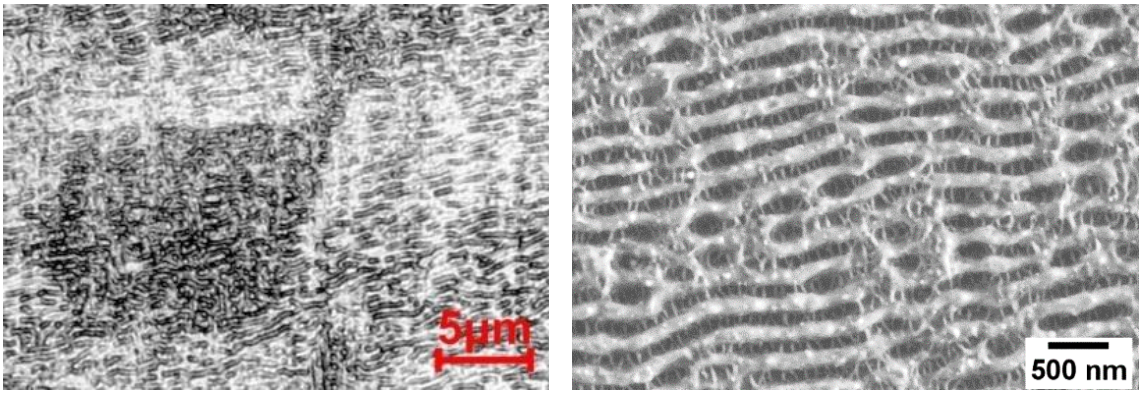

Figure 5.4: Image of surface produced with laser parameters F_0=1.98 J/cm^2, Δx=16.8µm, Δy=20µm, Nsc=15, and Fa^{max}=30.8 J/cm^2; (left) Optical scan & (right) SEM micrograph

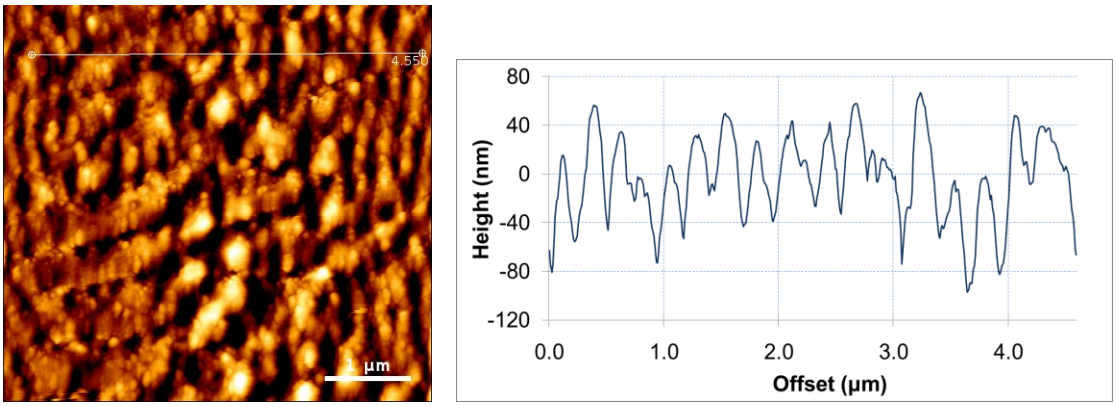

Figure 5.5: AFM scan of 5x5 µm from an area scan with Δx=16.8 µm, Δy=20 µm and Nsc=15 (left) AFM scan with a profile line drawn over the features; (right) plot of the profile.

5.2.3 Surface texturing in the air under the impact of laser plasma plumes

The next set of experiments focuses on the generation of HSFL structures. A novel method is discussed that potentially confines the free expansion of the laser plasma plume and utilises it as one of the impacting parameters to affect the growth of surface structure on the surface of stainless steel 316L workpiece.

5.2.3.1 Experimental procedure

The input fluence F_0=0.20±0.02 J/cm^2 at a frequency of f_{laser}=404.7 kHz was maintained throughout the study. The laser parameters of pulse-to-pulse distance (Δx), hatch distance (Δy) and the number of over-scans (Nsc) were varied in the range of 10 – 40 μm, 10 – 40 μm and 1 – 20, respectively, to identify cases of LIPSS structures. The line scans were performed on X-axis, and the hatch distance was applied on the Y-axis, as shown in Figure 3.20. First, tests with variations in laser parameters were conducted on a workpiece to identify a case of well-defined LIPSS features. The laser parameters of the selected test case were used to study the effect of obstruction on the expansion of the laser plasma plume on the growth of laser induced features. A borosilicate glass cover was used to obstruct the expansion of the laser plasma. The glass material has a transmissivity of ~90% at 355 nm wavelength. The glass cover was placed on the sample surface, as shown in Figure 5.6. The gap between the glass cover and the surface of the workpiece (Δz) was increased in steps over the workpiece surface using a Z-axis stage (gap width of ~0.3 μm to 1 mm). The growth of high spatial LIPSS features was primarily studied along with the formation of LSFL features at later stages. The laser surface textures were topographically characterised by scanning electron microscope (SEM) and atomic force microscopy (AFM) for imaging and profile measurements.

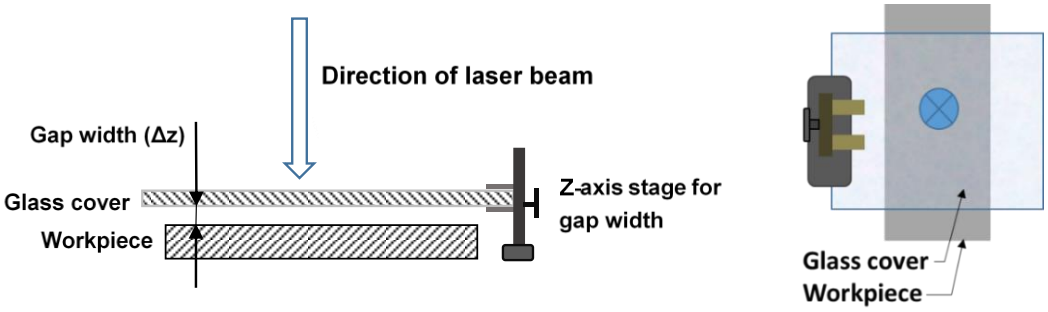

Figure 5.6: Section view of the substrate over sample setup (left); Top view of the setup. Here, the blue circle with the cross is the laser beam (right)

5.2.3.2 Identification of LIPSS structures for no-glass cover condition

Single pulse ablation measurements for input fluence of F_0=0.20±0.02 J/cm^2 show a spot diameter of 48 μm. The results obtained from modifying the laser parameters for the first step of the study show the presence of visual ablation for pulse-to-pulse distance (Δx) and hatch distance (Δy) less than 15 μm. Focusing on the cases with the presence of periodic structures, uniform low spatial frequency LIPSS features and sparse availability of high spatial frequency LIPSS features were observed for both Δx and Δy between 20 - 30 μm, i.e. 40 – 60% spot overlap at the number of over-scans (Nsc) between 14-19. The maximum accumulated fluence (Fa^{max}) was estimated using equation 3.13 [190].

The result for pulse-to-pulse distance Δx=23 μm and hatch distance Δy=20 μm is shown in Figure 5.7, with HSFL and LSFL features obtained at max accumulated fluence 1.5 J/cm^2 and 6.8 J/cm^2 respectively (input fluence F_0=0.19 J/cm^2). The HSFL based surface shows a LIPSS periodicity of 90±5 nm, and the LSFL based surface has LIPSS with a periodicity of 240±30 nm and a high peak-valley depth of 78±15 nm. LSFL surface also contains HSFL features within the LSFL features, showing a periodicity of 65±5 nm. The presented case was selected for investigating the effect of obstruction of free expansion of the laser plasma plumes using a glass cover over the surface of the workpiece.

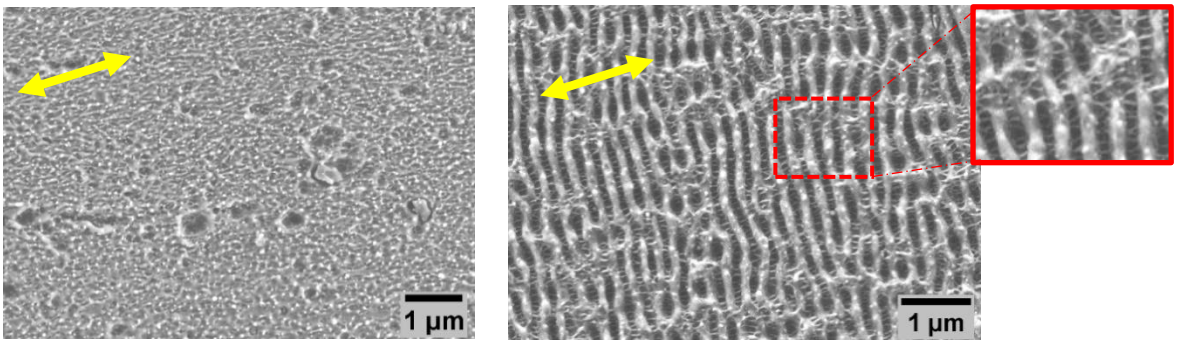

Figure 5.7: SEM micrographs of LIPSS features obtained for no-glass cover case (F_0=0.19 J/cm^2, Δx=23 µm, Δy=20 µm). The polarisation vector of the laser is shown as a yellow arrow; (left) HSFL features at Fa^{max}=1.5 J/cm^2; (right) LSFL features at Fa^{max}=6.8 J/cm^2

5.2.3.3 High spatial LIPSS features growth under glass cover condition

The impact of a glass cover over the sample surface was studied comparatively between with and without glass cover setups. The input fluence was F_0=0.20±0.02 J/cm^2, and the spot diameter was 48 µm. Figure 5.8 shows the growth of laser-induced features for Δx=23 µm, Δy=20 µm, N_{SC}= 8, and max accumulated fluence Fa^{max}=3.01 J/cm^2 for both cases with and without glass cover. The glass cover case (gap width Δz = 300 µm) shows the onset of LIPSS structures sparsely spread on the surface, Figure 5.9(a), along with complex bulb-like feature growth of sizes 100±20 nm, Figure 5.9(b). It highlights the possibility of creating features smaller than the LIPSS structures. However, the standard case shows the initial stage of LSFL features covered surface. It should be noted that the glass cover reduces the input fluence by 10-15% due to transmission losses and affects the formation of laser induced structures.

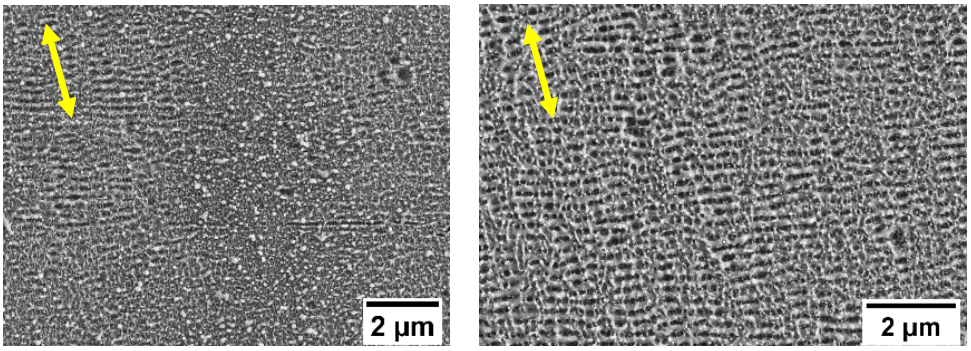

(a) With glass cover (Δz=300 µm) **(b) Without glass cover**

Figure 5.8: SEM micrograph of SS316L surface with laser processing with F_0=0.19 J/cm^2, Δx=23 µm, Δy=20 µm, and Nsc=8 (Fa^{max}=3.01 J/cm^2). The polarisation vector is shown with the yellow arrow.

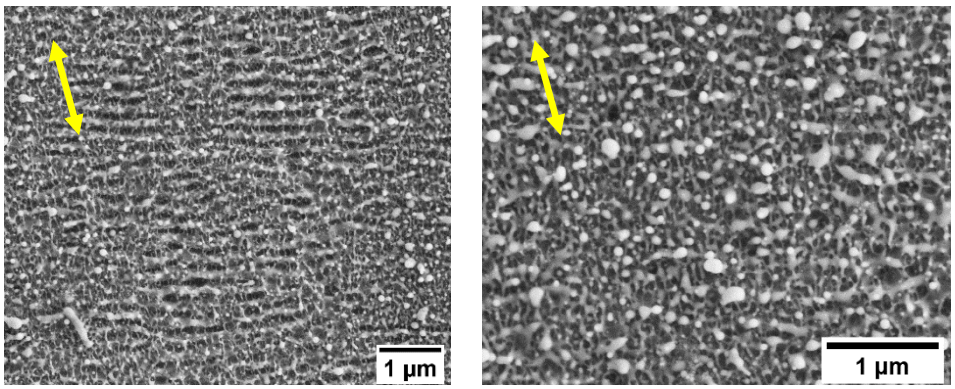

Figure 5.9: SEM micrographs of laser induced features seen at different locations on the surface. Laser processing was done with parameters F_0=0.19 J/cm^2, Δx=23 µm, Δy=20 µm, and Nsc=8 (Fa^{max}=3.01 J/cm^2), and with a glass cover over the sample surface at gap width Δz=300 µm. The polarisation vector is shown with the yellow arrow; (left) An onset of LIPSS can be seen on the surface; (right) bulb-like features are seen at a different location.

The glass cover case displayed the possibility of creating small nanoscale features on the surface. Figure 5.11 explains the growth of nano-scale features on the surface for F_0=0.20 J/cm^2, Δx=23 µm, Δy=20 µm, and gap width Δz = 450 µm for a number of scan repetitions N_{SC} from 1 to 18. The effect of laser processing can be noticed from Nsc=3 (Fa^{max}= 1.13 J/cm^2), as the surface shows initial signs of surface modifications without any distinguishable features. HSFL features are noticed from Nsc=4 to 7. Figure 5.10 shows

the periodicities of the identified HSFL features at to their max accumulated fluences. The surface structures begin to be prominent from Nsc=4 (Fa^{max}=1.51 J/cm^2), as a spurt of high spatial frequency LIPSS (HSFL) like features is observed over the entire scan region. The periodicity (Δ_{LIPSS}) of the features is 82±7 nm and the width of the valleys is 25±5 nm. The feature growth continues, and high density shallow HSFL features are noticed in the Nsc=5 (Fa^{max}=1.89 J/cm^2 and HSFL Δ_{LIPSS}=80±10 nm). On increasing the scan count, the accumulated fluence per spot increases and the effect is noticed in the depth of the HSFL in the case shown in Nsc=6 (Fa^{max}=2.37 J/cm^2 and HSFL Δ_{LIPSS} = 88±15 nm). With further increase in the scan count, the HSFL features start to disintegrate due to more fluence in the region, and the features are less indistinguishable from Nsc=7 (Fa^{max}= 2.64 J/cm^2 and HSFL Δ_{LIPSS}=82±8 nm), and nano bulb-like features appear later on. These features appear early in the scan count with higher pulse overlap, as demonstrated in Figure 5.9(d). The bulb-like features are likely to cause high scattering of the laser beam, causing increased interference with the incoming beam and likely to develop into low spatial frequency LIPSS. The light interference-based approach for explaining LIPSS formation is already studied in the literature. The growth of laser-induced structures continues, and well-formed low spatial frequency LIPSS (LSFL) features are observed from Nsc=13 (Fa^{max}= 5.16 J/cm^2) onwards. The hair-like HSFL features are again observed from Nsc=15 (Fa^{max}= 5.65 J/cm^2) onwards and are well-formed by Nsc=18 (Fa^{max}= 6.8 J/cm^2). The periodicity of the LSFL features is 215±15 nm, and the width of the valleys is 75±10 nm. Melt pools are noticed on the surface at high scan counts, and their size increases with the scan count. However, the formation of the melt pools is not noticed in the standard case scenario (without glass cover), hinting towards the accumulation of high-pressure plasma plume near the surface and increased material ablation.

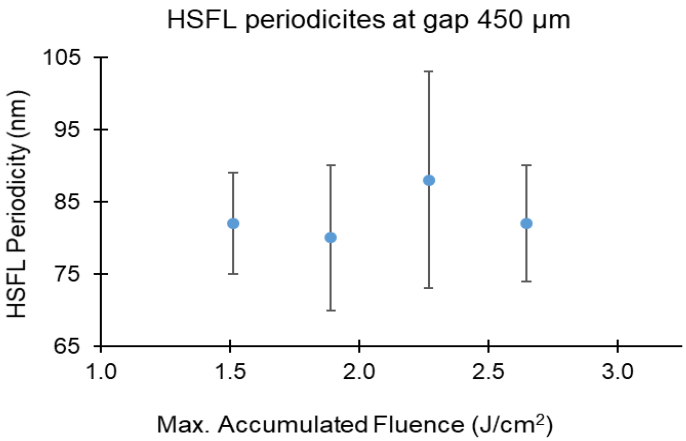

Figure 5.10: Graph of HSFL features periodicities at a gap width of 450 µm

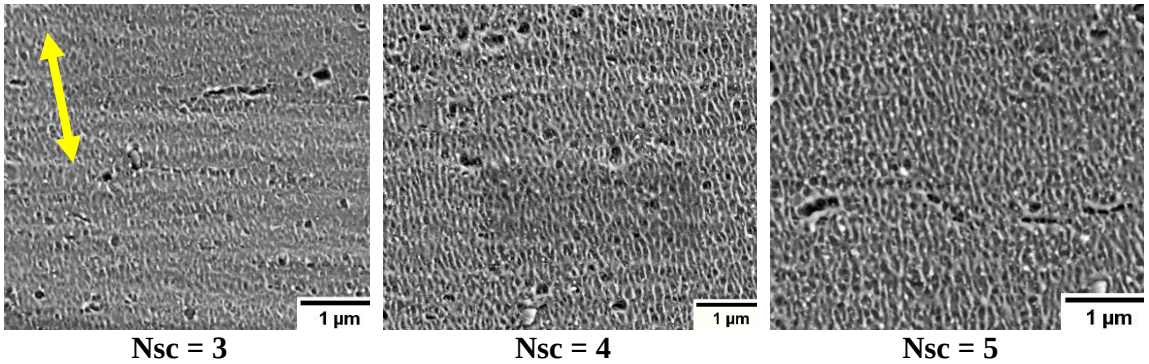

Nsc = 3 **Nsc = 4** **Nsc = 5**

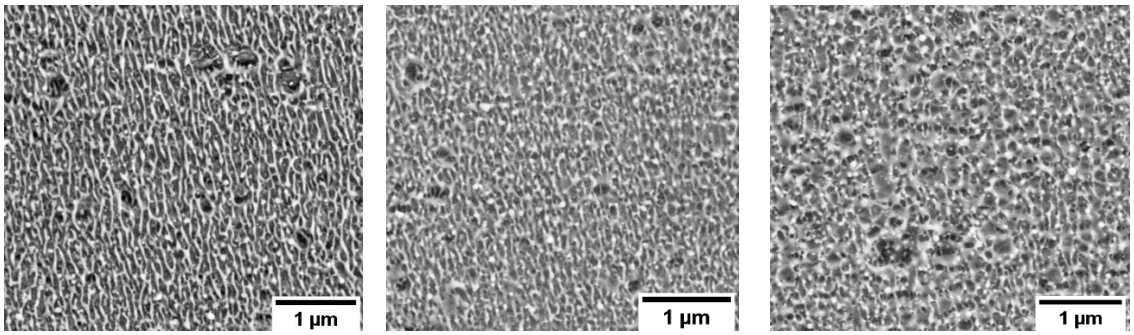

Nsc = 6 **Nsc = 7** **Nsc = 8**

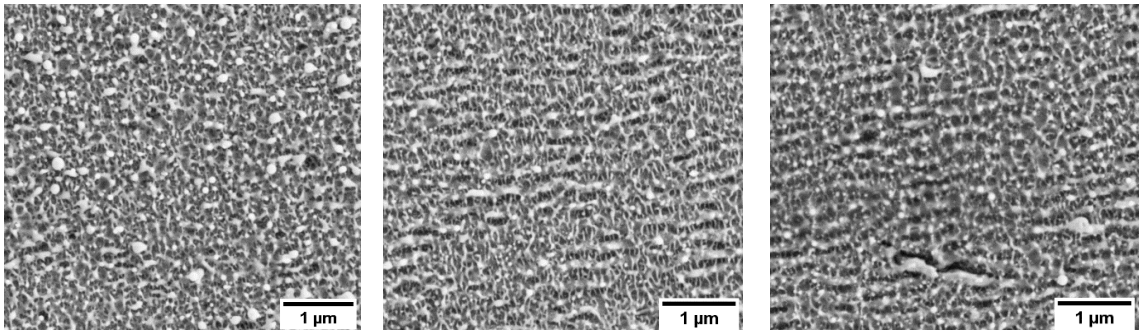

Nsc = 9 **Nsc = 10** **Nsc = 12**

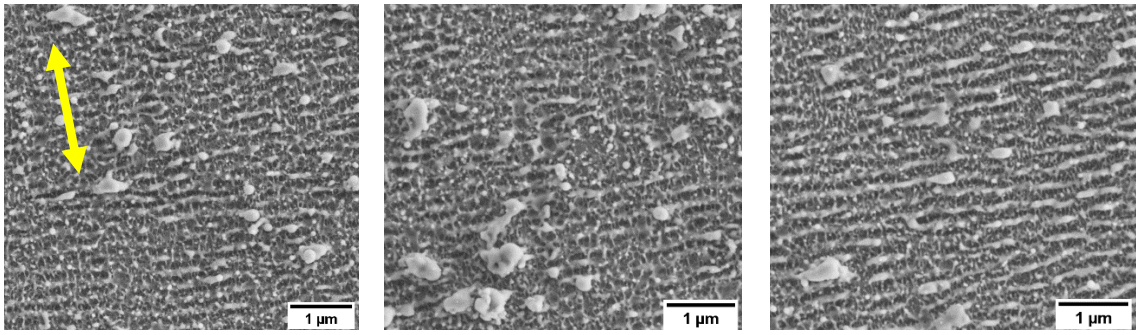

Nsc = 13 **Nsc =15** **Nsc = 18**

Figure 5.11: SEM micrographs showing growth of features under glass cover from HSFL to LSFL features (laser parameters: F_0=0.20 J/cm^2, Δx=23 µm, Δy=20 µm, Δz=450 µm). The scan count (Nsc) is mentioned for each SEM micrograph. HSFL features are visible from Nsc=4-7. Initial signs of LSFL features are visible from Nsc=10-12. LSFL features and melt pools appear from Nsc=13 onwards. The polarisation vector is the yellow arrow.

5.2.3.4 Impact of glass cover gap width on HSFL features

A higher occurrence of HSFL features was noticed after adding a glass cover on the surface of the workpiece, as compared to the case with no glass cover. HSFL features were primarily observed in the max accumulated fluence between 1.2 J/cm^2 and 3.1 J/cm^2 for the laser parameters of pulse-to-pulse distance Δx=23 µm and hatch distance Δy=20 µm. However, for the same input laser parameters, periodicities of HSFL features changed by varying the gap width between the sample and the glass cover. Figure 5.12 presents the observed HSFL features with their estimated periodicities for the different gap width conditions. The periodicity of the features was observed to be high for low gap widths, such as an average periodicity of around 90 nm at the gap width region until 300 µm. AFM analysis on the surface demonstrated a roughness average Ra=11 nm and peak-to-valley depth of 35±10 nm. The periodicity of the HSFL features is reduced with the increase in the gap width, and the average periodicity stands around 75 nm. Figure 5.13 shows the comparative HSFL features at the max accumulated fluence of 2.27 J/cm^2 at gap widths

300 and 750 µm, with a periodicity of 90 and 75 nm, respectively. Nano-bubbles can be observed on the HSFL feature at a gap width of 300 µm. With increasing gap widths, the occurrence of HSFL features is also reduced.

Low spatial frequency LIPSS (LSFL) features were obtained at higher fluence regions between 5.6 J/cm^2 and 6.8 J/cm^2. The periodicity of the features was 215±20 nm, and the width of the valleys was 75±15 nm. Similar to the no-glass cover case, bridge-like HSFL features formed within the LSFL features show a periodicity of 60±10 nm. Also, the formation of melt pools was noted on the surface at smaller gap widths, and the frequency of the melt pools increased with the increase in the accumulated fluence. The formation of the melt pools was not seen in the standard case scenario, i.e. without the glass cover.

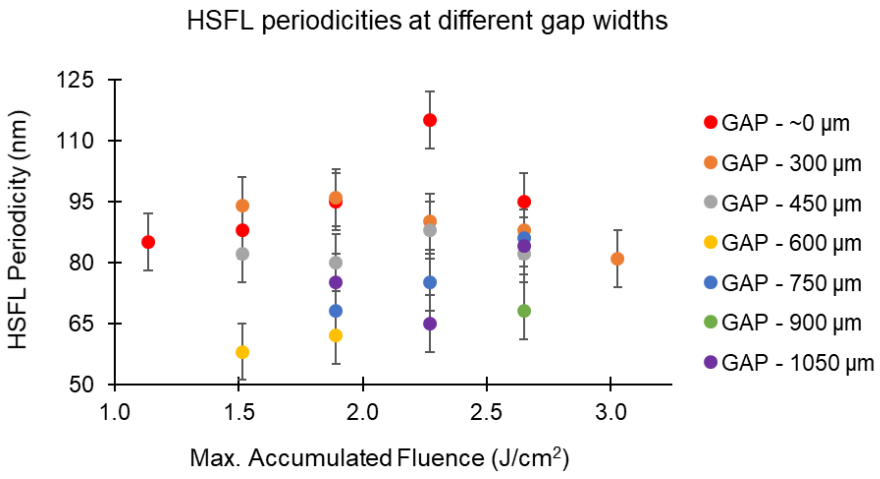

Figure 5.12: Plot of periodicities of the HSFL features observed at max accumulated fluence for different gap widths.

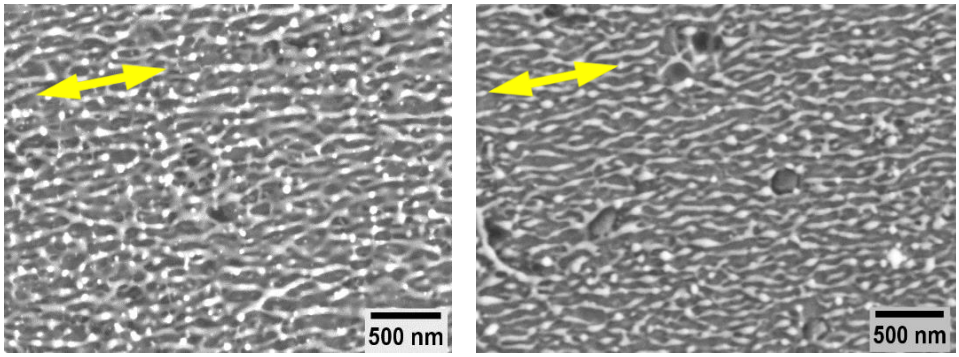

Figure 5.13: SEM micrograph of HSFL features formed at different gap widths for Fa^{max}=2.27 J/cm^2. The polarisation vector is the yellow arrow; (left) 300 µm gap with Δ_{LIPSS}=90±20 nm. Contains nano-dots on peaks; (right) 750 µm gap with Δ_{LIPSS} = 75±15 nm.

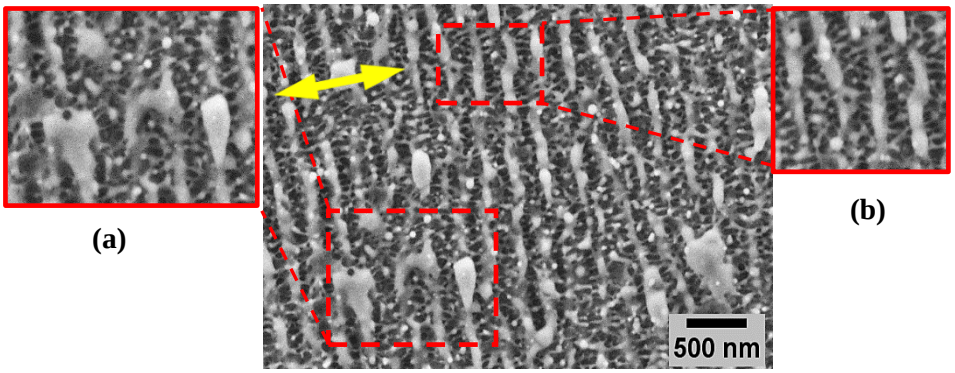

Figure 5.14: SEM micrograph showing LSFL features obtained at a gap width of 300 µm at Fa^{max}=6.8 J/cm^2. The polarisation vector is shown in yellow. LSFL features periodicity Δ_{LIPSS}=215±20 nm; (a) Accumulation of dross-like features over the surface; (b) Cross-linking bridge-like HSFL features with Δ_{LIPSS} = 60±10 nm.

The study shows that by blocking the free expansion of the laser plasma plumes with a glass cover over the surface of the workpiece, the growth of surface structures can be altered. High spatial frequency LIPSS structure growth was promoted on the surface for the same laser parameters compared to the standard case scenario of no-glass cover. Also, the periodic feature properties, such as the periodicity and the peak-to-valley depth, can be controlled to some extent.

High spatial frequency LIPSS structures are shallow compared to low spatial frequency LIPSS structures. Hence, HSFL features are helpful in applications with the need for shallow laser features at the nano-scale, such as functionalising the surface of the electrode in a mass spectrometer to improve the resistance to contamination.

5.2.4 Discussion of results: Picosecond laser processing

The picosecond laser (λ=355nm, t_{pulse}=10ps, f_{laser}=404.7kHz, linear polarisation) used for the research is a high-power laser. The ablation threshold was estimated at 0.32 J/cm^2 using the graphical-based approach for the polished SS316L samples. Laser induced features were generated by controlling the laser parameters, i.e. fluence, pulse-to-pulse distance, hatch distance and the number of over scans. Low spatial frequency LIPSS (LSFL) were obtained at a max accumulated fluence of around 31±3 J/cm^2. The peak-to-valley depth of the LSFL features is high considering the size of the contaminant, i.e. bovine protein, and so the method to generate shallow features such as high spatial frequency LIPSS (HSFL) was studied.

A novel method was developed to generate uniform laser induced features using the laser plasma plume as one of the impacting parameters. The novel method involved using a transparent medium such as glass to cover the sample surface and obstruct the free expansion of the laser plasma plume. If the high temperature plasma plume can be reflected on the surface, it increases the surface temperature and reduces the ablation threshold. A lower ablation threshold affects the laser-surface interaction and generation of laser induced features. The experimental results affirm the hypothesis as HSFL features at different periodicities were obtained for the same laser processing parameters and only varying the gap between the sample surface and the glass cover. The effect of the plasma

plume was studied in the literature [98,211–216]. It can be seen from the literature that the input fluence highly affects the generation of the laser plasma plume, and the plume has almost 10-15% of the input fluence energy. The fluence is also affected by other laser processing parameters.

In our study, the input fluence used is very low (0.20±0.02 J/cm^2) compared to the previous research in the literature, so it significantly affects the size of the generated plasma plume. Since the plasma plume has gas velocities around 5000-7000 m/s [211,217], it will likely reflect from the glass cover over the sample surface if the gap width is small. For example, for the gap width of 300 μm, the plasma only requires 0.52±0.08 ns to reach the glass cover, so in less than 1.2 ns, the plasma spreads back on the sample surface. Moreover, our laser's pulse-to-pulse time is ~2.4 μs (laser frequency is 404.7 kHz). It provides enough time for the plasma to spread over the surface before the next laser pulse, affecting the surface properties. In the cases of increased over scans Nsc=13-18, the melt pools were noticed on the surface, and LSFL features indicate higher ablation and ejection of material from the surface. The ejected material does not escape freely as in the case of standard laser processing in the air but seems to be circulating with the plasma plume and coagulating as melt pools. The analytical modelling of the plasma plume expansion for the studied case is needed to understand the flow of the plasma plume over the surface. However, the discussed novel method provides a direction to create HSFL sized features on the surface.

5.3 Laser processing of aperture plate electrodes

The aperture plates were laser processed with selected cases of LSFL and HSFL features identified earlier during our picosecond laser texturing experimentation investigation. These laser processed aperture plates were tested for protein contamination behaviour using bovine insulin protein (having a diameter of ~2.5 nm) in the test rig based on the mass spectrometer.

5.3.1 Aperture plate with LSFL features (processed in the air)

The laser parameters for processing the aperture plate were input fluence of 1.98±0.2 J/cm^2, pulse-to-pulse distance Δx=18 μm and hatch distance Δy=20 μm. Low spatial frequency LIPSS (LSFL) features were obtained at a number of over scans Nsc=12 and above. The laser beam was linearly polarised with a beam diameter of 24 μm was used for processing the aperture plate in an air medium. Figure 5.15 shows the SEM micrograph of LSFL features with periodicity 253±6.8 nm on the aperture plate surface. These LIPSS features were obtained at number of over scans Nsc=13, i.e. at the max accumulated fluence Fa^{max}=26.4 J/cm^2. Nano-interlinking bridges are seen in the cavity region of the LIPSS features and nano-dots of diameter 42±3 nm on the LIPSS peaks. The AFM scan (Figure 5.16) confirms the peak-to-valley depth of 59±10.5 nm, average profile roughness Ra=14.52±3.22 nm, and area surface roughness Sa=22.35±0.51 nm. The presence of nano-dots can induce errors in estimating the peak-to-valley in the AFM scan since the structures are not adequately identifiable in the AFM compared to the SEM micrograph. Laser induced periodic structures are visible in the scan.

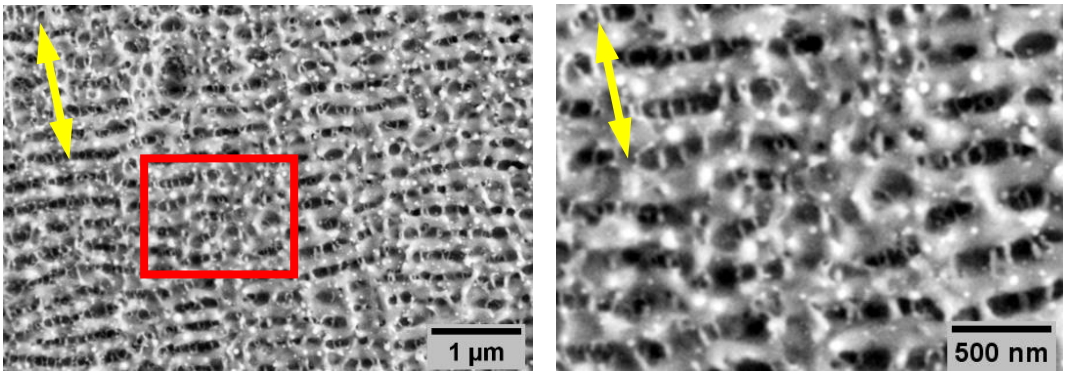

Figure 5.15: SEM micrograph of LSFL features on aperture plate surface processed with F_0=1.98 J/cm^2, Δx=18 µm, Δy=20 µm, Nsc=13, and Fa^{max}=26.4 J/cm^2. A yellow arrow represents the polarisation vector; (left) LSFL surface with a region of interest in red; (right) a magnified view of the surface showing embedded inter-linking bridges in the LSFL cavities and nano-dots on LSFL peaks.

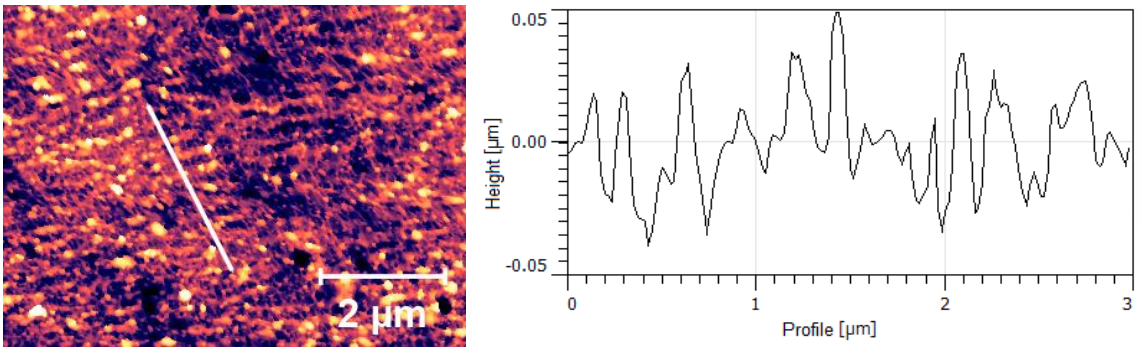

Figure 5.16: AFM scan of LSFL features at Δx=18 µm, Δy=20 µm, and Fa^{max}=26.4 J/cm^2. (left) AFM scan with profile line in white; (right) the plot of the profile line on the AFM scan.

5.3.2 Aperture plate with HSFL features (processed with glass cover)

High spatial frequency LIPSS (HSFL) features based surface was generated on the aperture plate surface using an input fluence of 0.22±0.01 J/cm^2, pulse-to-pulse distance Δx=22 µm, hatch distance Δy=20 µm and spot diameter 48 µm. The novel method for creating laser induced features, such as HSFL features as discussed in section 5.2.3, was used in processing the aperture plate surface. The novel method uses a glass cover over the

sample surface to obstruct the free expansion of the laser plasma plumes and impact the surface properties. The experiment was done with a gap width of 0.3 µm (glass cover almost over the surface of the aperture plate). HSFL features were obtained at 1.30 to 2.27 J/cm^2. Figure 5.17 shows the laser processing result at max accumulated fluence Fa^{max}=1.82 J/cm^2 (Nsc=4). HSFL features with periodicity 95±18 nm, along with nano-dots on the HSFL peaks, are observed in the SEM micrograph. The AFM analysis of the surface reveals the peak-to-valley depth as 24.1±3.6 nm, average roughness Ra=9.0±0.9 nm, and area roughness Sa=9.6±0.4 nm. The AFM analysis image (Figure 5.18) confirms the presence of nano-dots on the surface. The presence of nano-dots can induce errors in estimating the peak-to-valley height and surface roughness values, as the height of these nano-dots is not identifiable.

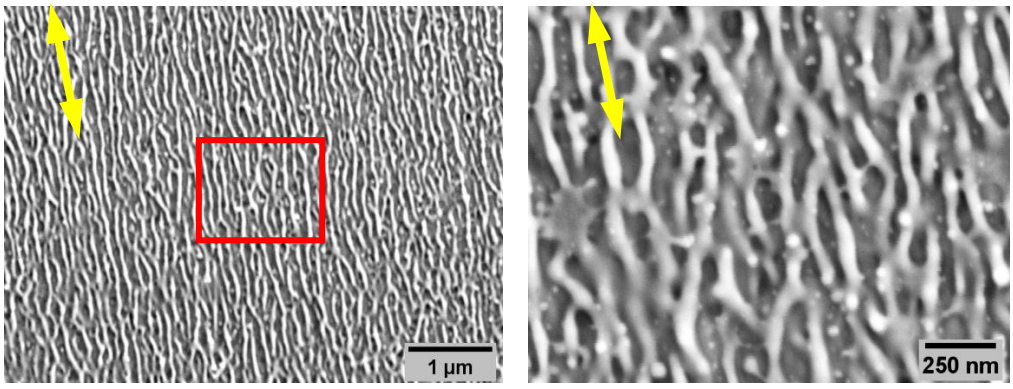

Figure 5.17: SEM micrograph of HSFL features on the surface processed with F_0=0.22 J/cm^2, Δx=22 µm, Δy=20 µm, Nsc=4, and Fa^{max}=1.82 J/cm^2. Polarisation vector as the yellow arrow; (left) HSFL features on the surface with the region of interest marked in red; (right) Magnified image of the region.

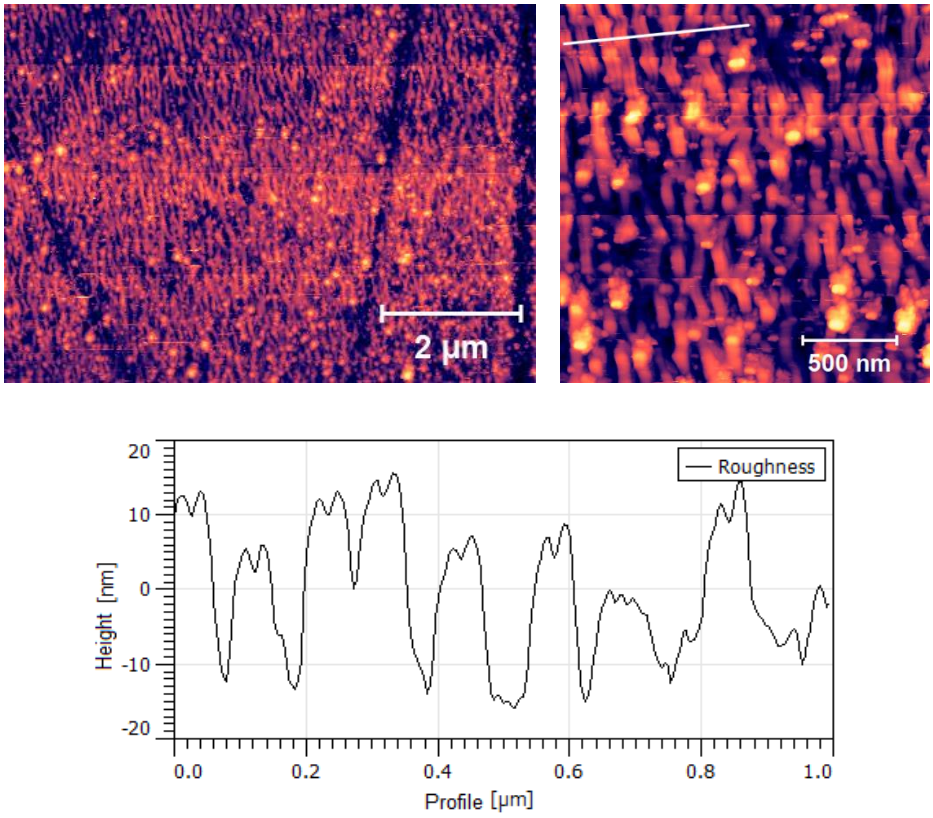

Figure 5.18: AFM scan of HSFL features on surface processed with F_0=0.22 J/cm^2, Δx=22 µm, Δy=20 µm, Nsc=4, and Fa^{max}=1.82 J/cm^2; (top row) AFM scan with different magnification showing HSFL features on the surface. Nano-dots can be seen on the surface; (bottom row) plot of the profile line in white drawn on AFM scan.

5.4 Protein contamination behaviour of laser processed aperture plates

The laser processed aperture plates were experimented with for protein contamination behaviour in the test rig at the Waters facility. The experimental process parameters and the methodology, as explained in section 3.6.1 above, were consistent for all the aperture plates. The data set for resolution and surface charging obtained from the test rig were analysed to understand the behaviour of the plates towards protein adsorption. After protein testing, the surface composition was analysed using XPS. The XPS was

conducted away from the slot to understand the surface composition. The presence of protein contamination on the surface was done using ToF-SIMS on the aperture plates' ion beam facing side. ToF-SIMS was done in the region where the ion beam collides with the surface to verify the surface contaminants, i.e. bovine insulin protein residue.

5.4.1 Results of protein contamination behaviour tests

The experimentation consisted of running cycles of 120 sweeps of the instrument. Here, the 'sweep' is the custom term for a pre-set calibration test used by Waters (refer to section 3.6.1). The optimum (maximum) resolution and surface charge were recorded to qualitatively compare and demonstrate the protein contamination behaviour of the aperture plate electrode.

5.4.1.1 Surface charging of the aperture plates

The **surface charge profile** is plotted for the laser processed surface containing LSFL features (Figure 5.19) and HSFL features (Figure 5.20). All the plots are done with a moving average of 5; hence, it is presented from sweeps 5-120. The test cycles shown in the surface charge profile plots were done consecutively on the aperture plate, such as in the order 'UV1', 'UV2', 'UV3', and 'UV4' for the LSFL case (Figure 5.19). A short gap was introduced between cycle runs without venting the instrument.

All the profiles follow a gradual increase of surface charge trend, similar to those observed in the reference electrode (Figure 3.22) and the nanosecond laser processed plates (section 4.4.1.1). It indicates a potential insulating layer build-up on the surface, even for picosecond laser processed plates. The profile plots also demonstrate that the insulating layer falls from the surface in the gap between the two cycles and even during the test run

cycle. The HSFL case (Figure 5.20) follows a trend similar to the nanopolish in the air (Figure 4.25) and the shallow LIPSS (Figure 4.27) cases, where the slopes of the cycles are considerably similar. On the other hand, the LSFL case highlights the possibility of surface contamination staying on the surface for a longer time. It can be noticed that 'UV2' almost starts with the voltage offset from where 'UV1' ends and similarly for the other cycles. Also, the fall and build-up of the insulating layer are more prominent in the later cycles in the LSFL case, such as the test cycle 'UV4'. The rapid rise and fall of the voltage offset can result from faster contamination build-up and then fall due to the inability to sustain the weight. It indicates two possibilities, i.e. the surface topography is conducive for the protein ions to stick, and the protein ions are weakly connected to the surface. These possibilities also give a high probability of protein ions being connected to the surface by the physical surface adsorption phenomenon.

The surface charge trend was quantified using the slopes of the profile, as presented in Table 5.2. The slope here is the charging rate of the aperture plate, measured in mV/sweep and calculated using the sweep data from 21-120 only. The initial 20 sweeps were skipped as they are considered the instrument's settling-in period. Compared with the slope data for the reference electrode (9.21 mV/sweep), picosecond based plates with charging rates of 5.30 mV/sweep (LSFL surface) and 6.67 mV/sweep (HSFL surface) fare better. Also, the HSFL case has a very low deviation and shows a more stable charging profile.

Hence, the surface of the laser processed plates seems more resistant to protein adsorption than the reference plate's surface, even though contamination still occurs in all these plates. Thus, based on the current results, it may be stated that laser processed plates show an improvement in surface charging.

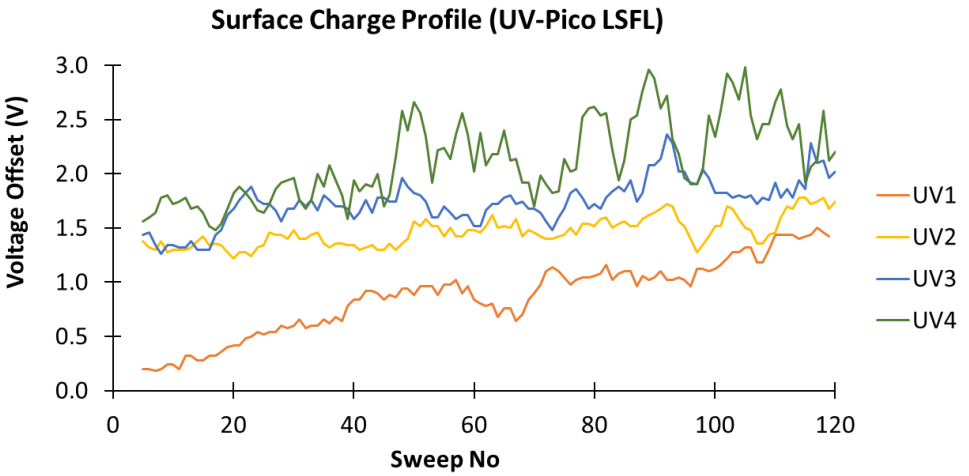

Figure 5.19: Plot of the surface charge profile of LSFL features based surface. The voltage offset is the difference in the end voltage from 17V.

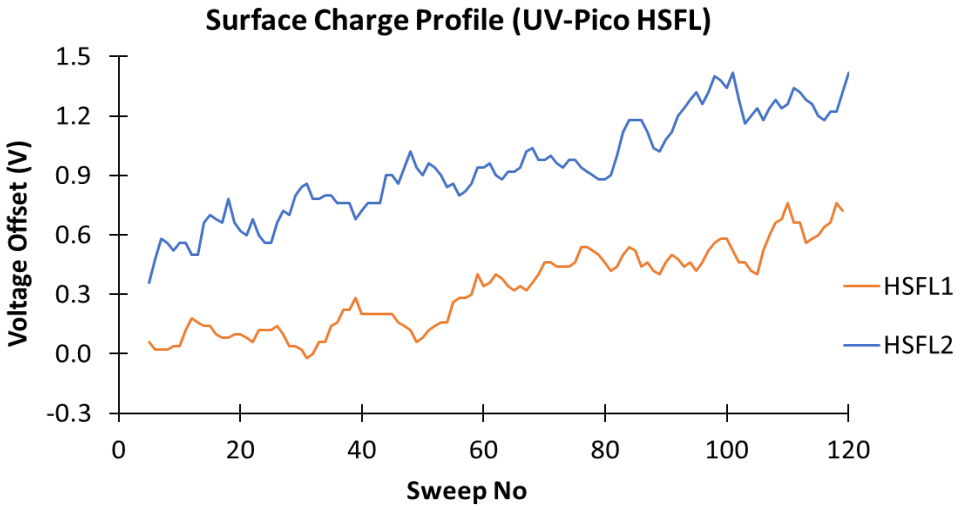

Figure 5.20: Plot of the surface charge profile of HSFL features based surface.

Table 5.2: Surface charging profile for picosecond laser processed aperture plates

Description	Experiment No	Max Offset Charge (V)	Charging Rate (Slope) (mV/Sweep)	Average charging rate (mV/Sweep)	Std. Deviation σ (mV/Sweep)
Reference electrode*	Ref 1	1.72	6.94	9.21	3.20
	Ref 2	1.88	11.48		
Laser – LSFL LIPSS case	UV1	1.50	8.27	5.30	2.74
	UV2	1.78	3.03		
	UV3	2.36	2.93		
	UV4	2.98	6.99		
Laser – HSFL case under glass	HSFL1	0.76	6.42	6.67	0.35
	HSFL2	1.42	6.91		

* refer Table 3.5 and section 3.6.2 for details on reference electrode.

5.4.1.2 Effect on the resolution of the instrument

The **optimum (maximum) resolution** allows us to understand the instrument's stability during one test run cycle of 120 sweeps. It can be considered another indicator of understanding protein contamination behaviour. The profile plot of the resolution vs sweep is done using the sweep data from 1 to 120, as the resolution information is obtained from the instrument directly. The resolution data profile of the test cycles for LSFL based surface (Figure 5.21) and HSFL based surface (Figure 5.22) is shown below. It is noticeable from the profile plots that the optimum/maximum resolution mainly decreases during the test cycle run. However, it does not follow a distinct trend, as seen in the surface charge profile.

The first 20 sweeps are considered the settling-in period of the test cycle run and are skipped from the resolution drift rate calculation. The resolution drift rate, i.e. the slope of the resolution profile, is measured as resolution/sweep and is dimensionless. Table 5.3 list the resolution drift rates for the picosecond laser processed aperture plates for each test

cycle run and the reference aperture plate electrode. The average resolution drift for the laser processed plates is relatively high (-14.64 and -12.96) compared to the reference electrode (-2.4). The results suggest that even though the surface charging is lower than the reference electrode, a faster resolution drift will likely affect the instrument sensitivity in the long run.

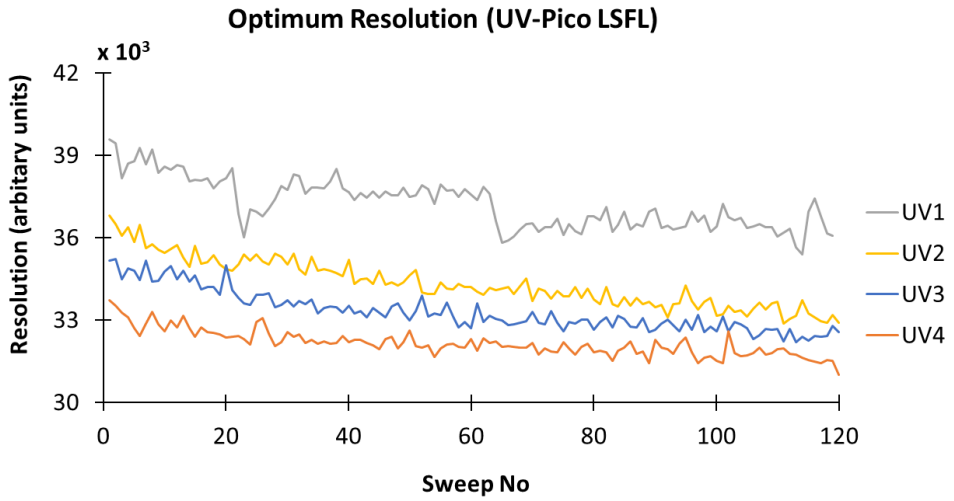

Figure 5.21: Plot of resolution profile of picosecond processed aperture plate surface with low spatial frequency LIPSS (LSFL) features.

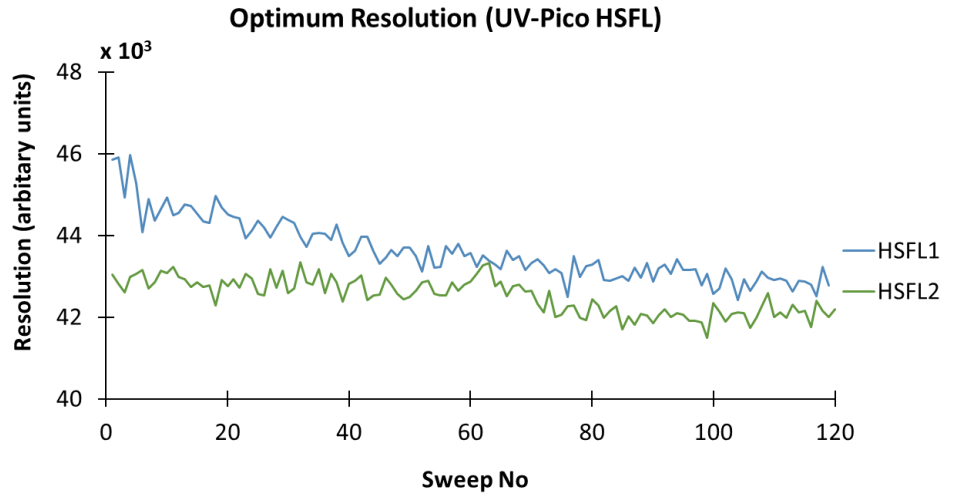

Figure 5.22: Plot of resolution profile of picosecond processed aperture plate surface with high spatial frequency LIPSS (HSFL) features.

Table 5.3: Trend of the optimum resolution for picosecond laser processed aperture plates

Description	Experiment No	Average resolution in each cycle	Resolution drift rate (Slope) (resolution/sweep)	Avg. resolution drift rate (resolution/sweep)	Std. Deviation σ (resolution/sweep)
Reference electrode*	Ref 1	44753.86	-7.21	-2.4	6.80
	Ref 2	41230.64	2.41		
Laser – LSFL LIPSS case	UV1	36946.86	-16.44	-14.64	5.44
	UV2	34060.86	-21.04		
	UV3	33053.20	-12.90		
	UV4	32012.94	-8.19		
Laser – HSFL case under glass	HSFL1	43364.56	-14.99	-12.96	2.87
	HSFL2	42435.47	-10.93		

* Please refer to Table 3.6 and section 3.6.2 for details on the reference electrode.

5.4.1.3 Protein testing behaviour: Summary

The surface charge and resolution results show the trend of the contamination build-up on the aperture plate and the overall instrument stability during the instrument's operation time. Both the picosecond cases show improved behaviour towards surface charging. But, the optimum resolution drifts faster than the reference electrode. Also, the number of test cycles tested is low and needs more data to understand the difference in the contamination behaviour between LSFL and HSFL feature based aperture plates. However, the results prove that picosecond laser processing on the aperture plate affects protein contamination behaviour, which gives us a direction to explore further in this regard.

5.4.2 XPS results: Surface chemistry analysis after protein testing

The surface chemistry of the aperture plate with HSFL features was analysed using XPS to ascertain the changes in the surface due to laser processing. A location away from the slot on the aperture surface was analysed to understand the surface composition. The results contain the wide area survey spectrum and the core level spectra of various elements. The XPS analysis was conducted through Lucideon Ltd.

The survey spectrum, shown in Figure 5.23, highlights the identified primary peaks of the elements along with carbon and oxygen. It was recorded with a pass energy of 160 eV at a step size of 1 eV. The components of stainless steel 316L identified in the survey spectra are iron (9.51%), chromium (7.19%), nickel (0.64%), molybdenum (0.22%), manganese (0.31%) and phosphorous (0.06%). The values are presented in atomic weight percentages. Apart from that, there is carbon (26.04%), oxygen (54.22%) and nitrogen (0.39%). A significant change in the percentage of iron and chromium for the nanopolish surface compared to the reference electrode surface (iron: 10.89%, and chromium 3.31%), hinting towards changes in the passivated oxide layer of the nanopolish surface. The carbon layer on the surface is formed due to the adsorption of air-borne carbonaceous material when the surface is exposed to the atmosphere [192]. The oxygen layer is from the thin passivating oxide layer on the surface [151,193]. The survey spectrum was recorded with a pass energy of 160 eV at a step size of 1 eV.

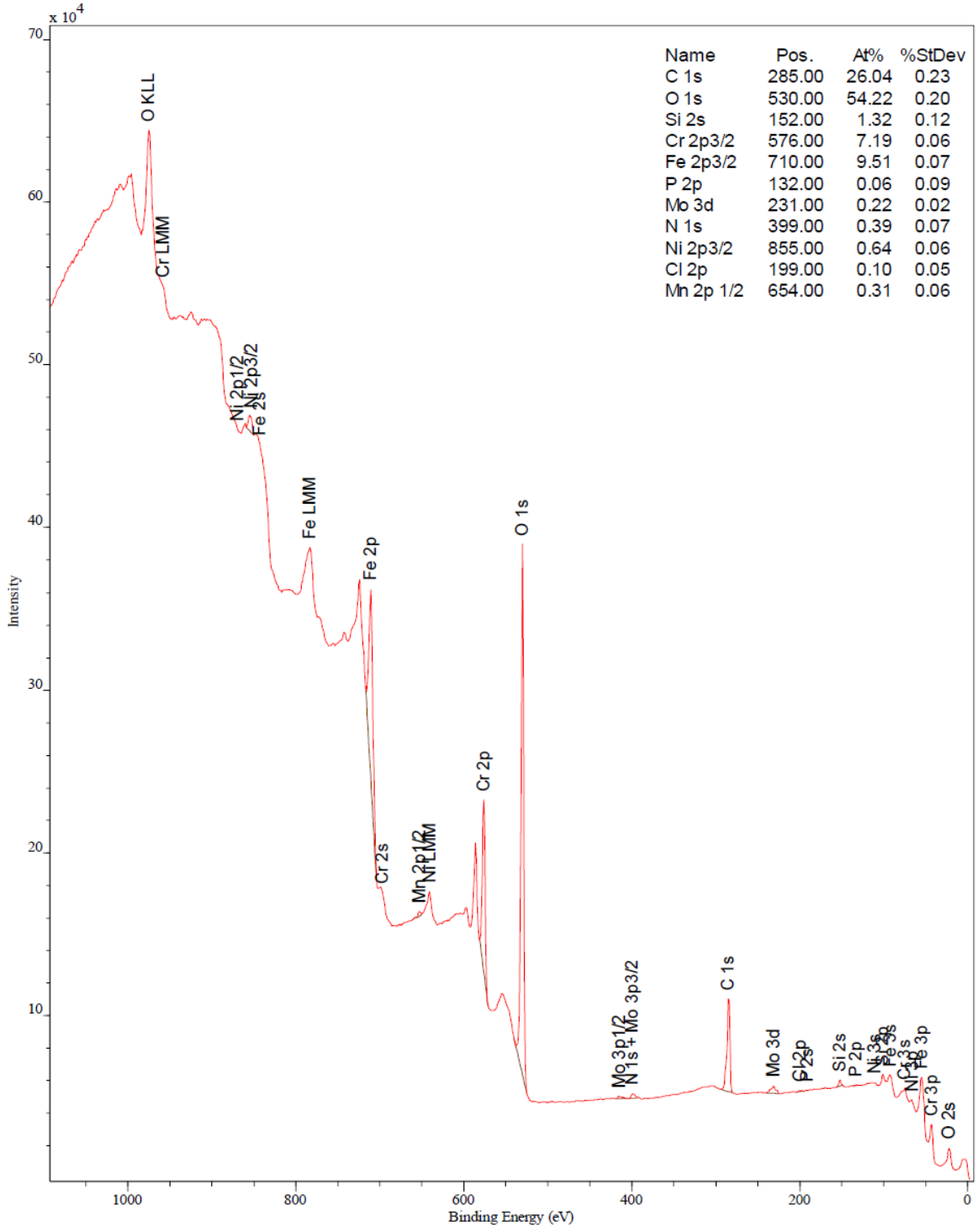

Figure 5.23: XPS survey spectrum of UV-Picosecond laser processed aperture plate (with HSFL features on the surface).

The core level spectra of O 1s, C 1s, Fe 2p, Cr 2p, Ni 2p and Mo 3d are shown in Figure 5.24. The binding energies were calibrated similarly to the reference electrode, i.e.

by setting the C 1s signal corresponding to C–C and C–H at 285.0 eV [194,195]. The significant peaks in the C 1s spectrum, i.e. C–N & C–O single bonds (286.45 eV) and O=C–O & O=C–N peptide bonds (288.65 eV), are organic/polymeric materials, as noticed for the reference electrode also. The core O 1s spectra show the presence of metal oxides (530.19 eV), metal hydroxides (531.41 eV) and hydroxyl groups from aromatic compounds (533.01 eV). A slight increase in oxide and reduction in the metal hydroxide is observed for the HSFL based aperture plate compared to the reference electrode surface. Iron is mainly in the oxide form (710.72 eV), as seen in the Fe 2p spectra, along with iron precipitate in the metallic form (706.69 eV) in a ratio of 5.1:1. Similarly, chromium is mainly in the Cr (III) oxide (576.80 eV) with a small amount of Cr (II) oxide form (575.80 eV). There is a decrease in iron oxide and a significant increase in chromium oxide, hinting towards changes in the surface oxide layer due to laser processing. Nickel is present primarily in oxide (855.72 eV) and metallic form (852.78 eV), along with some portions as saturated nickel precipitate (861.74 eV). The core level spectra of Mo 3d show double peaks for the metallic form Mo (0) and its oxide forms of Mo (II), Mo (IV) and Mo (VI), but the significant contribution is from the metallic Mo (0) and the oxide Mo (IV).

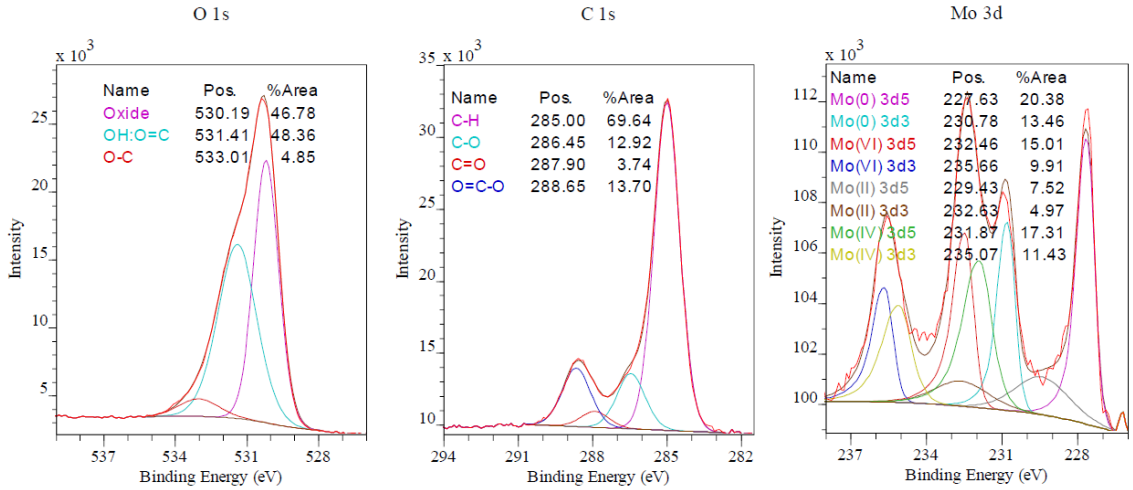

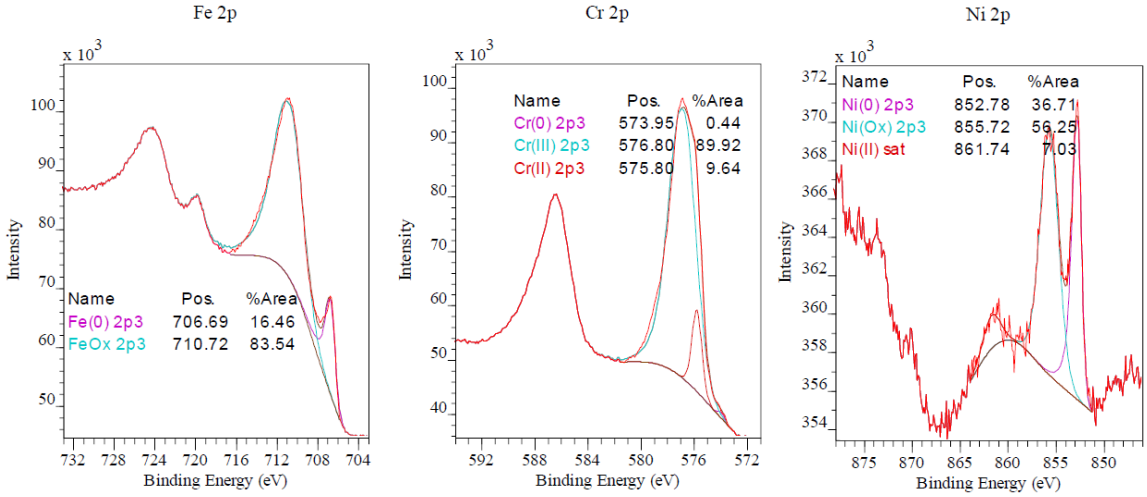

Figure 5.24: High resolution XPS spectra of Fe 2p, Cr 2p, Ni 2p, Mo 3d, O 1s and C 1s of the UV-Picosecond laser processed aperture plate (having HSFL features on the surface).

The XPS analysis of the HSFL surface was done at a location away from the ion beam location, so it mainly provides the surface composition of the laser processed surface. The surface composition shown in Table 5.4 highlights the surface chemistry changes and compares it to the reference aperture plate electrode. A summary of the oxide:metal is listed in Table 5.5. A quick look into Table 5.4 shows a rise in chromium and nickel oxides and a reduction in iron and silicon oxides in the HSFL surface. Also, the HSFL surface shows increased iron, nickel and molybdenum precipitates. The characteristically massive change in the surface's Cr(III) oxide of the laser processed electrode, i.e. around 227% increase along with a reduction in iron's percentage, hints at passivation of the surface and regeneration of the oxide layer. The significant changes in the composition of iron, chromium, nickel and manganese highlight the change in surface chemistry. The changes in surface chemistry of the laser processed aperture plate also demonstrated the potential changes in the surface after laser processing on a mechanically polished surface.

Table 5.4: XPS Surface Composition Table (At%): Picosecond laser processed plates

Elements	Reference Electrode	HSFL Surface
Carbon	**21.9**	**26**
σ	*0.2*	*0.2*
C-C:C-H	11.2	18.1
C-O:C-N	3.62	3.36
C=O:N-C=O	0.65	0.97
O=C-O	6.36	3.57
Oxygen	**60.53**	**53.93**
σ	*0.2*	*0.2*
Oxide	24.1	25.4
OH:O=C	33.4	26.2
O-C	3.03	2.63
Iron	**10.9**	**9.51**
σ	*0.1*	*0.07*
Fe(0)	0.47	1.57
FeOx	10.4	7.94
Nickel	**0.53**	**0.63**
σ	*0.06*	*0.06*
Ni(0)	0.18	0.23
Ni(Ox)	0.35	0.4
Nitrogen	**0.8**	**0.39**
σ	*0.06*	*0.07*
Amine:Amide	0.8	0.39

Elements	Reference Electrode	HSFL Surface
Molybdenum	**0.18**	**0.22**
σ	*0.02*	*0.02*
Mo(0)	0.04	0.07
Mo(II)	0.03	0.03
Mo(IV)	0.06	0.06
Mo(VI)	0.05	0.05
Chromium	**3.31**	**7.19**
σ	*0.05*	*0.06*
Cr(0)	0.13	0.03
Cr(II)	0.33	0.69
Cr(III)	2.85	6.47
Manganese	**0.04**	**0.31**
σ	*0.04*	*0.06*
Mn(II)	NA	NA
Mn(III)	NA	NA
Silicon	**1.07**	**1.32**
σ	*0.12*	*0.12*
Si(0)	0.35	0.19
Si-C	0.72	1.13
Phosphorus (PO_4)	**0.71**	**0.06**
σ	*0.09*	*0.09*

Table 5.5: Oxide:Metal & Elemental Ratios by XPS of laser processed aperture plates

Comparison	Reference electrode**	HSFL based surface
Fe(Ox):Fe(0)	22	5.1
Cr(Ox):Cr(0)	24	239
SS(Ox):SS(0)*	17	8.2
Cr:Fe	0.30	0.76
Mn:Fe	0.004	0.03
Ni:Fe	0.05	0.07
Mo:Fe	0.02	0.02

**** Reference electrode data added for comparison (refer to Table 3.8 in section 3.6.2.2)**

***SS(Ox) = sum of the principal SS 316 elements (Fe, Cr, Ni, Mo, Mn) in their oxidised states.**

SS(0) = sum of the principal SS 316 elements (Fe, Cr, Ni, Mo, Mn) in their metallic state.

5.4.3 ToF-SIMS Results: Protein contamination analysis

ToF-SIMS analysis was conducted on the aperture plate with HSFL features to understand the protein contamination. The ToF-SIMS surface imaging measurements were done using an ION-TOF instrument by Lucideon Ltd. The primary ion source was bismuth (Bi^{3+}) with an ion energy of 30 keV. The analysis was conducted on an area of 20x20 mm^2 with an analysis current was 0.2 pA. The wide area scan provided an overview of the central slot in the aperture plate, the ion beam shape, and its collision location. The image overlay of the aperture plate, shown in Figure 5.25, presents the summation of bovine insulin and stainless steel constituents on the surface of the plates. It also provides an overview of the central slot in the aperture plate and the residue of the ion beam around the opening. Figure 5.25 highlights that the organic contamination is concentrated in a region with a shape potentially of the ion beam. A similar pattern of results was obtained in the ToF-SIMS analysis of the reference electrode (refer to Figure 3.26). Unfortunately, the thickness of

the organic residue layer could not be determined due to the unavailability of the depth profile information.

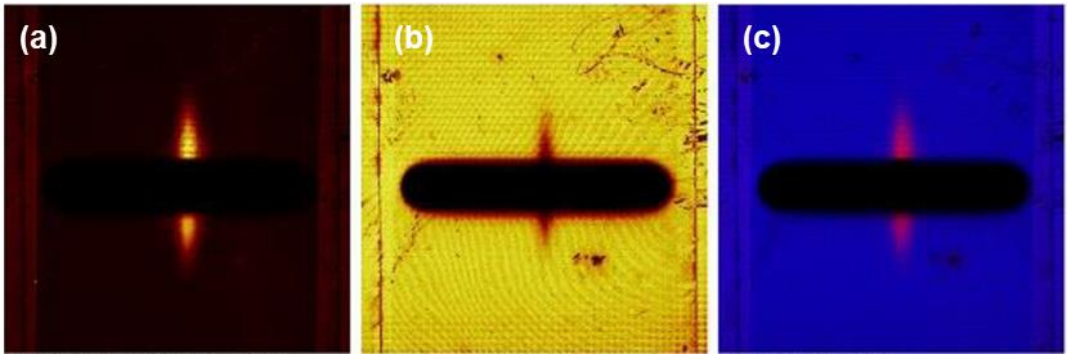

Figure 5.25: Image overlay of ToF-SIMS scan of 20x20 mm^2 of the aperture plate with having HSFL features based surface; (a) Bovine Insulin (summed image), (b) Stainless steel (summed image), (c) Bovine Insulin (red) & stainless steel (blue)
Spectrum parameter: Species Bi3+, Area 20x20 mm2, Polarity positive

The positive ion polarity ToF-SIMS spectra, shown in Figure 5.26, was generated for a scan area of 400x400 μm^2 from a location near the central slot within the bovine insulin summed region. Amino acid signal identifiers for bovine insulin (refer to Table 3.4) were detected as peaks in the spectra and are listed as CH_2N^+ (m/z: 28), CH_4N^+ (m/z: 30) [*Glycine*], $C_2H_6N^+$ (m/z: 44), $C_2H_6NO^+$ (m/z: 60) [*Serine*], $C_4H_8N^+$ (m/z: 70) [*Proline*], $C_4H_{10}N^+$ (m/z: 72) [*Valine*], $C_5H_{10}N^+$ (m/z: 84) [*Lysine*], $C_5H_{12}N^+$ (m/z: 86) [*Isoleucine/Leucine*], $C_5H_8N_3^+$ (m/z: 110) [*Histidine*], $C_8H_{10}N^+$ (m/z: 120) [*Phenylalanine*], and $C_8H_{10}NO^+$ (m/z: 136) [*Tyrosine*]. These signal identifiers were used for the summation of the bovine insulin image shown in Figure 5.25. The results confirm the presence of bovine insulin protein residue on the surface.

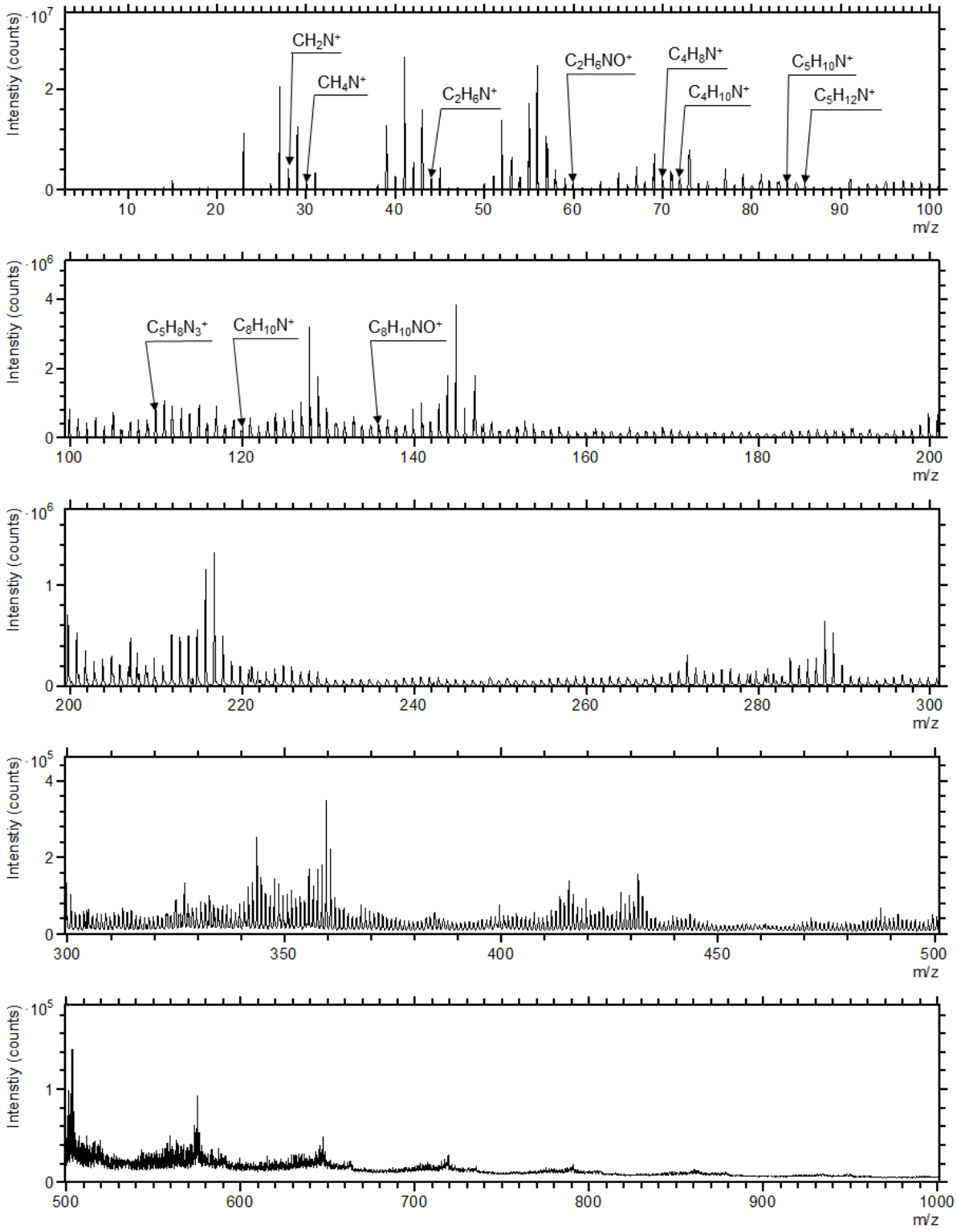

Figure 5.26: ToF-SIMS spectrum of HSFL surface based aperture plate highlighting the bovine insulin signal identifiers. The data was collected from a location within the ion beam collision region shown in the summed image of bovine insulin.

Spectrum parameter: Species Bi^{3+}, Area 400x400 μm^2, Polarity positive.

5.5 Conclusion

The effect of laser processing with a 355 nm picosecond laser on stainless steel 316L was studied. Experiments were conducted to create laser induced features on the material surface. Low spatial frequency features (LSFL) were generated with comparatively high peak-to-valley depths. HSFL feature generation was demonstrated with a novel method using the laser plasma plume as one of the influencing parameters. Laser processing also demonstrated control of the feature growth as HSFL features with different periodicities were obtained for a similar laser processing setup.

LSFL and HSFL feature cases were reproduced on aperture plate surfaces. A protein contamination behaviour test was performed on the laser processed aperture plates using the test rig at the Waters Corporation facility in Wilmslow. LSFL and HSFL showcased promising surface charging results compared to the reference aperture plate electrode. Therefore, they can be considered better in terms of resistance to surface contamination. But, resolution drift rates were also higher, which is disappointing, as it means the aperture plate may reach the lower threshold of the instrument's resolution sooner, leading to instrument downtime. However, since our current result set data is small, predicting a conclusive trend in protein contamination behaviour is complex. Nonetheless, the results indicate that picosecond laser processing influences protein contamination behaviour, paving a direction for future research.

Chapter 6

Femtosecond Laser Processing Results

The results of the investigation with femtosecond laser processing on the stainless steel 316L surface are reported in this chapter. The laser allowed for experimenting with structured femtosecond vector fields benchmarked against uniform fields, using experimental conditions representative of typical industrial operations. Laser induced surface structures were the investigation's focus, aiming to understand the effect of surface structuring on protein contamination behaviour.

Unfortunately, the chapter does not contain the protein contamination behaviour results. It is due to the non-availability of opportunity to produce laser processed aperture plates and test them for protein contamination behaviour. However, our results using radial and azimuthal fields clarify the modality for using these beams, paving the way for use in industrial applications.

6.1 Introduction

In the last 10 years, commercial ultrashort pulse laser sources providing high average powers and pulse repetition rates have become more widely available [218]. The resulting

improvements in achievable processing speed have led to a recent uptake in industrial applications, for example, the replication of microstructures in roll-to-roll processes [219]. Besides these developments, there has also been significant progress in tools and methods to control laser beams' optical characteristics, such as their intensity profiles, wavefront geometry and polarisation state [220]. Several recent publications [147,221,222] presented various methods to produce structured beams spatially shaped with high resolution and purity and, in some cases, modify these parameters dynamically during a process [223]. Recently, applications using intensity shaping with Bessel or annular beams have been demonstrated [224,225]. Beam wavefronts can be shaped by Computer Generated Holograms leading to specific distributions in the focal plane, for example, to produce parallel diffractive laser spots and increase processing speed by orders of magnitude [226]. In another fascinating development, dynamic wavefront shaping enabled the production of conductive pathways and optical waveguides buried in fused silica or diamond by using real-time compensation of optical distortions, finding applications in security marking and beam detector manufacturing [223].

Polarisation shaping has also attracted significant interest in recent years. Complex polarisation states, including radial and azimuthal, help to create micro and nano-scale structures on surfaces with unprecedented flexibility and precision [145,227–230]. Many potential applications are expected to benefit from these emerging laser-based manufacturing processes, for example, using textured electrodes in mass spectroscopy to minimize surface contamination or superhydrophobic surfaces for microfluidic flow control or self-cleaning [147,231].

The availability of beam shaping optics compatible with higher average power ultrashort pulse lasers [226] means many of these laser processing methods are now

compatible with industrial manufacturing. This study focuses on some possibilities for using femtosecond vector field shaping for surface structuring applications. A low numerical aperture f-theta lens combined with a scanning galvanometer is used, with stainless steel 316L as the work-piece material since they represent realistic conditions for manufacturing operations. Radial and azimuthal polarisations are selected as the types of beam most likely to be used in industry.

6.2 Experimental configurations

The femtosecond laser source is a Coherent Libra Ti-Sapphire femtosecond laser (λ=800nm, t_{laser}=100fs, 5mm beam diameter, linear polarisation and maximum pulse energy E_p=1mJ). The laser source configuration is explained in section 3.2.3.

The work-pieces are AISI316L stainless steel plates, polished to <50 nm finish (Goodfellow). All experiments are carried out in the air.

6.3 Optical characterisation

It is important to clarify the expected focusing properties of each beam type since both Gaussian beams (linear and circular polarisations) and annular beams (radial and azimuthal polarisations) were used in our experiments. The focused beam's equivalent numerical aperture (NA) is 0.025 under our experimental conditions. According to Rayleigh's diffraction principles, the expected focal resolution is 1.22λ/NA, corresponding to 39 μm in our experiments. However, this assumes a diameter definition where intensity drops to zero.

The intensity of a Gaussian beam is typically described as follows:

$$I_g(r) = I_0 * e^{-2\left(\frac{r}{w0}\right)^2} \quad \text{..... Eq 6.1}$$

And that of a first order annular beam as:

$$I_g(r) = 2I_0 * \left(\frac{r}{w0}\right)^2 * e^{-2\left(\frac{r}{w0}\right)^2} \quad \text{..... Eq 6.2}$$

Where I_0 is the peak intensity amplitude, and w_0 is the beam waist radius[232]. At the Gaussian beam radius r=w_0, amplitude drops by $1/e^2$, and this is used as the beam radius definition henceforth. The numerical characterisation of focal intensity profiles using Richard Wolf integrals is shown in Figure 6.1. It can be seen that the $1/e^2$ Gaussian diameter is 24λ, or 19.2 μm and the peak diameter of the annular beam is 27λ i.e. 21.6 μm at our wavelength 800 nm. The Matlab program to generate the intensity profiles using Richard Wolf integrals can be referred from Appendix A.2.

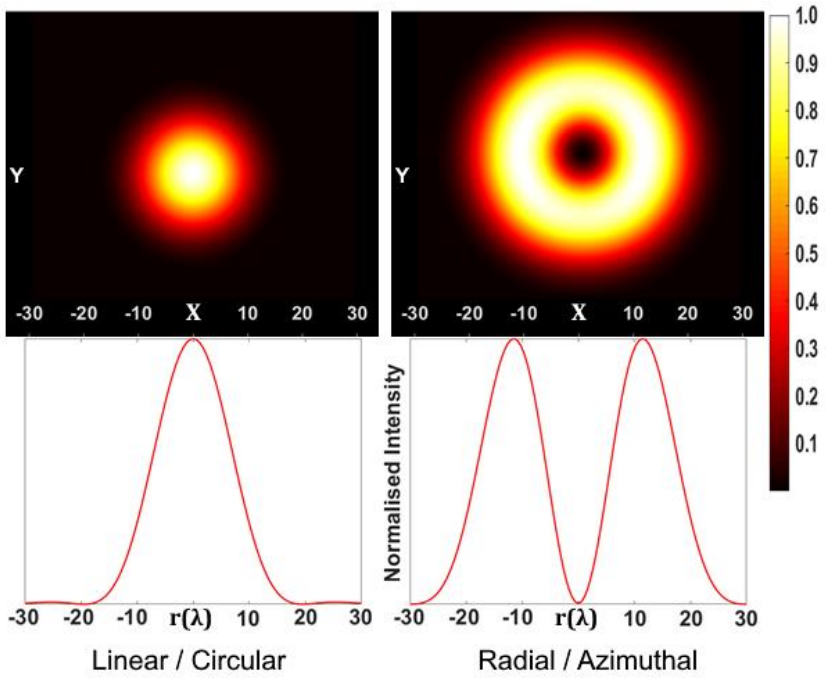

Figure 6.1: Numerical representation of the focal fields of the laser beam (left) linear/circular polarisation and (right) radial or azimuthal polarisation.

Before surface texturing experiments were carried out, collimated beam profiles were verified, and their polarisation purity was analysed using a polarizing filter and CCD profiler. The measured profiles, shown in Figure 6.2, had the expected geometry from linear or circular polarized Gaussian and radial or azimuthal polarized annular beams analysed through a polarizing filter with its transmission axis oriented horizontally. It is noted that the diffraction rings around the edges were induced by the polarizing filter and did not affect the surface processing experiments. The polarisation purity values, measured just before the scanning galvanometer, were found to be 96.6, 95.5 and 93.8 for circular, radial and azimuthal polarisations, respectively.

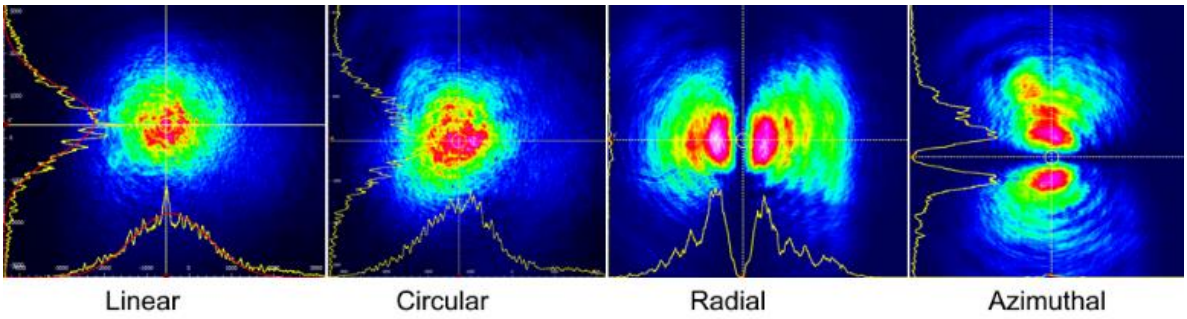

Figure 6.2: Beam intensity profiles (in arbitrary units) at different vector fields.
The radial and azimuthal polarised beams were analysed with a polarizing filter with its transmission axis set to horizontal, producing the expected double-lobe profiles.

6.4 Ablation threshold measurements

Single pulse ablation measurements were carried out so that the laser-materials interactions of each type of beam are accurately characterised for our chosen work-piece material. Figure 6.3 shows the dependence of ablation crater diameters squared versus pulse energy for Linear and Circular polarized Gaussian beams. Both these beams followed the same trend, albeit with a slightly higher material damage threshold for linear

polarisation. By fitting natural logarithm curves to the data points, the ablation damage threshold and beam radius w_0 values can be identified using the graphical-based method described, for example, in [104,221]. From the resulting curve fitting parameters, the pulse energy thresholds obtained were 11.8 μJ and 9.0 μJ for linear and circular polarized beams, respectively, with a beam radius w_0 of 20 μm, leading to fluence thresholds of 0.89 J/cm^2 for linear and 0.72 J/cm^2 for circular polarisation. These values are consistent with femtosecond pulse ablation thresholds identified elsewhere in the literature for steels [104].

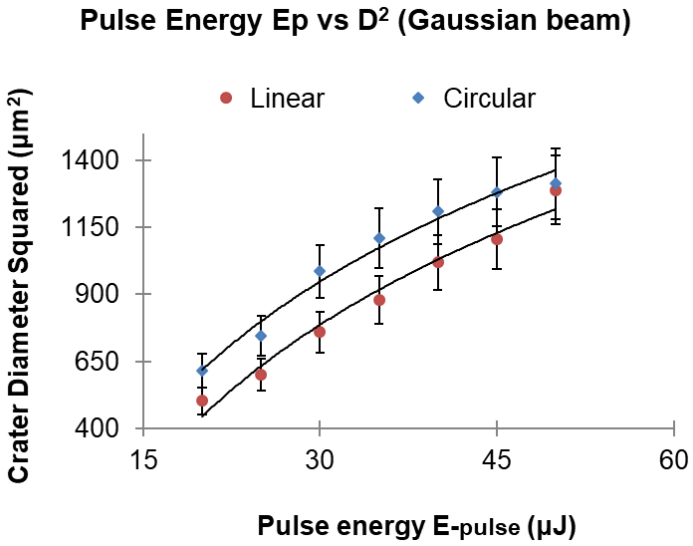

Figure 6.3: Plot showing the diameter squared versus pulse energy for Gaussian beam (Linear and Circular polarised) single pulse focused on SS316L polished surfaces.
The points show experimental data, and continuous lines are fitted to the data used to estimate single pulse ablation thresholds.

Estimating ablation thresholds of radial and azimuthal polarised beams is more complex since these beams produce ablation diameters that converge to their peak diameter rather than a zero value, as is the case with Gaussian beams. It means the ablation thresholds and beam parameters cannot be established using the traditional curve fitting methods. Instead, the peak diameter needs to be established first. Figure 6.4 shows our measurements of the ablation diameters squared for a radially polarized beam. The blue and red data points

represent the outer and inner diameters of the ablation ring, respectively. The curves intersect around 13 µJ pulse energy and crater diameter squared value of 1350 $\mu m^{2,}$ i.e. 37 µm peak diameter ring. From our curve fit and using $1/e^2$ area, we obtain an ablation threshold fluence of 0.62 J/cm^2. Although this value is lower than that of the Gaussian beams described above, it is consistent with what may be expected. It can be explained by the fact that radial polarisation focused at low NA produces local linear polarisation on the surface, thus leading to similar fluence thresholds. Importantly, this confirms that the ablation threshold and beam parameters measurements can be carried out with structured vector beams.

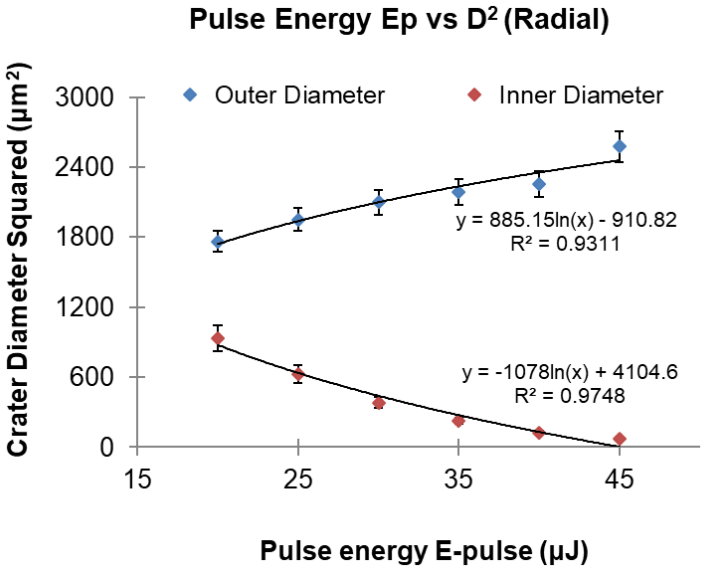

Figure 6.4: Plot showing the diameter squared versus pulse energy for radially polarised single pulse focused on SS316L polished surfaces.
The points show experimental data and continuous lines are fitted to the data to estimate single pulse ablation thresholds. The plot's blue and red data points for radial polarised pulses represent the ablation rings' outer and inner diameters, respectively.

6.5 Ablation spot characterisation

SEM micrographs of focal ablation spots produced with 100 femtosecond pulses are shown in Figure 6.5. The pulse energy was Ep=2.3 ±0.2 μJ, i.e. fluence of ~0.18 J/cm^2 for the linear and circular polarisation and ~0.11 J/cm^2 for the radial and azimuthal polarisation. It is to be noted that these fluences are lower than the ablation thresholds identified earlier in section 6.4. This is due to the number of pulses here (N_p=100) that leads to strong incubation effects, hence the requirement for lower fluence. The top row shows full ablation spots produced with each polarisation state. The linear and circular polarisations each produced 30±5 μm diameter circular or elliptical spots. The ellipticity induced with circular polarisation is attributed to the slight astigmatism of the beam in this case. The radial and azimuthal polarisations produced annular ablation profiles with an outer diameter of 50±5 μm and an estimated peak diameter of 32±5 μm. Considering experimental uncertainty, this agrees with the theoretical values discussed above, i.e. annular peak diameter of ~27 μm (refer to Figure 6.1) and with the curve fitting method shown in Figure 6.4. The larger experimental spot diameter of the Gaussian beams compared with the numerical value ~19 μm is simply due to the choice of fluence and pulse number. Within each spot, self-induced microstructures called LIPSS are induced. LIPSS typically develop orthogonal to polarisation. Hence it can be used as an empirical method to map the local polarisation states within the focal region [145]. The focused linearly polarized beam produced clear LIPSS aligned orthogonally to the incident polarisation (shown as a yellow arrow in Figure 6.5). Radial and azimuthal polarized beams produced LIPSS patterns consistent with their local polarisation states. Unexpectedly, the circularly polarized beam also produced LIPSS, although with poorer contrast than the other beams.

This may be due to the purity of its polarisation state being 96.6%, leading to a residual ellipticity that influenced the way LIPSS developed on the surface.

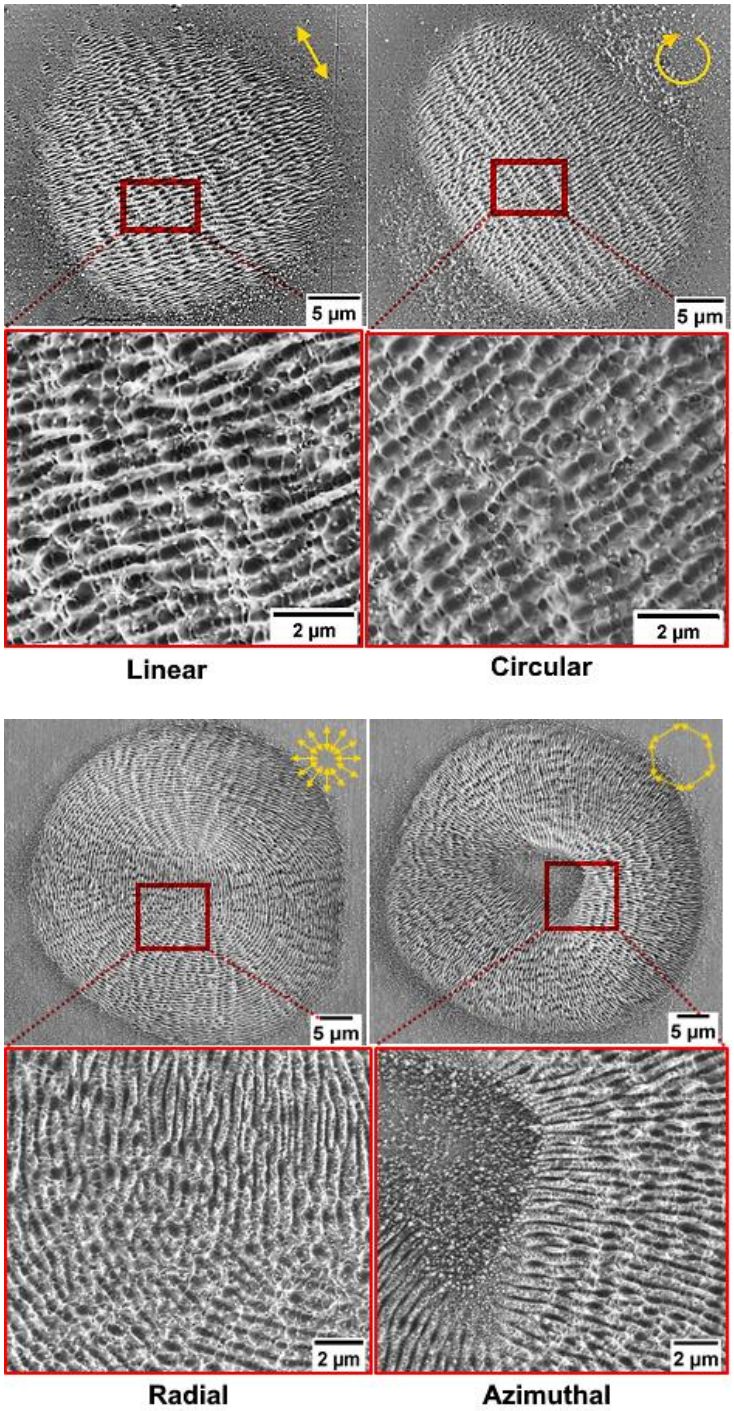

Figure 6.5: SEM micrographs of the focal ablation spots produced on polished surfaces of SS316L with 100 pulses at Ep=2.3 ±0.2 µJ. The polarisation vector is shown as a yellow arrow. (Upper row) linear and circular; (Lower row) for radial and azimuthal polarisations.

Figure 6.6 show an ablation spot produced with an azimuthally and a radially polarized beam, respectively, in the same conditions as that in Figure 6.5. The higher magnification here allows us to illustrate the range of micro and nano-scale structures produced. Granular structures are visible on the left, where each "grain" is ~30 nm in size and 90-180 nm in pitch. The larger structures on the right-hand side are LIPSS. Nanometre scale structures are also visible in the troughs between the main LIPSS peaks, and these are similar to higher spatial frequency LIPSS discussed in the literature [145]. This micrograph was taken near the edge of the laser ablation spot, where the fluence gradient was the steepest (see Eq. 6.2). This means the regions on the right-hand side were produced at fluences ~0.11 J/cm^2, whereas on the left-hand side, the fluence was near the 1/e^2 threshold, i.e. ~0.03 J/cm^2. Adjusting the fluence of the beam would allow one to promote either type of structure. For example, lowering overall fluence is expected to lead to the formation of uniform nano-grains without any LIPSS.

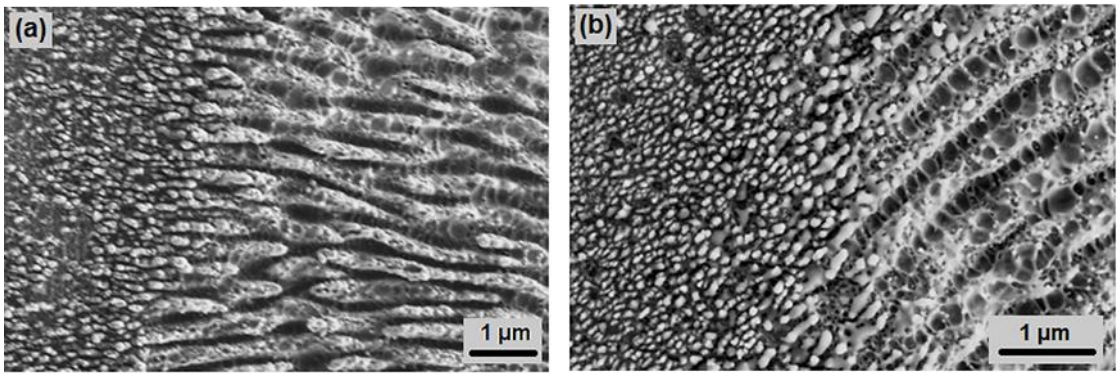

Figure 6.6: SEM micrograph showing a region at the edge of the ablation spot produced with a focused (a) azimuthally polarised beam and (b) radially polarised beam, irradiating the surface with 100 pulses at Ep= 2.3 ±0.2 µJ.

All these structures were further characterized using an AFM to clarify the aspect ratio that can be achieved. Figure 6.7 shows that the pitch and depth of these structures were influenced by the state of polarisation, with linear and circular polarisations inducing

600±50 nm pitch and 200±50 nm peak-to-peak depths. In contrast, radial and azimuthal polarisation produced larger pitch values of 800±50 nm. Azimuthal polarisation clearly produced higher peak-to-peak values than other beams. This is an important result since it confirms that vector field shaping can be used to control the aspect ratio of produced microstructures.

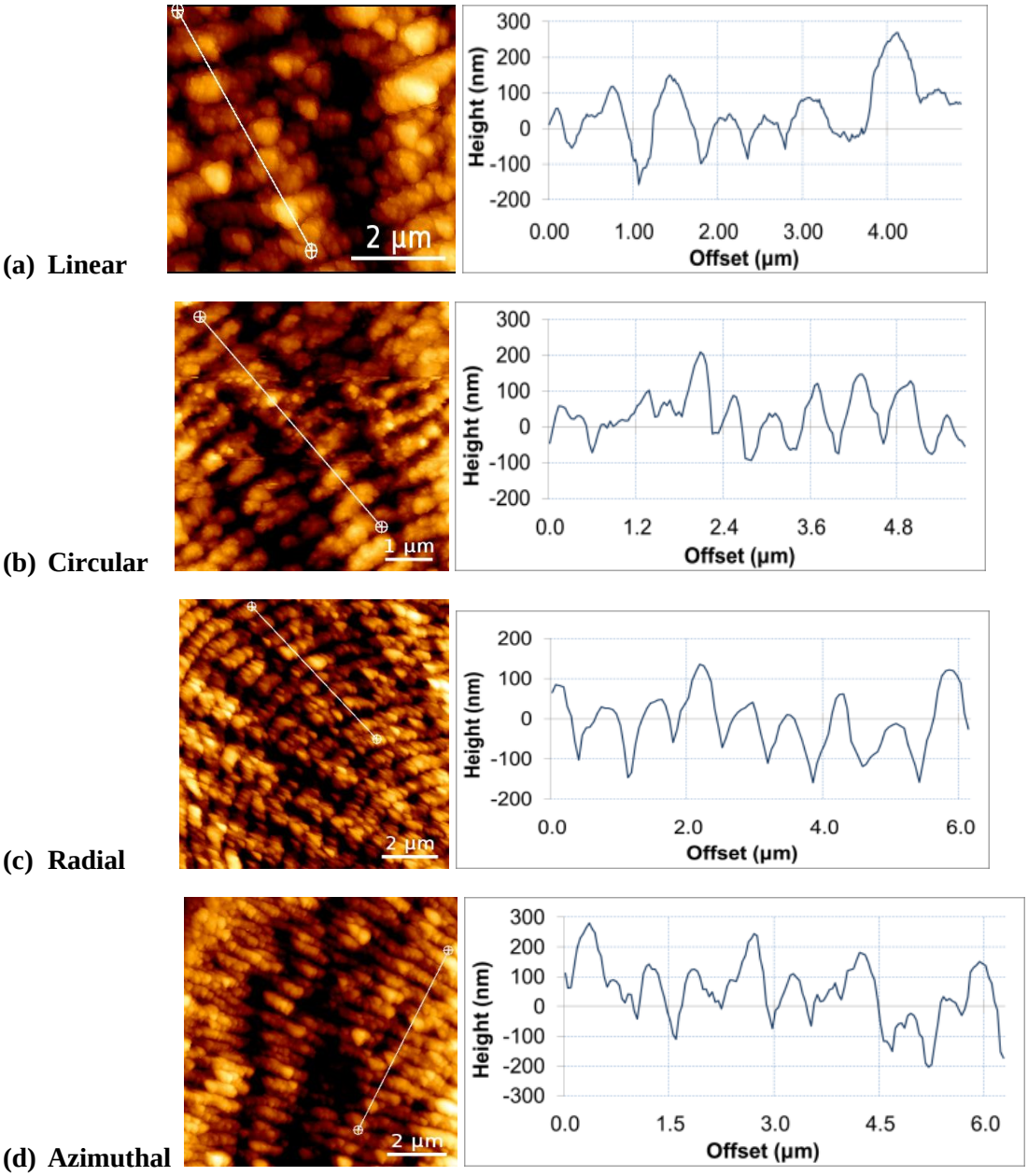

Figure 6.7: AFM profiles of laser induced structures produced by focusing 100 pulses at Ep=2.3±0.2 µJ using (a) linear, (b) circular, (c) radial and (d) azimuthal

6.6 Surface texturing results

The surface texturing experiments consisted of testing potential surface texturing applications using each type of laser beam. Laser processing with different beams were tested as ablation tracks. Area level laser processing with a single or combination was beam types was tried to understand the potential surfaces that can be generated with the femtosecond laser.

6.6.1 Surface ablation tracks

Surface ablation tracks were produced by scanning the beams at 5 mm/s (pulse-to-pulse distance Δx=5 μm) and using a pulse energy Ep=10 ±1 μJ. Based on the experimental Gaussian beam diameters $2w_0$ calculated above (~40 μm), this leads to a pulse overlap of ~8 along each track, appropriate to promote LIPSS. It can be seen that, within each track, LIPSS developed and formed complex patterns with each type of beam. Figure 6.8 shows SEM micrographs of ablation tracks formed for the linearly polarised beam with periodicity Δ_{LIPSS}=675±50 nm. The LIPSS shown in the figure is low spatial frequency LIPSS (LSFL). Embedded high spatial frequency LIPSS (HSFL) features in the LSFL cavities and nano-dots of diameters 75±20 nm on the LSFL peaks can be seen in the magnified image. The ablation track of circular polarisation should not show an identifiable periodic pattern. However, in our case, slightly lower beam purity of the circular polarisation resulted in sporadically spread LIPSS, as seen in Figure 6.9. The ablation tracks of the radial and azimuthal polarisations (Figure 6.10) show multiple linear LIPSS patterns at different polarisation vector directions. The results demonstrate the range of patterns that can be

imprinted on the surfaces and may be used as a powerful tool for designing specific and well-controlled functional surfaces.

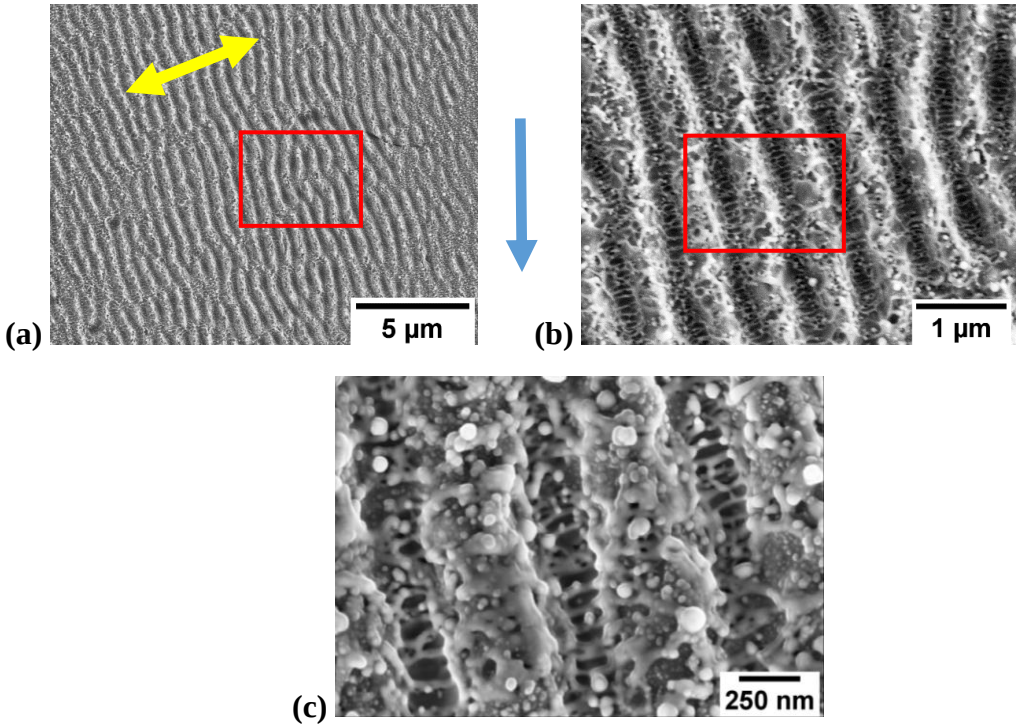

Figure 6.8: SEM micrographs of the ablation tracks of the linear polarised beam at different magnifications on polished SS316L. Scan parameters: Pulse energy Ep=10±1 µJ, V_{SC}=5mm/s. Yellow arrow is the polarisation vector, blue arrow shows scan direction and the region of interest is marked in red; (a) LIPSS features; (b) Magnified view of the marked region in (a); (c) Magnified view of the region marked in (b). LIPSS surface is clearly visible with inter-linked bridges in LSFL valleys and nano-dots on LSFL peaks.

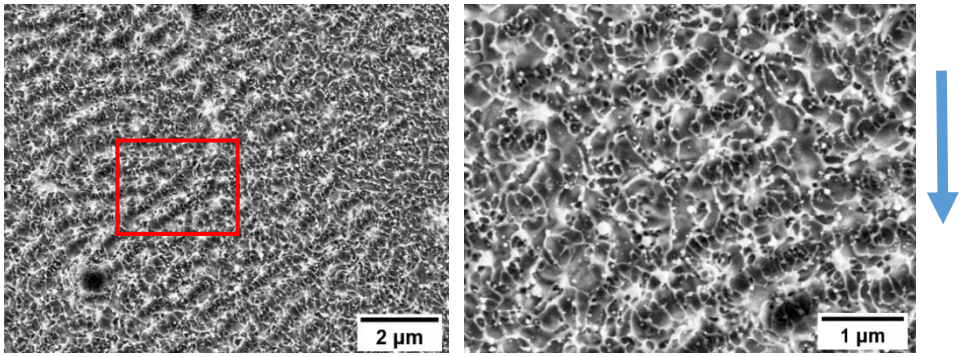

Figure 6.9: SEM micrographs of the ablation tracks of the circular polarised beam on polished SS316L. Scan parameters: Pulse energy Ep=10±1 µJ, V_{SC}=5mm/s; Blue arrow shows scan direction; (right) magnified view of marked region

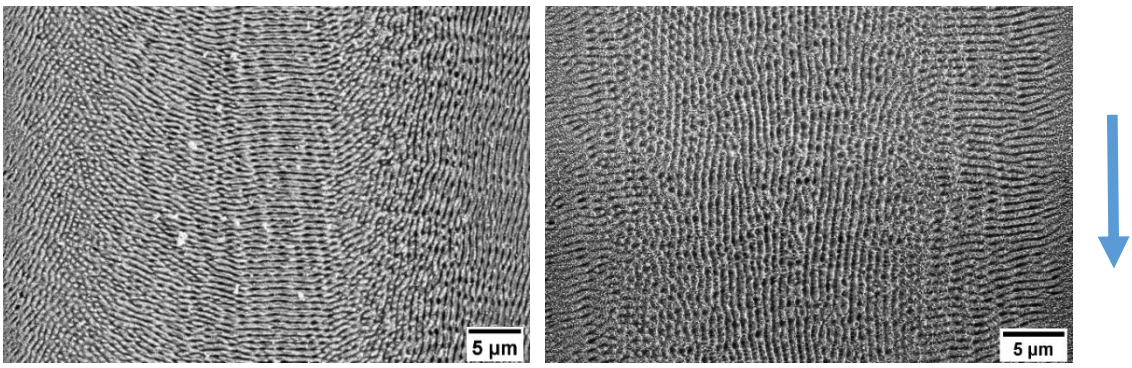

Radial **Azimuthal**

Figure 6.10: SEM micrographs of the ablation tracks of the radial and azimuthal polarised beam on polished SS316L. Scan parameters: Pulse energy Ep=10±1 µJ, V_{SC}=5mm/s; Blue arrow shows scan direction.

6.6.2 Surface texturing results along with a potential industrial application

As an example, a QR code was imprinted on a 316L stainless steel surface using the same process parameters as the tracks shown in Figure 6.10 and using two orthogonal directions of linear polarisation. This led to the production of a concealed QR code that can only be read under illumination at specific angles, thanks to the diffractive properties of the induced microstructures (Figure 6.11, top row). Other examples are shown in the middle and bottom rows in Figure 6.11, using concentric square geometry and parallel linear tracks, respectively. These structures were produced using a combination of linear and radial polarisations in both cases. After laser inscription, the produced microstructures were illuminated with a light source at various incidence angles to test their diffractive properties, and this confirmed that the induced diffraction was highly directional. It means illuminating the structures under different angles changed their appearance, for example, revealing concealed features. This direction dependant reflectivity effect can be seen in Figure 6.11, where specific regions appear dark or bright depending on the incident

illumination. It may find application for imprinting decorative or anti-counterfeiting features directly onto surfaces of high-value components.

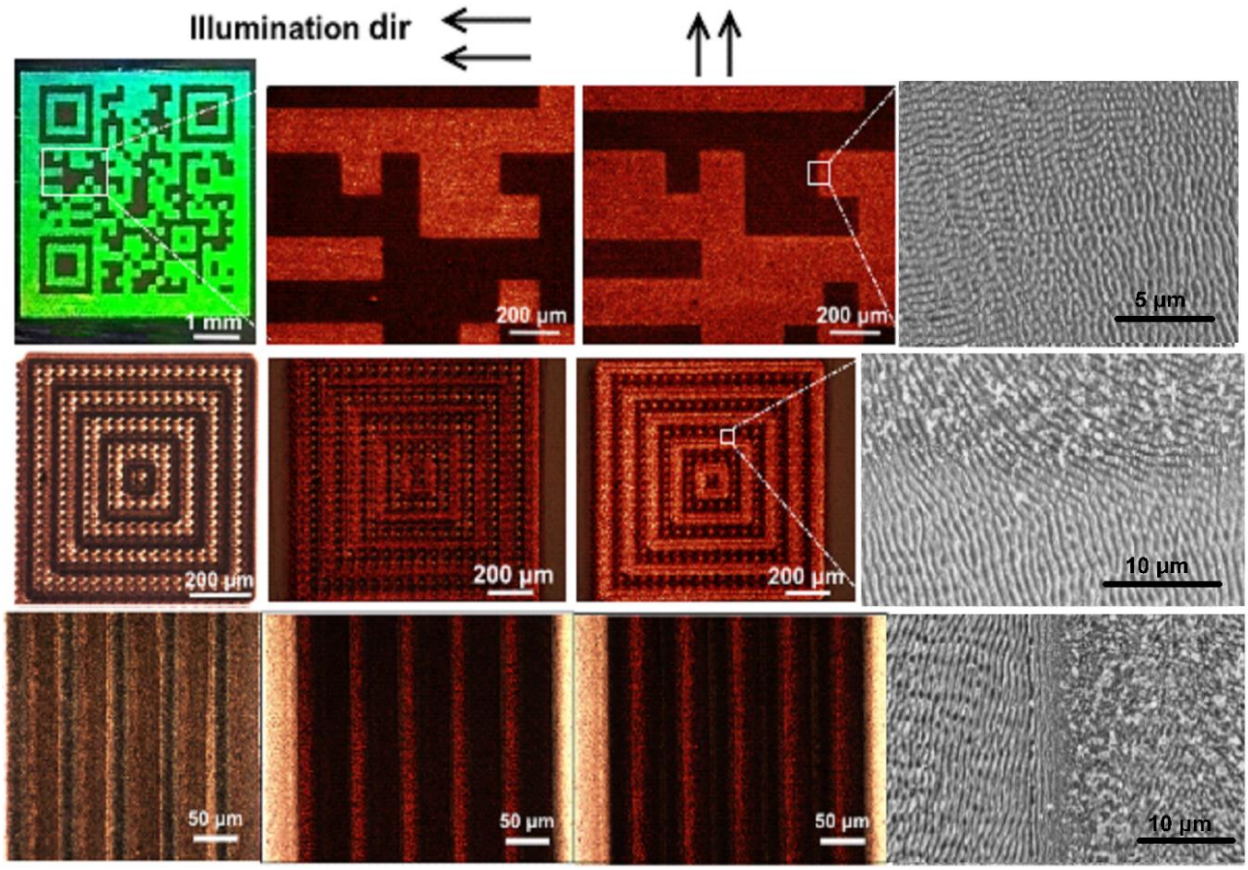

Figure 6.11: Optical and SEM micrographs of surface texturing applications.
The top row shows a QR code with selective illumination of surface structures from different directions, with LIPSS in orthogonal directions. The middle row shows the interaction of linear LIPSS with radial LIPSS and selective illumination of the structures. The lower row shows the interaction of parallel radial polarisation line tracks. All these structures were produced by scanning focused beams of pulse energy Ep= 10 ±1 µJ at 5mm/s on SS316L.

6.7 Conclusion

This study presented the modalities for using femtosecond vector field shaping for surface texturing applications, using experimental conditions representative of typical

manufacturing operations and with polished 316 stainless steel as the work-piece material. It was found that the ablation thresholds and focused beam parameters can be characterized for the selected vector beam using a curve-fitting method by analysing ablation craters diameters. It was also confirmed that the polarisation structures could be accurately mapped by analysing LIPSS patterns induced within the ablation spots. Furthermore, it was shown that the size and aspect ratio of induced surface structures could be controlled by finely adjusting fluence and appropriately selecting the polarisation field. Granular structures with a minimum feature size of ~30 nm and 90-180 nm in pitch could be produced on the surface. Finally, surface texturing applications were presented, and the results clearly demonstrated the improved control of laser-material interactions gained, which allowed the production of tailored surface geometries with complex shapes. The highly controllable nature of microstructures induced using structured optical fields means they can be used in many applications besides the examples shown here. Our future work will explore the texturing of functional electrode surfaces in liquid chromatography mass spectroscopy instrumentation.

Chapter 7

Conclusions and Further Work

7.1 Conclusions

The thesis investigated the effect of laser surface modification on the aperture plate electrode of the mass spectrometer and on its surface contamination behaviour during instrument operations. The study used bovine insulin protein as the surface contaminant since organic contamination by protein ions in the mass spectrometer was the focus of this research. In the first step of the experimental study, surface texturing processes using short and ultra-short pulse lasers were used to create nanoscale features and investigate their relevance to the research goals. AISI 316L stainless steel was chosen as the workpiece material for the research, as it is also the material for manufacturing the aperture plate electrode. The second step of the research focused on understanding the contamination behaviour of proteins on the aperture plate electrode' surfaces. A reduction in the contamination build-up rate was observed on the aperture plates with laser machined surfaces. A summary of the results and key findings from the research are set out below.

7.1.1 Laser surface texturing

The possibilities of laser surface texturing to generate nanoscale structures are examined in this work in separate chapters for the nanosecond (chapter 4), picosecond

(chapter 5) and femtosecond (chapter 6). Liu's graphical model-based approach was used to estimate the single-pulse ablation thresholds on stainless steel 316L surfaces for the laser systems used. The single pulse ablation threshold of the nanosecond laser (λ=532 nm, t_{laser}=7 ns, f_{laser}=30 kHz) was estimated to be 1.71 J/cm^2. Uniform LIPSS features with a periodicity within 0.8λ -0.9λ of the laser wavelength were generated on the 316L stainless steel surfaces with input fluences near and much lower than the ablation threshold. The LIPSS with a fluence near the ablation threshold was found to have a low aspect ratio (0.038) with low surface roughness. An aspect ratio reduction of about 34% was achieved using input fluences much lower than the ablation threshold. The thesis referred to these LIPSS with low peak-to-valley depth as 'shallow LIPSS'. It was found that the number of effective pulses at a spot (N_{eff}) had to be increased significantly to produce laser-induced features when using low fluences. The benefits of low fluence laser processing were further demonstrated by producing surfaces with a reduced surface roughness compared to the original mechanically polished surface, with reductions as low as 60%. These surfaces, referred to in the thesis as 'nanopolished' surfaces, showed no identifiable features and appeared to smoothen out the peaks and corners of the scratches from the mechanically polished surfaces. From the surface chemistry analysis of the laser processed aperture plates, it was confirmed that the surface was reformed since it was observed that the concentration of Cr(III) oxide on the developed surfaces had increased significantly. The result showed that laser processing could produce a surface polishing effect on the surface and provides a direction for further studies on surface polishing using lasers.

Chapter 5 examines the laser surface texturing of picosecond laser (λ=355 nm, t_{laser}=10 ps, f_{laser}= 404.7kHz) related to research. Liu's model estimated the single pulse ablation threshold to be 0.32 J/cm^2. It is known that a UV picosecond laser is a high-

intensity laser. Therefore, the laser-induced features generated during the study had higher aspect ratios compared to the nanosecond laser results. Similar to the nanosecond, low spatial frequency LIPSS (LSFL) features were obtained for input fluences at higher and near the ablation threshold fluence. But the peak-to-valley depth is reduced in low fluence cases. In this study, a novel approach to generate HSFL features on the surface was demonstrated. It uses the high-temperature laser plasma plume created during laser processing to affect the surface conditions. A glass cover reflected the laser plasma plume on the sample surface. HSFL features at periodicities between 80 and 120 nm were generated at the laser process parameters. The method demonstrated that by changing the gap width between the sample surface and the glass cover only, HSFL periodicities could be affected. The new approach hypothesised that the surface ablation threshold could be reduced due to surface preheating by the generated high-temperature laser plasma plume, thereby affecting laser-induced feature generation. However, the effectiveness of the novel method has only been verified experimentally, and further research in this area is needed to understand the effects of the laser plasma plume on the surface.

Laser experimentation was carried out with the femtosecond laser (λ=800 nm, t_{laser}=100 fs, f_{laser}= 1000 Hz) to investigate the modalities for using femtosecond vector field shaping for surface texturing applications, using experimental conditions representative of typical manufacturing operations. It was found that the ablation thresholds and focused beam parameters can be characterised for the selected vector beam using a curve-fitting method by analysing ablation crater diameters. It was also confirmed that the polarisation structures could be accurately mapped by analysing LIPSS patterns induced within the ablation spots. Furthermore, it was shown that the size and aspect ratio of induced surface structures could be controlled by finely adjusting fluence and appropriately selecting the

polarisation field. Granular structures with a minimum feature size of ~30 nm and 90-180 nm in pitch could be produced on the surface. Finally, surface texturing applications were presented, and the results demonstrated the improved control of laser-material interactions gained, which allowed the production of tailored surface geometries with complex shapes. The highly controllable nature of microstructures induced using structured optical fields means they can be used in many applications besides the examples in the chapter.

7.1.2 Protein contamination behaviour of aperture plate electrode

The second step of the research involved analysing the protein contamination behaviour of the aperture plate electrodes. The experimental test methodology is presented in Chapter 3. The methodology is industry internal, so a brief introduction is included here for the reader's reference. The experiments, performed on a test rig emulating a time-of-flight mass spectrometer, were made available by the company for this study. The company's accelerated surface contamination testing system was used to reduce the testing time. The test system used the sweep method, which increases the potential in steps of a specific range relevant to the electrode and identifies the maximum resolution of the instrument and the corresponding applied potential/end voltage at the electrode. Since the aperture plates were rated at 17V, the sweep operated between 16V and 21V in 0.1V increments. We used the end voltage and the resolution as indicators to analyse the electrode's surface condition.

The protein contamination behaviour was studied on selected nanosecond (Chapter 4) and picosecond (Chapter 5) laser processing cases. A non-laser processed as-is machined unmodified aperture plate (Chapter 3), referred to as the 'reference electrode' in the thesis, was analysed to understand the contamination behaviour and to compare laser

processed cases. The analysis of the contamination behaviour is presented in the specified chapters. Due to limited opportunities because of COVID-19 restrictions, no analysis was performed using aperture plates processed with the femtosecond laser. The contamination build-up rate (or the surface charging rate) was estimated as the change in end voltage on the aperture plate surface over the test run cycle. It directly reflected the surface condition of the aperture plate during testing. The contamination build-up rate of the laser processed aperture plates was slower than that of the reference electrode. Significant results were obtained on nanosecond shallow LIPSS and nano-polish surface processed in air, and picosecond LSFL and HSFL based surfaces. In addition, the picosecond LSFL surface had the lowest contamination build-up rate, followed by the nanosecond's shallow LIPSS case.

A drop in instrument resolution was noted over time in the aperture plates, with the worst being the picosecond laser processed aperture plates. The picosecond laser induced feature based surfaces are complex and can allow the charged protein ions to stay on the surface longer. Furthermore, according to the literature, the protein ions are gelatinous structures, and surfaces with nanoscale irregularities are conducive to these ions. On the other hand, the surface roughness of the shallow LIPSS and nanopolish surfaces from nanosecond are much lower. The profile roughness average of the surface on the peaks and valleys of shallow LIPSS was found to be between Ra = 1.5–2.2 nm. Thus, based on indicators, the shallow LIPSS case from nanosecond results can be considered an improvement over the reference electrode where surface Ra (ref) = 10.5nm.

In addition, these results also highlighted an important aspect of contamination behaviour, namely the unpredictability of surface charge and resolution change in a test cycle. Although the results show increasing surface charge, a non-uniform rise and fall in

surface charge were observed across all aperture plate electrodes. Based on our knowledge, this can be attributed to contamination accumulating and removing inconsistently throughout the test run cycle, with no predictable pattern. Furthermore, the literature on the interaction of irradiated ions colliding with surfaces with soft landing energies is scarce. And the most likely explanation we have is the physical adsorption of the ions linked to the surface by weak Van der Waal forces. Because of this unpredictability of protein contamination behaviour and our small results set, no clear trend can be drawn.

However, based on the results, the main conclusion that can be drawn is that laser processing affected the surface morphology and influenced the protein contamination behaviour of the aperture plate electrodes. Also, the work has shown promising results and given us a direction for work. Therefore, the role of laser processing in improving the electrode surfaces should be explored further. Even Waters Corporation is motivated to investigate further in this aspect. Furthermore, the versatility of laser surface texturing allows the current results to be adapted to other electrodes with the possibility of surface degradation by ions. Moreover, the problem addressed in the thesis is important to the LC-MS technology. Improvements in the electrode's robustness affect the instrument's performance and will reduce the frequency of instrument downtime for preventive maintenance. Therefore, improvements in this research area are directly linked to the commercial viability of the industry.

7.2 Recommendations for future work

The work carried out during this research project has attempted to address one of the crucial areas of electrode improvement in the LC-MS technology. Some of the key results

of this multidisciplinary research have shown potential for further investigation beyond the scope of the current work. Based on the key findings, a number of recommendations for future research are given below.

7.2.1 In the area of laser surface processing

Nanopolished surfaces made with nanosecond lasers have been a useful research find. It shows great potential in the field of laser-based surface polishing, since the surface produced does not contain any identifiable features. The surface analysis showed that after the laser processing, the sharp corners and edges of the scratches left from the mechanically polished surface were smoothed out. A detailed study of the generated surface is required to understand this effect. The feasibility of repeating laser processing with nanopolish parameters on the surface to achieve higher surface roughness reduction can be investigated, and the limitations of the process can be identified. Applying such a process can reduce the cost of surface finishing compared to other polishing operations.

As demonstrated in this work, LIPSS with a very low aspect ratio (~0.025) can be produced with the nanosecond laser. Uniform LIPSS were generated with a peak-to-valley depth of ~15 nm, and due to the nature of the ablation mechanism, very smooth surfaces on the order of roughness average Ra = 1.5–2.2 nm were obtained. These highlight almost flat features. Further study may identify the feasibility of further reducing the peak-to-valley depth, moving towards the regime of near-flat features. With the control in the direction of polarisation of LIPSS, application areas such as friction reduction can be explored. Moreover, future research could continue to explore these features in reduction of surface contamination of electrodes in mass spectrometers, as they have shown promising results in the current work.

The novel method for generating HSFL features with a picosecond laser presented in Chapter 5 of this work demonstrated its effectiveness experimentally. The laser-plasma plume dynamics involved in the process are only hypothesized using the previous research on the mechanism of free expansion of plasma plume expansion. Although the literature on plume dynamics in a confined region is limited, it mainly relates to pulsed laser deposition (PLD). To the author's understanding, no study has investigated the expansion mechanism when the gap between the sample surface and the cover is less than 1 mm. Additional studies are needed to more fully understand the mechanism of plume expansion after reflection from the transparent cover on top of the sample. The mechanism can potentially affect the surface properties and the laser-material interaction thereafter.

7.2.2 In the area of protein contamination behaviour

One of the primary sources of organic contamination of electrodes in mass spectrometers is the irradiation of soft-landed protein ions. The high vacuum of the mass spectrometer affects the interaction of the electrodes with the contaminants. However, the interaction of proteins irradiated onto the material surface under vacuum conditions has rarely been studied directly. Understanding this aspect is critical for future attempts to overcome surface contamination. Future research should also address reducing contamination from surface chemistry. For example, applying a thin film coating of aluminium oxide using methods such as atomic layer deposition after laser machining the electrode surface can reduce protein contamination. However, the impact on the ion transport mechanism needs to be analysed for this process.

Appendix

A.1. UV Laser Galvo response

250 loops were marked using the laser of a square of size 30mm x 30mm, resulting in a total marked line of 30000 mm. Table A.1 shows the Galvo head response to the Digistruct control software.

Table A.1 IR Laser Galvo head response

Software input scan speed (mm/sec)	Marking time (secs)	Computed speed of Galvo head (mm/sec)	Percentage deviation (%)
1000	30.41	986.4	1.36
2000	15.35	1954.2	2.29
3000	10.31	2909.0	3.03
4000	7.80	3843.8	3.91
5000	6.30	4765.7	4.69
6000	5.30	5662.9	5.62
7000	4.57	6567.3	6.18
8000	4.03	7439.7	7.00
9000	3.61	8307.5	7.69
10000	3.28	9146.0	8.54
11000	3.00	9994.5	9.14
12000	2.78	10793.5	10.05
13000	2.58	11620.2	10.61
14000	2.42	12381.1	11.56
15000	2.28	13147.8	12.35
16000	2.16	13897.9	13.14
17000	2.05	14634.9	13.91
18000	1.95	15415.7	14.36
19000	1.87	16078.5	15.38
20000	1.79	16759.5	16.20

A.2. Matlab program to plot intensity profiles

The Matlab code to generate intensity profiles using Richard Wolf integrals for NA=0.025 and wavelength 800nm.

```
%initialize Matlab environment
clear
close all
clc
tic;
set(0,'DefaultAxesFontName','Times New Roman')
set(0,'DefaultAxesFontSize',11)
%set(0,'DefaultUnits','normalized');
set(0,'defaultuicontrolunits','normalized');
%% %%%%%%%program body%%%%%%%%%%%%%

%Type of polarisation
all_options = ["x-linear" "y-linear" "leftcircular" "rightcircular"
"elliptical" "Radial" "Azimuthal"];

%basic input parameters
NA=0.025;         %Numerical Aperture of Objective Lens
n=1;              %Refractive index of immersion medium (n=1.33 water,
n=1 air)
lambda=800e-9;    %Wavelength of light
ImgScale=30;      %Observation scale in µm

%% %%%%%%%%%%%%%%%%%%%%%%%%%%%%%
%Image plane in Cartesian coordinates
xGrid_size=101;     %Discretization of image plane
yGrid_size=101;     %Discretization of image plane

ImgScale_actual = ImgScale * 1e-6;
xGrid_vec=linspace(-ImgScale_actual,ImgScale_actual,xGrid_size);
yGrid_vec=linspace(-ImgScale_actual,ImgScale_actual,yGrid_size);

[X2,Y2]=meshgrid(xGrid_vec,yGrid_vec);
Z2=0;

%%%%%%%%%%%%%%%%%%%%%%%%%%%%%%%
%% Test for polarisation - Radial
Polar_Type = 6;       %Polarisation type (Input)
[Ix2_1, Iy2_1, Iz2_1] = GenerateIntensityVectors(X2, Y2, Polar_Type,
lambda, NA, n);

%Intensity plot for XY plane
```

```
Ixy2_1=Ix2_1 + Iy2_1;
CreateIntensityPlots(Ixy2_1, X2, Y2, xGrid_size,
all_options(Polar_Type));

%Intensity plot for XZ plane
Ixz2_1=Ix2_1 + Iz2_1;
CreateIntensityPlots(Ixz2_1, X2, Y2, xGrid_size,
all_options(Polar_Type));

%%%%%%%%%%%%%%%%%%%%%%%%%%%%%%%%
%% Test for polarisation - Linear
Polar_Type = 1;      %Polarisation type (Input)
[Ix2_2, Iy2_2, Iz2_2] = GenerateIntensityVectors(X2, Y2, Polar_Type,
lambda, NA, n);

%Intensity plot for XY plane
Ixy2_2=Ix2_2 + Iy2_2;
CreateIntensityPlots(Ixy2_2, X2, Y2, xGrid_size,
all_options(Polar_Type));

%% %%

toc             %count execution time
%%%%%%%%%endprogram%%%%%%%%%%%%%%%
%%%%%%%%%%%%%%%%%%%%%%%%%%%%%%%%%%%%%%%%%%%%%%%%%%%%%%%%%%%%%%%%%%%%%%%


%% %%%%%%%%%%%%%% Functions are below this line %%%%%%%%%%%%%%%%%%%%%%%%%

function [Ix2, Iy2, Iz2] = GenerateIntensityVectors(X2, Y2, polar,
lambda, NA, n)

alpha=asin(NA/n);           %maximum open angle of OL
k=2*pi*n/lambda;            %wave number
w0=1.22*lambda/NA;

%normalization and steps of integral
Ex2=0;              %Ex-component in focal
Ey2=0;              %Ey-component in focal
Ez2=0;              %Ez-component in focal
N_theta=50;
N_phi=50;
delta_theta=alpha/N_theta;
delta_phi=2*pi/N_phi;
Z2 = 0;

%starting loop
for theta=eps:delta_theta:alpha
  for phi=eps:delta_phi:2*pi
    %integration of sin(theta).A(theta, phi).B(theta, phi).P(theta, phi)
    %A(theta, phi) = Amplitude of the incident beam
    %A_theta_phi = 1;                        %Uniform
    A_theta_phi = exp(-(X2.^2 + Y2.^2)/(w0.^2));   %Gaussian

    %B(theta, phi)is the apodization factor,
    B_theta_phi = sqrt(cos(theta));
```

```
    %P(theta, phi) indicates the polarisation state of the EM field in
the focal region
    %P(theta, phi) = T(theta, phi).P(theta, phi)
    %T(theta, phi) is the conversion matrix of the polarisation
    %from the object field to the image field
    a = 1 + (cos(theta)-1)*(cos(phi))^2;
    b = (cos(theta)-1)*cos(phi)*sin(phi);
    c = -sin(theta)*cos(phi);
    d = 1+(cos(theta)-1)*(sin(phi))^2;
    e = -sin(theta)*sin(phi);
    ff = cos(theta);
    T_theta_phi = [a b c; b d e; -c -e ff];

    %Incident beam polarisation cases
    P0_x=[1, 0, 1/sqrt(2), 1i/sqrt(2), 2/sqrt(5), cos(phi), -sin(phi)];
    P0_y=[0, 1, 1i/sqrt(2),1/sqrt(2),  1i/sqrt(5),sin(phi), cos(phi)];
    P0_z=0;

    %selected incident beam polarisation
    P0_theta_phi=[P0_x(1,polar);P0_y(1,polar);P0_z];

    %polarisation in focal region
    P_theta_phi=T_theta_phi*P0_theta_phi;

    %numerical calculation of field distribution in focal region
    Expo_part =
1i*k*n*(Z2*cos(theta)+sin(theta).*(X2*cos(phi)+Y2*sin(phi)));

    Ex2=Ex2 +
1i*sin(theta).*A_theta_phi.*B_theta_phi.*P_theta_phi(1,1).*exp(Expo_part
)*delta_theta*delta_phi;
    Ey2=Ey2 +
1i*sin(theta).*A_theta_phi.*B_theta_phi.*P_theta_phi(2,1).*exp(Expo_part
)*delta_theta*delta_phi;
    Ez2=Ez2 +
1i*sin(theta).*A_theta_phi.*B_theta_phi.*P_theta_phi(3,1).*exp(Expo_part
)*delta_theta*delta_phi;

    end
end

%intensity of different components
Ix2=conj(Ex2).*(Ex2);
Iy2=conj(Ey2).*(Ey2);
Iz2=conj(Ez2).*(Ez2);
end

%% %%%%%%%%%%%%%%%%%%%%%%%%%%%%%%%%%%%%%%%%%%%%%%%%%%%%%%%%%%%%%%%%%%%
function CreateIntensityPlots(II2, X2, Y2, xGrid_size, polarSTR)

%Intensity area plot
s1 = strcat(polarSTR, ' Polarisation');
fig1 = figure;
fig1.Name = s1;
set(gcf,'PaperPositionMode','auto')
MM2=max(max(II2));
```

```
pcolor(X2*1e6,Y2*1e6,II2/MM2);
shading interp
% title(s1);
% xticks([-20,-10,0,10,20]);
% xticklabels({'-20','-10','X','10','20'});
ax = gca; % current axes
ax.TickDir = 'out';
ax.TickLength = [0.01 0.02];
ax.XTick = [-30:10:30];
ax.XTickLabel = {'-30','-20','-10','X','10','20','30'};
ax.YTick = [0];
ax.YTickLabel = {'Y'};
ax.FontName = 'Arial';
ax.FontSize = 15;
ax.FontWeight = 'bold';
% ax.XRuler.TickLabelGapOffset = -30;    % negative numbers move the
ticklabels down (positive -> up)
% ax.YRuler.TickLabelGapOffset = -30;
%xlabel('X'); %,'fontweight','bold');
% ylabel('Y'); %,'FontWeight','bold');
axis equal
axis tight
view(0,90);
hold off
colormap(hot)

%Intensity profile
s2 = strcat(polarSTR, ' - Intensity profile');
fig2 = figure;
fig2.Name = s2;
Centre_row = ceil(xGrid_size/2);
X2_centre = X2(Centre_row,:)*1e6;
II2_centre_row=II2(Centre_row,:);
MM3 = max(max(II2_centre_row));
p = plot(X2_centre,II2_centre_row/MM3,'r-');
p(1).LineWidth = 1.5;
% title(s2);
% xticks([-30,-20,-10,0,10,20,30]);
% xticklabels({'-30','-20','-10','r({\lambda})','10','20','30'});
ax = gca; % current axes
ax.YTick = [];
ax.FontName = 'Arial';
ax.FontSize = 15;
ax.FontWeight = 'bold';
ax.XTick = [-30:10:30];
ax.XTickLabel = {'-30','-20','-10','r({\lambda})','10','20','30'};
% xlabel('r({\lambda})'); %,'fontweight','bold');
ylabel('Normalised Intensity'); %,'fontweight','bold');



end
%%%%%%%%%%%%%%%%%%%%%%%%%%%%%%%%%%%%%%%%%%%%%%%%%%%%%%%%%%%%%%%%%%%%%%%
```

References

[1] Heftmann, E., (1983) *Chapter 2 History of chromatography and electrophoresis*, in: Journal of Chromatography Library, 1983: pp. A19–A26. doi:10.1016/S0301-4770(08)60863-5.

[2] Niessen, W.M.A., (2006) *Chapter 1 - Liquid chromatography and sample pretreatment*, in: Liquid Chromatography-Mass Spectrometery, 3rd ed., Taylor & Francis Ltd., 2006.

[3] Thammana, M., (2016) *A Review on High Performance Liquid Chromatography (HPLC)*, Research & Reviews: Journal of Pharmaceutical Analysis. 5 pp:1–7.

[4] Moreno-Arribas, M.V., & Polo, M.C., (2003) *CHROMATOGRAPHY | High-performance Liquid Chromatography*, in: Encyclopedia of Food Sciences and Nutrition, Elsevier, 2003: pp. 1274–1280. doi:10.1016/B0-12-227055-X/00232-7.

[5] Swartz, M.E., (2005) *UPLC™: An introduction and review*, Journal of Liquid Chromatography and Related Technologies. 28 pp:1253–1263. doi:10.1081/JLC-200053046.

[6] Griffiths, J., (2008) *A Brief History of Mass Spectrometry*, Analytical Chemistry. 80 pp:5678–5683. doi:10.1021/ac8013065.

[7] Arpino, P., (2006) *History of LC–MS Development and Interfacing*, in: Wilfried Niessen (Ed.), The Encyclopedia of Mass Spectrometry, 2006.

[8] Famiglini, G., Palma, P., Termopoli, V., & Cappiello, A., (2021) *The history of electron ionization in LC-MS, from the early days to modern technologies: A review*, Analytica Chimica Acta. 1167 pp:338350. doi:10.1016/j.aca.2021.338350.

[9] Perrenoud, L., Saugy, M., & Saudan, C., (2009) *Detection in urine of 4-methyl-2-hexaneamine, a doping agent*, Journal of Chromatography B. 877 pp:3767–3770. doi:10.1016/j.jchromb.2009.09.013.

[10] Settle, F.A., (1998) *Handbook of Instrumental Techniques for Analytical Chemistry*, 1998. doi:10.1080/10826079808006889.

[11] Sudhakar, P., Latha, P., & Reddy, P.V., (2016) *Analytical techniques*, in: Phenotyping Crop Plants for Physiological and Biochemical Traits, Elsevier, 2016: pp. 137–149. doi:10.1016/B978-0-12-804073-7.00017-X.

[12] Lee, M.S., & Kerns, E.H., (1999) *LC/MS applications in drug development*, Mass Spectrometry Reviews. 18 pp:187–279. doi:10.1002/(SICI)1098-2787(1999)18:3/4<187::AID-MAS2>3.0.CO;2-K.

[13] Lee, M.S., (2002) *LC/MS Applications in Drug Development*, 2002. doi:10.1002/0471218812.

[14] Cobice, D.F., Goodwin, R.J.A., Andren, P.E., Nilsson, A., Mackay, C.L., & Andrew, R., (2015) *Future technology insight: Mass spectrometry imaging as a tool in drug research and development*, British Journal of Pharmacology. doi:10.1111/bph.13135.

[15] Antonio, C., Larson, T., Gilday, A., Graham, I., Bergström, E., & Thomas-Oates, J., (2008)

Hydrophilic interaction chromatography/electrospray mass spectrometry analysis of carbohydrate-related metabolites fromArabidopsis thaliana leaf tissue, Rapid Communications in Mass Spectrometry. 22 pp:1399–1407. doi:10.1002/rcm.3519.

[16] Hong, Y.-J., Barrett, D.M., & Mitchell, A.E., (2004) *Liquid Chromatography/Mass Spectrometry Investigation of the Impact of Thermal Processing and Storage on Peach Procyanidins*, Journal of Agricultural and Food Chemistry. 52 pp:2366–2371. doi:10.1021/jf0306082.

[17] de Pascual-Teresa, S., Santos-Buelga, C., & Rivas-Gonzalo, J.C., (2002) *LC-MS analysis of anthocyanins from purple corn cob*, Journal of the Science of Food and Agriculture. 82 pp:1003–1006. doi:10.1002/jsfa.1143.

[18] Wang, Y., Catana, F., Yang, Y., Roderick, R., & van Breemen, R.B., (2002) *An LC-MS Method for Analyzing Total Resveratrol in Grape Juice, Cranberry Juice, and in Wine*, Journal of Agricultural and Food Chemistry. 50 pp:431–435. doi:10.1021/jf010812u.

[19] Careri, M., Bianchi, F., & Corradini, C., (2002) *Recent advances in the application of mass spectrometry in food-related analysis*, Journal of Chromatography A. 970 pp:3–64. doi:10.1016/S0021-9673(02)00903-2.

[20] Di Stefano, V., Avellone, G., Bongiorno, D., Cunsolo, V., Muccilli, V., Sforza, S., Dossena, A., Drahos, L., & Vékey, K., (2012) *Applications of liquid chromatography–mass spectrometry for food analysis*, Journal of Chromatography A. 1259 pp:74–85. doi:10.1016/j.chroma.2012.04.023.

[21] Richardson, S.D., (2001) *Mass Spectrometry in Environmental Sciences*, Chemical Reviews. 101 pp:211–254. doi:10.1021/cr990090u.

[22] Yu, H., & Lee, S.-H., (2012) *Chemical ionisation mass spectrometry for the measurement of atmospheric amines*, Environmental Chemistry. 9 pp:190. doi:10.1071/EN12020.

[23] Widmer, L., Watson, S., Schlatter, K., & Crowson, A., (2002) *Development of an LC/MS method for the trace analysis of triacetone triperoxide (TATP)*, The Analyst. 127 pp:1627–1632. doi:10.1039/B208350G.

[24] Van Puyvelde, B., Van Uytfanghe, K., Tytgat, O., Van Oudenhove, L., Gabriels, R., Bouwmeester, R., Daled, S., Van Den Bossche, T., Ramasamy, P., Verhelst, S., De Clerck, L., Corveleyn, L., Willems, S., Debunne, N., Wynendaele, E., De Spiegeleer, B., Judak, P., Roels, K., De Wilde, L., Van Eenoo, P., Reyns, T., Cherlet, M., Dumont, E., Debyser, G., T'Kindt, R., Sandra, K., Gupta, S., Drouin, N., Harms, A., Hankemeier, T., Jones, D.J.L., Gupta, P., Lane, D., Lane, C.S., El Ouadi, S., Vincendet, J.-B., Morrice, N., Oehrle, S., Tanna, N., Silvester, S., Hannam, S., Sigloch, F.C., Bhangu-Uhlmann, A., Claereboudt, J., Anderson, N.L., Razavi, M., Degroeve, S., Cuypers, L., Stove, C., Lagrou, K., Martens, G.A., Deforce, D., Martens, L., Vissers, J.P.C., & Dhaenens, M., (2021) *Cov-MS: A Community-Based Template Assay for Mass-Spectrometry-Based Protein Detection in SARS-CoV-2 Patients*, JACS Au. 1 pp:750–765. doi:10.1021/jacsau.1c00048.

[25] Hober, A., Tran-Minh, K.H., Foley, D., McDonald, T., Vissers, J.P., Pattison, R., Ferries, S., Hermansson, S., Betner, I., Uhlén, M., Razavi, M., Yip, R., Pope, M.E., Pearson, T.W., Andersson, L.N., Bartlett, A., Calton, L., Alm, J.J., Engstrand, L., & Edfors, F., (2021) *Rapid and sensitive detection of SARS-CoV-2 infection using quantitative peptide enrichment LC-MS analysis*, ELife. 10. doi:10.7554/eLife.70843.

[26] MarketWatch, (2023) *LC-MS Market and its Economic Impact on Industry : Growth And Trend 2028*, Market Watch. [Online] Avaliable at: https://www.marketwatch.com/press-release/lc-ms-market-and-its-economic-impact-on-industry-growth-and-trend-2028-2023-02-09#:~:text=Due to the COVID-19,Percent during the review period. (accessed February

20, 2023).

[27] Oudenhove, L. Van, Claereboudt, J., Moore, R., Vissers, H., Puyvelde, B. Van, Daled, S., Deforce, D., Uytfanghe, K. Van, Silvester, S., Hannam, S., Jones, D., Lane, D., Gupta, P., Ng, L., & Dhaenens, M., (2020) *Comprehending COVID-19: Maximizing LC-MS Detection Dynamic Range for Multiple Reaction Monitoring Based SARS-CoV-2 Analysis*, 2020. [Online] Avaliable at: https://www.waters.com/waters/library.htm?locale=en_US&lid=135075039.

[28] Oehrle, S., Oudenhove, L. Van, Claereboudt, J., Vissers, H., Puyvelde, B. Van, Daled, S., Uytfanghe, K. Van, Deforce, D., & Dhaenens, M., (2020) *Comprehending COVID-19: Application of UniSpray and Electrospray Ionization for the Detection of Proteolytic Digested SARS-CoV-2 Proteins*, 2020. [Online] Avaliable at: https://www.waters.com/nextgen/gb/en/library/application-notes/2020/comprehending-covid-19-application-of-unispray-and-electrospray-ionization-for-the-detection-of-proteolytic-digested-sars-cov-2-proteins.html.

[29] Suvarna, K., Pai, M.G.J., Srivastava, S., Bhattacharyya, D., & Hassell, K., (2021) *LC-MS for detection of SARS-CoV-2 viral and host proteins*, 2021. [Online] Avaliable at: https://assets.thermofisher.com/TFS-Assets/CMD/Technical-Notes/tn-65974-lc-ms-detection-sars-cov2-viral-host-proteins-tn65974-en.pdf.

[30] Lane, C.S., Puyvelde, B. Van, Uytfanghe, K. Van, & Dhaenens, M., (2020) *Targeted assay for quantification of proteins from the SARS-CoV-2 coronavirus*, 2020. [Online] Avaliable at: https://www.sciex.com/tech-notes/life-science-research/proteomics/targeted-assay-for-quantification-of-proteins-from-the-sars-cov-2-coronavirus.

[31] Bruce, S.J., Tavazzi, I., Parisod, V., Rezzi, S., Kochhar, S., & Guy, P.A., (2009) *Investigation of Human Blood Plasma Sample Preparation for Performing Metabolomics Using Ultrahigh Performance Liquid Chromatography/Mass Spectrometry*, Analytical Chemistry. 81 pp:3285–3296. doi:10.1021/ac8024569.

[32] Niessen, W.M.A., (2006) *Liquid Chromatography-Mass Spectrometery*, 3rd ed., Taylor & Francis Ltd., 2006.

[33] Dempster, A.J., (2015) *Chapter 5 : Mass spectrometry | CH5_MS_Part1_2017.pdf*, Chemistry Lecture Notes, Whitman College. 1 pp:1–4. [Online] Avaliable at: https://www.whitman.edu/chemistry/edusolns_software/FAAS_ICP_2017/.

[34] Calctool.org, (2019) *CalcTool: Protein size calculator.*,. [Online] Avaliable at: http://www.calctool.org/CALC/prof/bio/protein_size (accessed August 31, 2019).

[35] Iancu, C. V., Ding, H.J., Morris, D.M., Dias, D.P., Gonzales, A.D., Martino, A., & Jensen, G.J., (2007) *The Structure of Isolated Synechococcus Strain WH8102 Carboxysomes as Revealed by Electron Cryotomography*, Journal of Molecular Biology. 372 pp:764–773. doi:10.1016/j.jmb.2007.06.059.

[36] Kittel, C., (2004) *Introduction to solid state physics*, 8th ed., John Wiley & Sons, Ltd, 2004.

[37] Martínez-Calderon, M., Rodríguez, A., Dias-Ponte, A., Morant-Miñana, M.C., Gómez-Aranzadi, M., & Olaizola, S.M., (2016) *Femtosecond laser fabrication of highly hydrophobic stainless steel surface with hierarchical structures fabricated by combining ordered microstructures and LIPSS*, Applied Surface Science. 374 pp:81–89. doi:10.1016/j.apsusc.2015.09.261.

[38] Keller, B.O., Sui, J., Young, A.B., & Whittal, R.M., (2008) *Interferences and contaminants encountered in modern mass spectrometry*, Analytica Chimica Acta. 627 pp:71–81. doi:10.1016/j.aca.2008.04.043.

[39] Dee, K.C., Puleo, D.A., & Bizios, R., (2003) *Proteins*, in: An Introduction To Tissue-Biomaterial Interactions, John Wiley & Sons, Inc., New York, USA, 2003: pp. 15–35. doi:10.1002/0471270598.ch2.

[40] Blanco, A., & Blanco, G., (2017) *Proteins*, in: Medical Biochemistry, Elsevier, 2017: pp. 21–71. doi:10.1016/B978-0-12-803550-4.00003-3.

[41] Feng, J., Pandey, R.B., Berry, R.J., Farmer, B.L., Naik, R.R., & Heinz, H., (2011) *Adsorption mechanism of single amino acid and surfactant molecules to Au {111} surfaces in aqueous solution: design rules for metal-binding molecules*, Soft Matter. 7 pp:2113. doi:10.1039/c0sm01118e.

[42] National Human Genome Research Institute, (n.d.) *Protein,*. [Online] Avaliable at: http://www.genome.gov/genetics-glossary/Protein (accessed June 6, 2019).

[43] Erickson, H.P., (2009) *Size and Shape of Protein Molecules at the Nanometer Level Determined by Sedimentation, Gel Filtration, and Electron Microscopy*, Biological Procedures Online. 11 pp:32–51. doi:10.1007/s12575-009-9008-x.

[44] Courses.lumenlearning.com, (2019) *Protein Structure | Biology for Majors I.,*. [Online] Avaliable at: https://courses.lumenlearning.com/wm-biology1/chapter/reading-protein-structure/ (accessed August 16, 2019).

[45] Kebarle, P., & Verkerk, U.H., (2009) *Electrospray: From ions in solution to ions in the gas phase, what we know now*, Mass Spectrometry Reviews. 28 pp:898–917. doi:10.1002/mas.20247.

[46] Banerjee, S., & Mazumdar, S., (2012) *Electrospray Ionization Mass Spectrometry: A Technique to Access the Information beyond the Molecular Weight of the Analyte*, International Journal of Analytical Chemistry. 2012 pp:1–40. doi:10.1155/2012/282574.

[47] Dahlin, A., (2015) *ESI positive mode, Own Work, CC BY 2.0,*. [Online] Avaliable at: https://commons.wikimedia.org/w/index.php?curid=72802277.

[48] Patriksson, A., Marklund, E., & van der Spoel, D., (2007) *Protein Structures under Electrospray Conditions*, Biochemistry. 46 pp:933–945. doi:10.1021/bi061182y.

[49] Ostatná, V., Uslu, B., Dogan, B., Ozkan, S., & Paleček, E., (2006) *Native and denatured bovine serum albumin. D.c. polarography, stripping voltammetry and constant current chronopotentiometry*, Journal of Electroanalytical Chemistry. 593 pp:172–178. doi:10.1016/j.jelechem.2006.03.037.

[50] Matsuo, K., Sakurada, Y., Yonehara, R., Kataoka, M., & Gekko, K., (2007) *Secondary-Structure Analysis of Denatured Proteins by Vacuum-Ultraviolet Circular Dichroism Spectroscopy*, Biophysical Journal. 92 pp:4088–4096. doi:10.1529/biophysj.106.103515.

[51] Ouyang, Z., (2003) *Preparing Protein Microarrays by Soft-Landing of Mass-Selected Ions*, Science. 301 pp:1351–1354. doi:10.1126/science.1088776.

[52] Johnson, G.E., Gunaratne, D., & Laskin, J., (2016) *Soft- and reactive landing of ions onto surfaces: Concepts and applications*, Mass Spectrometry Reviews. 35 pp:439–479. doi:10.1002/mas.21451.

[53] Volný, M., Elam, W.T., Branca, A., Ratner, B.D., & Tureček, F., (2005) *Preparative Soft and Reactive Landing of Multiply Charged Protein Ions on a Plasma-Treated Metal Surface*, Analytical Chemistry. 77 pp:4890–4896. doi:10.1021/ac0507136.

[54] Benavidez, T.E., Torrente, D., Marucho, M., & Garcia, C.D., (2015) *Adsorption of Soft and Hard Proteins onto OTCEs under the Influence of an External Electric Field*, Langmuir. 31 pp:2455–2462. doi:10.1021/la504890v.

[55] Laskin, J., Wang, P., Hadjar, O., Futrell, J.H., Alvarez, J., & Cooks, R.G., (2007) *Charge retention by peptide ions soft-landed onto self-assembled monolayer surfaces*, International Journal of Mass Spectrometry. 265 pp:237–243. doi:10.1016/j.ijms.2007.02.013.

[56] Laskin, J., Wang, P., & Hadjar, O., (2008) *Soft-landing of peptide ions onto self-assembled monolayer surfaces: an overview*, Phys. Chem. Chem. Phys. 10 pp:1079–1090. doi:10.1039/B712710C.

[57] Gologan, B., Green, J.R., Alvarez, J., Laskin, J., & Graham Cooks, R., (2005) *Ion/surface reactions and ion soft-landing*, Physical Chemistry Chemical Physics. 7 pp:1490. doi:10.1039/b418056a.

[58] Artioli, Y., (2008) *Adsorption*, in: Encyclopedia of Ecology, Elsevier, 2008: pp. 60–65. doi:10.1016/B978-008045405-4.00252-4.

[59] Hu, H., & Xu, K., (2020) *Physicochemical technologies for HRPs and risk control*, in: High-Risk Pollutants in Wastewater, Elsevier, 2020: pp. 169–207. doi:10.1016/B978-0-12-816448-8.00008-3.

[60] Hlady, V., & Buijs, J., (1996) *Protein adsorption on solid surfaces*, Current Opinion in Biotechnology. 7 pp:72–77. doi:10.1016/S0958-1669(96)80098-X.

[61] Silva-Bermudez, P., & Rodil, S.E., (2013) *An overview of protein adsorption on metal oxide coatings for biomedical implants*, Surface and Coatings Technology. 233 pp:147–158. doi:10.1016/j.surfcoat.2013.04.028.

[62] Hedberg, Y.S., Killian, M.S., Blomberg, E., Virtanen, S., Schmuki, P., & Odnevall Wallinder, I., (2012) *Interaction of Bovine Serum Albumin and Lysozyme with Stainless Steel Studied by Time-of-Flight Secondary Ion Mass Spectrometry and X-ray Photoelectron Spectroscopy*, Langmuir. 28 pp:16306–16317. doi:10.1021/la3039279.

[63] Hedberg, Y., Wang, X., Hedberg, J., Lundin, M., Blomberg, E., & Odnevall Wallinder, I., (2013) *Surface-protein interactions on different stainless steel grades: Effects of protein adsorption, surface changes and metal release*, Journal of Materials Science: Materials in Medicine. 24 pp:1015–1033. doi:10.1007/s10856-013-4859-8.

[64] Atapour, M., Wei, Z., Chaudhary, H., Lendel, C., Odnevall Wallinder, I., & Hedberg, Y., (2019) *Metal release from stainless steel 316L in whey protein - And simulated milk solutions under static and stirring conditions*, Food Control. 101 pp:163–172. doi:10.1016/j.foodcont.2019.02.031.

[65] Herting, G., Odnevall Wallinder, I., & Leygraf, C., (2007) *Metal release from various grades of stainless steel exposed to synthetic body fluids*, Corrosion Science. 49 pp:103–111. doi:10.1016/j.corsci.2006.05.008.

[66] Lundin, M., Hedberg, Y., Jiang, T., Herting, G., Wang, X., Thormann, E., Blomberg, E., & Wallinder, I.O., (2012) *Adsorption and protein-induced metal release from chromium metal and stainless steel*, Journal of Colloid and Interface Science. 366 pp:155–164. doi:10.1016/j.jcis.2011.09.068.

[67] Hedberg, Y., Karlsson, M.-E., Wei, Z., Žnidaršič, M., Odnevall Wallinder, I., & Hedberg, J., (2017) *Interaction of Albumin and Fibrinogen with Stainless Steel: Influence of Sequential Exposure and Protein Aggregation on Metal Release and Corrosion Resistance*, CORROSION. 73 pp:1423–1436. doi:10.5006/2504.

[68] Okazaki, Y., & Gotoh, E., (2008) *Metal release from stainless steel, Co–Cr–Mo–Ni–Fe and Ni–Ti alloys in vascular implants*, Corrosion Science. 50 pp:3429–3438. doi:10.1016/j.corsci.2008.09.002.

[69] Glišić, B.Đ., Rychlewska, U., & Djuran, M.I., (2012) *Reactions and structural*

characterization of gold(iii) complexes with amino acids, peptides and proteins, Dalton Transactions. 41 pp:6887. doi:10.1039/c2dt30169e.

[70] Welinder, A.C., Zhang, J., Steensgaard, D.B., & Ulstrup, J., (2010) *Adsorption of human insulin on single-crystal gold surfaces investigated by in situ scanning tunnelling microscopy and electrochemistry*, Physical Chemistry Chemical Physics. 12 pp:9999. doi:10.1039/c0cp01021a.

[71] Rodriguez, J.A., & Hrbek, J., (2002) *Interaction of sulphur with bimetallic surfaces: Effects of structural, electronic and chemical properties*, in: D.P. Woodruff (Ed.), Surface Alloys and Alloys Surfaces, Elsevier Ltd., 2002: pp. 466–494. doi:10.1016/S1571-0785(02)80100-6.

[72] Wang, P., & Laskin, J., (2008) *Helical Peptide Arrays on Self-Assembled Monolayer Surfaces through Soft and Reactive Landing of Mass-Selected Ions*, Angewandte Chemie International Edition. 47 pp:6678–6680. doi:10.1002/anie.200801366.

[73] Volný, M., Elam, W.T., Ratner, B.D., & Tureček, F., (2005) *Preparative Soft and Reactive Landing of Gas-Phase Ions on Plasma-Treated Metal Surfaces*, Analytical Chemistry. 77 pp:4846–4853. doi:10.1021/ac0505019.

[74] Blacken, G.R., Volný, M., Diener, M., Jackson, K.E., Ranjitkar, P., Maly, D.J., & Tureček, F., (2009) *Reactive landing of gas-phase ions as a tool for the fabrication of metal oxide surfaces for in situ phosphopeptide enrichment*, Journal of the American Society for Mass Spectrometry. 20 pp:915–926. doi:10.1016/j.jasms.2009.01.006.

[75] Mayer, P.S., Tureček, F., Lee, H.-N., Scheidemann, A.A., Olney, T.N., Schumacher, F., Štrop, P., Smrčina, M., Pátek, M., & Schirlin, D., (2005) *Preparative Separation of Mixtures by Mass Spectrometry*, Analytical Chemistry. 77 pp:4378–4384. doi:10.1021/ac050444j.

[76] Kadlec, J., Joska, Z., & Pokorny, Z., (2011) *Plasma Treatment of Stainless Steel Surface*, ECS Transactions. 32 pp:69–72. doi:10.1149/1.3641841.

[77] Lin, J.-W., & Chang, H.-C., (2011) *Surface modification of SUS304 stainless steel by atmospheric pressure Ar/N2/O2 plasma*, Nuclear Instruments and Methods in Physics Research Section B: Beam Interactions with Materials and Atoms. 269 pp:1801–1808. doi:10.1016/j.nimb.2011.05.004.

[78] Sönmez, T., Fazeli Jadidi, M., Kazmanli, K., Birer, Ö., & Ürgen, M., (2016) *Role of different plasma gases on the surface chemistry and wettability of RF plasma treated stainless steel*, Vacuum. 129 pp:63–73. doi:10.1016/j.vacuum.2016.04.014.

[79] B10NUMB3R5, (1998) *Geometric diameter of Bovine Serum Albumin*,. [Online] Avaliable at: https://bionumbers.hms.harvard.edu/bionumber.aspx?id=103736&ver=6 (accessed September 1, 2019).

[80] Galli, C., Collaud Coen, M., Hauert, R., Katanaev, V.L., Gröning, P., & Schlapbach, L., (2002) *Creation of nanostructures to study the topographical dependency of protein adsorption*, Colloids and Surfaces B: Biointerfaces. 26 pp:255–267. doi:10.1016/S0927-7765(02)00015-2.

[81] Galli, C., Collaud Coen, M., Hauert, R., Katanaev, V.L., Wymann, M.P., Gröning, P., & Schlapbach, L., (2001) *Protein adsorption on topographically nanostructured titanium*, Surface Science. 474 pp:L180–L184. doi:10.1016/S0039-6028(00)01054-2.

[82] Elter, P., Lange, R., & Beck, U., (2012) *Atomic force microscopy studies of the influence of convex and concave nanostructures on the adsorption of fibronectin*, Colloids and Surfaces B: Biointerfaces. 89 pp:139–146. doi:10.1016/j.colsurfb.2011.09.021.

[83] Rechendorff, K., Hovgaard, M.B., Foss, M., Zhdanov, V.P., & Besenbacher, F., (2006)

Enhancement of Protein Adsorption Induced by Surface Roughness, Langmuir. 22 pp:10885–10888. doi:10.1021/la0621923.

[84] Webster, T., Ercan, Khang, D., & Carpenter, J., (2013) *Using mathematical models to understand the effect of nanoscale roughness on protein adsorption for improving medical devices*, International Journal of Nanomedicine. pp:75. doi:10.2147/IJN.S47286.

[85] Arslan, A., Masjuki, H.H., Kalam, M.A., Varman, M., Mufti, R.A., Mosarof, M.H., Khuong, L.S., & Quazi, M.M., (2016) *Surface Texture Manufacturing Techniques and Tribological Effect of Surface Texturing on Cutting Tool Performance: A Review*, Critical Reviews in Solid State and Materials Sciences. 41 pp:447–481. doi:10.1080/10408436.2016.1186597.

[86] Cai, Y., Chang, W., Luo, X., Sousa, A.M.L., Lau, K.H.A., & Qin, Y., (2018) *Superhydrophobic structures on 316L stainless steel surfaces machined by nanosecond pulsed laser*, Precision Engineering. 52 pp:266–275. doi:10.1016/j.precisioneng.2018.01.004.

[87] Rajab, F.H., Liauw, C.M., Benson, P.S., Li, L., & Whitehead, K.A., (2017) *Production of hybrid macro/micro/nano surface structures on Ti6Al4V surfaces by picosecond laser surface texturing and their antifouling characteristics*, Colloids and Surfaces B: Biointerfaces. 160 pp:688–696. doi:10.1016/j.colsurfb.2017.10.008.

[88] Kudryashov, S.I., Nguyen, L. V., Kirilenko, D.A., Brunkov, P.N., Rudenko, A.A., Busleev, N.I., Shakhmin, A.L., Semencha, A. V., Khmelnitsky, R.A., Melnik, N.N., Saraeva, I.N., Nastulyavichus, A.A., Ionin, A.A., Tolordava, E.R., & Romanova, Y.M., (2018) *Large-Scale Laser Fabrication of Antifouling Silicon-Surface Nanosheet Arrays via Nanoplasmonic Ablative Self-Organization in Liquid CS 2 Tracked by a Sulfur Dopant*, ACS Applied Nano Materials. 1 pp:2461–2468. doi:10.1021/acsanm.8b00392.

[89] Gould, R.G., (1959) *The LASER, Light Amplification by Stimulated Emission of Radiation*, in: P.A. Franken, R.H. Sands (Eds.), The Ann Arbor Conference on Optical Pumping, the University of Michigan, Michigan, 1959.

[90] Einstein, A., (1917) *Zur Quantentheorie der Strahlung (On the Quantum Theory of Radiation)*, Physika Zeitschrift. pp:121–128.

[91] MAIMAN, T.H., (1960) *Stimulated Optical Radiation in Ruby*, Nature. 187 pp:493–494. doi:10.1038/187493a0.

[92] Steen, W.M.W.M., & Mazumder, J., (2010) *Basic Laser Optics*, in: Laser Material Processing, Springer London, London, 2010: pp. 79–130. doi:10.1007/978-1-84996-062-5_3.

[93] People.seas.harvard.edu, (2017) *Elementary Laser Models.*,. [Online] Avaliable at: http://people.seas.harvard.edu/~jones/ap216/lectures/ls_2/ls2_u5/ls2_unit_5.html (accessed August 3, 2017).

[94] Brown, M.S., & Arnold, C.B., (2010) *Fundamentals of Laser-Material Interaction and Application to Multiscale Surface Modification*, in: Springer Series in Materials Science, Springer, Berlin, Heidelberg, 2010: pp. 91–120. doi:10.1007/978-3-642-10523-4_4.

[95] Harilal, S.S., Freeman, J.R., Diwakar, P.K., & Hassanein, A., (2014) *Femtosecond Laser Ablation: Fundamentals and Applications*, in: S. Musazzi, U. Perini (Eds.), Laser-Induced Breakdown Spectroscopy, Springer Berlin Heidelberg, Berlin, Heidelberg, 2014: pp. 143–166. doi:10.1007/978-3-642-45085-3_6.

[96] Steen, W.M., & Mazumder, J., (2010) *Laser Ablative Processes – Macro- and Micromachining*, in: Laser Material Processing, Springer London, London, 2010: pp. 371–387. doi:10.1007/978-1-84996-062-5_9.

[97] Phillips, K.C., Gandhi, H.H., Mazur, E., & Sundaram, S.K., (2015) *Ultrafast laser processing of materials: a review*, Advances in Optics and Photonics. 7 pp:684. doi:10.1364/AOP.7.000684.

[98] LaHaye, N.L., Harilal, S.S., Diwakar, P.K., & Hassanein, A., (2013) *The effect of laser pulse duration on ICP-MS signal intensity, elemental fractionation, and detection limits in fs-LA-ICP-MS*, Journal of Analytical Atomic Spectrometry. 28 pp:1781. doi:10.1039/c3ja50200g.

[99] Elliott, D.J., (1995) *Micromachining*, in: Ultraviolet Laser Technology and Applications, Elsevier, 1995: pp. 287–315. doi:10.1016/B978-0-12-237070-0.50013-3.

[100] Cristoforetti, G., Legnaioli, S., Palleschi, V., Tognoni, E., & Benedetti, P.A., (2008) *Observation of different mass removal regimes during the laser ablation of an aluminium target in air*, Journal of Analytical Atomic Spectrometry. 23 pp:1518. doi:10.1039/b800517f.

[101] Trtica, M.S., Radak, B.B., Gakovic, B.M., Milovanovic, D.S., Batani, D., & Desai, T., (2009) *Surface modifications of Ti6Al4V by a picosecond Nd:YAG laser*, Laser and Particle Beams. doi:10.1017/S0263034609000123.

[102] Hashida, M., Semerok, A.F., Gobert, O., Petite, G., Izawa, Y., & Wagner, J.F., (2002) *Ablation threshold dependence on pulse duration for copper*, in: Applied Surface Science, 2002. doi:10.1016/S0169-4332(02)00463-4.

[103] Raciukaitis, G., Brikas, M., Gecys, P., & Gedvilas, M., (2008) *Accumulation effects in laser ablation of metals with high-repetition-rate lasers*, in: C.R. Phipps (Ed.), High-Power Laser Ablation VII, 2008: p. 70052L. doi:10.1117/12.782937.

[104] Mannion, P.., Magee, J., Coyne, E., O'Connor, G.., & Glynn, T.., (2004) *The effect of damage accumulation behaviour on ablation thresholds and damage morphology in ultrafast laser micro-machining of common metals in air*, Applied Surface Science. 233 pp:275–287. doi:10.1016/j.apsusc.2004.03.229.

[105] Wellershoff, S.-S., Hohlfeld, J., Güdde, J., & Matthias, E., (1999) *The role of electron-phonon coupling in femtosecond laser damage of metals*, Applied Physics A: Materials Science & Processing. 69 pp:S99–S107. doi:10.1007/s003390051362.

[106] Güdde, J., Hohlfeld, J., Müller, J.G., & Matthias, E., (1998) *Damage threshold dependence on electron-phonon coupling in Au and Ni films*, Applied Surface Science. doi:10.1016/S0169-4332(98)00002-6.

[107] Yahng, J.S., Nam, J.R., & Jeoung, S.C., (2009) *The influence of substrate temperature on femtosecond laser micro-processing of silicon, stainless steel and glass*, Optics and Lasers in Engineering. 47 pp:815–820. doi:10.1016/j.optlaseng.2009.02.001.

[108] Zhu, S., Lu, Y.F., Hong, M.H., & Chen, X.Y., (2001) *Laser ablation of solid substrates in water and ambient air*, Journal of Applied Physics. 89 pp:2400–2403. doi:10.1063/1.1342200.

[109] Gamaly, E.G., Madsen, N.R., Duering, M., Rode, A. V., Kolev, V.Z., & Luther-Davies, B., (2005) *Ablation of metals with picosecond laser pulses: Evidence of long-lived nonequilibrium conditions at the surface*, Physical Review B - Condensed Matter and Materials Physics. doi:10.1103/PhysRevB.71.174405.

[110] Ahmmed, K., Grambow, C., Kietzig, A.-M.M., Tanvir Ahmmed, K.M., Grambow, C., & Kietzig, A.-M.M., (2014) *Fabrication of Micro/Nano Structures on Metals by Femtosecond Laser Micromachining*, Micromachines. 5 pp:1219–1253. doi:10.3390/mi5041219.

[111] Smirl, A.L., Boyd, I.W., Boggess, T.F., Moss, S.C., & van Driel, H.M., (1986) *Structural changes produced in silicon by intense 1-μm ps pulses*, Journal of Applied Physics. 60

pp:1169–1182. doi:10.1063/1.337362.

[112] Tull, B.R., Carey, J.E., Mazur, E., McDonald, J.P., & Yalisove, S.M., (2006) *Silicon Surface Morphologies after Femtosecond Laser Irradiation*, MRS Bulletin. 31 pp:626–633. doi:10.1557/mrs2006.160.

[113] Birnbaum, M., (1965) *Semiconductor Surface Damage Produced by Ruby Lasers*, Journal of Applied Physics. 36 pp:3688–3689. doi:10.1063/1.1703071.

[114] Bonse, J., Höhm, S., Kirner, S., Rosenfeld, A., & Krüger, J., (2016) *Laser-induced Periodic Surface Structures - A Scientific Evergreen*, Conference on Lasers and Electro-Optics. 23 pp:STh1Q.3. doi:10.1364/CLEO_SI.2016.STh1Q.3.

[115] Bonse, J., Höhm, S., Hartelt, M., Spaltmann, D., Pentzien, S., Koter, R., Marschner, S., Rosenfeld, A., & Krüger, J., (2015) *Femtosecond laser-induced surface nanostructures for tribological application*, in: K. König, A. Ostendorf (Eds.), Optically Induced Nanostructures, DE GRUYTER, 2015. doi:10.1515/9783110354324.

[116] Bonse, J., & Gräf, S., (2020) *Maxwell Meets Marangoni—A Review of Theories on Laser-Induced Periodic Surface Structures*, Laser and Photonics Reviews. 14 pp:1–25. doi:10.1002/lpor.202000215.

[117] Litwin, J.A., Sipe, J.E., & van Driel, H.M., (1985) *Picosecond and nanosecond laser-induced second-harmonic generation from centrosymmetric semiconductors*, Physical Review B. 31 pp:5543–5546. doi:10.1103/PhysRevB.31.5543.

[118] Sipe, J.E., Young, J.F., Preston, J.S., & van Driel, H.M., (1983) *Laser-induced periodic surface structure. I. Theory*, Physical Review B. 27 pp:1141–1154. doi:10.1103/PhysRevB.27.1141.

[119] Florian, C., Kirner, S. V., Krüger, J., & Bonse, J., (2020) *Surface functionalization by laser-induced periodic surface structures*, Journal of Laser Applications. 32 pp:022063. doi:10.2351/7.0000103.

[120] Ahmmed, K.M.T., Ling, E.J.Y., Servio, P., & Kietzig, A.-M., (2015) *Introducing a new optimization tool for femtosecond laser-induced surface texturing on titanium, stainless steel, aluminum and copper*, Optics and Lasers in Engineering. 66 pp:258–268. doi:10.1016/j.optlaseng.2014.09.017.

[121] Groenendijk, M.N.W., & Meijer, J., (2006) *Surface Microstructures obtained by Femtosecond Laser Pulses*, CIRP Annals. 55 pp:183–186. doi:10.1016/S0007-8506(07)60394-1.

[122] Zhao, Q.Z., Malzer, S., & Wang, L.J., (2007) *Formation of subwavelength periodic structures on tungsten induced by ultrashort laser pulses*, Optics Letters. 32 pp:1932. doi:10.1364/OL.32.001932.

[123] Yao, Y.L., Chen, H., & Zhang, W., (2005) *Time scale effects in laser material removal: a review*, The International Journal of Advanced Manufacturing Technology. 26 pp:598–608. doi:10.1007/s00170-003-2026-y.

[124] Fiorucci, M.P., López, A.J., & Ramil, A., (2015) *Surface modification of Ti6Al4V by nanosecond laser ablation for biomedical applications*, Journal of Physics: Conference Series. 605 pp:012022. doi:10.1088/1742-6596/605/1/012022.

[125] Simões, J.G.A.B., Riva, R., & Miyakawa, W., (2018) *High-speed Laser-Induced Periodic Surface Structures (LIPSS) generation on stainless steel surface using a nanosecond pulsed laser*, Surface and Coatings Technology. 344 pp:423–432. doi:10.1016/j.surfcoat.2018.03.052.

[126] Rebollar, E., Sanz, M., Pérez, S., Hernández, M., Martín-Fabiani, I., Rueda, D.R., Ezquerra, T.A., Domingo, C., & Castillejo, M., (2012) *Gold coatings on polymer laser induced periodic surface structures: assessment as substrates for surface-enhanced Raman scattering*, Physical Chemistry Chemical Physics. 14 pp:15699. doi:10.1039/c2cp43049e.

[127] Sanz, M., Rebollar, E., Ganeev, R.A., & Castillejo, M., (2013) *Nanosecond laser-induced periodic surface structures on wide band-gap semiconductors*, Applied Surface Science. 278 pp:325–329. doi:10.1016/j.apsusc.2012.11.137.

[128] von der Linde, D., Sokolowski-Tinten, K., & Bialkowski, J., (1997) *Laser–solid interaction in the femtosecond time regime*, Applied Surface Science. 109–110 pp:1–10. doi:10.1016/S0169-4332(96)00611-3.

[129] Shinonaga, T., Tsukamoto, M., Kawa, T., Chen, P., Nagai, A., & Hanawa, T., (2015) *Formation of periodic nanostructures using a femtosecond laser to control cell spreading on titanium*, Applied Physics B. 119 pp:493–496. doi:10.1007/s00340-015-6082-4.

[130] Wallat, K., Dörr, D., Le Harzic, R., Stracke, F., Sauer, D., Neumeier, M., Kovtun, A., Zimmermann, H., & Epple, M., (2012) *Cellular reactions toward nanostructured silicon surfaces created by laser ablation*, Journal of Laser Applications. 24 pp:042016. doi:10.2351/1.4732594.

[131] Bonse, J., Koter, R., Hartelt, M., Spaltmann, D., Pentzien, S., Höhm, S., Rosenfeld, A., & Krüger, J., (2014) *Femtosecond laser-induced periodic surface structures on steel and titanium alloy for tribological applications*, Applied Physics A. 117 pp:103–110. doi:10.1007/s00339-014-8229-2.

[132] Rajab, F.H., Liauw, C.M., Benson, P.S., Li, L., & Whitehead, K.A., (2018) *Picosecond laser treatment production of hierarchical structured stainless steel to reduce bacterial fouling*, Food and Bioproducts Processing. 109 pp:29–40. doi:10.1016/j.fbp.2018.02.009.

[133] Moradi, S., Kamal, S., Englezos, P., & Hatzikiriakos, S.G., (2013) *Femtosecond laser irradiation of metallic surfaces: Effects of laser parameters on superhydrophobicity*, Nanotechnology. 24. doi:10.1088/0957-4484/24/41/415302.

[134] Ardron, M., Weston, N., & Hand, D., (2014) *A practical technique for the generation of highly uniform LIPSS*, Applied Surface Science. 313 pp:123–131. doi:10.1016/j.apsusc.2014.05.154.

[135] Wang, Z., & Zhao, Q.-Z., (2018) *Friction reduction of steel by laser-induced periodic surface nanostructures with atomic layer deposited TiO2 coating*, Surface and Coatings Technology. 344 pp:269–275. doi:10.1016/j.surfcoat.2018.03.036.

[136] Vorobyev, A.Y., & Guo, C., (2008) *Femtosecond laser-induced periodic surface structure formation on tungsten*, Journal of Applied Physics. 104 pp:063523. doi:10.1063/1.2981072.

[137] Maragkaki, S., Derrien, T.J.Y.-Y., Levy, Y., Bulgakova, N.M., Ostendorf, A., & Gurevich, E.L., (2017) *Wavelength dependence of picosecond laser-induced periodic surface structures on copper*, Applied Surface Science. 417 pp:88–92. doi:10.1016/j.apsusc.2017.02.068.

[138] Gedvilas, M., Mikšys, J., & Račiukaitis, G., (2015) *Flexible periodical micro- and nano-structuring of a stainless steel surface using dual-wavelength double-pulse picosecond laser irradiation*, RSC Advances. 5 pp:75075–75080. doi:10.1039/C5RA14210E.

[139] Qi, L., Nishii, K., & Namba, Y., (2009) *Regular subwavelength surface structures induced by femtosecond laser pulses on stainless steel*, Optics Letters. 34 pp:1846. doi:10.1364/OL.34.001846.

[140] Nathala, C.S.R., Ajami, A., Ionin, A.A., Kudryashov, S.I., Makarov, S. V, Ganz, T., Assion,

A., & Husinsky, W., (2015) *Experimental study of fs-laser induced sub-100-nm periodic surface structures on titanium*, Optics Express. 23 pp:5915. doi:10.1364/OE.23.005915.

[141] Ionin, A.A., Kudryashov, S.I., Makarov, S. V., Seleznev, L. V., Sinitsyn, D. V., Ligachev, A.E., Golosov, E. V., & Kolobov, Y.R., (2013) *Sub-100 nanometer transverse gratings written by femtosecond laser pulses on a titanium surface*, Laser Physics Letters. 10 pp:056004. doi:10.1088/1612-2011/10/5/056004.

[142] Pan, A.F., Wang, W.J., Mei, X.S., Yang, H.Z., & Sun, X.F., (2017) *The formation mechanism and evolution of ps-laser-induced high-spatial-frequency periodic surface structures on titanium*, Applied Physics B. 123 pp:21. doi:10.1007/s00340-016-6613-7.

[143] Li, X.-F., Zhang, C.-Y., Li, H., Dai, Q.-F., Lan, S., & Tie, S.-L., (2014) *Formation of 100-nm periodic structures on a titanium surface by exploiting the oxidation and third harmonic generation induced by femtosecond laser pulses*, Optics Express. doi:10.1364/oe.22.028086.

[144] Bonse, J., & Gräf, S., (2021) *Ten Open Questions about Laser-Induced Periodic Surface Structures*, Nanomaterials. 11 pp:3326. doi:10.3390/nano11123326.

[145] Ouyang, J., Perrie, W., Allegre, O.J., Heil, T., Jin, Y., Fearon, E., Eckford, D., Edwardson, S.P., & Dearden, G., (2015) *Tailored optical vector fields for ultrashort-pulse laser induced complex surface plasmon structuring*, Optics Express. 23 pp:12562. doi:10.1364/OE.23.012562.

[146] Allegre, O.J., Jin, Y., Perrie, W., Ouyang, J., Fearon, E., Edwardson, S.P., & Dearden, G., (2013) *Complete wavefront and polarization control for ultrashort-pulse laser microprocessing*, Opt. Express. 21 pp:15942–15948. doi:10.1364/OE.21.021198.

[147] Skoulas, E., Manousaki, A., Fotakis, C., & Stratakis, E., (2017) *Biomimetic surface structuring using cylindrical vector femtosecond laser beams*, Scientific Reports. 7 pp:45114. doi:10.1038/srep45114.

[148] Drevinskas, R., Zhang, J., Beresna, M., Gecevičius, M., Kazanskii, A.G., Svirko, Y.P., & Kazansky, P.G., (2016) *Laser material processing with tightly focused cylindrical vector beams*, Applied Physics Letters. doi:10.1063/1.4953455.

[149] Sgobba, S., (2006) *Materials for high vacuum technology : an overview*, Proceedings of the CAS—CERN Accelerator School and ALBA Synchrotron Light Facility: Course on Vacuum in Accelerators. pp:117–143.

[150] Kerber, S.J., & Tverberg, J., (2000) *Stainless Steel*, Advanced Materials & Processes. pp:33–36.

[151] Tardio, S., Abel, M.-L., Carr, R.H., Castle, J.E., & Watts, J.F., (2015) *Comparative study of the native oxide on 316L stainless steel by XPS and ToF-SIMS*, Journal of Vacuum Science & Technology A: Vacuum, Surfaces, and Films. 33 pp:05E122. doi:10.1116/1.4927319.

[152] Mandrino, D., Godec, M., Torkar, M., & Jenko, M., (2008) *Study of oxide protective layers on stainless steel by AES, EDS and XPS*, Surface and Interface Analysis. 40 pp:285–289. doi:10.1002/sia.2718.

[153] Global Metals, (2018) *STAINLESS STEEL - 316 / 316L,*. [Online] Avaliable at: http://www.globalmetals.com.au/_pdf/Stainless_Steel/Stainless_Steel_316.pdf.

[154] Fredriksson, W., Malmgren, S., Gustafsson, T., Gorgoi, M., & Edström, K., (2012) *Full depth profile of passive films on 316L stainless steel based on high resolution HAXPES in combination with ARXPS*, Applied Surface Science. 258 pp:5790–5797. doi:10.1016/j.apsusc.2012.02.099.

[155] Olsson, C.-O.., & Landolt, D., (2003) *Passive films on stainless steels—chemistry, structure and growth*, Electrochimica Acta. 48 pp:1093–1104. doi:10.1016/S0013-4686(02)00841-1.

[156] Olefjord, I., & Elfstrom, B., (1982) *The Composition of the Surface during Passivation of Stainless Steels*, CORROSION. 38 pp:46–52. doi:10.5006/1.3577318.

[157] Park, C., Ha, T., & Cho, B., (2016) *Thermal outgassing rates of low-carbon steels*, Journal of Vacuum Science & Technology A: Vacuum, Surfaces, and Films. 34 pp:021601. doi:10.1116/1.4936840.

[158] Ishikawa, Y., Koguchi, Y., & Odaka, K., (1991) *Outgassing rate of some austenitic stainless steels*, Journal of Vacuum Science & Technology A: Vacuum, Surfaces, and Films. 9 pp:250–253. doi:10.1116/1.577529.

[159] Test.laservall-usa.com, (2017) *Laservall North America: Violino 532 nm (Green) Series DPSS Nd:YVO4 OEM Laser Sources*,. [Online] Avaliable at: http://www.test.laservall-usa.com/products/marking/violino_green/ (accessed August 1, 2018).

[160] Edge-wave.de, (2017) *Ultra short pulse lasers | EdgeWave*,. [Online] Avaliable at: https://www.edge-wave.de/web/en/produkte/ultra-short-pulse-systeme/px-serie/ (accessed August 1, 2018).

[161] F-214B-355 Vonjan-tech.de., (2017) *Lens - VON.JAN Technology (en).*,. [Online] Avaliable at: http://www.vonjan-tech.de/en/lens.html (accessed August 1, 2018).

[162] Laser Control., (2017) *Digi-Cube II from Laser Control Systems.*,. [Online] Avaliable at: http://www.lasercontrols.com/digi-cube-ii-laser-scan-head/ (accessed August 1, 2018).

[163] Laser Control., (2017) *Digi-Struct Software - Laser Control.*,. [Online] Avaliable at: http://www.lasercontrols.com/digi-struct-software/ (accessed August 1, 2018).

[164] Evans, C.H., (1986) *Introduction to mass spectrometry*, Trends in Biochemical Sciences. 11 pp:124–125. doi:10.1016/0968-0004(86)90058-7.

[165] Watson, J.T., & Sparkman, O.D., (2008) *Introduction*, in: Introduction to Mass Spectrometry, John Wiley & Sons, Ltd, Chichester, UK, 2008: pp. 1–52. doi:10.1002/9780470516898.ch1.

[166] Przybylski, M., (2014) *Mass Spectrometry*, in: Handbook of Spectroscopy, Wiley-VCH Verlag GmbH & Co. KGaA, Weinheim, Germany, 2014: pp. 355–406. doi:10.1002/9783527654703.ch11.

[167] Hoffmann, E. de, & Stroobant, V., (2007) *Mass Analysers*, in: Mass Spectrometry Third Edition: Principles and Applications, 3rd ed., Wiley-Interscience, 2007.

[168] Che, F.Y., Deng, H.T., & Ding, S.J., (2015) *Mass spectrometry applications in biomedical research*, BioMed Research International. doi:10.1155/2015/827370.

[169] Flowers, P., Robinson, W.R., Langley, R., & Theopold, K., (2015) *2.3 Atomic Structure and Symbolism*, in: Chemistry, OpenStax, Houston, Texas, 2015. [Online] Avaliable at: https://openstax.org/books/chemistry/pages/2-3-atomic-structure-and-symbolism.

[170] Image, (2017) *Liquid Chromatography Mass Spectrometer - Wikimedia Commons*,. [Online] Avaliable at: https://commons.wikimedia.org/wiki/File:Liquid_Chromatography_Mass_Spectrometer.png (accessed June 18, 2018).

[171] Keyence.co.uk, (2017) *VHX-5000 - Digital Microscope | VHX-5000 series | KEYENCE UK & Ireland.*,. [Online] Avaliable at: http://www.keyence.co.uk/products/microscope/digital-microscope/vhx-5000/models/vhx-5000/index.jsp (accessed August 4, 2017).

[172] Keyence.com, (2018) *3D Laser Scanning Microscope, VK-X200*,. [Online] Avaliable at:

https://www.keyence.com/keyence-tv/VK-X200_3D_Laser_Scanning_Microscope.jsp (accessed June 4, 2019).

[173] Inkson, B.J., (2016) *Scanning electron microscopy (SEM) and transmission electron microscopy (TEM) for materials characterization*, in: Materials Characterization Using Nondestructive Evaluation (NDE) Methods, Elsevier, 2016: pp. 17–43. doi:10.1016/B978-0-08-100040-3.00002-X.

[174] JPK AG, (2018) *NanoWizard® 4 NanoScience AFM - JPK BioAFM | Bruker*,. [Online] Avaliable at: https://www.jpk.com/products/atomic-force-microscopy/nanowizard-4-nanoscience (accessed June 10, 2019).

[175] BudgetSensors, (2018) *AFM Tip: Tap300Al-G*, BudgetSensors. [Online] Avaliable at: https://www.budgetsensors.com/tapping-mode-afm-probe-aluminum-tap300al.

[176] Bruker, (2018) *AFM Tip: HAR1-200A-10*, Bruker. [Online] Avaliable at: https://www.brukerafmprobes.com/p-3976-har1-200a-10.aspx.

[177] Fadley, C.S., (2010) *X-ray photoelectron spectroscopy: Progress and perspectives*, Journal of Electron Spectroscopy and Related Phenomena. 178–179 pp:2–32. doi:10.1016/j.elspec.2010.01.006.

[178] Engelhard, M.H., Droubay, T.C., & Du, Y., (2017) *X-Ray Photoelectron Spectroscopy Applications*, in: Encyclopedia of Spectroscopy and Spectrometry, Elsevier, 2017: pp. 716–724. doi:10.1016/B978-0-12-409547-2.12102-X.

[179] Harvey, D., (2022) *21.2: Spectroscopic Surface Methods*, in: Instrumental Analysis (LibreTexts), DePauw University, 2022. [Online] Avaliable at: https://chem.libretexts.org/Bookshelves/Analytical_Chemistry/Instrumental_Analysis_(LibreTexts)/21%3A_Surface_Characterization_by_Spectroscopy_and_Microscopy/21.02%3A_Spectroscopic_Surface_Methods.

[180] Muramoto, S., Graham, D.J., Wagner, M.S., Lee, T.G., Moon, D.W., & Castner, D.G., (2011) *ToF-SIMS Analysis of Adsorbed Proteins: Principal Component Analysis of the Primary Ion Species Effect on the Protein Fragmentation Patterns*, The Journal of Physical Chemistry C. 115 pp:24247–24255. doi:10.1021/jp208035x.

[181] SERC-Carleton.edu, (2007) *Schematic diagram of the IonTOF ToF-SIMS instrument*,. [Online] Avaliable at: https://serc.carleton.edu/download/images/8384/evans_trift_system_and_camecas_1172767017.v2.jpg.

[182] Mantus, D.S., Ratner, B.D., Carlson, B.A., & Moulder, J.F., (1993) *Static secondary ion mass spectrometry of adsorbed proteins*, Analytical Chemistry. 65 pp:1431–1438. doi:10.1021/ac00058a021.

[183] Henry, M., & Bertrand, P., (2009) *Surface composition of insulin and albumin adsorbed on polymer substrates as revealed by multivariate analysis of ToF-SIMS data*, Surface and Interface Analysis. 41 pp:105–113. doi:10.1002/sia.2993.

[184] Henry, M., Dupont-Gillain, C., & Bertrand, P., (2008) *Characterization of Insulin Adsorption in the Presence of Albumin by Time-of-Flight Secondary Ion Mass Spectrometry and X-ray Photoelectron Spectroscopy*, Langmuir. 24 pp:458–464. doi:10.1021/la701850p.

[185] Liu, J.M., (1982) *Simple technique for measurements of pulsed Gaussian-beam spot sizes*, Optics Letters. 7 pp:196. doi:10.1364/OL.7.000196.

[186] Sun, Z., Lenzner, M., & Rudolph, W., (2015) *Generic incubation law for laser damage and ablation thresholds*, Journal of Applied Physics. 117 pp:073102. doi:10.1063/1.4913282.

[187] Jee, Y., Becker, M.F., & Walser, R.M., (1988) *Laser-induced damage on single-crystal metal surfaces*, Journal of the Optical Society of America B. 5 pp:648. doi:10.1364/JOSAB.5.000648.

[188] Di Niso, F., Gaudiuso, C., Sibillano, T., Mezzapesa, F.P., Ancona, A., & Lugarà, P.M., (2014) *Role of heat accumulation on the incubation effect in multi-shot laser ablation of stainless steel at high repetition rates*, Optics Express. 22 pp:12200. doi:10.1364/OE.22.012200.

[189] Di Niso, F., Gaudiuso, C., Sibillano, T., Mezzapesa, F.P., Ancona, A., & Lugarà, P.M., (2013) *Influence of the Repetition Rate and Pulse Duration on the Incubation Effect in Multiple-Shots Ultrafast Laser Ablation of Steel*, Physics Procedia. 41 pp:698–707. doi:10.1016/j.phpro.2013.03.136.

[190] Mezera, M., & Römer, G.R.B.E., (2019) *Model based optimization of process parameters to produce large homogeneous areas of laser-induced periodic surface structures*, Optics Express. 27 pp:6012. doi:10.1364/OE.27.006012.

[191] ROSENBERG, B., (1962) *Electrical Conductivity of Proteins*, Nature. 193 pp:364–365. doi:10.1038/193364a0.

[192] Williams, D.F., Kellar, E.J.C., Jesson, D.A., & Watts, J.F., (2017) *Surface analysis of 316 stainless steel treated with cold atmospheric plasma*, Applied Surface Science. 403 pp:240–247. doi:10.1016/j.apsusc.2017.01.150.

[193] Castle, J.E., (2008) *The Composition of Metal Surfaces After Atmospheric Exposure: An Historical Perspective*, The Journal of Adhesion. 84 pp:368–388. doi:10.1080/00218460802004477.

[194] Frateur, I., Lecoeur, J., Zanna, S., Olsson, C.-O.A., Landolt, D., & Marcus, P., (2007) *Adsorption of BSA on passivated chromium studied by a flow-cell EQCM and XPS*, Electrochimica Acta. 52 pp:7660–7669. doi:10.1016/j.electacta.2006.12.060.

[195] Azioune, A., Siroti, F., Tanguy, J., Jouini, M., Chehimi, M.M., Miksa, B., & Slomkowski, S., (2005) *Interactions and conformational changes of human serum albumin at the surface of electrochemically synthesized thin polypyrrole films*, Electrochimica Acta. 50 pp:1661–1667. doi:10.1016/j.electacta.2004.10.014.

[196] Smith, M., Scudiero, L., Espinal, J., McEwen, J.-S., & Garcia-Perez, M., (2016) *Improving the deconvolution and interpretation of XPS spectra from chars by ab initio calculations*, Carbon. 110 pp:155–171. doi:10.1016/j.carbon.2016.09.012.

[197] De Vito, E., & Marcus, P., (1992) *XPS study of passive films formed on molybdenum-implanted austenitic stainless steels*, Surface and Interface Analysis. 19 pp:403–408. doi:10.1002/sia.740190175.

[198] Marcus, P., & Olefjord, I., (1988) *A Round Robin on combined electrochemical and AES/ESCA characterization of the passive films on Fe-Cr and Fe-Cr-Mo alloys*, Corrosion Science. 28 pp:589–602. doi:10.1016/0010-938X(88)90026-1.

[199] Maurice, V., Peng, H., Klein, L.H., Seyeux, A., Zanna, S., & Marcus, P., (2015) *Effects of molybdenum on the composition and nanoscale morphology of passivated austenitic stainless steel surfaces*, Faraday Discussions. 180 pp:151–170. doi:10.1039/C4FD00231H.

[200] Wang, Z., Di-Franco, F., Seyeux, A., Zanna, S., Maurice, V., & Marcus, P., (2019) *Passivation-Induced Physicochemical Alterations of the Native Surface Oxide Film on 316L Austenitic Stainless Steel*, Journal of The Electrochemical Society. 166 pp:C3376–C3388. doi:10.1149/2.0321911jes.

[201] Van Ham, R., Adriaens, A., Van Vaeck, L., & Adams, F., (2006) *The use of time-of-flight*

static secondary ion mass spectrometry imaging for the molecular characterization of single aerosol surfaces, Analytica Chimica Acta. 558 pp:115–124. doi:10.1016/j.aca.2005.11.041.

[202] Li, J., Xie, W., Weng, L., Chan, C.K., & Chan, C., (2020) *Effects of pretreatment temperature on the analysis of size-fractionated aerosol particles using ToF-SIMS*, Surface and Interface Analysis. 52 pp:264–271. doi:10.1002/sia.6751.

[203] Font Palma, C., Evans, G.J., & Sodhi, R.N.S., (2007) *Imaging of aerosols using time of flight secondary ion mass spectrometry*, Applied Surface Science. 253 pp:5951–5956. doi:10.1016/j.apsusc.2006.12.126.

[204] Cheng, W., Weng, L.-T., Li, Y., Lau, A., Chan, C., & Chan, C.-M., (2014) *Characterization of size-segregated aerosols using ToF-SIMS imaging and depth profiling*, Surface and Interface Analysis. 46 pp:480–488. doi:10.1002/sia.5552.

[205] Lu, Y., Shi, X., Huang, Z., Li, T., Zhang, M., Czajkowski, J., Fabritius, T., Huttula, M., & Cao, W., (2017) *Nanosecond laser coloration on stainless steel surface*, Scientific Reports. 7 pp:7092. doi:10.1038/s41598-017-07373-8.

[206] Eichstädt, J., Römer, G.R.B.E., & Huis in 't Veld, A.J., (2013) *Determination of irradiation parameters for laser-induced periodic surface structures*, Applied Surface Science. 264 pp:79–87. doi:10.1016/j.apsusc.2012.09.120.

[207] Reif, J., Costache, F., Varlamova, O., Jia, G., & Ratzke, M., (2009) *Self-organized regular surface patterning by pulsed laser ablation*, Physica Status Solidi (C). 6 pp:681–686. doi:10.1002/pssc.200880719.

[208] Cha, D., & Axinte, D., (2021) *Transient thermal model of nanosecond pulsed laser ablation: Effect of heat accumulation during processing of semi-transparent ceramics*, International Journal of Heat and Mass Transfer. 173 pp:121227. doi:10.1016/j.ijheatmasstransfer.2021.121227.

[209] Pauzon, C., Hryha, E., Forêt, P., & Nyborg, L., (2019) *Effect of argon and nitrogen atmospheres on the properties of stainless steel 316 L parts produced by laser-powder bed fusion*, Materials & Design. 179 pp:107873. doi:10.1016/j.matdes.2019.107873.

[210] Spiro, A., Lowe, M., & Pasmanik, G., (2012) *Drilling rate of five metals with picosecond laser pulses at 355, 532, and 1064 nm*, Applied Physics A. 107 pp:801–808. doi:10.1007/s00339-012-6910-x.

[211] Suwardy, J., Akhir, M.P.M., Kurniawan, R., Hermanto, B.R., Anshori, I., & Fauzi, M.H., (2022) *Simulation of Laser-Heating and Energetic Plasma Plume Expansion in Pulsed Laser Deposition of Y3Fe5O12*, Micromachines. 13 pp:2012. doi:10.3390/mi13112012.

[212] Hussein, A.E., Diwakar, P.K., Harilal, S.S., & Hassanein, A., (2013) *The role of laser wavelength on plasma generation and expansion of ablation plumes in air*, Journal of Applied Physics. 113. doi:10.1063/1.4800925.

[213] Diwakar, P.K., Harilal, S.S., Phillips, M.C., & Hassanein, A., (2015) *Characterization of ultrafast laser-ablation plasma plumes at various Ar ambient pressures*, Journal of Applied Physics. 118 pp:043305. doi:10.1063/1.4927625.

[214] Farid, N., Harilal, S.S., Ding, H., & Hassanein, A., (2014) *Emission features and expansion dynamics of nanosecond laser ablation plumes at different ambient pressures*, Journal of Applied Physics. 115. doi:10.1063/1.4862167.

[215] Pangovski, K., Otanocha, O.B., Zhong, S., Sparkes, M., Liu, Z., O'Neill, W., & Li, L., (2017) *Investigation of plume dynamics during picosecond laser ablation of H13 steel using high-speed digital holography*, Applied Physics A. 123 pp:114. doi:10.1007/s00339-016-0589-3.

[216] Cirisan, M., Jouvard, J.M., Lavisse, L., Hallo, L., & Oltra, R., (2011) *Laser plasma plume structure and dynamics in the ambient air: The early stage of expansion*, Journal of Applied Physics. 109 pp:103301. doi:10.1063/1.3581076.

[217] Bleiner, D., Chen, Z., Autrique, D., & Bogaerts, A., (2006) *Role of laser-induced melting and vaporization of metals during ICP-MS and LIBS analysis, investigated with computer simulations and experiments*, Journal of Analytical Atomic Spectrometry. 21 pp:910–921. doi:10.1039/b602800d.

[218] Russbueldt, P., Weitenberg, J., Schulte, J., Meyer, R., Meinhardt, C., Hoffmann, H.D., & Poprawe, R., (2019) *Scalable 30 fs laser source with 530 W average power*, Optics Letters. doi:10.1364/ol.44.005222.

[219] Bruening, S., Jarczynski, M., Du, K., & Gillner, A., (2018) *Large scale ultrafast laser micro texturing with multi-beams*, Journal of Laser Micro Nanoengineering. doi:10.2961/jlmn.2018.03.0019.

[220] Rubinsztein-Dunlop, H., Forbes, A., Berry, M. V., Dennis, M.R., Andrews, D.L., Mansuripur, M., Denz, C., Alpmann, C., Banzer, P., Bauer, T., Karimi, E., Marrucci, L., Padgett, M., Ritsch-Marte, M., Litchinitser, N.M., Bigelow, N.P., Rosales-Guzmán, C., Belmonte, A., Torres, J.P., Neely, T.W., Baker, M., Gordon, R., Stilgoe, A.B., Romero, J., White, A.G., Fickler, R., Willner, A.E., Xie, G., McMorran, B., & Weiner, A.M., (2017) *Roadmap on structured light*, Journal of Optics. 19 pp:013001. doi:10.1088/2040-8978/19/1/013001.

[221] JJ Nivas, J., Allahyari, E., Cardano, F., Rubano, A., Fittipaldi, R., Vecchione, A., Paparo, D., Marrucci, L., Bruzzese, R., & Amoruso, S., (2018) *Surface structures with unconventional patterns and shapes generated by femtosecond structured light fields*, Scientific Reports. doi:10.1038/s41598-018-31768-w.

[222] Nivas, J.J.J., Shutong, H., Anoop, K.K., Rubano, A., Fittipaldi, R., Vecchione, A., Paparo, D., Marrucci, L., Bruzzese, R., & Amoruso, S., (2015) *Laser ablation of silicon induced by a femtosecond optical vortex beam*, Optics Letters. doi:10.1364/ol.40.004611.

[223] Sun, B., Salter, P.S., & Booth, M.J., (2015) *Pulse front adaptive optics: a new method for control of ultrashort laser pulses*, Optics Express. doi:10.1364/oe.23.019348.

[224] Govekar, E., Jeromen, A., Kuznetsov, A., Levy, G., & Fujishima, M., (2018) *Study of an annular laser beam based axially-fed powder cladding process*, CIRP Annals. doi:10.1016/j.cirp.2018.04.082.

[225] Duocastella, M., & Arnold, C.B., (2012) *Bessel and annular beams for materials processing*, Laser & Photonics Reviews. 6 pp:607–621. doi:10.1002/lpor.201100031.

[226] Zhu, G., Whitehead, D., Perrie, W., Allegre, O.J., Olle, V., Li, Q., Tang, Y., Dawson, K., Jin, Y., Edwardson, S.P., Li, L., & Dearden, G., (2018) *Investigation of the thermal and optical performance of a spatial light modulator with high average power picosecond laser exposure for materials processing applications*, Journal of Physics D: Applied Physics. doi:10.1088/1361-6463/aaa948.

[227] Allegre, O.J., Li, Z., & Li, L., (2019) *Tailored laser vector fields for high-precision micro-manufacturing*, CIRP Annals. 68 pp:193–196. doi:10.1016/j.cirp.2019.04.125.

[228] Weber, R., Michalowski, A., Abdou-Ahmed, M., Onuseit, V., Rominger, V., Kraus, M., & Graf, T., (2011) *Effects of radial and tangential polarization in laser material processing*, in: Physics Procedia, 2011. doi:10.1016/j.phpro.2011.03.004.

[229] Wang, H., Shi, L., Lukỳanchuk, B., Sheppard, C., & Chong, C.T., (2008) *Creation of a needle of longitudinally polarized light in vacuum using binary optics*, Nature Photonics.

doi:10.1038/nphoton.2008.127.

[230] Cheng, H., Li, P., Liu, S., Chen, P., Han, L., Zhang, Y., Hu, W., & Zhao, J., (2017) *Vortex-controlled morphology conversion of microstructures on silicon induced by femtosecond vector vortex beams*, Applied Physics Letters. doi:10.1063/1.4994926.

[231] Jin, Y., Perrie, W., Harris, P., Allegre, O.J., Abrams, K.J., & Dearden, G., (2015) *Patterning of Aluminium thin film on polyethylene terephthalate by multi-beam picosecond laser*, Optics and Lasers in Engineering. 74 pp:67–74. doi:10.1016/j.optlaseng.2015.04.006.

[232] Zhan, Q., (2009) *Cylindrical vector beams: from mathematical concepts to applications*, Advances in Optics and Photonics. 1 pp:1. doi:10.1364/AOP.1.000001.

[233] Watson, J.T., & Sparkman, O.D., (2007) *Introduction to Mass Spectrometry: Instrumentation, Applications and Strategies for Data Interpretation*, 4th ed., Wiley, 2007. doi:10.1002/9780470516898.

[234] Gross, J.H., (2017) *Mass Spectrometry*, 3rd ed., Springer International Publishing, Cham, 2017. doi:10.1007/978-3-319-54398-7.